

Vibrational Spectroscopy at High Pressures

A thesis presented for the degree of Doctor of Philosophy

in

Faculty of Science

By

ALAN DAVID WILLIAMS

University of Leicester

1980

UMI Number: U311423

All rights reserved

INFORMATION TO ALL USERS

The quality of this reproduction is dependent upon the quality of the copy submitted.

In the unlikely event that the author did not send a complete manuscript and there are missing pages, these will be noted. Also, if material had to be removed, a note will indicate the deletion.



UMI U311423

Published by ProQuest LLC 2015. Copyright in the Dissertation held by the Author.
Microform Edition © ProQuest LLC.

All rights reserved. This work is protected against
unauthorized copying under Title 17, United States Code.



ProQuest LLC
789 East Eisenhower Parkway
P.O. Box 1346
Ann Arbor, MI 48106-1346



THESIS
612389
20 " 80

x752951113

Statement

The work presented in this thesis is original unless acknowledged in the text or by reference, and was carried out by the author in the Department of Chemistry of the University of Leicester between October 1976 and May 1979. This work has not been, nor will be presented for any other degree.

A handwritten signature in black ink, appearing to read 'A. Williams', with a long, sweeping horizontal stroke extending to the right.

A. D. Williams

VIBRATIONAL SPECTROSCOPY AT HIGH PRESSURES

ALAN DAVID WILLIAMS

ABSTRACT

A review of high pressure work is presented with over 100 references spanning the period from October 1976 to March 1979. A full discussion is given of the history of Diamond Anvil Cell (DAC) design.

Two new designs of DAC are tested, as are two different types of diamond anvil. Pressures in excess of 0.25 Megabars have been generated, and a study of benzene has been undertaken to test one of the new cells.

Mid and far infrared spectra of ferrocene were recorded and compared with existing data on the solid state properties of this material.

Raman and far infrared spectra of K_2PtCl_6 and K_2ReCl_6 at various temperatures and pressures have been obtained, and with thermal expansion and compressibility data, an attempt to relate the frequency shifts to anharmonic parameters has been performed. This study was extended to cover the pressure dependence of a further ten compounds of the form A_2MX_6 .

The phase behaviour of calcite ($CaCO_3$) has been examined using mid and far infrared spectroscopy to 40 kbar, and the data analysed in conjunction with the results of Fong and Nicol.

The effect of pressure and hence spin state on the far infrared spectra of some complexes of the form $Fe\text{phen}_2X_2$ has been studied.

Acknowledgements

I would like to extend sincere thanks to my supervisor, Dr. David Adams, whose extensive aid and encouragement has proved so vital in the production of this work.

My thanks also go to the technical staff of the Chemistry Department, and of the Computer Facility at Leicester University. Dr. Roger Appleby deserves a special mention as a source of friendship and help in the first year of my course, as do all my contemporaries in the high pressure group, for making my years pleasurable.

Thanks to Mrs. A. Crane for drawing or tracing the majority of the figures in this thesis, and special thanks to Mrs. S. Crowe for turning a totally indecipherable text into this script.

Finally, I would like to thank all my relations, especially my wife Carolyn, for constant encouragement, and I acknowledge the receipt of a maintenance grant from the Science Research Council.

TO CAROLYN

CONTENTS

	Page	
Chapter 1	A Review of Vibrational Spectroscopy of Solids at High Pressures.	1
Chapter 2	The Operation of the Diamond Anvil Cell and Ancillary Equipment.	27
Chapter 3	The Diamond Anvil Cell; History and Test of Two New Cells and Anvil Design.	50
Chapter 4	An Infrared Study of Ferrocene at High Pressures and Low Temperatures.	127
Chapter 5	A Study of the Infrared, Raman and X ray Diffraction spectra of K_2PtCl_6 and K_2ReCl_6 at High Pressures and Low Temperatures.	151
Chapter 6	An Infrared and Raman Study of the Pressure Dependence of some complexes of the form A_2MX_6 .	228
Chapter 7	An Infrared Study of the Metastable Phases of $CaCO_3$.	281
Chapter 8	A Study of the Effect of Pressure on the Far Infrared Spectra of some complexes $Fe(o\text{-phenanthraline})_2 X_2$.	309

CHAPTER 1

A REVIEW OF VIBRATIONAL SPECTROSCOPY OF SOLIDS

AT HIGH PRESSURES

CHAPTER 1

A REVIEW OF VIBRATIONAL SPECTROSCOPY OF SOLIDS AT HIGH PRESSURE

1.1 Introduction

The field of research into the effects of high pressures on solids is now well established. With respect to vibrational spectroscopy, better, more stable cells and improvements in optical coupling to spectrometers has led to great interest in this type of work. This chapter is intended as an introduction to the work performed in this field from October 1976 to March 1979, both on equipment and spectroscopic data. The references given have been compiled by following Chemical Abstracts for that period. Reviews of the trends in high pressure research have been performed by Payne (1) and Appleby (2). These cover the literature to ca. August 1976.

In a very detailed review on the applications of Fourier transform interferometry to infrared studies at high pressures, Lauer (3), considered the instrumentation involved in containing samples under high pressure. The advantages of interferometers over dispersive instruments, and applications of the studies to gases, liquids and solids together with reaction studies at high pressures were also reviewed.

The problems of accurately measuring the pressure to which a sample is subjected is clearly of paramount importance. A review by Akimoto (4) of very high pressure calibration, and high pressure/temperature X ray studies has recently been published.

There have been two excellent reviews of high pressure - high temperature phases of the elements. Young (5) has compiled phase diagrams for all the reported solid-solid and solid-liquid phase boundaries, whilst Cannon (6) published a similar report which is restricted to those materials for which the crystal structures of the high pressure phases have been identified either by X ray or neutron diffraction techniques. This latter report, which contains some sixty phase diagrams is a critical evaluation of the phase boundaries, and contains tables of the crystallographic data from the individual phases.

Merill (7) has presented a survey of polymorphic phase diagrams as functions of pressure and temperature for the elements and simple inorganic compounds, and contains tables of crystallographic data for various high pressure and high temperature phases of the elements, together with ca. 220 simple AB type compounds.

A review of the effects of high hydrostatic pressures on the mechanical properties of solids has also been published recently (8).

This review of the literature is mainly concerned with high pressure vibrational spectroscopy, but several references to X ray work are given, since when attempting to interpret the vibrational spectra of solids, it is generally desirable to obtain as much information about the structure of the material as possible. Hence crystallography and vibrational spectroscopy are complementary when studying high pressure responses of materials.

1.2 Cells and ancillary equipment

The advances in pressure cell design over the last few years have been rapid, achieving higher pressures and larger, more controllable temperature ranges.

Holzapfel (9) has reported a device using tungsten carbide or boron carbide anvils, capable of attaining pressures of ca. 140 kbar and cooled by liquid helium. This then can operate on an X ray diffractometer in Debye Scherrer geometry. A high pressure study of polycrystalline bismuth to 2K has been performed in a variable temperature cell by Spain (10), who, in another article, gives some simple improvements which can be made to a DAC (Diamond Anvil Cell) to make it more suitable for X ray diffraction studies (11); a similar report by Schiferl (12) gives details of improved beryllium supports upon which the diamond anvils are seated.

The lowest temperature reported in a DAC is that of Webb (13) in which a cryostat, capable of 100 kbar, and 0.03K was used to study the transition temperature in aluminium. The cooling is provided by a $^3\text{He} - ^4\text{He}$ dilution refrigerator, and changes in the magnetic moment of the sample are detected using a super conducting quantum interference device.

Holzapfel (14) has used a DAC for single crystal studies up to 100 kbar. A similar DAC was used by Schiferl (15) to study antimony to 26 kbar. This he later extended (16) to a device capable of 90 kbar to be used on an automatic four circle diffractometer. An adaption of a DAC has been devised by Bassett (17) to investigate

the strain ellipsoids and hence the strength of materials under pressure up to 300 kbar. A technique has been evolved by Schulz (18) for measuring high pressure data collected on a four circle X ray diffractometer.

Considerable equipment and expertise has been developed in order to couple high pressure cells to spectroscopic or crystallographic apparatus. Adams and Sharma (19) have undertaken a precise analysis of the optics of a DAC, and subsequently designed a simple refracting beam condenser to be used in coupling the DAC to an infrared spectrometer. The problems associated with high pressure Raman spectroscopy has been investigated by Schoen, Schnur and Sheridan (2) and techniques for observing weak signals in the DAC discussed. These involve arranging for the laser to enter the DAC with 15° off-normal incidence. Webber (21) has described and used an optical system for both UV/visible and infrared transmittance in which spectra have been obtained up to 200 kbar. The same system can be used to make reflectance measurements at pressures around 70 kbar (22).

Bassett (23) has developed an apparatus in which high temperatures are generated with the use of a Nd/YAG laser, focussed upon the sample contained within the DAC, thus greatly simplifying the heating of a sample under pressure.

Calibration of the pressure within the cell is of obvious importance, and considerable work has been performed to this end. A cell using sapphire windows (24) has been used down to temperature of 4.2K for Raman spectroscopy, the pressure on the sample determined by the shift of the R_1 and R_2 lines of the windows.

The most common method of pressure determination in DAC's is to include a small chip of ruby with the sample, and monitor the behaviour of the R_1 , R_2 lines. Research by Shchanov (25) has covered the shift of the R_1 band up to 550 kbar; Mao and Bell have measured the position of the R_1 fluorescence line against X ray specific volume measurements on Cu, Mo, Pd and Ag, and obtained a relation which extends the usefulness of ruby to 1 Megabar and beyond (26).

DAC use has not been confined to solid state research. A novel series of experiments were performed by Piermarini (27) to estimate the viscosity of a 4:1 mixture of methanol:ethanol (the most common hydrostatic medium used in high pressure research); these consisted of observation of a nickel alloy sphere falling under gravity through the medium, and led the authors to conclude that methanol:ethanol remains liquid to 70 kbar, although at this pressure the viscosity of the fluid is very high. Application of high pressures to gases (28) has resulted in the observation of high pressure phases of CO_2 and $n\text{-D}_2$.

Currently the highest static pressure generated in a DAC is that attained by Mao and Bell (29), who generated 1.72 Megabar between a pair of bevelled diamond anvils, and observed macroscopic plastic deformation of one of the diamond pressure faces.

1.3 Diamond Anvils

The reaction of the diamond anvils to high applied pressures, and selection of suitable diamonds for spectroscopic applications have been considered in two papers by Adams (30, 31). The first of these considers choice of material for diamond anvils, gives infrared and Raman spectra of several stones, and outlines criteria for selection of suitable anvil material. The second contains results of extensive computer aided design work on diamond anvils under a wide variety of loading conditions and constraints.

The Raman spectrum of diamond under elevated pressures has been studied, and comparison of spectroscopic mode Grüneisens with thermodynamic data suggests that nearest neighbour interactions dominate the harmonic and anharmonic behaviour of diamond (32).

To observe the mode of deformation of diamond anvils when subjected to high pressures Ruoff (31) forced small, spherically polished diamond indentors into flat polished diamond, and reports the effects. Mao and Bell (34) have studied the pressure distribution about the face of the diamond anvils with a variety of gaskets at varying pressures, and concluded that to generate the highest pressures it was preferable to bevel the faces of the diamond anvils, and attained 1.5 Megabar with a pair of anvils which had a 2° bevel ground onto the diamond faces. Dunn (35) has investigated the yield stress of opposed anvils, as has Mao (36) who presents a more general analysis of the whole of the diamond anvil cell.

1.4 Studies in Vibrational Spectroscopy and X ray Diffraction at high pressures

The reasons for interest in high pressure vibrational spectroscopy, and X ray diffraction are many fold. The first and foremost is to study phases of systems not stable at ambient conditions. A second reason is that knowledge of the behaviour of various vibrational frequencies can aid in understanding the ambient spectrum. A further reason is that research of this kind can help to answer the fundamental question, why does a particular material adopt some particular structure at ambient conditions, whereas a similar substance may adopt some different form?

Reports of work appearing in the literature of interest in this area are summarised below, divided into two sections, organic and inorganic systems.

1.4.1 Organic Systems

Relatively few reports of vibrational or crystallographic work on organic compounds have been noted during the period covered by this review. However, considerable interest has developed in high pressure studies of the fluorescence and visible/UV properties of organic materials, but these are strictly outside the scope of this work.

Adams and Appleby (37) demonstrated the versatility of the diamond anvil cell in a study of the high pressure phases of benzene in the mid infrared, far infrared and Raman; Benzene I and II were characterised and the existence of benzene III was postulated. Benzene was also studied by Medina (38) in Brillouin zone scattering experiments up to 3.3 kbar. p-Dichlorobenzene polymorphism has also been investigated by Raman spectroscopy (39).

The effect of pressure on the infrared spectra of alkali and alkaline earth formates was the subject of work by Hamman (40), who discovered two new phases of HCO_2Na at elevated pressures, and one for each of the potassium, rubidium and caesium salts; high pressure forms of the calcium, barium and anhydrous lithium salts are proposed, though not observed in the range 0 - 42 kbar. A further study of phase transitions of the formates of the rare earths by high pressure infrared was performed (41), as was work on 12 compounds with the general formula XY_2ZO_4 (42). The influence of pressure on the rates of deuteration of formate and acetate ions in liquid D_2O has been investigated to 8 kbar (43). Ammonium formate has been studied, together with several deuterated forms (44) by infrared spectroscopy, and spectral changes occurring during a phase transition at 12 kbar suggest that the intermolecular $\text{NH} \dots \text{O}$ hydrogen bonding weakens, and more intimate packing occurs. Hydrogen bonding in compounds with strong $\text{X}-\text{H} \dots \text{Y}$ (45) and $\text{X}-\text{H} \dots \text{X}$ (46) has been investigated with the observation of Fermi resonance "windows" forming upon compression for two of the substances under consideration.

The phase diagram of polythene has been under investigation for some time (see for example 47, 48, 49). A recent paper (50) studies the growth of an extended chain crystal of polythene under high pressure, and determines the temperature dependence of its lattice parameters.

Studies of single crystals are becoming more common, and a single crystal and powder study of dianthracene, the photodimer of anthracene formed in the solid state, have been performed to 32 kbar, and in a temperature range of 77 to 410K (51).

Above pressures of 10 kbar, a fluorescence background appears in the Raman spectrum, which is attributed to direct excitation of close coupled sandwich like dimer defects created and trapped in the crystal under pressure.

The effect of pressure on molecular conformations has been investigated by Whalley (52) with a study of the internal rotation angle in trithiane, which tests a suggestion by Hamman et al. (53) that the molecule goes into a flat conformation from the puckered at a few tens of kilobars, and this, to a large extent is borne out by the Raman work of Whalley.

Fast scan Fourier transform interferometry has been used to study far infrared spectra at high pressures, specifically to investigate the effect of pressure on various 1,4, dihalocyclohexanes (54).

In a series of papers Newman et al (55, 56, 57, 58) reported the effect of pressure and temperature on polymers by X ray diffraction techniques utilising hexamethylenetriamine in a DAC in the range 0 - 15 kbar.

1.4.2 Inorganic Systems

An appreciable amount of work has been performed investigating the response of elemental solids to high pressures. As previously related, measurements of the specific volume of four metals have been performed to extend the ruby pressure gauge (26). α Selenium and α tellurium, which both have trigonal structures at ambient pressure, with infinite helices parallel to the c axis have been studied up to 86 and 40 kbar respectively by single crystal X ray diffraction (59), and deviations from structural homology are observed as the high pressure phase

transitions are approached. Polymorphism in gallium at high pressure has been observed (60) by X ray methods, and Ga II noted, being body centred cubic, and Ga III, which is related to a body centred tetragonal system. The only report of high pressure vibrational studies on solid state elements is that of Asami and Minomura (61) in which the first order Raman spectrum of Ge is studied, and the existence of Ge III was confirmed, formed by initial compression of Ge to 100 kbar, which transforms to metallic Ge II, a β Sn-type structure, and subsequent pressure release, the Ge being retained as metastable Ge III.

The phase diagrams of both sodium and potassium cyanides have been subjects of considerable interest. Dultz (62) proposes phase diagrams for NaCN and KCNS in the range 110 - 300K, and 7 - 55 kbar, obtained by a study of the Raman spectra of the various phases involved. The two orthorhombic low temperature phases have been observed at pressures up to 6 kbar (63) with a doubling of the unit cell in going from the disordered phase D_{Zh}^{25} , to the ordered low temperature phase, D_{Zh}^{13} .

Adams and Sharma (64) have also investigated the Raman spectra of NaCN and KCN to 37 and 55 kbar respectively. Results for NaCN confirm those of Dultz et al, up to 6 kbar. Also noted is a change in gradient, $\frac{dw}{dP}$ for the CN band above 21 kbar, coupled with a similar change in gradient for two of the low frequency bands, but no structural significance is assigned to these changes. The appearance of a broad doublet in the lattice mode spectrum is assigned to KCN (IV), both KCN (I) and KCN (III) having no distinct lattice mode spectra.

Wang (65) has, by Raman spectroscopy, studies the pressure induced phase transition between KCN(I) and KCN(II), which is reversible, and takes place over a range of 3 kbar. KCN(II) is metastable, the orientation of the CN^- ion being disordered, as in KCN(I), and a discussion of the mechanism giving rise to strong scatter near the exciting line is given. Hochheimer (66) has performed high pressure Brillouin scattering studies of the order-disorder transition in KCN in the range 0 - 7 kbar.

The pressure dependence of KNO_3 has been investigated by Raman spectroscopy (67) (together with high pressure modifications of ice), Iqbal (68) suggests that a lowering of structural symmetry is undergone in going from the antiferroelectric phase (II), to KNO_3 (IV) at ca. 3 kbar.

Adams and Sharma (69) investigated the temperature and pressure dependence (to $>180^\circ\text{C}$ and 40 kbar) of the infrared spectrum of silver nitrate, and draw comparisons of the spectra of AgNO_3 (II) and AgNO_3 (III) with those of KNO_3 (I) and KNO_3 (IV) respectively, and find a metastable phase, AgNO_3 (V) obtained by rapid application of pressures of ca. 60 kbar.

Holzappel (70) has performed high pressure low temperature Raman matrix isolation studies of nitrite ions in KI and Ar, at 77K and 5K, and up to 8 kbar. The results are discussed in terms of anharmonic effects. A review of the crystal chemistry of univalent nitrites, together with a study of the high pressure phase behaviour of silver nitrate, including data for NaNO_2 and KNO_2 has been presented by Clark (71).

Some research on iron bearing systems has been undertaken. Bassett (72, 73) has performed bulk modulus calculations for haematite ($\alpha\text{-Fe}_2\text{O}_3$) and magnetite (Fe_3O_4) using X ray diffraction techniques up to 100 and 70 kbar respectively. Olivine was the subject of work by Mao and Bell (74), in which above 100 kbar, disproportionation equilibria were studied and geochemical applications discussed. Ferraro (75) has investigated the mechanism and nature of high-low spin transitions by variable pressure and temperature X ray and magnetic moment measurements on Fe(II) and Fe(III) systems, and gives evidence for the existence of intermediate spin states. A review of the high pressure chemistry and physics of iron bearing systems has been given by Akimoto, Matsui and Syano (76).

The chlorides and bromides of mercury I and II have been studied. Whalley (77) who reports on the Raman spectra of HgCl_2 and HgBr_2 , found bands occurring which are forbidden by the crystallographic symmetry $I4/m$, and attributed these to disorder within the crystal; this disorder appears to increase as pressure increases. Adams and Appleby (78, 79, 80) undertook extensive spectral investigation of HgCl_2 and HgBr_2 , by both Raman and far infrared methods; Phases I, II and IV are characterised for the chloride, and I, II, III and IV for the bromide, and a discussion of the structures of the high pressure phases is given on the basis of the spectral evidence.

Hochheimer (81) has studied the low temperature pressure dependence of the TO phonon anomaly in the Raman spectrum of Cu(I)Cl at 40K up to 7 kbar,

whilst a more general investigation of the structural phases of CuI has been performed by Brafman (82) who observed successive transitions zincblende-rhombohedral-tetragonal by Raman spectroscopy. Salts containing the CuCl_4^{2-} moiety have been studied by Ferraro (83), who indicates the importance of a distorted structure to enable solid state interconversions to occur under pressure, and a further investigation (84) involved a systematic study concerning complexes with counterions unable to provide hydrogen bonding to the chlorines of the MCl_4^{2-} entity, and those complexes which show a high degree of hydrogen bonding. Wong (85) has considered a complex in which a tetrahedral ZnCl_4^{2-} unit is distorted with pressure, and studied the anharmonicities of the vibrational modes of the unit.

Tetrahedral coordination at high pressures has also been studied by Spain (86), whose results show that at high pressure, several compounds assume the "ionic" NaCl structure. Phase transformations in tetrahedrally coordinated semiconductors has also been investigated (87).

Ammonium bromide and iodide, under elevated pressure, have been studied by Hochheimer (88) using Raman techniques, and have been found to exist in three CsCl type phases (II \rightarrow IV) differing in the orientation of the NH_4^+ tetrahedra. The spectra of these phases differ considerably.

The pressure/temperature phase diagrams of normal and deuterated triammonium hydrogen (deuterium) phosphate up to 9 kbar and between 190 and 300K have been compiled by Gesi et al (89, 90).

SrCl_2 has been prepared in an orthorhombic space group by using high pressure to convert it from its less dense established cubic space group (91). High pressures have also been employed to generate new phases of SiO_2 and GeO_2 (92), by compression of glass samples to 250 kbar in a DAC then heating with a Nd/YAG laser. New modifications have been indexed as being hexagonal.

Formation and subsequent quenching of high pressure phases have been successfully performed on CsBF_4 and CsClO_4 (93). Crystallographic data suggest that these phases, CsBF_4 (IV) and CsClO_4 (IV), contain the large cations in eightfold coordination and the smaller anions in tetrahedral coordination. Nicol (94) has performed Raman spectroscopic studies of the high pressure phases of NaClO_3 between 0 and 40 kbar. Successful formation and quenching of new phases have also been observed in the KInS_2 and RbInS_2 (II). The stable high pressure modification KInS_2 (III) has the $\propto \text{FeO}_2$ structure, while pressure treatment of RbInS_2 yields an uncharacterised phase with a diffuse X ray pattern.

Studies of phase transitions under pressure have also been performed for the following; NiF_2 (96), silveroxide (to 39 kbar) (97), lead (II) iodide (98) thallium azide (99), paratellurite (100) and a series of ABCl_3 crystals where $\text{B} = \text{M(II)}$ (101).

High pressure vibrational studies of some octahedral complexes of several hexafluorometallate compounds have been performed by Breiteringer (102), and the far infrared spectra of some hexammine complexes of Ni(II) and Co(III) under high pressures have been studied by Adams and Payne (103). The effect of pressure on the phase transition temperature of cobalt hexafluorosilicate hexahydrate,

and cobalt hexafluorozirconate hexahydrate has been investigated (102). Arndt (105) has, by using high pressures, synthesised and transformed alkali oxofluorometallates of the types $\text{Cs}_2 \text{NaMO}_x\text{F}(6-x)$ and $\text{Rb}_2\text{LiMO}_x\text{F}(6-x)$. The effect of hydrostatic pressures of up to 5 kbar on successive phase transitions in $\text{K}_2\text{Pb}(\text{NO}_2)_6$ results in lowering of the transition temperatures for the I \rightarrow II and II \rightarrow III transitions (106).

The pressure dependence of the Raman active vibrational modes in lead uranium zirconium oxide ($\text{PbTi}(1-x)\text{Zr}_x\text{O}_3$) has been studied to 70 kbar (107). Spain (108) has investigated the pressure induced structural phase transition in the gallium/indium/antimony alloy system, and polymorphism and crystal structures of three high pressure phases of indium antimonide, In Sb (II) being body centred tetragonal, and In Sb (III) orthorhombic, as is In Sb (IV) (109).

Nicol (110) has employed mid infrared and visible absorption spectroscopy to monitor pressure induced metal-ligand electronic transfer of some Pt (II) glyoximes, and notes a decrease in the $\text{C}=\text{N}$ frequency with pressure, indicating enhancement of the $d\pi \rightarrow \pi^*$ electron transfer at high pressure.

Soft modes, and their response to applied pressure have been studied in two papers, one by Samara (111), the other by Holzapfel, who investigated the pressure dependence of the impurity soft modes in Li and Na doped KTaO_3 to 60 kbar (112).

1.5 Summary

Growing interest in all aspects of high pressure research has required that diverse techniques and equipment be developed. The diamond anvil cell has proved to be the most powerful compact method of generating high pressures, and coupled to infrared/Raman and X ray equipment has proven the most comprehensive source of information on many aspects of solid state research.

References

1. Payne, S.J., PhD Thesis, (1975).
2. Appleby, R., PhD Thesis, (1977).
3. Lauer, J.L., Fourier Transform Infrared Spectroscopy
(Ed. J.R. Ferraro) 1 169 (1978).
4. Akimoto, S., Oyo Butsuri 46 709 (1977).
5. Young, D.A., UCRL 51902 (1975).
6. Cannon, J.F., J. Phys. Chem. Ref. Data 3 781 (1974).
7. Merrill, L., NBS Sp. Pub 496, 100, (1977).
8. Pugh, H.L.D., Chandler, E.F., High Pressure Technol.
1 547 (1977).
9. Syassen, K., Holzapfel, W.B., Rev. Sci. Instrum. 49 1107 (1978).
10. Skelton, E.F., Liu, C.Y., Spain, I.L., Carpenter, E.R.,
Rev. Sci. Instrum 48 79 (1977).
11. Skelton, E.F., Liu, C.Y., Spain, I.L., High Temp, High Pressures
9 19 (1977).
12. Schiferl, D., High Temp, High Pressures 9 71 (1977).
13. Webb, A.W., Gulser, D.V., Towle, L.C., Rev. Sci. Instrum.
47 59 (1976).

14. Keller, R., Holzapfel, W.B., Rev. Sci. Instrum. 48 517 (1977).
15. Schiferl, D. Rev. Sci. Instrum. 48 24 (1977).
16. Schiferl, D. Rev. Sci. Instrum. 49 359 (1978).
17. Kinsland, G.L. Bassett, W.A., Rev. Sci. Instrum. 47 130 (1976).
18. Denner, W., Schulz, H., D'Amour, H., J. Appl. Crystallog. 11 266 (1978).
19. Adams, D.M., Sharma, S.K., J. Phys. E. 10 838 (1977).
20. Schoen, P.E., Schnur, J.M., Sheridan, J.P., Spec. Techniques 31 337 (1977).
21. Webber, B., Rev. Sci. Instrum. 47 183 (1976).
22. Webber, B., Rev. Sci. Instrum. 48 395 (1977).
23. Bassett, W.A., Ming, I.C., Phys. Chem. Miner. Rocks. NATO Adv. Study Inst. "Petrophys" (1974) (Pub. 1976) 365.
24. Fabre, D., High Temp. High Pressures 8 689 (1976).
25. Shchanov, M.F., Subbotu, S.I., Prib. Tetc'n Eksp. 246 (1977).
26. Mao, H.K., Bell, P.M., J. Appl. Phys. 49 3276 (1978).
27. Piermarini, G.J., Forman, R.A., Block, S. Rev. Sci. Instrum. 49 1061 (1978).

28. Liebenberg, D.H., Mills, R.L., Bronson, J.C., Schmidt, L.C.,
Phys. Lett. 67A 162
29. Mao, H.K., Bell, P.M., Science 200 1145 (1978)
30. Adams, D.M., Sharma, S.K., J. Phys. E 10 680 (1977).
31. Adams D.M., Shaw, A.C. Submitted for publication.
32. Parsons, B., J. Diamond Research (1976), 33.
33. Ruoff, A.L., Wanagel, J., Science 198 1037 (1977).
34. Mao, H.K., Bell, P.M., Carnegie Inst. of Washington Year Book
(1976 - 1977) 646.
35. Dunn, K.J., J. Appl. Phys. 48 1829 (1977).
36. Sung, C-M., Goetze, C., Mao, H.K., Rev. Sci. Instrum.
48 1386 (1977).
37. Adams, D.M., Appleby, R. J.C.S. (Faraday II) 1896 (1977).
38. Medina, F.D., O'Shea, D.C., J. Chem. Phys. 66 1940
39. Shabanov, V.F. Kristallografiya 22 988 (1977).
40. Hamman, S.D., Spinner, E., Aust. J. Chem. 30 957 (1977).
41. Hamman, S.D., High Temp. High Pressures 9 57 (1977).

42. Hamman, S.D., High Temp. High Pressures 9 63 (1977).
43. Hamman, S.D., Linton, M., Aust. J. Chem. 30 1883 (1977).
44. Hamman, S.D., Spinner, E., Aust. J. Chem. 30 2591 (1977).
45. Hamman, S.D., Aust. J. Chem. 30 71 (1977).
46. Hamman, S.D., Aust. J. Chem. 31 11 (1978).
47. Van Valkenberg, A., Powers, S., J. Appl. Phys., 34 2433. (1963)
48. Basett, D.C., Block, S., Piermarini, G.J., J. Appl. Phys. 45 4146 (1974)
49. Wu, C.K., J. Polym. Sci. Polym. Phys. Ed., 12 2493. (1974)
50. Yasuriwa, M., Enoshita, R., Takemura, T., Jpn. J. Appl. Phys. 15, 1421 (1976).
51. Ebisuzaki, Y., Taylor, T.J., Woo, J.T., Nicol, M.J., J.C.S. (Faraday II) 73 253 (1977).
52. Lewis, G.J., Whalley, E.J., J. Chem. Phys. 68 1119 (1978)
53. Hamman, D., Linton, M., Pistorius, C.W., F.T., High Temp. High Pressures 5 575 (1973).
54. Klaeboc, P., Woldback, T., Appl. Spectrosc. 32 588 (1978)
55. Newman, B.A., Sham, T.P., Pal, K.D., J. Mater. Sci. 12 1064 (1977).

56. Newman, B.A., Pae, K.D., Sham, T.P., J. Mater. Sci. 12 1697 (1977).
57. Newman, B.A., Pae, K.D., Sham, T.P., J. Mater. Sci. 12 1793 (1977).
58. Newman, B.A., Pae, K.D., Sham, T.P., J. Appl. Phys. 48 4092 (1977).
59. Keller, R., Holzappel, W.B., Schulz, H., Phys. Rev. B. 16 4404 (1977).
60. Bosio, L., J. Chem. Phys. - Chim. Biol. 75 145 (1978).
61. Asaumi, K., Minomura, S., J. Phys. Soc. Jpn. 45 1061 (1978).
62. Dultz, W., Proc. Int. Conf. Raman Spectrosc. 5th (1976) 604.
63. Dultz, W., Krause, H., Winchester, L.W., J. Chem. Phys. 67 2560 (1977).
64. Adams, D.M., Sharma, S.K., J.C.S. (Faraday II) 74 1355 (1978).
65. Satija, S.K., Wang, C.H., J. Chem. Phys. 66 2221 (1977).
66. Hochheimer, H.D., Phys. Rev. Lett. 38 832 (1977).
67. Kennedy, J., Sherman, W.F., Treloar, N., Wilkinson, G.R., Proc. Int. Conf. Raman Spectrosc. 5th (1976) 600.
68. Iqbal, Z., Owens, F.J., Ferroelectrics 16 229 (1977).

69. Adams, D.M., Sharma, S.K., J.C.S. (Faraday II) 72 848 (1976).
70. Jodl, H.J., Holzapfel, W.B., Chem. Phys. Lett. 55 259 (1978).
71. Clark, J.B., Richter, P.W., Woburst, A.B., High Temp. High Pressures 9 103 (1977).
72. Wilburn, D.R., Bassett, W.A., Sato, Y., Akimoto, S.J., Geophys. Res. 83 3509 (1978).
73. Wilburn, D.R., Bassett, W.A., High Temp. High Pressures 9 35 (1977).
74. Mao, H.K., Bell, P.M., Energ. Geol. Processes (1977) 236 (Ed. Sascend. NY).
75. Ferraro, J.R., J.C.S. Chem. Comm. 22 910 (1976).
76. Akimoto, S., Matsui, Y., Syano, Y., Phys. Chem. Miner. Rocks NATO Adv. Study Inst. "Petrophys" 1974 (Pub. 1976) 509.
77. Richter, P.W., Wong, P.T.T., Whalley, E., J. Chem. Phys. 67 2348 (1977).
78. Adams, D.M. Appleby, R., J.C.S. Dalton 1530 (1977).
79. Adams, D.M. Appleby, R. J.C.S. Dalton 1535 (1977).
80. Adams, D.M., Appleby, R., J.C.S. Chem. Comm. 975 (1976).
81. Hochheimer, H.D., Frauzman, M., Shand, M.L., Potts, J.E., Hanson, R., Walker, C.T., Proc. Int. Conf. Raman Spectrosc. 5th (1976) 654.

82. Brafman, O., Cardona, M., Vardeny, Z., Phys. Rev. B. 15 1081 (1977).
83. Ferraro, J.R., J. Coord. Chem. 5 101 (1976).
84. Sherer, A.T., Ferraro, J.R., Inorg. Chim. Acta. 22 43 (1977).
85. Wong, P.T.T., J. Chem. Phys. 66 2347 (1977)
86. Yu, S.C., Spain, I.L., Skelton, E.F., Solid State Comm. 25 49, (1978)
87. Jayaraman, A., Derruer, P., Kasper, H.M., Maines, R.G., High Temp. - High Pressures 9 97 (1977).
88. Hochheimer, H.D., Gebhardt, W., Giesel, T., Spanner, E., High Temp. - High Pressures 8 647 (1976).
89. Gesi, K., Ozawa, K., J. Phys. Soc. Jpn. 43 570 (1977).
90. Gesi, K., Ozawa, K., Osaka, T., Makita, Y., J. Phys. Soc. Jpn. 44 689 (1978).
91. Brixner, L.H., Mat. Res. Bull. 11 1453 (1976).
92. Bassett, W.A., Liu, L., Sharry, J., J. Geophys. Res. 83 2301 (1978).
93. Richter, P.W., Whalley, E., Pistorius, C.W.F.T., Z. Naturforsch 31b 1456 (1976).

94. Nicol, M., Ganguly, B.N., Ellenson, W.D., Phys. Status. Solidi 3 83 K115 (1977).
95. Mahlberg, G., Range, K.J., Z. Naturforsch 30B 81 (1975).
96. Jamieson, J.C., Wu, A.Y., J. Appl. Phys. 48 4573 (1977).
97. Klement, W., Jr., Phys. Status Solidi 39A K45 (1977).
98. Carillon, C., Martinez, G., Nuovo, Cimento. Soc. Ital. Fio B 38 B 496 (1977).
99. Christoe, C.D., Iqbal, Z. J. Phys. Chem. Solids. 38 1391 (1977).
100. Adams, D.M., Sharma, S.K., J. Phys. Chem. Solids. 39 515 (1978).
101. Alexandrov, K.S., High Temp. - High Pressures 8 603 (1976).
102. Bretinger, D., Kristen, V., J. Sol. State. Chem. 22 233 (1977).
103. Adams, D.M., Payne, S.J., Inorg. Chim. Acta. 19 L49 (1976).
104. Dutta, R.S., Pal, A., Chosh, B., Chatteljee, N., Daw, A.N., J. Phys. C 10 L403 (1977).
105. Arndt, J., Rombach, N., Pausewang, G., Mater. Res. Bull. 12 803 (1977).
106. Kashida, S., Kaga, H., J. Phys. Soc. Jpn. 44 930 (1978).
107. Bourele, D., Holzapfel, W.B., Pinczuk, A., Yacoby, Y., Phys. Status. Solidi. B 83 99 (1977).

108. Liu, C.Y., Spain, I.L., Skelton, E.F., J. Phys. Chem. Solids 39 113 (1978).
109. Yu, S.C., Spain, I.L., Skelton, E.F., J. Appl. Phys. 49 4741 (1978).
110. Hara, Y., Nicol, M.F., Bull. Chem. Soc. Jpn. 51 1982. (1978)
111. Samara, G.A., Report 1977, SAND - 77 - 1188C. Avail. NTIS.
112. Holzapfel, W.B., Yacoby, Y., Bauerle, D., Sol. State. Comm. 23 947 (1977).

CHAPTER 2

THE OPERATION OF THE DIAMOND ANVIL CELL

AND ANCILLARY EQUIPMENT

CHAPTER 2

THE OPERATION OF THE DIAMOND ANVIL CELL, AND ANCILLARY EQUIPMENT

2.1 Introduction

This chapter is intended as an introduction to the techniques of preparing and loading a diamond anvil cell, and coupling it to the spectrophotometers available.

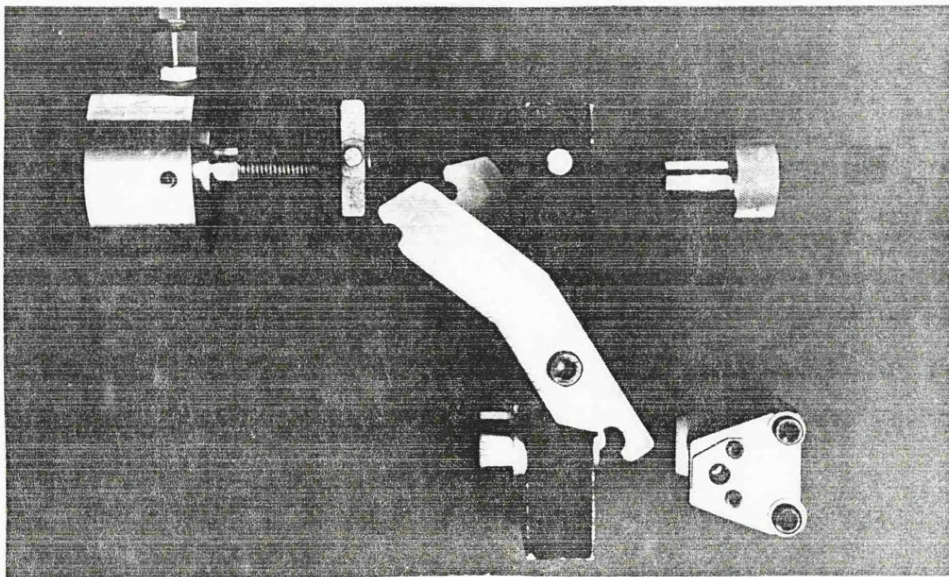
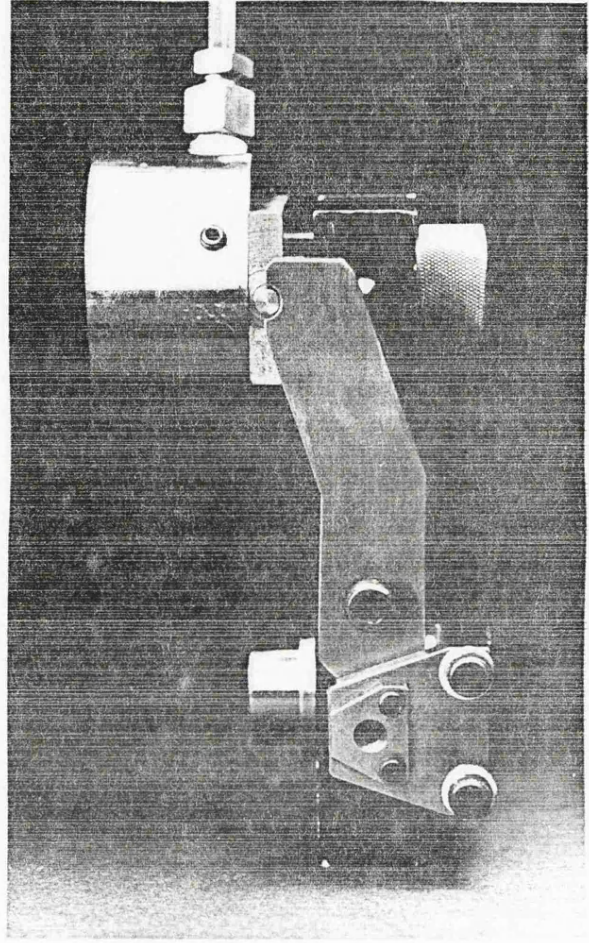
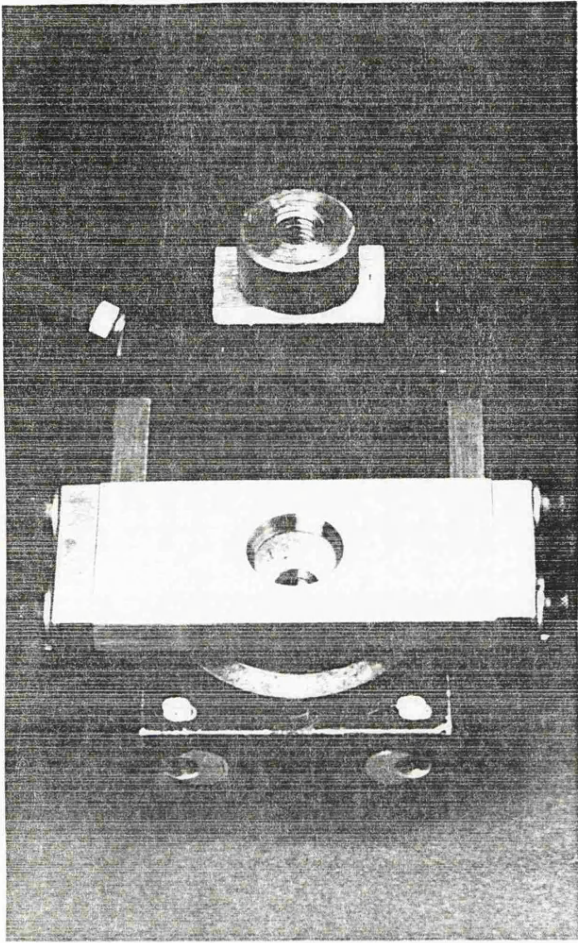
The use of diamond anvil cells to obtain high pressure vibrational spectra of solids at highly elevated pressures has now become a standard technique, and has been the subject of several reviews (1, 2, 3). Working with sample volumes of less than 20 nanolitres, and a cell with transmission as low as 1% (4), the success of the system is principally determined by its correct manipulation, and proper coupling to the relevant spectrometer.

2.2 DAC Operation

Having manufactured the DAC, selection of suitable diamond anvils poses the first problem. This is discussed fully by Adams and Payne (5), and Adams and Sharma (6). Essentially the criteria are that the anvil should be mechanically sound, and should be of type IIA or IIB. The latter type is the most suitable for Raman spectroscopy due to its very low fluorescence characteristics. However it absorbs a little more strongly in the mid infrared than type IIA stones.

Figure 2.1

- (i) Assembled MkIIa cell. Plan view
- (ii) Assembled MkIIa cell. Side view
- (iii) Exploded view of MkIIa cell
 - (a) hydraulic ram
 - (b) piston plate
 - (c) backing screw
 - (d) lever arm
 - (e) presser plate
 - (f) cell body
 - (g) central insert



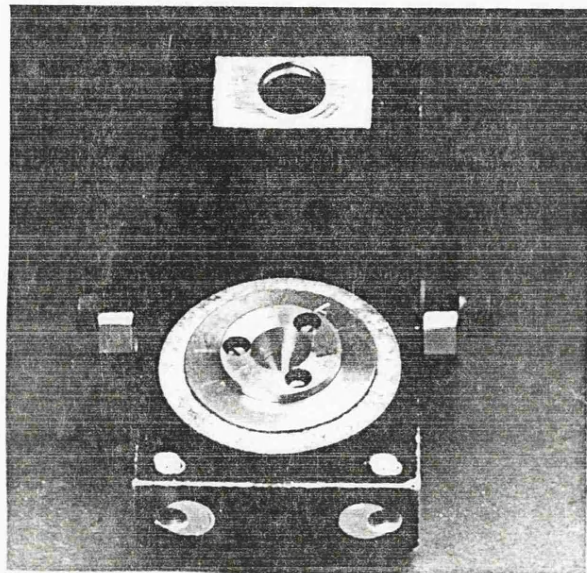
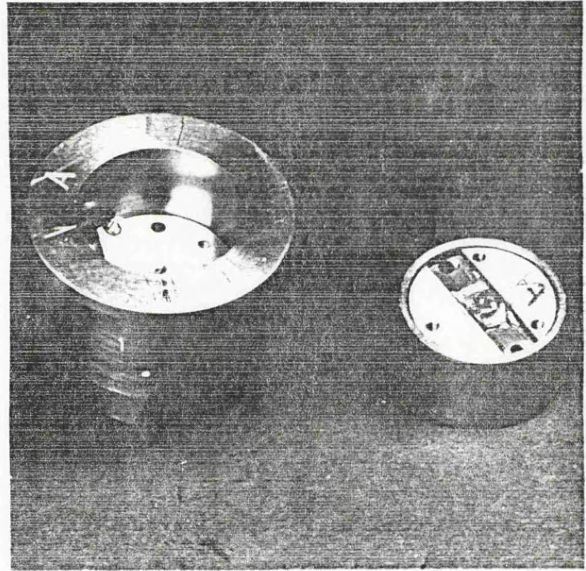
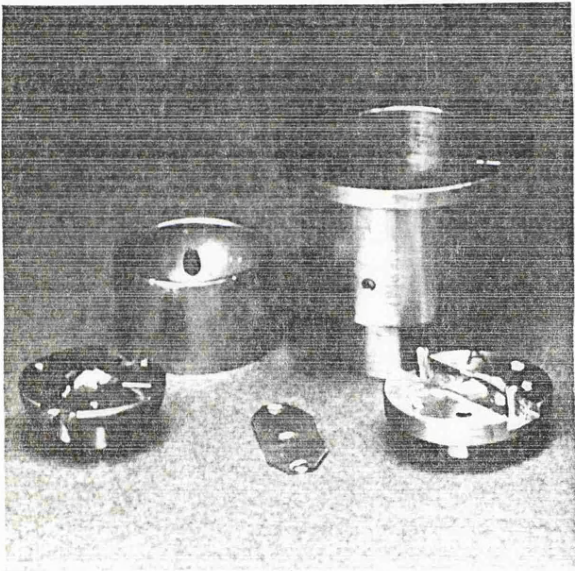
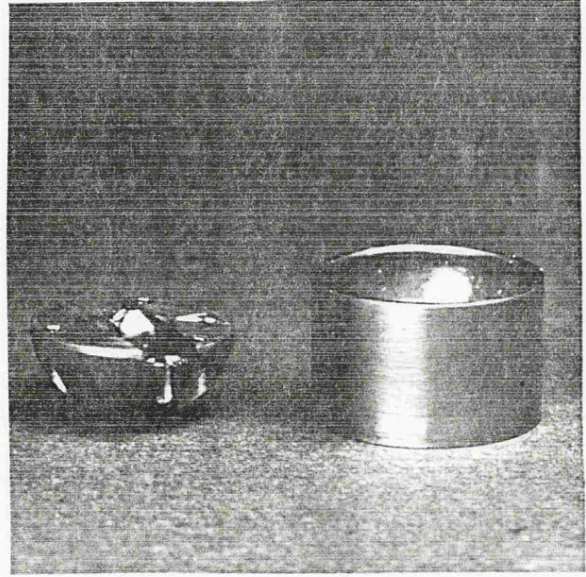
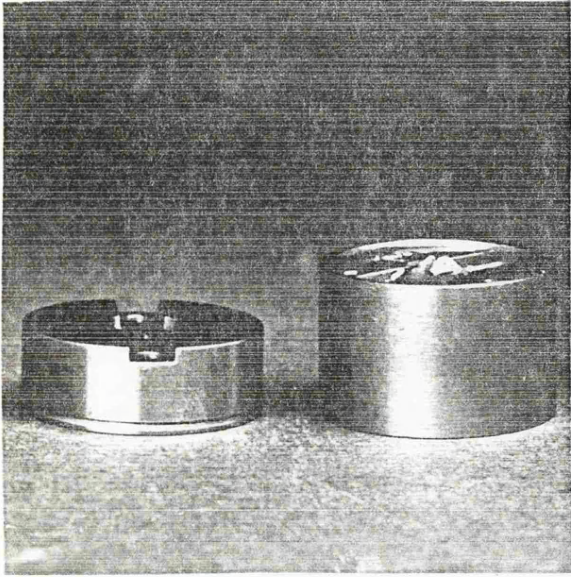
Having selected two suitable anvils these must be mounted in the DAC. All anvils are mounted onto an optically flat anvil support, generally fashioned from EN58 stainless steel. Utilising a binocular microscope, first the anvil support is inspected to ensure the absence of indentations or scratches which would clearly cause the support to fail in its function of giving even support to the anvil. If these are observed, the mount is removed and repolished. In the earlier cells (Mk I and Mk II) a locating ring was mounted onto the support, and the diamond centred within this ring. This idea was abandoned in later designs, the diamond being located in a groove running diametrically across the support, as can be seen in Figures 2.2a to 2.2d. The anvil is cemented in place with Araldite (slow setting) initially with 2 strands, running to the edges of the grooves. When the Araldite has become viscous (but not rigid), final alignment is accomplished using a monocular microscope with 100 X magnification.

The pair of diamonds are mounted in this fashion, ensuring that the centres of their faces are coincident. Newton's fringes should now be seen between the two faces. Adjustment of the cell is carried out until these fringes can be made to move around the circumference of the diamond faces with equal intensity by applying hand pressure on the moving anvil holder. This is taken as a first approximation to parallelism between the faces.

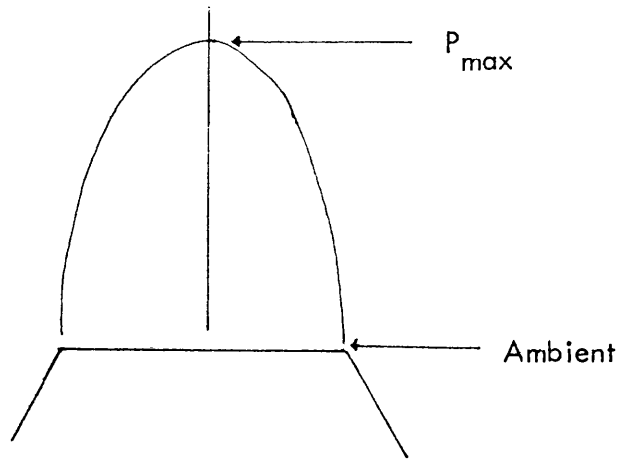
The assembled cell is now tested under pressure. The most suitable method of this is by the visual observation of low pressure phase transitions. Since the pressure distribution across a pair of ungasketed high pressure faces is approximately parabolic, with the maximum pressure experienced at the centre, falling to ambient

Figure 2.2

- (i) Comparison of the moving anvil of a Mark II (left) and Mark IIa moving anvil support.
- (ii) Diamond mounted on a MkIIa moving anvil support. Note ball and cup arrangement to allow adjustment of the anvil.
- (iii) Exploded MkIIa cell insert showing;
 - (a) moving anvil mounted on support 'ball'
 - (b) moving anvil mounted on support 'cup'
 - (c) central insert
 - (d) stationary anvil mounted on support
 - (e) gasket
- (iv) MkIIa cell insert assembled
- (v) MkIIa cell insert in cell body



at the edges, i.e.



This is the case when the two diamond faces are perfectly aligned.

In this ideal situation, therefore, we would expect to observe a phase transition to initiate at the centre of the diamond faces then, as the applied pressure is increased, should propagate across the faces, with the successive phase boundaries concentric. If this is observed, then we assume that the diamonds remain parallel up to this pressure. If the transition does not occur at the centre of the faces then the cell is disassembled, and the diamonds realigned. These tests were initially carried out using HgI_2 , which has a red to yellow phase transition at ca. 13 kbar, and also showed significant darkening at ca. 25 kbar. This was not thought to be due to a further phase, but to an optical phenomenon. Alignment of the anvils was checked after each high pressure experiment.

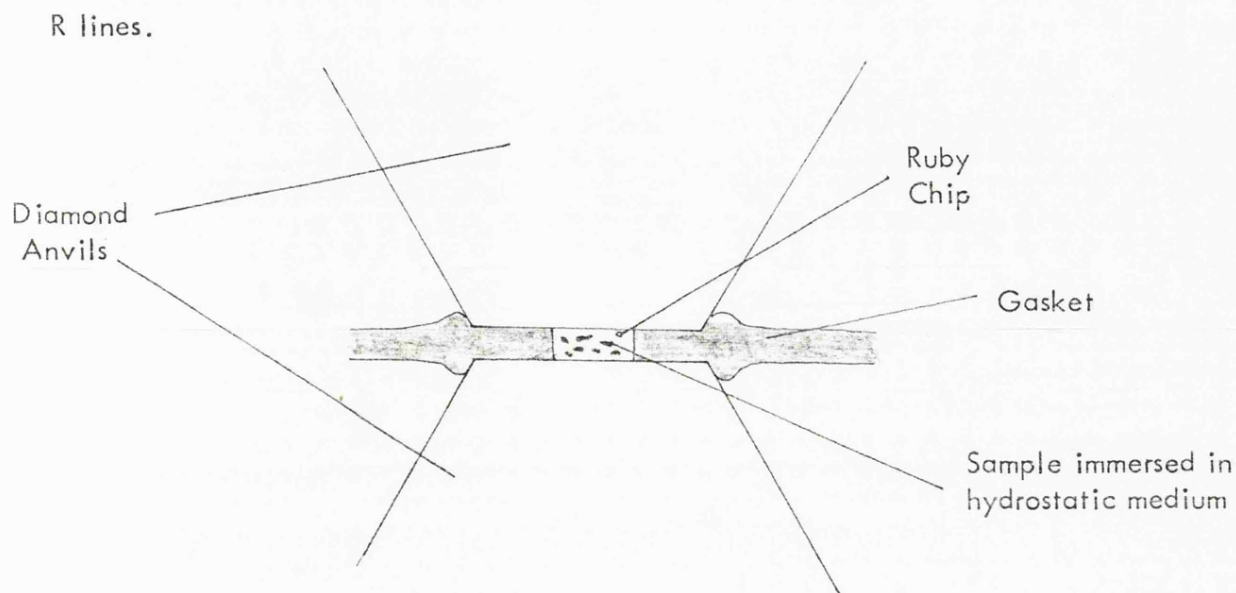
The cell can now be used in a mode described as 'ungasketed'. This means that the material under observation is placed on the diamond face and the cell assembled. Clearly, as described above, this will lead to a pressure gradient across the sample (7). In vibrational spectroscopy this can lead to peaks in the spectrum due to the sample at ambient pressure through to the maximum experienced. This can cause immense problems of interpretation. This pressure distribution can be removed by placing the sample in a hydrostatic environment. This can be achieved

by containing the sample in a gasket. These are fabricated from sheets of inconel (a Fe/Cr/Ni heat resisting alloy, from 0.025 to 0.2mm thick). A hole is drilled in this material, typically 0.5mm diameter. This cylinder, 0.5mm face by, say 0.05mm deep can be considered as the sample compartment.

These gaskets are manufactured by first drilling holes for the pins to locate the gasket. A gasket is shown in Figure 2.2iii. The cell is assembled, and a pressure of 100 psi is applied. This causes the diamonds to indent the gasket. The gasket is now removed, the indentation centre punched, observing it with a magnifying eye piece. Finally the required diameter hole is drilled using a hand drill, jig and all burrs removed. In practice several dozen gaskets were prepared at a time.

This sample compartment is now loaded using a binocular microscope, firstly locating the gasket over the diamond face, then a drop of liquid (typically Nujol, or 4:1 methanol/ethanol) placed in the hole. This fluid acts as a hydrostatic medium until it freezes. Then using a fine needle, some finely ground sample under investigation was inserted, and finally a chip of ruby (see below) was loaded. The sample compartment is now sealed by the fixed anvil. This is shown diagrammatically below. Approximately 60 psi is applied to keep the cell sealed.

It is important to note that the DAC is now effectively a sealed system, and can be moved from one spectrometer to another with no change in pressure. This is particularly relevant, as the DAC can always be placed into the Raman Spectrometer, and the pressure determined accurately from the shifts in the ruby



The cell is now ready for use. Having described the assembly and loading of the DAC, an outline of the methods used to obtain mid infrared, far infrared and Raman spectra, together with X ray diffraction photographs is given below. First, however, it will be useful to give some details of the use of ruby R lines to measure the pressure to which the sample is subjected.

2.3 Use of Ruby R lines as pressure sensors

Determination of the pressure experienced by a sample by load/area calculations were at best approximate in ungasketed samples, as these ignored friction within the system, etc. However, with the advent of gasketed work these calculations became even more inaccurate, as a considerable portion of the load to which the sample would have originally been subjected is now absorbed by the gasket. Hence the need for an internal calibrant came into existence, which in principle at least, is subjected to the same pressure as the sample. Thus, the calibrant having a known response to pressure, the pressure in the sample can be measured accurately.

It was recognised that R_1 and R_2 fluorescence lines of ruby are pressure dependent and to a good approximation have a linear response, the gradient of which has been the subject of considerable work (8, 9, 10, 11), and is taken as being $-0.76 \text{ cm}^{-1} \text{ kbar}^{-1}$. Under hydrostatic conditions the spacing between R_1 and R_2 remains constant at constant temperature, at $29.7 \pm 0.2 \text{ cm}^{-1}$. Thus if the separation changes between the two, this can be taken as a good indication of lack of hydrostaticity in the sample.

It was these factors which influenced us, and the majority of high pressure researchers to choose ruby as a good high pressure calibrant. It should be noted that as the R_1 and R_2 lines are exceptionally intense due to the highly allowed nature of the transitions involved, a very small piece of ruby is required. In fact finely powdered ruby is used, and a suitably small piece chosen using a microscope.

We will now consider the techniques in which a DAC can be used.

2.4 The Mid Infrared Region

Recently, a simple refracting beam condenser for mid infrared spectroscopy has been reported (12). In this, the optics of the DAC are discussed in terms of numerical aperture, and a beam condenser using KBr or KRS-5 lenses described. Using a beam condenser of this type, mid infrared spectra of ungasketed samples in a DAC have been obtained in a Perkin-Elmer 225 spectrophotometer, and reasonable quality spectra using gasketed samples have been recorded with a Perkin-Elmer 580. Gasketed spectra proved difficult to obtain on machines other

than the Perkin-Elmer 580, the reason being that the Perkin-Elmer 580 is a ratio recording spectrophotometer, and thus has a 'live zero'.

In a conventional optical null system, an optical wedge is moved in and out of the reference beam in order to balance the light passing onto the detector. The ratio recording instrument performs this electronically, and hence at low light levels gives a more accurate difference. In all work performed, slow scan speeds and wide slit programs (in order to improve the signal/noise ratio) were employed.

It must be noted that using a DAC and KBr beam condenser, the spectral range is limited to below ca. 1900cm^{-1} (due to the rising background caused by two phonon absorption of diamond) and ca. 450cm^{-1} , due to the KBr cut off at low frequencies. This low frequency region can be extended to ca. 300cm^{-1} by using KRS-5 lenses.

2.5 Raman Spectroscopy

The first laser Raman spectra of samples contained within a DAC were reported by Brasch et al (13) and Postumus (14) using 0° scattering geometry in which the laser was fired straight through the cell towards the entrance slit of the spectrometer. Mitra (15) was of the opinion that this limitation made the diamond anvil cell of little value in Raman spectroscopy. However, several workers have shown that 180° scattering geometry is feasible (10, 16). A report by this group (17) gives an improved method of coupling the DAC optically to a Coderg T800. Efficiency in this respect is necessary mainly because of the very small sample

areas involved, and the small solid angle of Raman radiation which can be inspected. To this end, a Brookdeal Ortec 5C1 photon counter and RCA C 31034-02 photomultiplier have been installed to supplement the existing DC detection and EMI 9558A photomultiplier.

2.6 Optics of the DAC

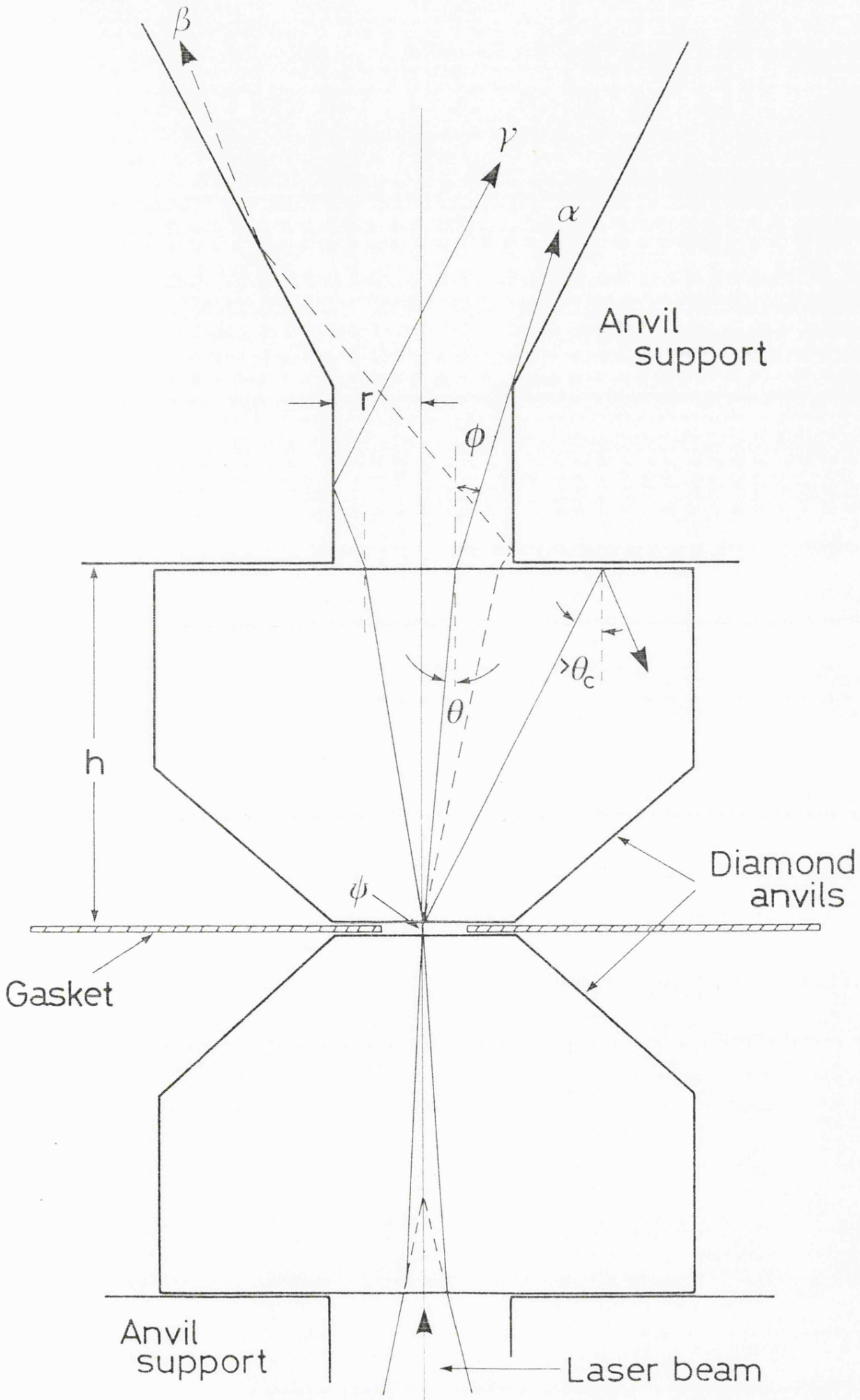
If Figure 2.3 is considered, we have a laser beam focussed such that the focus is at the sample contained within the gasket of the DAC. Since the sample is small it is treated as a point source.

The Raman scatter, from a sample in a 4:1 methanol/ethanol mixture, in a cone of apex semi angle of 25° will be collected and transmitted by the diamond anvil (Adams, Appleby and Sharma, 17). It is clear that the most critical limitation is set by the geometry of the anvil support material. Obviously some compromise must be arranged between the need for mechanical strength of this anvil support and the desirable large half angle of the cone.

In Figure 2.3 ϕ is the half angle of the emergent beam, θ is the angle of a ray to the normal in diamond. We find that for $r = 0.45\text{mm}$, $h = 2\text{mm}$ only rays $\theta \leq 5.8^\circ$ will pass directly out of the cell (eg. ray α), but others with $5.8^\circ < \theta \leq 12.7^\circ$ will be collected after reflection from the walls of the anvil support (eg. rays β, γ).

Figure 2.3

Ray paths through a DAC used in Raman Spectroscopy.



2.7 Collection of Radiation

In order to collect the scattered radiation from the DAC, a Perkin-Elmer 90° off axis ellipsoid with a numerical aperture of 0.7 (Figure 2.4) is used. This mirror was originally designed as part of a 6:1 beam condenser commonly used for infrared spectroscopy with DAC's. A 4mm hole has been drilled in this mirror, its axis parallel to the major axis of the ellipsoid to allow the laser beam to pass through it in either 0° or 180° scattering. Since the laser does not therefore pass into the monochromator, relatively high powers may be used without lowering the performance at low Raman shifts. This mirror turns the scattered light through 90° in both 0° and 180° scatter, matching many standard spectrometers.

2.8 Far Infrared Spectroscopy

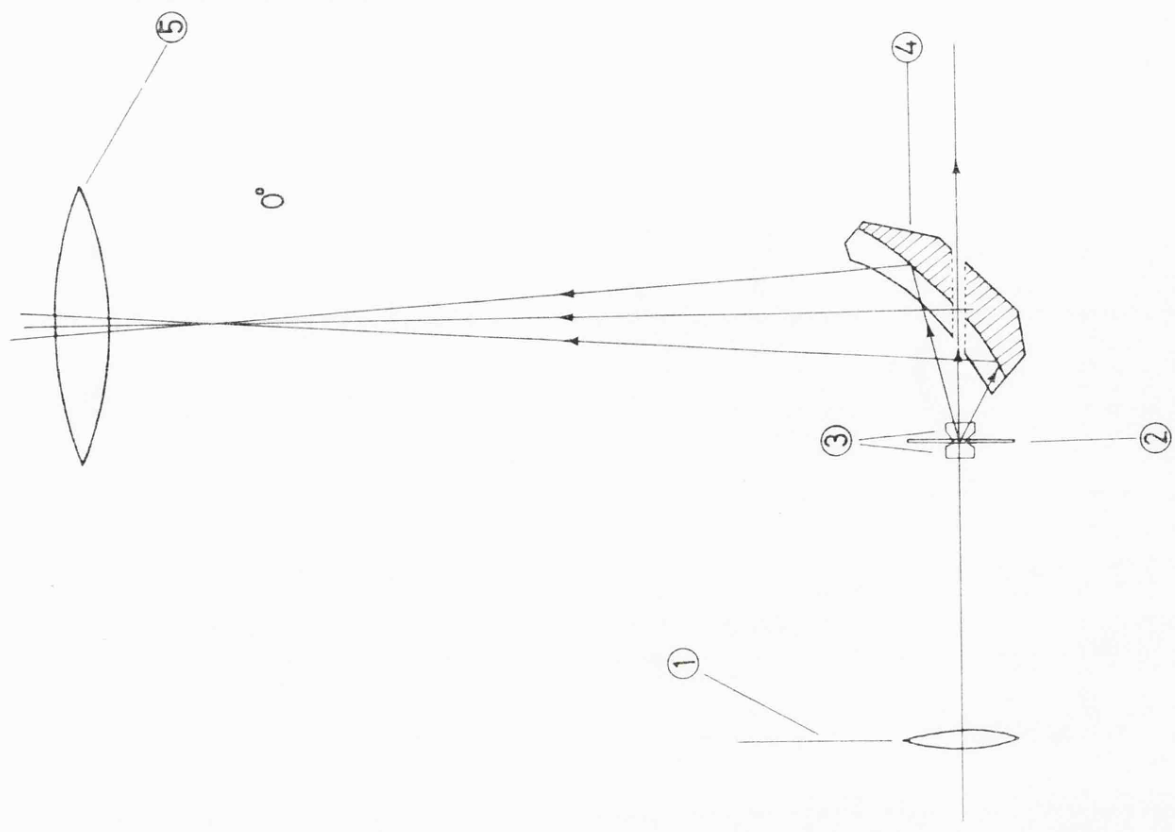
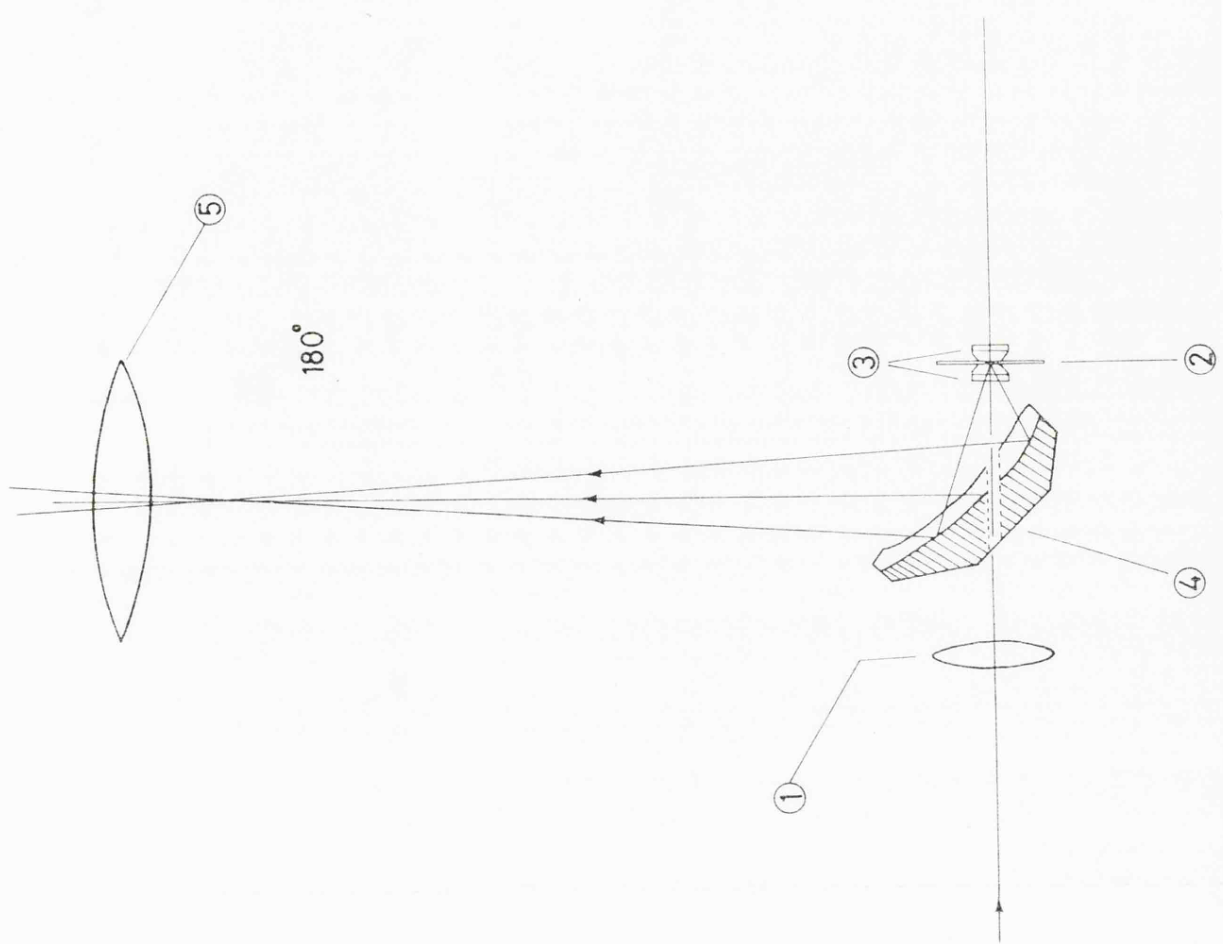
Use of ungasketed DAC's with interferometers has been reported (18, 19). To the authors' knowledge, no reports using gasketed DAC have been found outside *Leicester University*. Using a Beckman RIIC FS-720, Payne (20) obtained excellent results on ungasketed samples. Appleby (21) gives a description of the modifications to a Beckman RIIC FS 620 which allows far infrared spectra to be obtained using gasketed samples. This instrument proved most useful in the region 40 - 400cm⁻¹, although the performance below 100cm⁻¹ using a 25 # beam splitter was somewhat lacking, and could be improved by the use of a 50 # beam splitter.

Recent modifications include addition of a multiple scan unit, allowing advantage of the \sqrt{N} signal/noise improvement by performing N scans, and a overriding control box for the instrument. This control proved useful as, after

Figure 2.4

Collecting optics used to couple a DAC to a Coderg
T800 spectrometer.

1. Pre sample focussing lens
2. Gasket
3. Diamond Anvils
4. Off axis ellipsoidal mirror
5. Collecting lens



applying pressure to a system, a time lapse of ca. 6 hours was allowed prior to performing far infrared measurements. The control allowed automatic activation of the instrument after a preset time delay, together with system shutdown after performing N scans. Routine overnight running was then possible.

In the far infrared, choice of pressure transmitting fluid is critical, as the standard 4:1 MeOH/EtOH mixture is opaque in this region. The following liquids were found to be useful:-

<u>Liquid</u>	<u>Region of Transparency</u>
Nujol	0 - 4000cm ⁻¹
Octene	0 - 400cm ⁻¹
Silicone Oil	0 - 200cm ⁻¹

These all freeze and form glasses at pressures above 15 kbar but the R lines of ruby indicate that the sample is still under hydrostatic pressure to a good approximation to pressures of ca. 40 kbar.

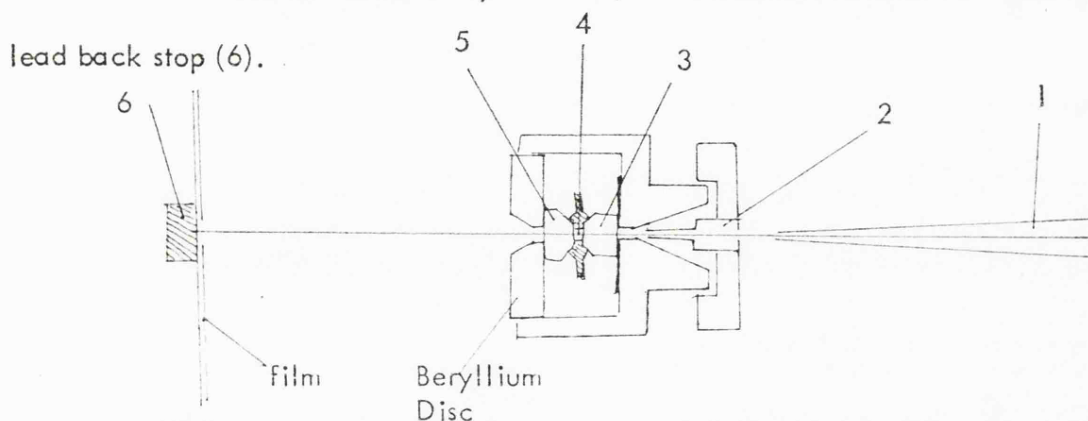
The output from the interferometers is in digital form on paper tape. This information, of course, must undergo Fourier analysis before an absorption spectrum can be constructed. This was achieved by using a program written by Dr. D.W. Waddington, which performs the inverse Fourier transform of the interferogram, and implemented on a Cyber 73 (Leicester University central computer).

2.9 X ray

Reports of the use of DAC's in X ray diffraction methods have now become fairly common (eg. 22, 23, 24). One of our DAC's was converted for use on an X ray diffractometer with a beryllium disc obtained from W.A. Bassett (University of Rochester, N.Y.). This was 12.7mm diameter by 3.2mm thick, with a small concentric hole .33mm and .76mm deep recessed in it to aid the positioning of the diamond, and a 1.0mm hole drilled through the centre. This material is transparent to X rays and therefore by simply incorporating one of these plates into the moving anvil holder, a cell was constructed transparent to X rays up to $20^{\circ} < 2\theta < 30^{\circ}$

The cell was mounted onto a standard Philips camera bracket using a mount designed and manufactured at the Chemistry Department at Leicester. A 0.5mm collimator and flat plate film cassette from a Philips Laue camera PW 1030 were used. A Philips PW 1009 generator run at 48 KV and 16 mA with a zirconium filter and a fine focus molybdenum tube were used. Small collimators (.1, .2 or .5mm) were mounted on the DAC to ensure that the X ray beam passed through the sample without being diffracted by the gasket hole.

The set up is shown below, with the beam passing through the zirconium filter, a standard three pin hole 0.5mm collimator (1), then through the small collimator (2), the first diamond (3), the gasket hole (4), then the back diamond (5), the diffracted radiation detected by the film, the undiffracted beam absorbed by a lead back stop (6).



The system could be used in low 2θ ($20^\circ < 2\theta < 30^\circ$) or if the sample diffracted X rays strongly, high 2θ ($20^\circ < 2\theta < 150^\circ$).

The DAC was loaded as described, then the collimator support attached to the nose piece of the DAC. The cell was then held over a table lamp, and the support adjusted so that the light could be seen through the small collimator with a microscope, ensuring that the X ray beam would not strike the edge of the gasket. The cell was finally aligned on the camera bracket by removing the lead backstop and placing a geiger counter behind the hole, and adjusting the cell for maximum count rate.

Typically, exposures of ca. 24 hours were found necessary using Kodirex X ray film. After an exposure at elevated pressure had been taken, an ambient pressure exposure was recorded on the same film for calibration purposes. A sample to film distance of 60mm was typical.

2.10 Summary

This chapter gives an outline of the operation of the DAC, including assembly, loading and coupling to various spectrometers.

References

1. Ferraro, J.R., Spectroscopy in Inorganic Chemistry (1971),
ed. Rao, C.N.R., Ferraro, J.R., Academic Press, N.Y. Vol. 2
2. Adams, D.M., Payne, S.J., Ann. Rep. Progr. Chem. (A) 69
3 (1972).
3. Lauer, J.L., Fourier Transform Infrared Spectroscopy (Ed. J.R.Ferraro)
1 169 (1978).
4. Adams, D.M., Sharma, S.K., J. Phys. E (1977).
5. Adams, D.M., Payne, S.J., J C S Dalton 407 (1974).
6. Adams, D.M., Sharma, S.K., J. Phys. E (1977).
7. Lippincott, E.R., Duecker, H.C., Science 144 1119 (1964).
8. Adams, D.M., Appleby, R., Sharma, S.K., J. Phys. E. 9 1140 (1976).
9. Piermarini, G.J., Block, S., Barnett, J.D., Formann, R.A.,
J. Appl. Phys. 46 2774 (1975).
10. Hawke, R.S., Syassen, K., Holzapfel, W.B., Rev. Sci. Instrum.
45 1598 (1974).
11. Piermarini, G.J., Block, S., Rev. Sci. Instrum. 46 973 (1975).
12. Adams, D.M., Sharma, S.K., J. Phys. E. 10 38 1977.

13. Brasch, J.W., Melveger, A.J., Lippincott, E.R., Chem. Phys. Letters 2 99 (1968).
14. Postumus, L., Maroni, V.A., Ferraro, J.R., Mitra, S.S., Inorg. Nucl. Chem. Letters 4 269. (1968)
15. Mitra, S.S., Indian J. Pure and App. Phys. 9 922 (1971).
16. Adams, D.M., Payne, S.J., Martin, K. Appl. Spectrosc. 27 377 (1973).
17. Adams, D.M., Appleby, R., Sharma, S.K., J. Phys. E. 9 1140 (1976).
18. Adams, D.M., Payne, S.J., J.C.S. Dalton 407 (1974).
19. Adams, D.M., Payne, S.J., J.C.S. Faraday II 70 1959 (1974).
20. Payne, S.J. PhD Thesis (1975).
21. Appleby, R., PhD Thesis (1977).
22. Skelton, E.F., Liu, C.Y., Spain, I.L., Carpenter, E.R., Rev. Sci. Instrum. 48 79 (1977).
23. Skelton, E.F., Liu, C.Y., Spain, I.L., High Temp - High Pressures 9 19 (1977).
24. Schiferl, D. Rev. Sci. Instrum. 49 359 (1978).

CHAPTER 3

THE DIAMOND ANVIL CELL;

HISTORY AND TEST OF TWO NEW CELLS AND ANVIL DESIGN

CHAPTER 3

THE DIAMOND ANVIL CELL : HISTORY AND TEST OF TWO NEW CELLS AND ANVIL DESIGNS

3.1 History

The use of a diamond anvil cell was first reported in the literature about twenty years ago (1). An outline of the cell, and section of the central portion are given in Figure 3.1. In essence, the central portion consisted of two opposed anvils; one attached to a stationary support (R), and the other to a movable holder (S). Pressure was generated by turning screw (T), which compressed a 'calibrated spring' (U), and which was transmitted via a pair of level arms (W) and presser plate (X); the sample was then compressed between the two opposed diamond anvils.

This initial design proved so successful that the majority of DACs (Diamond Anvil Cells) being used in current research still conform to it; that is they maintain the idea of using a cell body, lever arms and a presser plate as a means of applying pressure to a central high pressure region.

An exception to this is a cell used by Holzapfel. A cross section of Holzapfel's cell is shown in Figure 3.2. Here the pressure is generated on the central portion by a compact system of levers.

Figure 3.1

The Wier Cell

Parts labelled are:-

- | | |
|---|---------------------------|
| R | Stationary diamond holder |
| S | Movable diamond holder |
| T | Pressure generating screw |
| U | Spring |
| W | Lever arm |
| X | Presser plate |

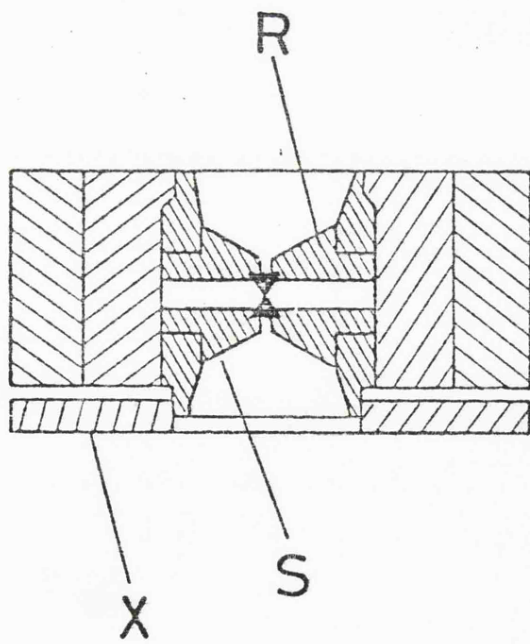
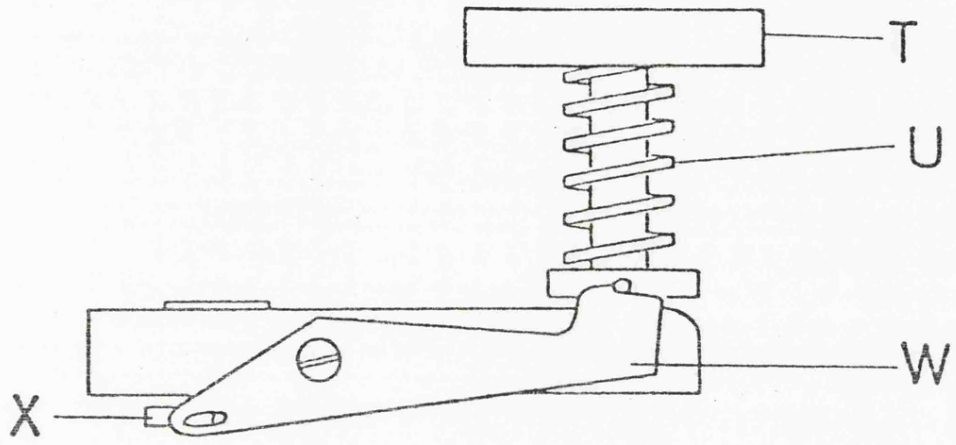
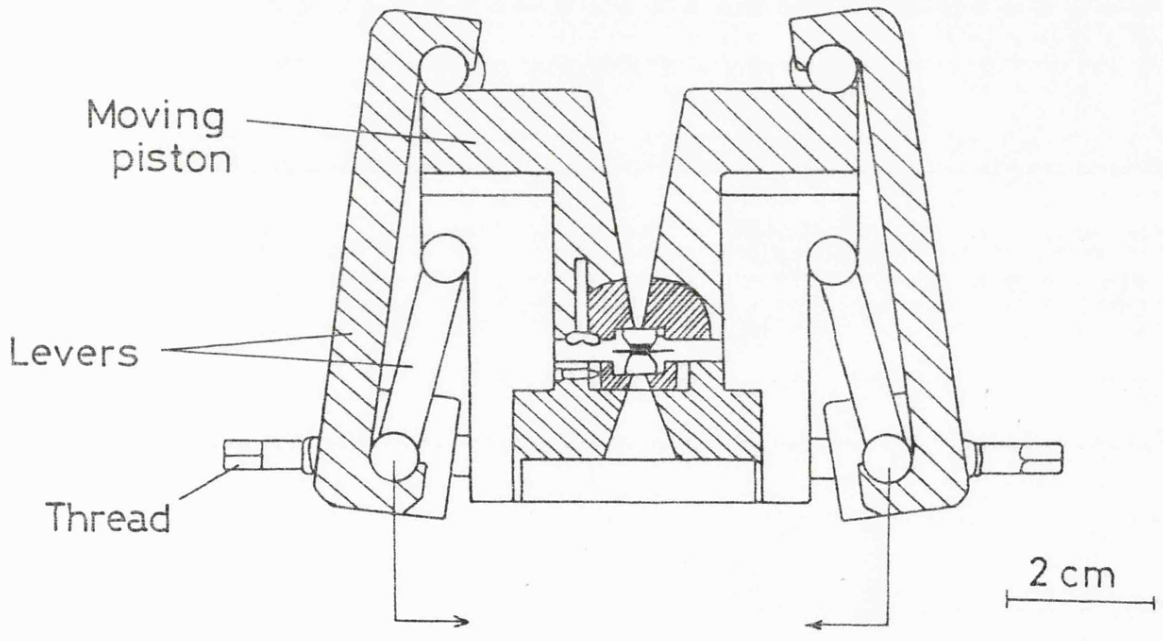


Figure 3.2

The Holzapfel cell; a unique approach to
DAC engineering.



Development of the central portion has taken place along several different, but essentially similar, lines; some of which are covered below.

The Wier cell was redesigned by Piermarini et al (2) in the USA, who developed the 'Waspaloy' cell, (see Figure 3.3) Waspaloy being an alloy manufactured for the Wasp helicopter, and used in the construction of this cell. This cell broke the barriers of high pressure work, and was taken to pressures of the order of 600 kbar.

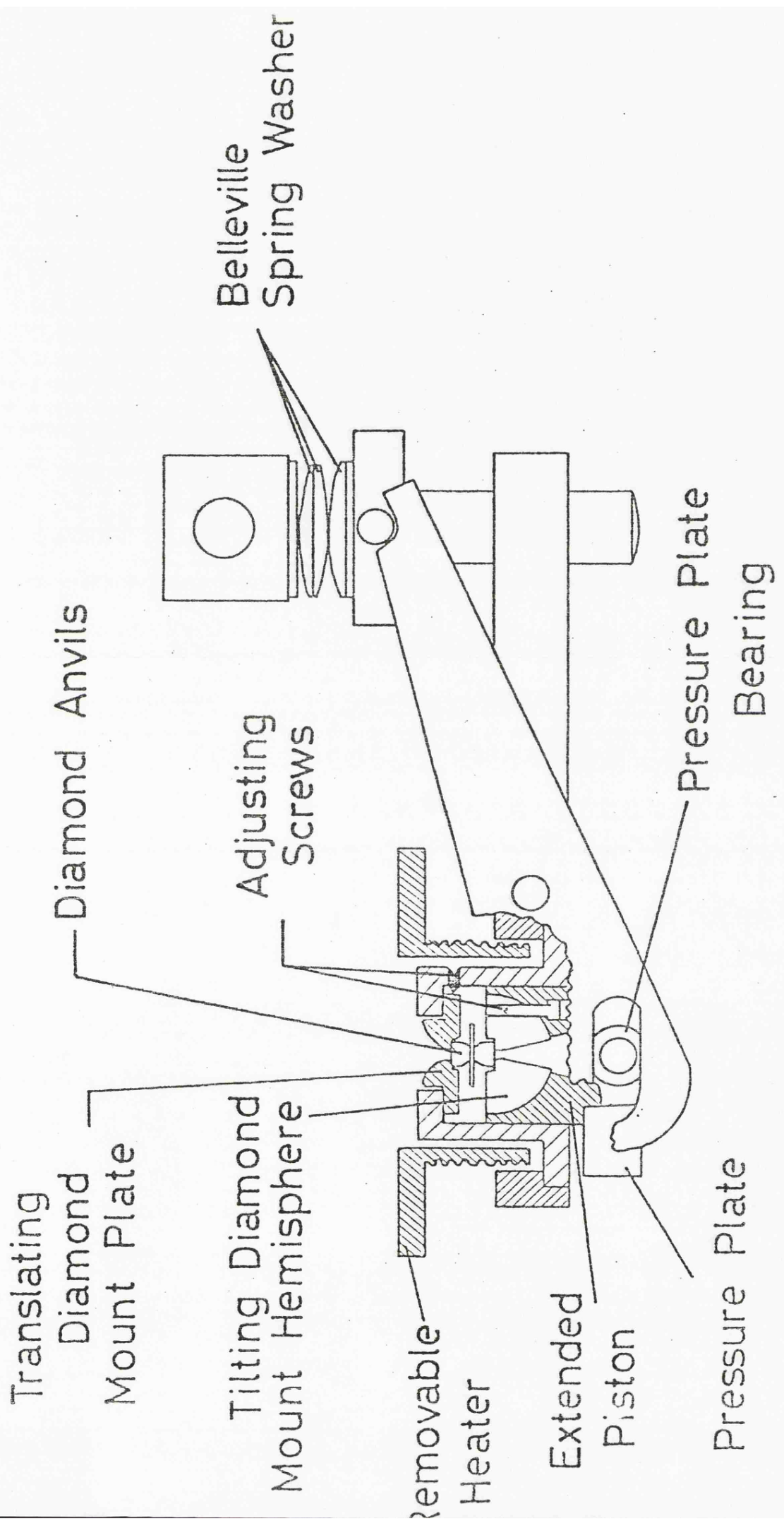
The main differences from the Wier cell were:-

- (i) It was larger, and made of stronger material, and thus more robust.
- (ii) The moving anvil was mounted on a hemisphere which facilitated more accurate alignment of the diamonds.
The anvil holder was also lengthened.
- (iii) The stationary anvil holder was provided with translation adjustment.
- (iv) The spring was replaced by Belleville spring washers.

Also in America, Bassett invented a very compact diamond anvil device (Figure 3.4a) (3) capable of reaching ca 25 kbar. He also designed a DAC with two half cylinders, or rockers, supporting the diamond anvils (Figure 3.4b) (4). These provide initial alignment of the diamonds, and also allow some translational freedom.

Figure 3.3

The Waspaloy Cell.



Translating
Diamond
Mount Plate

Tilting Diamond
Mount Hemisphere

Removable
Heater

Extended
Piston

Pressure Plate

Diamond Anvils

Adjusting
Screws

Belleville
Spring Washer

Pressure Plate
Bearing

Figure 3.4

The Bassett Cell

- (a) a simple diamond anvil device.
- (b) a more conventional cell, showing the first use of half cylinders as anvil supports.

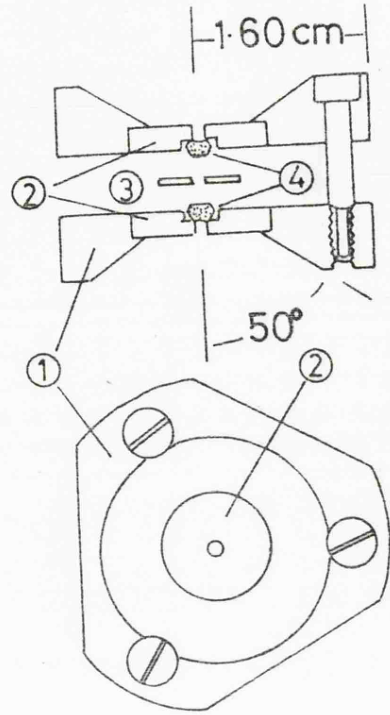
Parts Labelled (a)

- (1) Stainless Steel Platens
- (2) Beryllium Discs
- (3) Inconel Gasket
- (4) Diamond Anvils

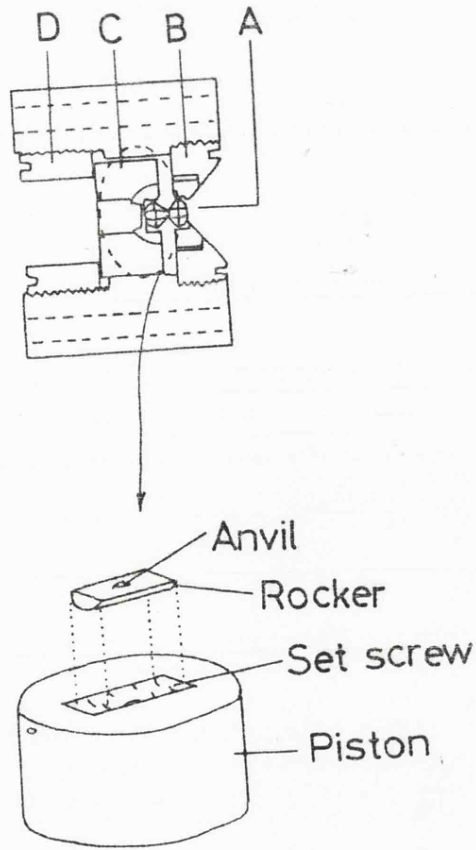
Parts Labelled (b)

- (A) Diamond Anvils
- (B) Stationary Piston
- (C) Sliding Piston
- (D) Driver Screw

a



b



In this group, the first DAC used was a version of the Wier cell from Optical Instruments Inc., U.S.A. From this our Mark I cell was developed in collaboration with Beckman RIIC. Ltd. (5) shown in Figure 3.5.

The body of the cell was made from aluminium alloy, and the rest of the parts from KE 896 steel. It differs from Wiers' cell in the following ways;

- (i) The pressure was applied by a hydraulic ram. This means that the applied pressure can be more closely monitored than if it were applied by turning a screw. This is a distinct advantage, especially when the cell is being utilised by inexperienced users.

A further advantage of this modification is that pressure can be applied while the cell is in an evacuated system (eg. a far infrared spectrometer).

- (ii) The pressure was transmitted from the presser plate (F) to the moving anvil (G) by means of a bearing (E). The idea behind the inclusion of (E) was that by making the actual point of contact between (G) and the moving anvil holder 'self levelling', it would not contribute to any misalignment of the cell. It is now known that this type of bearing can be ineffective under load, and can act in the same manner as a solid presser plate.

The Mark I cell was successful, but it was felt that it could be modified to give a cell which could combine high pressure performance with a variable temperature capability. The Mark II cell was thus designed (6) and is shown in Figure 3.6. The essential differences between this and the Mark I cell were the abandonment of the bearing in the presser plate, and modification of the central

Figure 3.5

The Leicester Mark I cell outline, and section of the central portion.

Parts labelled are:-

- A. Fixed Anvil
- B. Main Body of Cell
- C. Adjusting Screw
- D. Radial Locking Pin
- E. PTFE Lined Hemispherical Bearing
- F. Presser Plate
- G. Moving Anvil
- K. End of Lever Arm

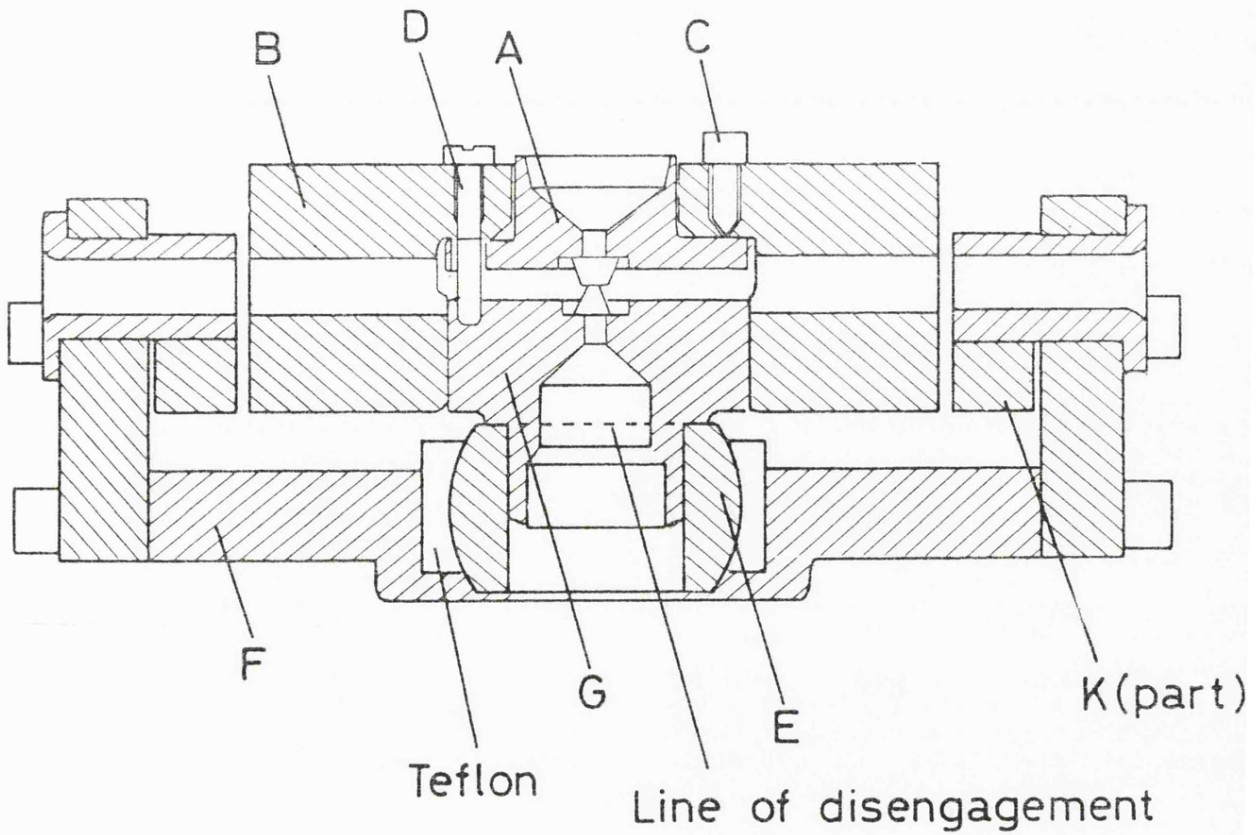
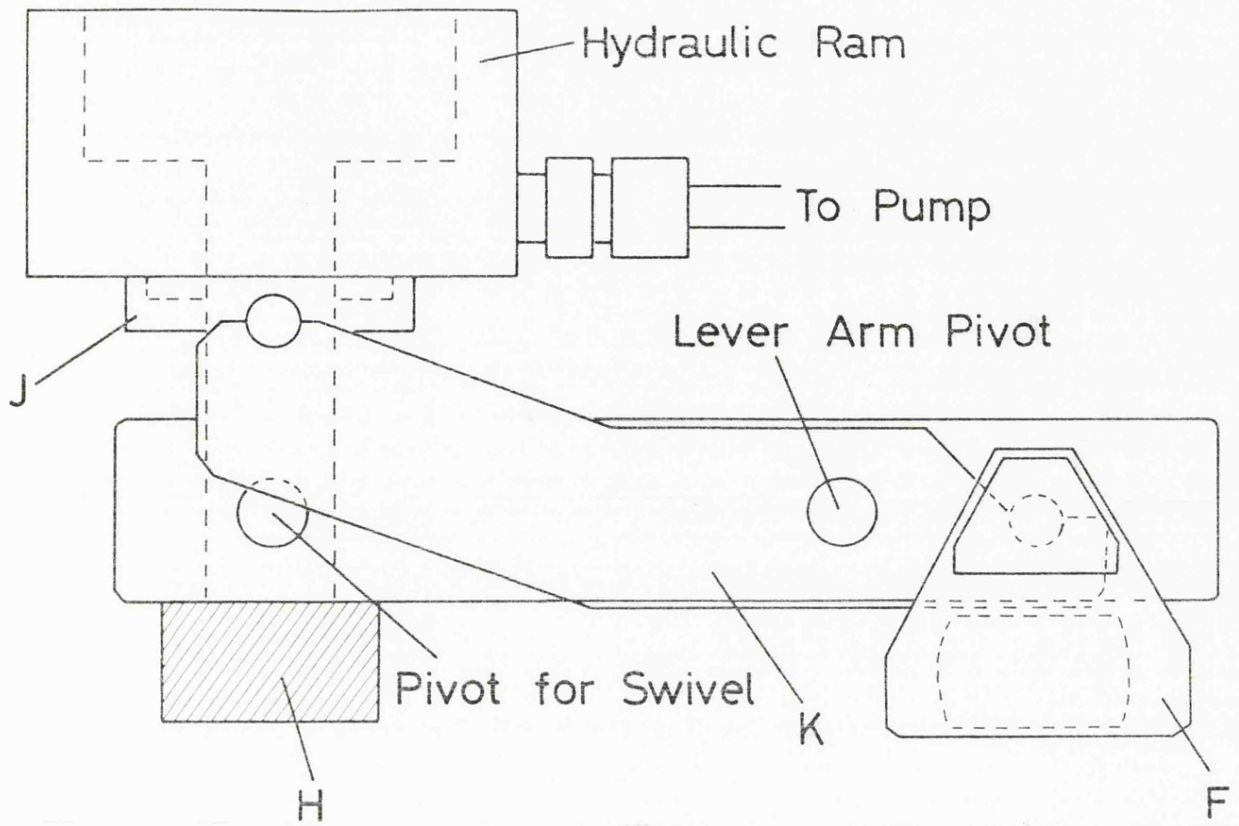


Figure 3.6

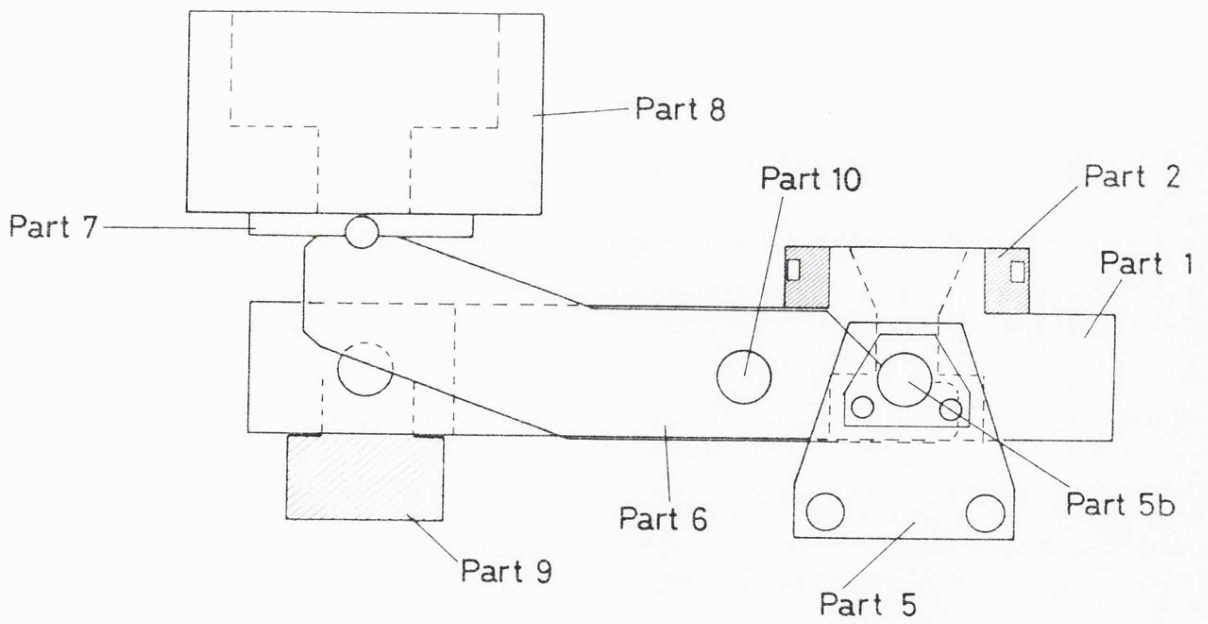
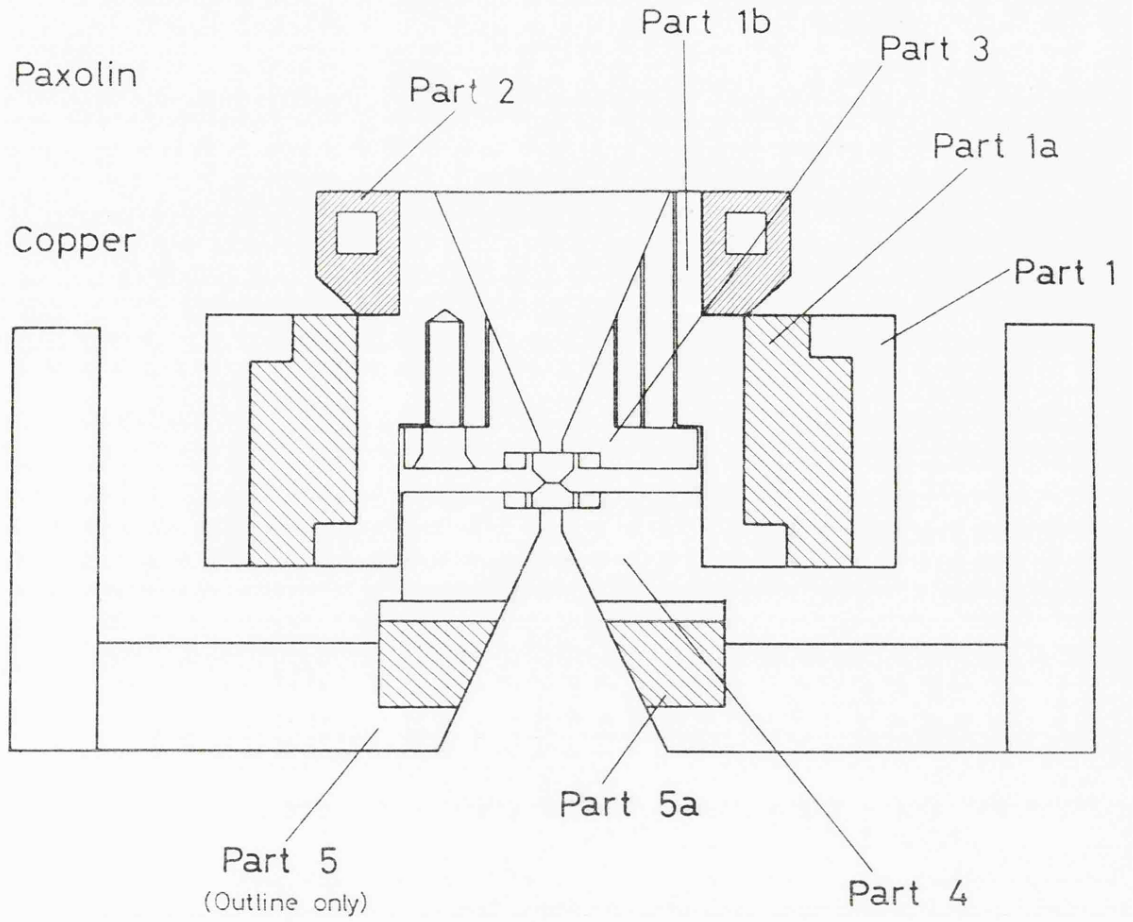
The Mark II cell outline, and section of central portion.

Parts labelled are:-

1. Cell body
- 1b. Central insert
2. Copper anulus
3. Fixed anvil holder
4. Moving anvil holder
5. Presser plate
- 5a. Paxolin washer
- 5b. Presser plate pivot
6. Lever arms
7. Piston plate
8. Hydraulic piston
9. Knurled backing screw
10. Central pivot

 Paxolin

 Copper



insert, part 1b. This central insert was insulated by paxolin pieces (1a and 5a). These were to lower the thermal load on any temperature controlling device, by removing any metal-metal contact between the heated/cooled insert and the remainder of the system. The "nose" of the insert was extended, onto which a heating or cooling coil (part 2) could be placed.

The radiation ports in the anvil supports were also altered, and polished to provide effective light pipes in an effort to improve the far infrared performance of the cell.

This Mark II cell was later modified by increasing the barrel length in the 'piston and cylinder' arrangement of the central insert. This led to increased mechanical stability, and helped to keep the generated pressure normal to the diamond faces, and thus decrease misalignment and ultimate failure of the anvil. A second locating pin was added such that a gasket with two locating holes drilled in it could be precisely positioned over the diamonds.

A 'Waspaloy' type insert was then designed, utilising the ball and cup system as an aid to diamond alignment. This was the Mark IIa cell, and is shown in Figure 37.

Several features of the Mark II and Mark IIa cells could, with hindsight, be criticised. The pressure capability of these cells is severely limited, to considerably less than 100 kbar, as the design material of the central insert (stainless steel) was less than ideal. This is due to two features of stainless steel; first, its relative

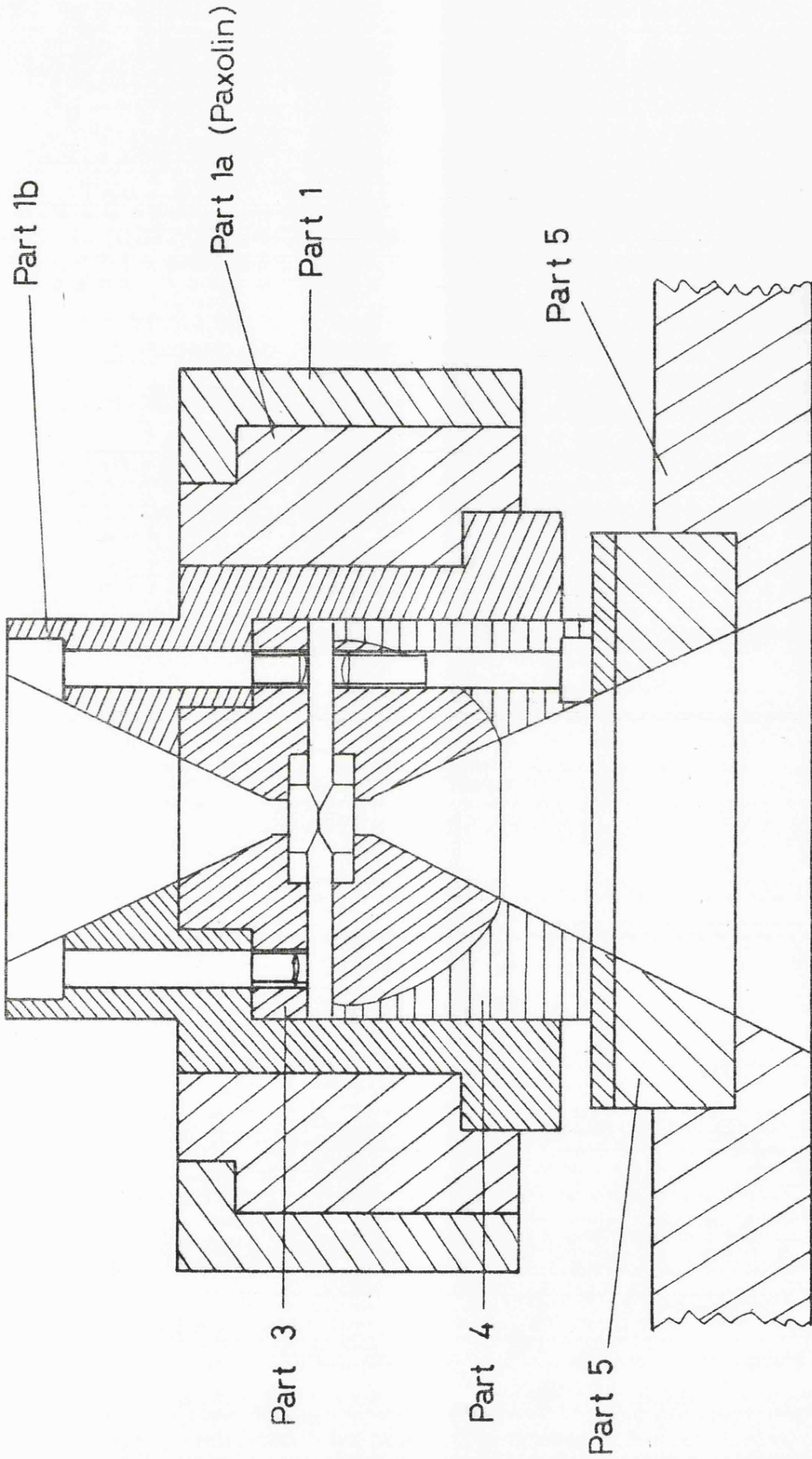
Figure 3.7

Mark IIa DAC - section through central insert.

The cell body remains the same as that for the Mark II cell.

Parts labelled are:-

1. Cell body
- 1a. Paxolin insulation
- 1b. Central insert
3. Fixed anvil holder
4. Moving anvil holder
5. Presser plate



weakness compared to other steels, and second, its low thermal conductivity, which limits temperature variation experiments.

The second weakness in the design of the cell is that the central insert was completely supported by paxolin, chosen for its thermal insulation, but clearly not suitable to be subjected to very high pressures.

Apart from these factors, the Mark II cells performed well, were used routinely to 50 kbar, were easily loaded and were very versatile in as much as they could be used in mid and far infrared, UV, and Raman spectrometers; with some modification high pressure X ray experiments could also be performed.

It was then decided to perform a full structural analysis of the Mark IIa DAC, and from this analysis, to design a cell capable of achieving a static pressure of 1 Mbar, retaining the ability to allow spectroscopic investigation of its contents. This analysis was carried out by R.Appleby (7), and consequently a new cell, the Mark III cell emerged, designed to satisfy the following conditions;

- (i) High Pressure Stability
- (ii) Variable Temperature capability.
- (iii) Overall compatibility with existing equipment.

The overriding limitation on the performance of a cell designed to observe high pressure vibrational spectra is the diamond, both in terms of size and shape.

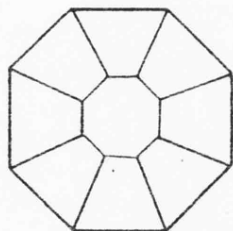
The major criterion the anvil must satisfy is that it must obey the "principle of massive support". Figure 3.8a and b shows diamonds which do not obey this principle.

Figure 3.8

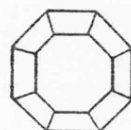
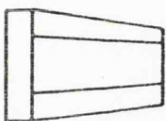
A variety of Diamond Anvils.

- (a), (b) Diamonds not obeying the principle of massive support.
- (c) Diamond used by author.
- (d) Diamond used by Piermarini (1973).
- (e) Diamond used by Holzapfel (1976).
- (f) Diamond used by Mao and Bell (1975).

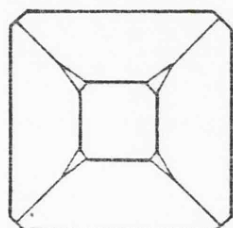
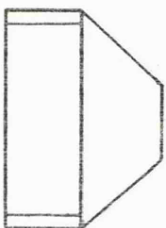
a



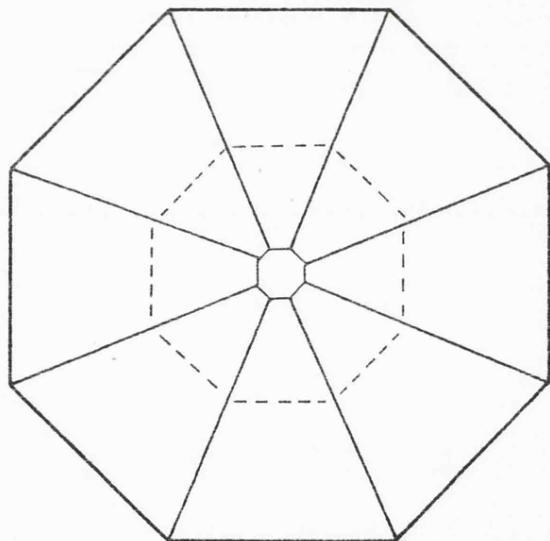
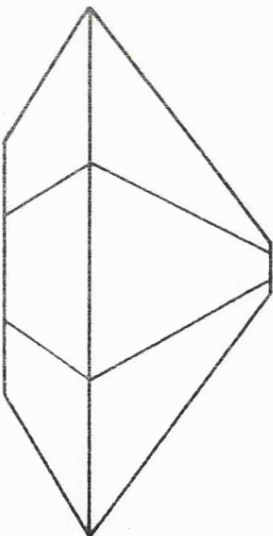
b



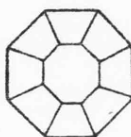
c



d



e



f



1mm

Figure 3.8c shows the standard anvil design used by the author, supplied by L.M. Van Moppes Ltd., Basingstoke; 8d is used by Piermarini, 8e by Holzapfel, and 8f by Mao and Bell.

The analysis of the cell showed that to generate a pressure of 1 Mbar (or 10^{11} Pa) in a Mark IIa type cell, over an area of 10^{-6} m², an oil pressure of 4×10^7 Nm⁻² (5730 psi) would be required, and the subsequent design geared to take high oil pressures.

The Mark III cell became known, affectionately or otherwise, as the 'Dynocell', firstly for the obvious pun on force, and secondly that the cell proved so large and unwieldy that it was thought that it would be the last of its kind.

The Mark III cell, described in more detail below, was adapted to give a further increase in mechanical stability by lengthening the piston and cylinder.

3.2 Constructional features of the Dynocell

The dynocell was made by A.S. Scientific products Ltd., and was machined throughout in McCreadys NSOH Steel (Carbon 1%, Chrome 1%, Manganese 1%). This material was not oil hardened, as hardening should only be performed when the substance is subjected to compression, whereas all parts of the cell (with the exception of the diamond anvil supports and the moving piston) are in tension. The diamond anvil supports were formed from EN 24 (1½% Ni-Cr-Mo steel) hardened to 95 tons/sq in.

The use of NSOH has a minor drawback as the surface easily becomes corroded, albeit a shallow corrosion. Thus the cell was continually coated with a film of oil, and occasional polishing with "tulip" paper was required.

An assembly drawing of the dynocell is given in Figure 3.9.

The hydraulics of the system were essentially the same as the earlier design, but with all dimensions increased. Special O rings, tested to 2000 psi were used in its construction, and the hydraulic tubing and tap which connected to cell to the oil pump (Tangyi hand pump - Tangyi Ltd., Birmingham) could withstand pressures in excess of 4000 psi. (It should be noted that, whereas it has previously been stated that oil pressures of ca.5700 psi are required to generate 1 Mbar over an area of 10^{-6} m^2 , normal anvil areas were of the order of $0.4 \times 10^{-6} \text{ m}^2$.)

Shell Tellus 27 oil was used to pressurise the system.

One of the major weaknesses of previous cell designs were the central pivots, about which the lever arms hinged. In the dynocell the bolts which formed these were replaced by press fit studs (Unbrako Ltd., Coventry) onto which the lever arms were merely slotted. The overall fit of the presser plate was sufficiently good to hold the lever arms in place with no appreciable lateral movement.

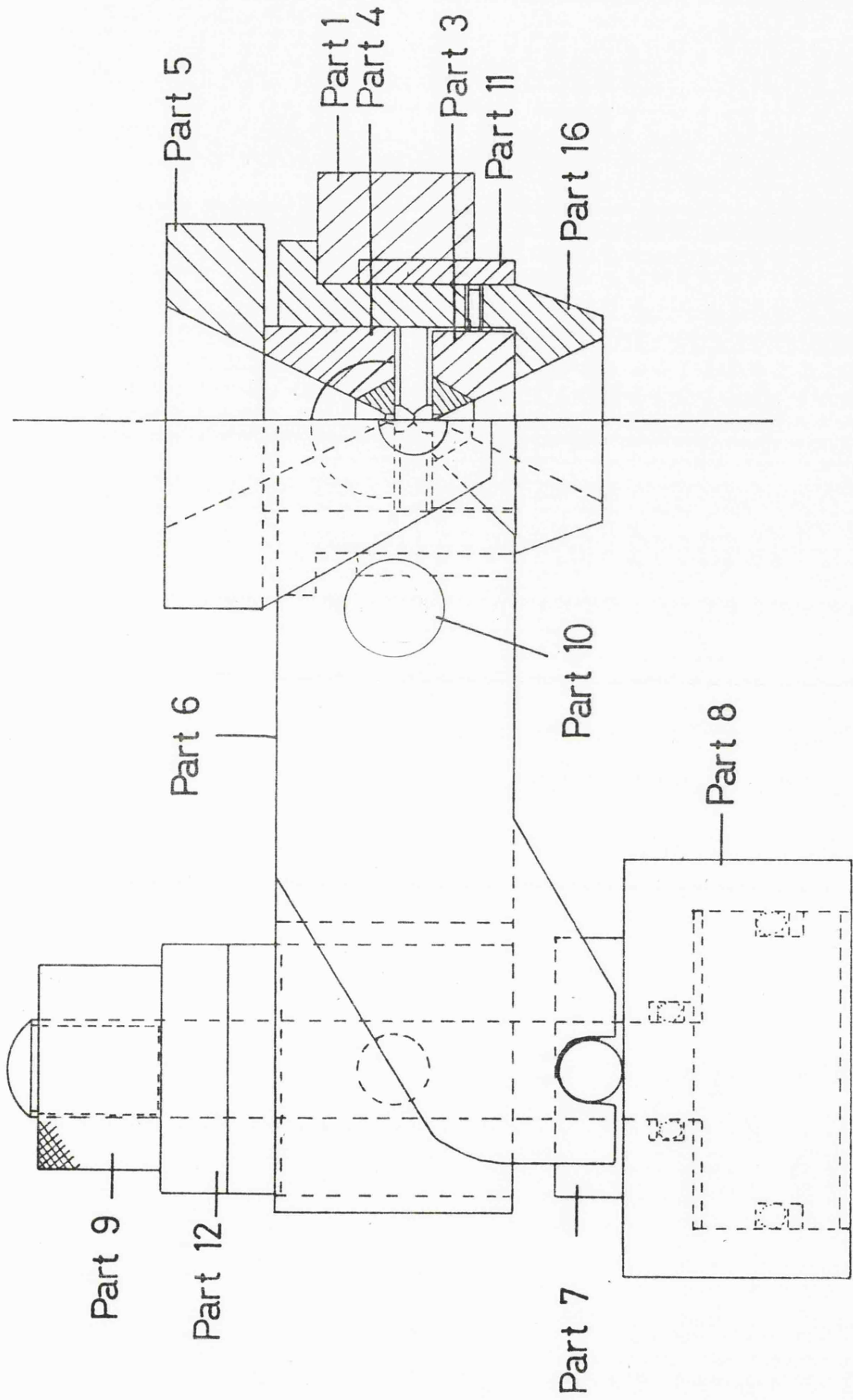
The knurled backing screw which secures the stationary part of the piston was supported on a V block assembly (see Figure 3.10). This was to remove any possibility of the cell body or rig twisting and forcing the presser plate to make imperfect contact with the moving anvil, and thus causing the anvils to misalign. This twisting was occasionally observed on the Mark IIa cell and could have been contributory to the indentation and ultimate failure of some diamonds. The V block appeared to perform satisfactorily, although after several excursions to pressures in

Figure 3.9

Assembly drawing of Mark III DAC (The 'Dynocell').

Parts labelled are:-

1. Cell body
16. Central insert
3. Fixed anvil holder
4. Moving anvil holder
5. Presser plate
6. Lever arms
7. Presser plate
8. Hydraulic piston
9. Knurled backing screw
10. Central pivot
11. Insulator
12. V block assembly



excess of 100 kbar, the V appeared to have compressed somewhat, and the clearance between the block and the cell body is less than that originally designed.

In its assembled form, the dynocell proved difficult to handle, due to its considerable weight, and the lack of flexibility of the rubber/steel hydraulic tubing when compared to the nylon tubing used in the hydraulics of its more pressure limited counterparts. (The nylon tubing was limited to oil pressures of ca.450 psi, and thus was clearly not suited to very high pressure experiments.) Indeed, the assembly of the cell itself was by no means trivial as the very fine tolerances required caused each portion to be a very close fit to its neighbour.

3.3 Use of the Dynocell

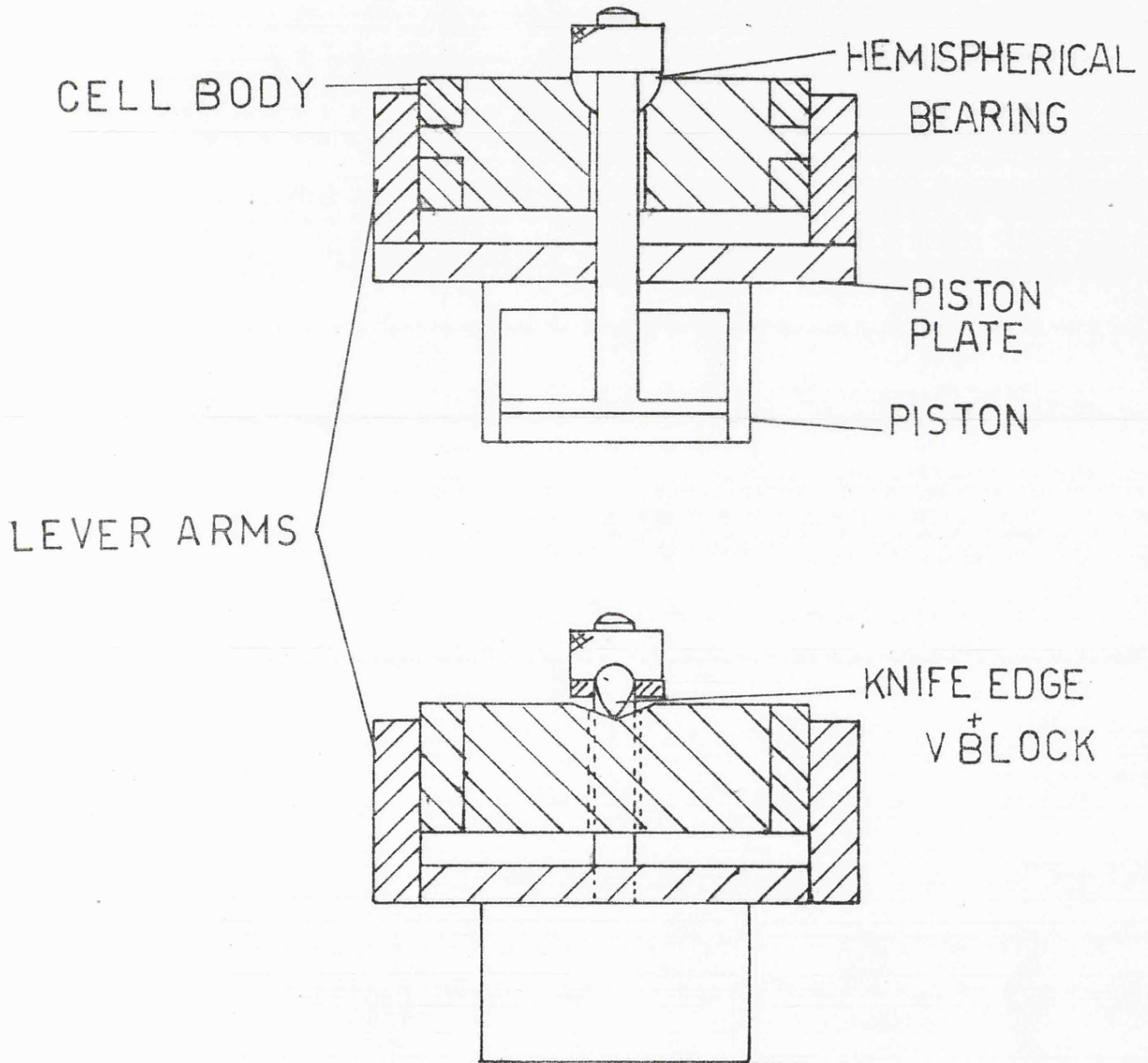
The dynocell followed the Waspaloy cell with regard^{to} anvil supports; that is, the fixed anvil was placed on a flat cylindrical support. A degree of lateral freedom to facilitate accurate vertical alignment of the anvils was allowed, the position of the support being controlled by means of four grub screws, placed at 90° to the next round the cylinder, which pushed the support into the required position. The moving anvil was attached to a hemispherical support, and provided the horizontal alignment (parallelism) of the anvils. Alignment was carried out as described in Chapter 2, and checked with HgI₂, KCl, and also AgI, which transforms from the stable ambient pressure phase AgI (II), with the wurtzite structure, to AgI (III) at ca.4 kbar, then to AgI (V) at pressures around 90 kbar, which may be tetragonal (8).

Figure 3.10

Two solutions to the problem of twisting of the cell body.

(a) Hemispherical bearing

(b) V block assembly



A matched pair of 0.75mm type II B diamond anvils were mounted in the cell, using procedures described elsewhere (p31).

Far Infrared

The bulk of the fittings associated with attaching the hydraulics to the ram on the dynocell posed serious problems when it was attempted to use the dynocell in the Beckman RIIC FS620 interferometer, and modification of the sample housing would have been necessary to accommodate the cell. This was given consideration but abandoned for the following reasons:-

To obtain far infrared spectra through a DAC, the maximum possible aperture was required. This necessitated gasket holes of ca. 0.6×10^{-3} m. It has been the author's experience that, in general, gasket holes open during high pressure experiments, and a ratio of ca 2 : 3 for gasket hole diameter to diamond face diameter has been taken as a general 'safety limit'. This requires diamonds with face areas of ca. 1×10^{-6} m². The large volume of diamond involved in such an anvil is very expensive and at risk at very high pressures. The large surface area of a 10^{-6} m² diamond requires a large applied oil pressure. Thus a situation where, to generate high pressures in the far infrared, higher oil pressures would be required, and larger, more expensive diamonds would be at risk.

Coupled with this is the fact that, to date, Nujol appears to be the best hydrostatic medium for work in the far infrared. Nujol freezes at around 15 kbar, so pressures greatly in excess of this depart increasingly from hydrostatic conditions, so the advantages over using non gasketed samples would therefore be diminished.

Hydrostatic high pressure far infrared spectra were not therefore obtained from the dynocell, and it was felt that a practical limit of ca. 50 kbar exists at present in the far infrared region.

Mid Infrared Region

It was found that with 0.75mm diamond faces of the diamonds in use, gasket holes of the order of 0.3×10^{-3} m diameter (for a 0.15×10^{-3} m thick gasket) were necessary to enable pressures in excess of 50 kbar to be generated. To test the cell, a study of benzene was undertaken, details of which are given later in this chapter. The dynocell was used in conjunction with a Mark I beam condenser, on a PE580 ratio recording infrared spectrometer. As pressure on the sample was increased, so the transmission through the cell increased, this being due to the increase in diameter of the gasket hole.

Raman Spectroscopy

Use of this cell with Raman equipment proved routine, the process for mounting being identical to that for any other DAC used by the group. The only drawback was again the rigidity of the connections to the pump.

3.4 The "Super Dynocell"

This cell was an extension of the dynocell, the basic difference being the length of the central insert, the 'super dynocell' having a much longer central insert (see Figure 3.11) than the dynocell. The materials used in the fabrication of this insert were the same as those used in the dynocell; i.e. McCreadys NSOH steel for the piston and cylinder. The anvil supports were made from EN24 hardened to

ca. 100 tons in $^{-2}$, with cobalt cemented tungsten carbide inserts upon which the anvils were selected.

This cell was used to test two new designs of diamond anvil, supplied by D. Drucker (Amsterdam), (see Figure 3.13) and departed from the normal anvils used in this research in being gem cut, with eight facets.

The difference between the two new anvil designs was that, whilst the first was a single stone, the second was a "composite anvil"; that is each anvil was composed of two stones, the upper a truncated octahedral pyramid, the lower an octahedral cuboid, the two stones being located and cemented before the anvil "assembly" was mounted. The reason for the selection of a two stage anvil was purely economic. It was envisaged that, when failure of the anvil occurred, the top section alone would be broken, the lower (and larger) portion staying undamaged, and capable of matching with further halves. As the cost of anvils is determined largely by their weight this proved sound economic sense.

If the radiation port behind the moving anvil was allowed to retain the 52° cone angle as in previous designs, the length of the piston would be clearly restricted. It was thus necessary to reduce the port to a simple hole drilled through the piston in order to allow the extreme length of the piston to be achieved. A consequence of this was that the cell was then restricted in its spectroscopic abilities to Raman spectroscopy, either in 0° geometry, where the laser beam could be passed through the hole in the piston, or 180° scatter, where the radiation enters and exits the same port.

Figure 3.11

The "Super Dynocell" central insert.

Dotted line indicates length of original dynocell insert.

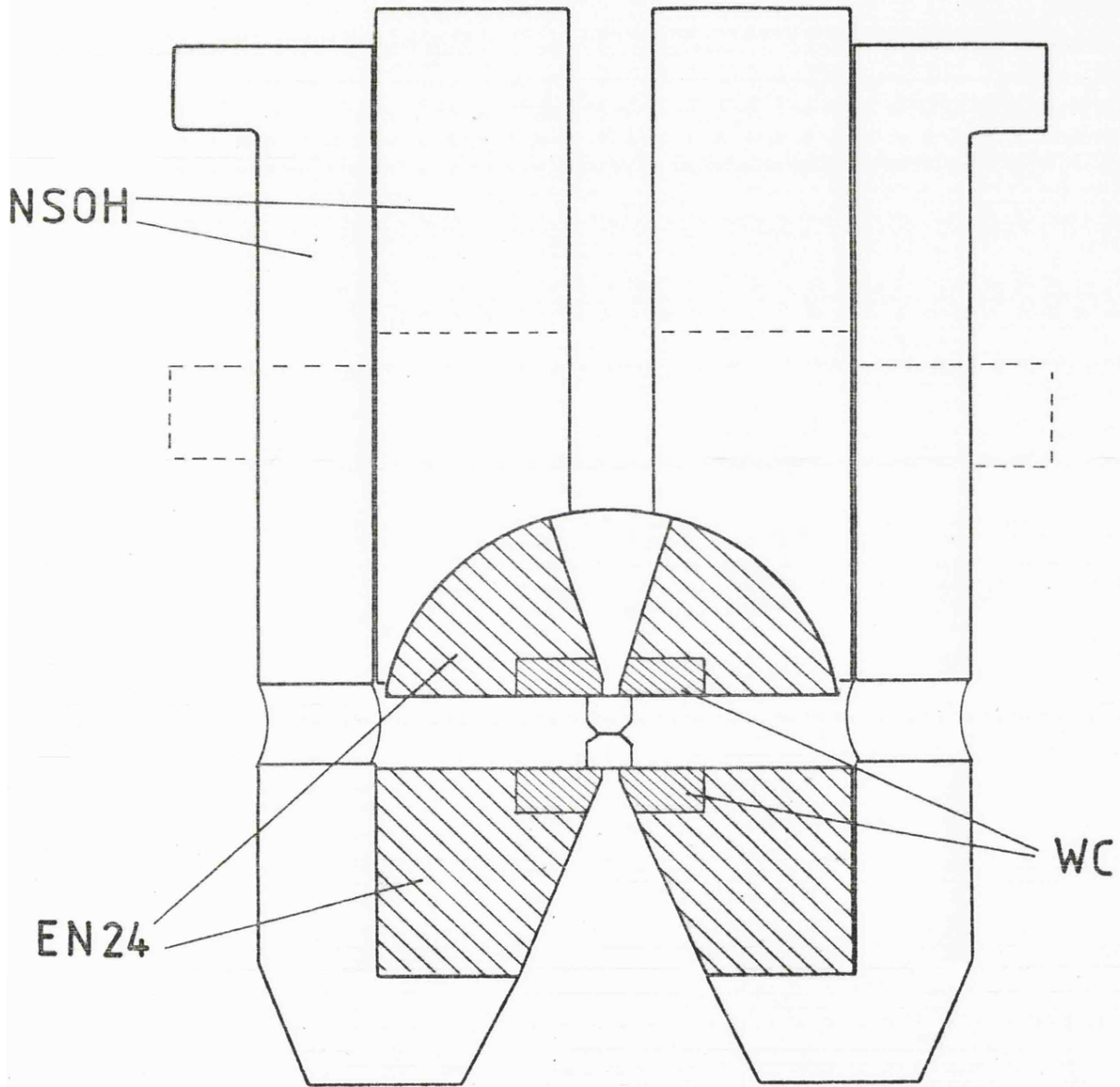
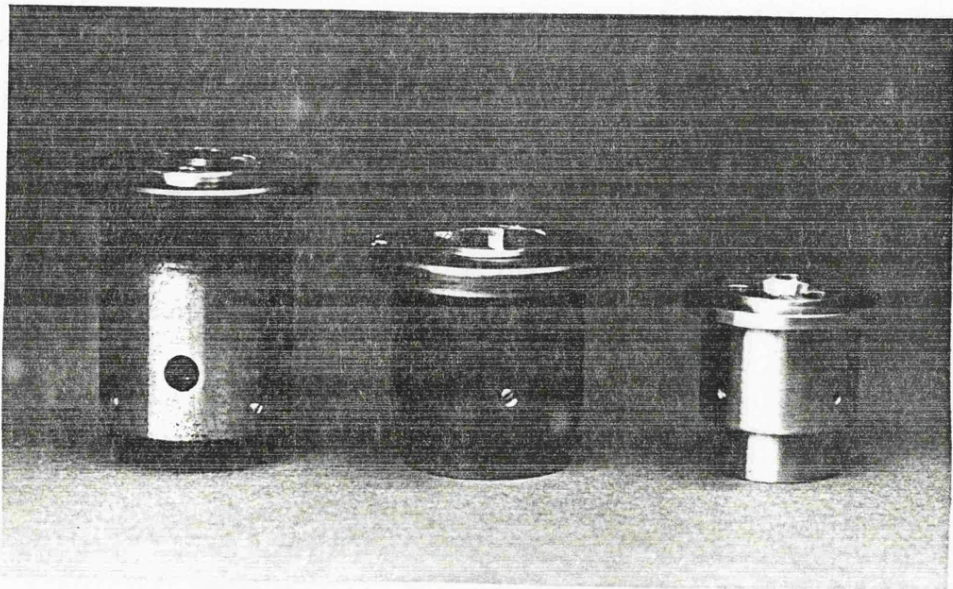
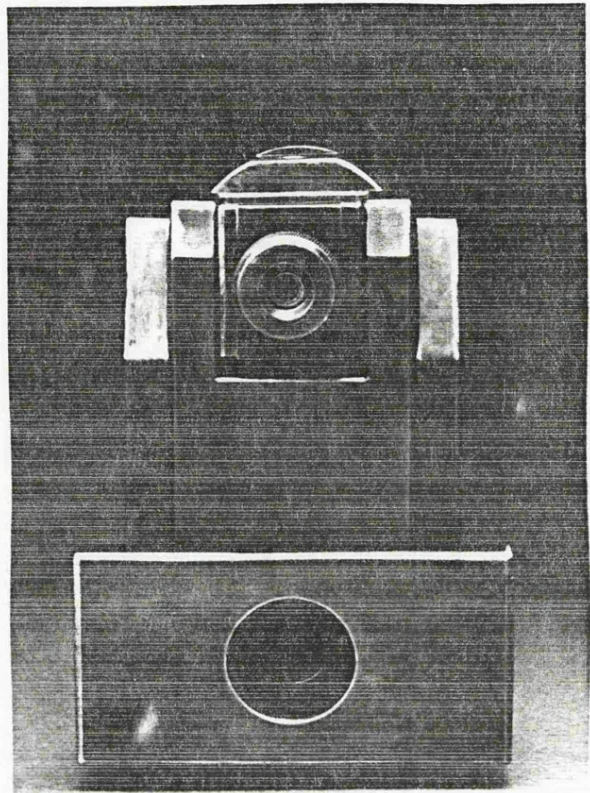
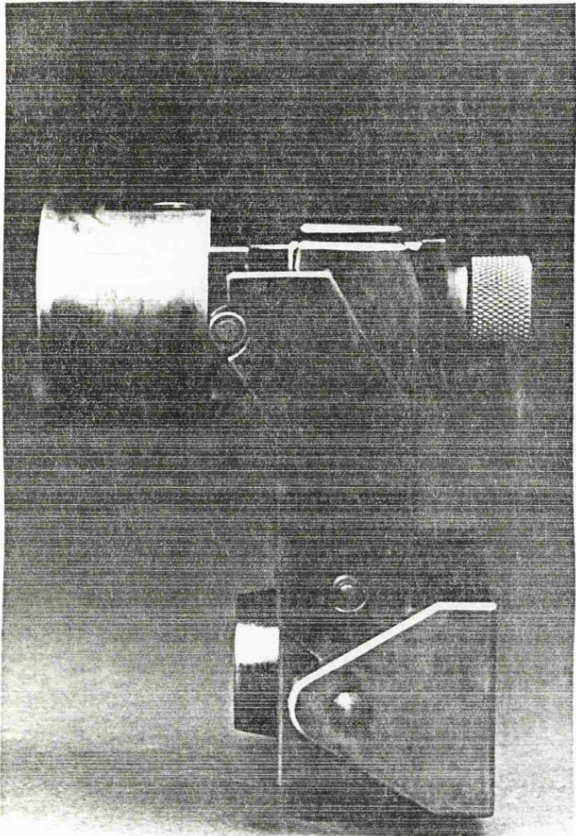


Figure 3.12

- (i) Photographs of the assembled dynocell
- (ii) The super dynocell, dynocell and MkIIa inserts respectively.



The diameter of the radiation port in the tungsten carbide supports was decreased in order to minimise the unsupported area of diamond. This aperture, 1mm in previous designs was altered to 0.75mm diameter.

A somewhat modified technique for mounting the diamonds had to be adopted for this cell. The stationary anvil could be mounted as before, centering the diamond face over the radiation port by use of a monocular microscope. The moving anvil, which, in other cells, would then be matched to the now fixed stationary anvil, was located independently over the centre of its radiation port, then the stationary anvil was adjusted, by means of the four grub screws around the central insert, to match the face of the moving anvil. This change in procedure was necessitated by the length of the insert, which exceeded the working distance of available monocular microscopes.

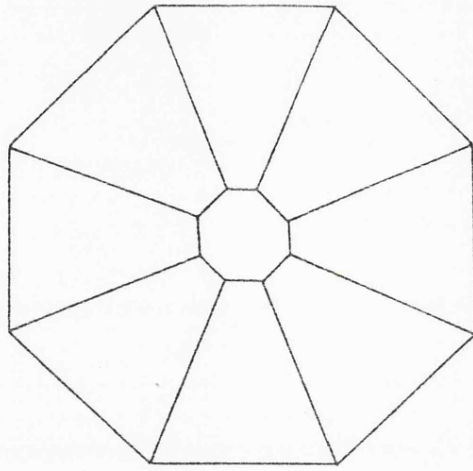
Vertical alignment too proved difficult, as the diameter of the radiation port was approximately the same as that of the pressure faces, whereas in the past the port has been considerably larger than the diamond face. Thus the edges of the diamond were not clearly visible through the support, and consequently "circular alignment" was difficult to observe.

This was aided, however, as was horizontal alignment by the provision of two observation ports in the central insert, which allowed a visual check to the approximate parallelism of the faces, before the more accurate process of observing the fringes formed between the faces, etc.

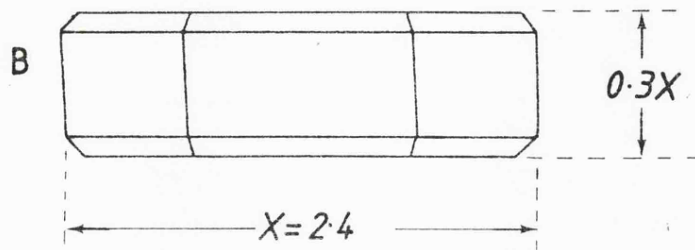
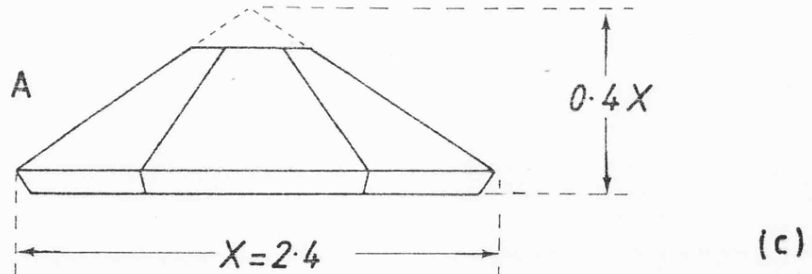
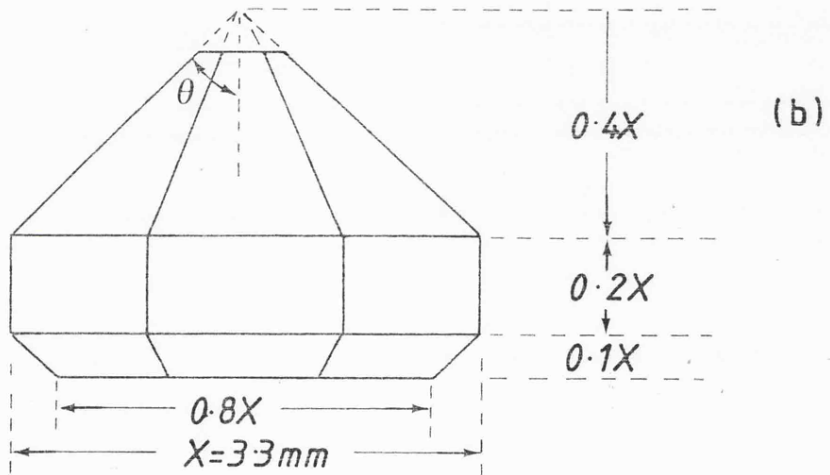
Figure 3.13

Two experimental designs of diamond anvil supplied by
D. Drucker (Amsterdam).

- (a) plan of 'solid' anvil
- (b) elevation of 'solid' anvil
- (c) elevation of composite anvil



(a)



3.5 Diamond Failure

3.5a The Dynocell

During the testing of the dynocell, an anvil failed at ca. 110 kbar. The appearance of the anvil suggested a mode of failure not previously observed by the author (Figures 3.14, 3.15). The upper face of stone was completely powdered. However the remainder of the stone was observed to have developed cleavages running radially from the applied pressure axis. The lower face was noted to have ejected a block of finely divided diamond. The overall symmetry of the failure suggests that loss of the plug (this unsupported area is subjected to large tensile stresses when the anvil is subjected to pressure) may have preceded the failure of the top of the anvil.

3.5b The Super Dynocell

Details of the anvils used are as follows. (See Figure 3.13).

(All dimensions in mm.)

All stones type 1.

Single Stone Anvils

height	2.2 ± 0.01
base	3.3 ± 0.01
upper face	0.6 ± 0.01

Figure 3.14

Upper face of conventional anvil having failed in the
dynocell at ca. 110 kbar.

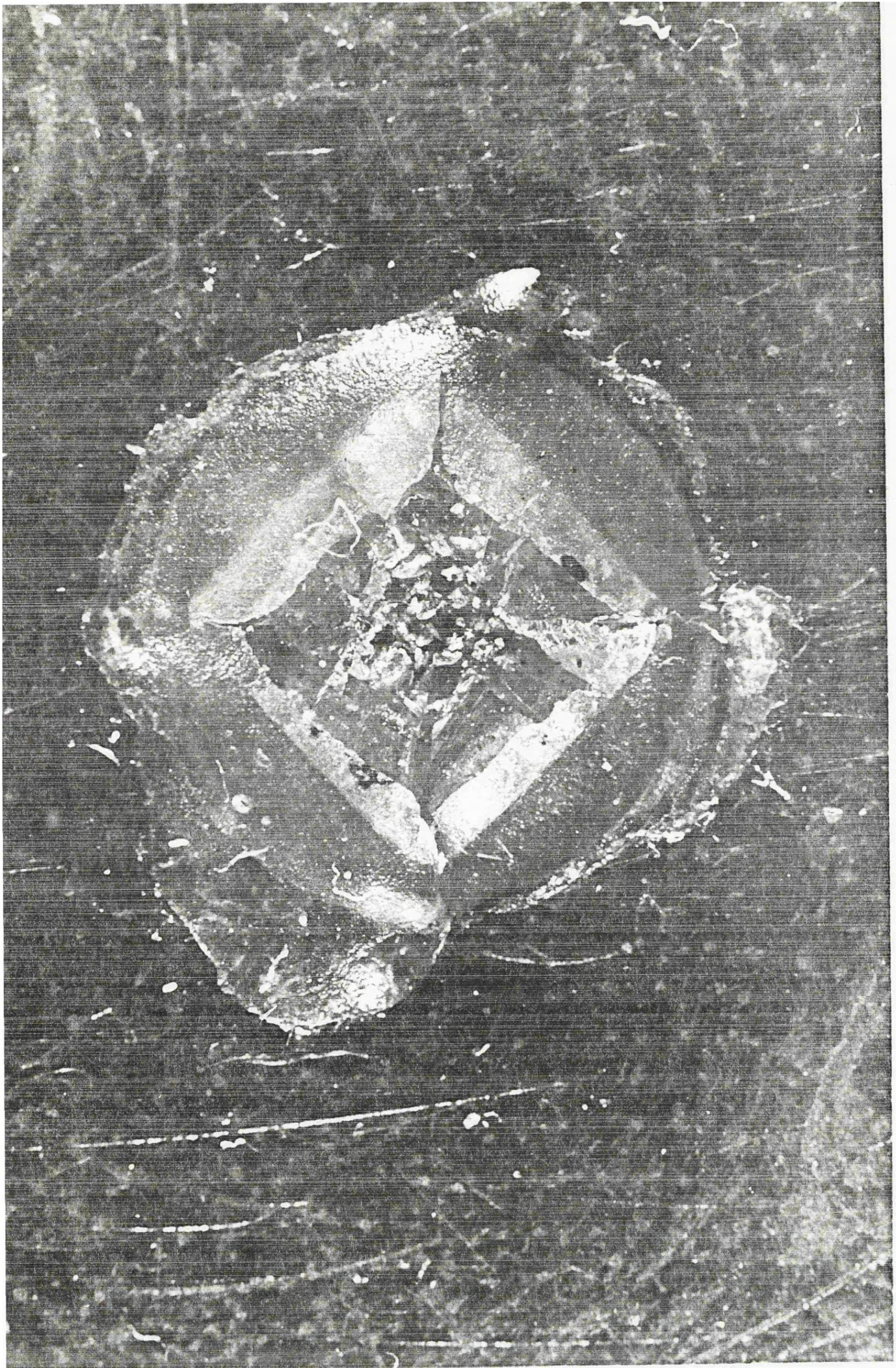
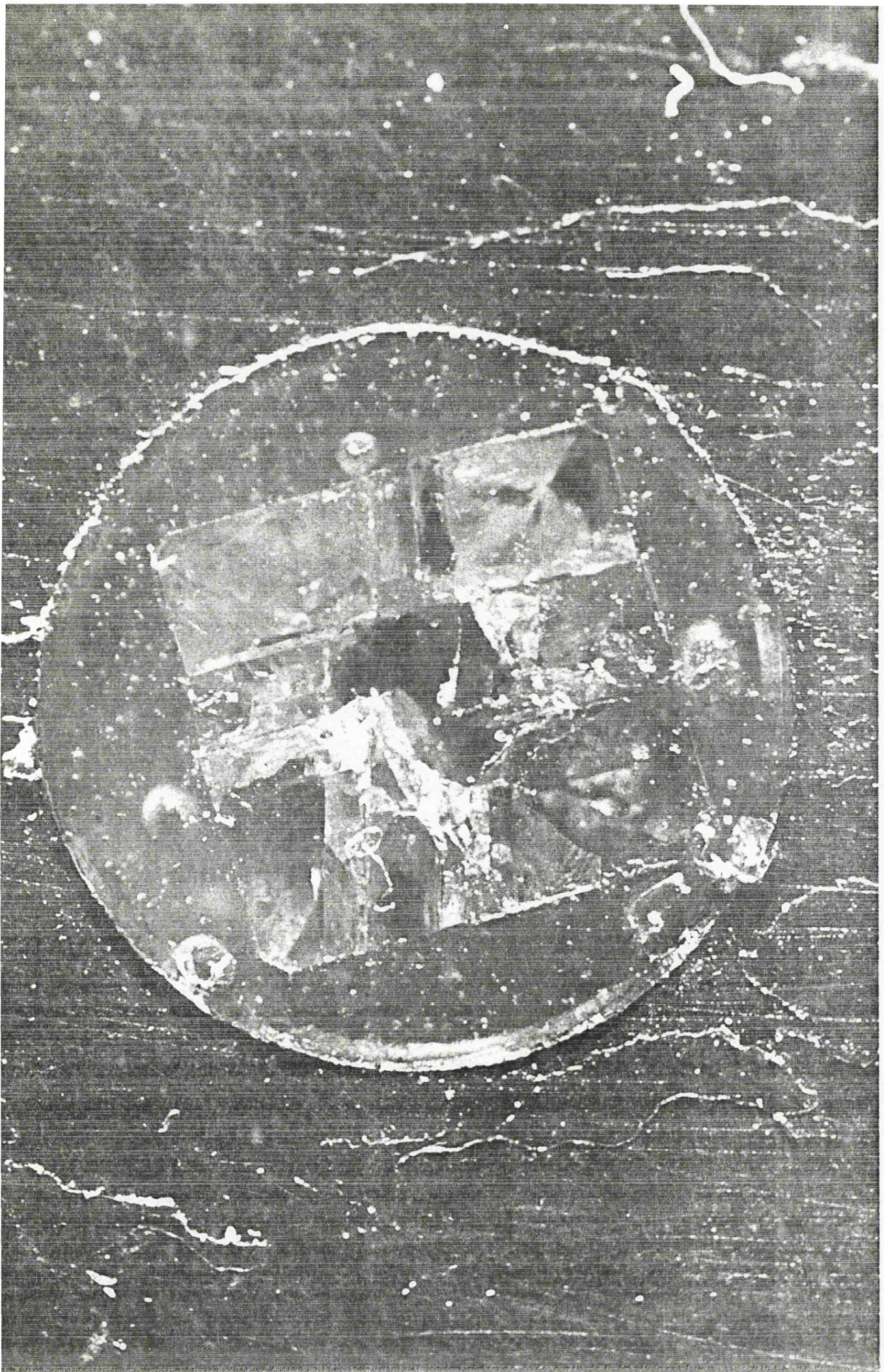


Figure 3.15

Lower face of conventional anvil having failed in the dynocell at ca. 110 kbar.

NB: Dark area in the centre of the stone is where the 'block' of diamond was ejected. Remainder of stone showed cleavage, but remained intact.



Split Anvils

These were supplied as two matched pairs of anvil "halves".

height	A ₁	0.94	B ₁	0.73
	A ₂	0.98	B ₂	0.73
width of all stones	2.4 ± 0.01			
upper face	0.63 ± 0.01			

All anvils were supplied with the culet cut parallel to the 100 crystallographic plane.

Single Stone Anvils

The above stones were tested to destruction. The first tests were performed on the single stones. These were mounted on the super dynocell as described above.

Initial alignment of the anvils by observation of Newtons Fringes between the stones proved difficult as the piston/cylinder system was of a sufficiently good fit to make tilting of the faces (by pressing alternately on opposing points of the cylinder) almost impossible.

Alignment checks thus consisted of observation of the phase transitions of various solids at known pressures. Materials used in these tests were HgI₂ (≈ 13 kbar), KCl (≈ 20 kbar), AgI (≈ 98 kbar). The cell was loaded, pressurised, the behaviour of the phase transition observed, the cell depressurised, adjusted, unloaded, loaded with a new sample, and the cycle repeated.

Having aligned the cell a 0.2mm thick piece of inconel was placed between the anvils, and indented by application of 100 psi. Chips of ruby were then placed in this indentation and the cell reassembled.

It was decided to use gaskets without holes in these experiments for two reasons. Firstly this would in theory remove the possibility of the gasket hole spreading, and allowing the anvils to come into contact; and secondly, 180° scatter would be employed to monitor the pressure within the cell, and hence no gasket hole was necessary.

The cell was then placed in the T800 Raman spectrometer and pressurised. Results are shown on Table 3.1.

The position of the ruby chips were critical. The first set of readings were observed to require large oil pressures to generate moderate changes in the pressure on the sample. It was noted that the ruby was in fact near the edge of the indentation. As can be seen the second set of measurements showed a marked increase in pressure sensitivity. The laser was focussed at various positions across the sample area, until the ruby R_1 band occurred at the highest Raman shift, this being an indication that the beam was striking the centre of the sample. The two ruby lines were not resolved however. This was assumed to be due to lack of accuracy in focussing the laser, and/or inclusion of a large ruby chip at the centre of the gasket. Re-emitted radiation from this would probably not be resolved as the chip would experience non hydrostatic pressure.

The application of pressure up to the maximum observed (266 kbar) took place over 3 days in order to allow stresses generated during pressure increase to minimise. As the applied pressure reached 800 psi, the pressure was noted to drop. When the cell was examined the moving anvil was found to have reduced to a powder.

Figure 3.16

Fluorescence profile of the solid type I diamond through which
Ruby fluorescence spectra in Figure 3.15 were obtained.
Spectral slit width 5cm^{-1} 400mw 5745Å at sample. Band at
 1331cm^{-1} is the symmetrical stretch (ν_1) of diamond.

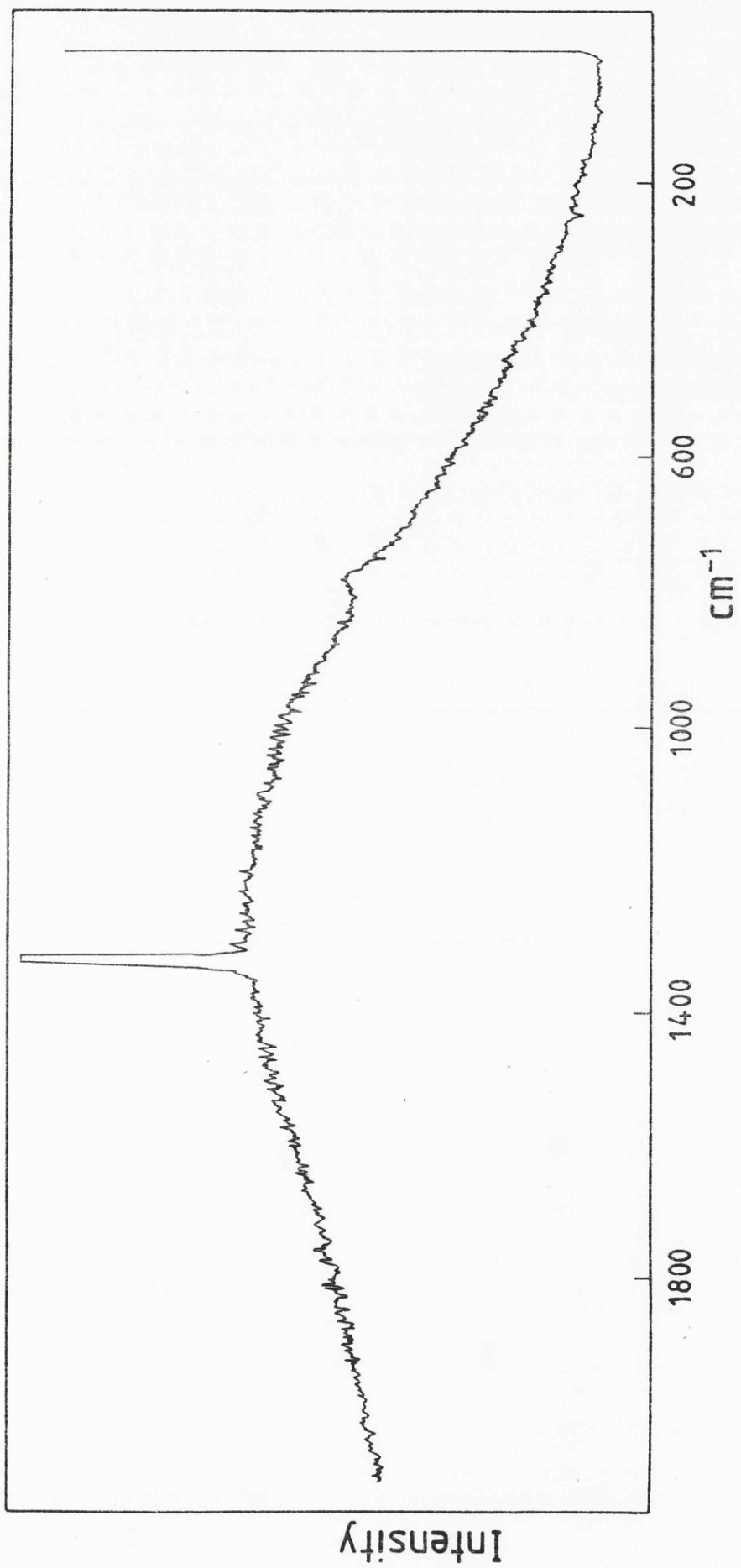


TABLE 3.1 Pressures attained in the 'Super Dynocell' using type I single stone anvils, together with applied oil pressures.

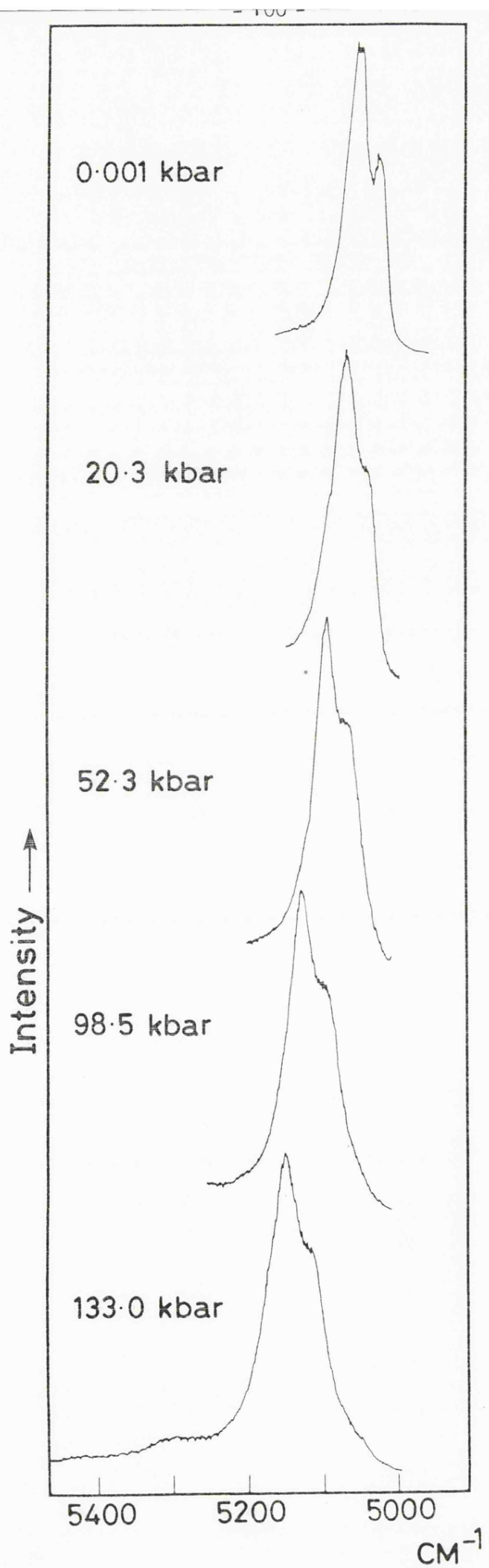
Pressure between anvils/kbar		Oil pressure/psi
24	1st load	150
43	1st load	300
78	1st load	400
126	2nd load	300
229	2nd load	600
266	2nd load	750
Anvil failure occurred		800

Figure 3.17

Raman spectra of the ruby R_1 and R_2 bands at various pressures.

These spectra were obtained using one composite and one solid anvil in the super dynocell. Failure of the upper half of the composite anvil occurred at ca. 155 kbar.

Spectra were recorded using 100mw of 5145\AA radiation at the sample, with a spectral slit width of 0.6cm^{-1} .



Examination of the gasket revealed large fractures in the metal, especially around the edge of the indentation, indicative of gasket failure under pressure.

The stationary anvil suffered some damage, and lost several facets. This indicated misalignment of the anvils at some stage. This damage definitely occurred during the experiment, and not in the preceding alignment tests.

A plausible scheme for the failure of the anvil is as follows;

(1) A flaw in the anvil material may have caused fracture of the anvil and deformation of the anvils may have taken place. Deformation of diamond anvils has been observed. Bassett (10) obtained Laue photographs of the deformation of diamond when a pellet of NaCl (of lesser diameter than the anvil face) was placed in a DAC and subjected to a pressure of ca. 100 kbar. Subsequent calculations showed the anvil face to have a radius of 12mm. Mao and Bell (11) have observed plastic deformation of bevelled diamond faces at 1.7 Mbar.

If this deformation of the anvils occurred, it would have resulted in partial misalignment of the stones, and may have resulted in the loss of the portion of the stationary anvil described above.

The new edge of the stationary anvil would now act as an indenter upon the already deformed opposing anvil, and cause large

pressure gradients to form around the area of contact which could ultimately cause the failure of the anvil.

It is realised that this postulate could be incorrect, and failure could have been caused by a flaw in the moving anvil opening under pressure, or by movement of the tungsten carbide insert, or the hemisphere, but the complete destruction of the diamond observed is unusual.

Split Anvils

These anvils, if adopted, would be restricted to lower working pressures. This would be necessary since increasing the number of surfaces to be 'mated' in the system would clearly increase the possibility of misalignment; this misalignment would become more important at higher pressures, hence the decision to restrict the pressure range of these anvils.

The anvil remaining from the previous experiment was used in opposition to each of the compound anvils. Whilst the use of this meant that the system contained unmatched pairs of stones, it was felt that the single stone would prove stronger than the split anvil for the reasons outlined above, and hence constituted a valid test of the strength of the split anvils.

Having joined the two halves of the split anvil, it was mounted and aligned as related.

The scattered light was collected at 180° to the incident radiation, this being through the stationary anvils so the same diamond fluorescence profile was observed as in Figure 3.16.

A 0.2mm thick piece of inconel was used in these experiments.

The assembly was placed in the T800 and pressure applied. As can be seen, the observed pressure increased fairly smoothly with applied pressure.

Two points of note are:-

- (i) The shape of the ruby bands were indicative of a more hydrostatic environment than was observed in the previous experiment.
- (ii) The rate of increase of pressure in the cell, with increase in oil pressure is less than in the previous experiment. This is a surprising result since in the first experiment a pair of stones were used, whereas in this experiment the split anvil was considerably smaller than the solid stone. Thus it would be expected that the pressure would increase, more rapidly in this case. The reason for this discrepancy was not understood.

Whilst the spectrum of the ruby at ca. 155 kbar was being measured, a distinct click was heard, and the intensity of scatter dropped to zero.

The split anvil was observed to have cracked, with cleavages running radially from the centre of the stone. (Figure 3.18). It was noted that the broken surface of the anvil formed a smooth hollow, and the shape of the undamaged gasket fitted this depression.

Figure 3.18

Upper face of the composite anvil having failed at
ca. 155 kbar. Note that although extensive damage has
occurred the shape of the anvil face has been retained.



Upon removal of the upper half of the anvil, the lower part could be seen to be completely undamaged. Apparently the energy stored in the system was dissipated in the fracture of the upper portion of the anvil. The WC support suffered no damage, neither did the stationary anvil.

The second split anvil ($A_2 + B_2$) was assembled and mounted in a similar manner to the first. However, during the alignment process the upper half of the anvil powdered at some pressure below 100 kbar. This was surprising as alignment checks with HgI_2 and KCl indicated that the alignment of the anvils was good.

One possibility for the cause of the failure of the anvil is that the interface between the two halves of the anvil was not perfect (although this was checked with x40 magnification prior to assembly), and yield of this under pressure gave rise to misalignment and subsequent failure of the anvil.

The lower portion of the composite anvil was again undamaged during the failure of the upper half.

The original dynocell was initially used to investigate the solid phases of benzene. Conclusions on the above sections will be given after the benzene work.

TABLE 3.2 Pressures attained in the "Super Dynocell" using one Type 1 single stone anvil, and one split anvil (parts A₁ and B₁).

Pressure between anvils/kbar	Oil pressure/psi
20.4	60
54.0	200
76.0	240
98.5	300
134.5	350
155 (Diamond failure)	410

Use of the Dynocell

Adams and Appleby (12) have performed a study of the solid phase of benzene, and gave evidence for the possible existence of a third solid phase, benzene III, formed above 34 kbar. It was decided to extend the measurements to 100 kbar to attempt to firmly establish the existence, or otherwise, of benzene III.

Experimental

Analar benzene was loaded into the Dynocell for both sets of experiments. Due to machine failure, the Raman and mid infrared spectra could not be obtained concurrently. No far infrared spectra were obtained as transmission was too low.

The sample was contained in a 0.2mm inconel gasket, with a 0.3mm gasket hole.

The cell was subjected to a pressure of 28.0 kbar, and heated overnight at 80°C. It was then allowed to cool and the spectrum shown in Figure 3.21 obtained. Thus C₆H₆ (II) had clearly been obtained. The cell was then subjected to further pressure of 45.3 kbar and again left overnight at 80°C, allowed to cool and mid infrared spectrum recorded.

The same procedure was followed with each application of pressure; this was repeated with the Raman experiments.

Results and Discussions

Raman spectra of benzene at various pressures are shown on Figure 3.19. Comparison of these spectra with those obtained by Adams and Appleby (12) show that the two higher frequency lattice modes are unresolved in the present work; the reason for this is not clear, but it was noted that considerable fluorescence of the sample was observed, presumably due to some trace impurity.

A plot of these frequencies versus pressure is given on Figure 3.20, together with those obtained by Adams and Appleby (12) and Ellenson and Nicol (13). As can be seen, the new points lie on a straight line, the gradient of which has been taken to indicate the pressure dependence of lattice modes in benzene II. No pressure dependence of the type observed by Adams and Appleby attributed to $C_6H_6(III)$ was noted.

Mid infrared spectra are given on Figure 3.21. Tables of mode frequency versus pressure are given on Table 3.6.

Assignment of the internal mode ir spectra

In both phase(I) and (II), D_{6h} molecules of benzene are on C_i sites: hence all u modes are ir active and have the same symmetry A_u . In $C_6H_6(I)$ correlation coupling leads to an ir active triplet (B_{1u}, B_{2u}, B_{3u}) from each site group mode, but in $C_6H_6(II)$ there is only a doublet ($A_u + B_u$) because the cell is halved with respect to that of phase I (see Table 3.5). For phase (I) almost all of the symmetry allowed splittings have been observed from the fundamentals, and accounted for by calculations based upon semi empirical atom-atom potential functions (14). We are not aware of any new

Figure 3.19

Raman spectra of benzene at various pressures.

Spectral slit width 3cm^{-1} . 250mw 5145\AA radiation at sample

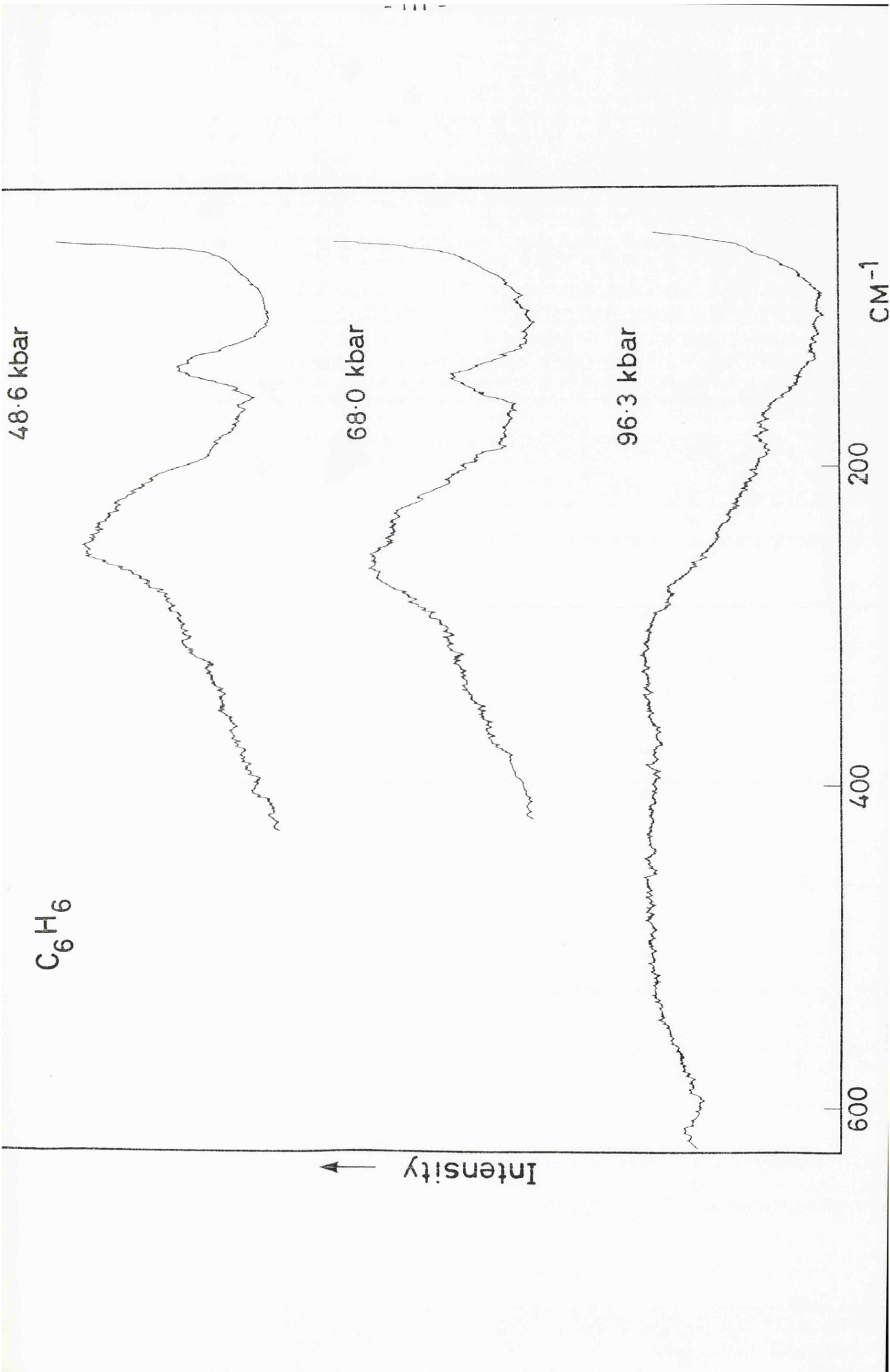


Figure 3.20

Plot of frequency shift (cm^{-1}) versus pressure (kbar) for
the benzene fundamentals

O = Ellenson and Nicol (13)

X = Adams and Appleby (12)

□ = Present work

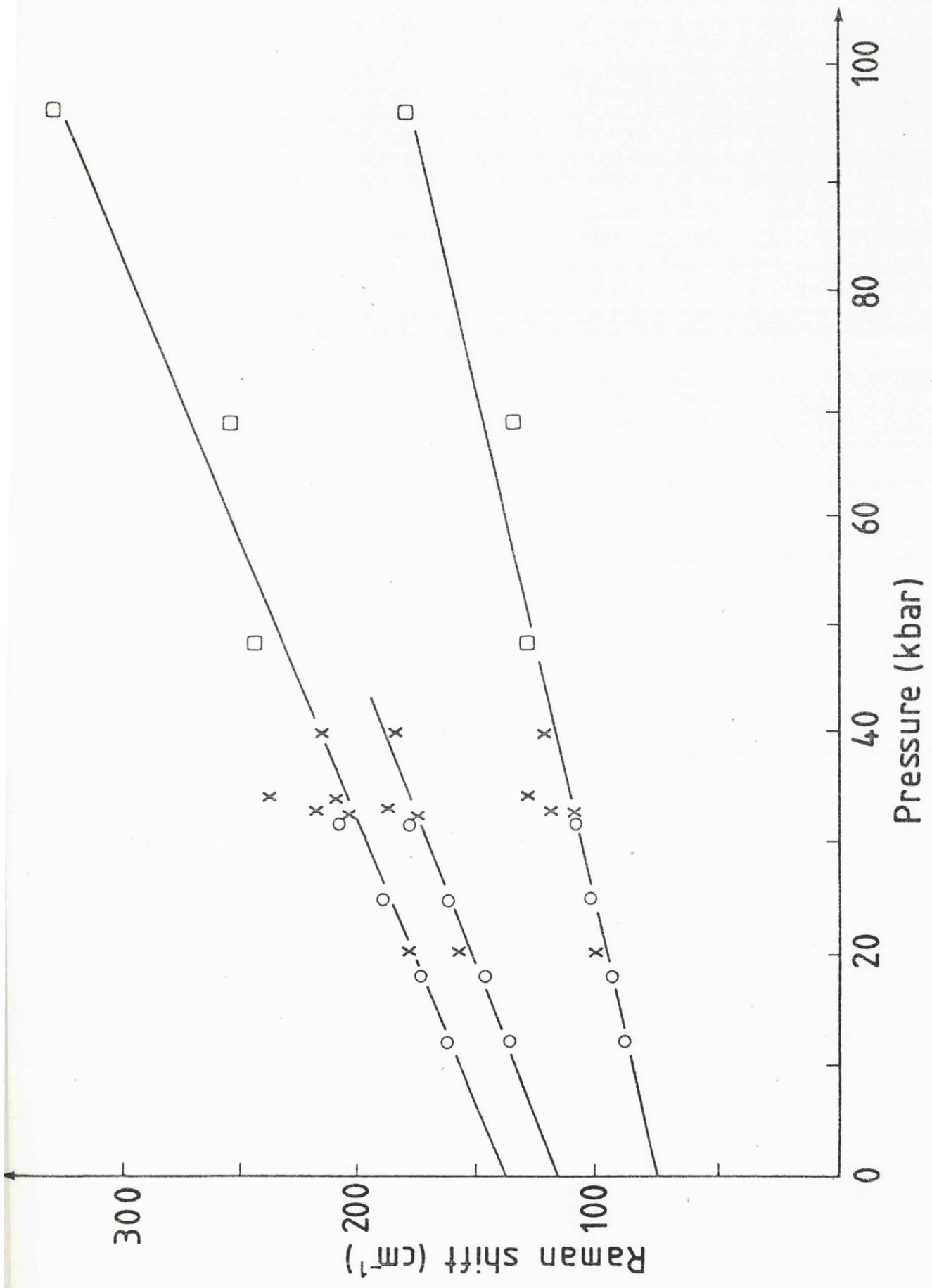


Figure 3.21

Mid infrared spectra of benzene at various pressures, recorded at 3.7 cm^{-1} resolution.

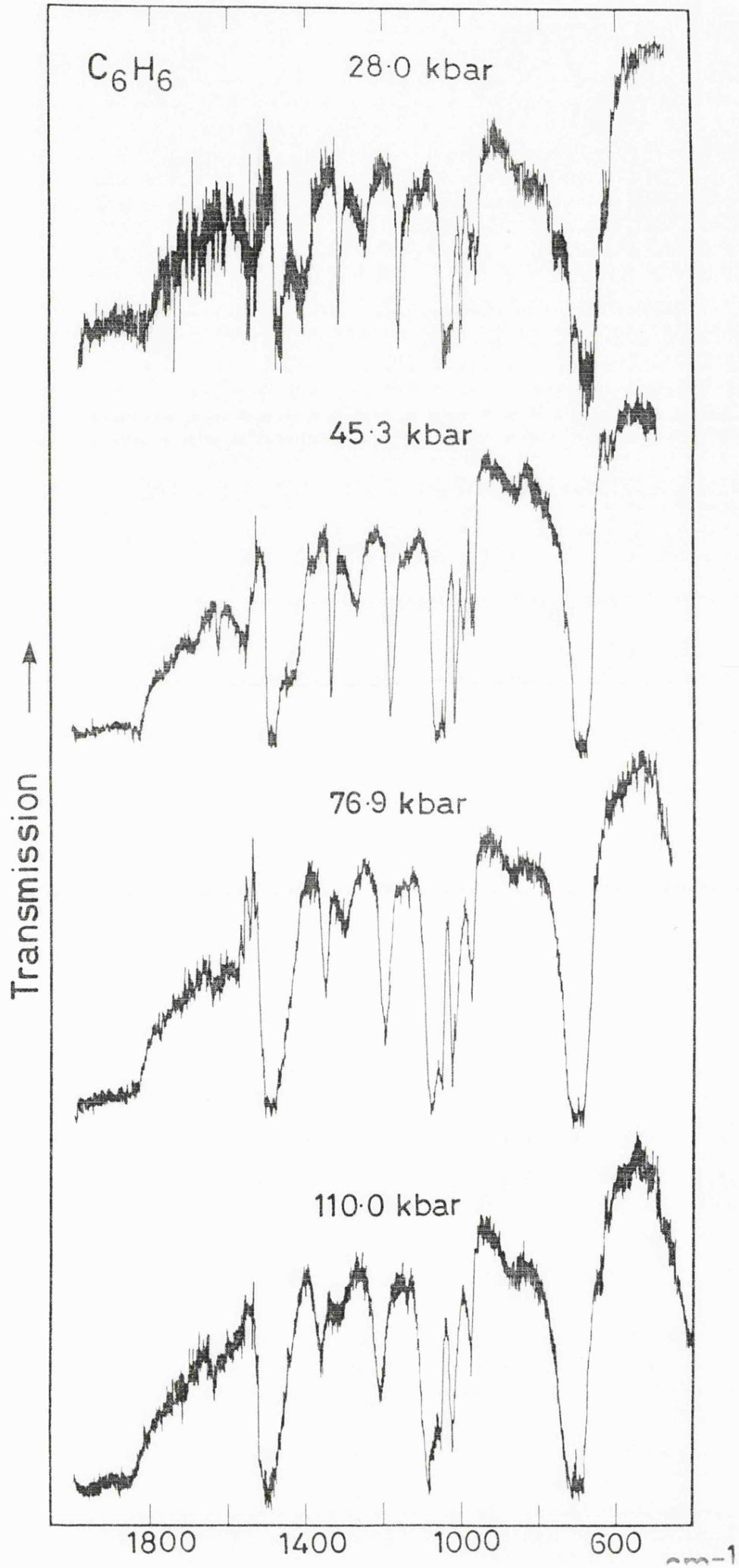


TABLE 3.3 Wavenumbers/cm⁻¹ for benzene fundamentals

	Frequency	Label
2 A _{1g}	3060, 990	ν ₂ , ν ₁
A _{2g}	1340	ν ₃
2 B _{2g}	995, 703	ν ₅ , ν ₄
4 E _{2g}	3040, 1596, 1174, 606	ν ₉ , ν ₈ , ν ₇ , ν ₆
E _{1g}	859	ν ₁₀
A _{2u}	687	ν ₁₁
2 B _{1u}	3069, 1010	ν ₁₃ , ν ₁₂
2 B _{2u}	1312, 1147	ν ₁₅ , ν ₁₄
2 E _{2u}	980, 410	ν ₁₇ , ν ₁₆
3 E _{1u}	3069, 1478, 1036	ν ₂₀ , ν ₁₉ , ν ₁₈

TABLE 3.4 Raman active lattice modes for benzene wavenumbers/cm⁻¹
at various pressures and ambient temperature

P/kbar		
48.6	127	242
68.0	132	252
96.3	175	320

TABLE 3.5 Correlation scheme for the infrared active modes of solid benzene.

<u>Phase I</u>			<u>Phase II</u>		
<u>Crystal</u>	<u>Site</u>	<u>Molecule</u>	<u>Site</u>	<u>Crystal</u>	
D_{2h}^{15}	x4 Ci	D_{6h}	Ci	x2 C_{2h}^5	
$(A_u)^a + B_{1u} + A_u$ $B_{2u} + B_{3u}$			A_u $A_u + B_u$		
			$\left. \begin{array}{l} A_{2u} \\ B_{1u} \\ B_{2u} \\ E_{1u} \\ E_{2u} \end{array} \right\}$		

^a inactive

TABLE 3.6 I.r. wavenumbers/cm⁻¹ for the solid benzene at various pressures and ambient temperature.

Assignment <u>a</u>	P/kbar	28.0	45.3	76.9	110.0
$\nu_4 + \nu_{17}, \nu_1 + \nu_{11}$			1690		
$\nu_6 + \nu_{12}$			1625		1632
$\nu_{10} + \nu_{11}$			1565		
ν_{19}		1480	1485	1488	1495
$\nu_5 + \nu_{16}$		1430	1450	<u>e</u>	
ν_{14}		1325	1335	1345	1358
$\nu_{10} + \nu_{16}$		1260	1270	1295	1318 <u>b</u>
ν_{15}		1175	1182	1195	1195
				1135	1138
ν_{18}		1050	1062	1072	1085
			1045	1050	1050
ν_{12}		1015	1020	1021	1025
		994	1000	1015	1020
ν_{17}		988	995	1005	
		978	980	<u>c</u>	
		970	970	<u>972</u>	974
$\nu_{11} + \nu_2$		<u>d</u>	865	869	870
		<u>726</u>	735		
ν_{11}		690	695	<u>700^f</u>	705

a Main & Hornig (16).

b becomes very broad at 76.9

c loses intensity, visible as a shoulder on 972 band at 76.9

d very broad

e lost under ν_{19} .

f splits into 2 components.

assignments of the infrared active combinations subsequent to the work of Main and Hornig (15). The vibrational representation of benzene with point group D_{6h} can be shown to be

$$= 2A_{1g} + A_{2g} + 2B_{2g} + 4E_{2g} + E_{1g} + A_{2u} + 2B_{1u} + 2B_{2u} + 2E_{2u} + 3E_{1u}$$

($3N - 6 = 30$)

All the fundamentals have been assigned, and are listed in table 3. Clearly in D_{6h} only ungerade, or modes are infrared active, hence any combinations which appear in the infrared spectrum must be a product of $u \times g = u$, or $g \times u = u$, and not $g \times g = g$ or $u \times u = g$. Hence first overtones are forbidden in the infrared spectrum.

Due to the very low light levels present, spectra were run with a spectral slit width of 3.7cm^{-1} . Hence most of the Davydov splittings predicted on symmetry arguments for benzene(II) were not resolved.

The very low signal/noise ratio in the region of ν_{11} , A_{2u} (ca. 680cm^{-1}) make it impossible to draw useful conclusions about the splitting of this band, but it can be seen to be split at pressures above 76 kbar. This may merely be indicative of a difference in pressure sensitivity of the Davydov components, which would manifest itself more clearly at high pressures.

Both the E_{1u} fundamentals ν_{18} and ν_{19} show pronounced broadening in phase II, i.e. at pressures shown on the figure. This could, as could the split in ν_{11}

be due to the development of shear stress in the sample, but two pieces of evidence point against this. Firstly the ruby R lines of the calibrant show no significant deviation of the kind attributable to shear stress; indeed, the R lines indicate that the ruby chip was under approximate hydrostatic conditions until very high pressures. The second indication of the absence of appreciable shear stresses are the observation of sharp bands, eg. the band at ca. 970, right up to 110.0 kbar. Thus it can reasonably be assumed that the broadening of ν_{18} and ν_{19} can be attributed to site group splittings, and in fact at pressures above 45.3 kbar, ν_{18} can be clearly seen to consist of at least two components, the asymmetry of the higher of these components suggesting perhaps further splittings, unresolved at these light levels.

The \underline{u} species inactive in D_{6h} but allowed by the virtue of the site field in the solid state are now considered. For benzene I these are;

ν_{17} , E_{2u}	975 m - s	ν_{15} B_{2u}	1144 m - s
	981 sh		1146 m - s
ν_{12} B_{1u}	1011 m	ν_{14} B_{2u}	1310 w - m

In phase II ν_{17} splits into the two doublets predicted by theory ($2A_u + 2B_u$).

As pressure is increased, it becomes clear that the higher frequency pair of the two doublets has a much higher pressure sensitivity, the more energetic of this pair shifting 26cm^{-1} as the pressure is increased from 28.0 to 110.0 kbar. Another feature of note is that there is a fairly major intensity change within these Davydov split doublets. The outer peaks of the group grow in intensity, until at 76.9 kbar, the lower frequency doublet is reduced to a band and shoulder at 972cm^{-1} . The

other three bands should each yield doublets in phase II, but none were resolved. Distinct broadening of ν_{14} and ν_{15} occurs above 75 kbar (whilst other bands remain fairly sharp). A feature of note is the drastically reduced pressure sensitivity of ν_{12} above 45.3 kbar. Below this pressure, $\frac{d\nu}{dp}$ for ν_{12} corresponds well with that found by Adams and Appleby, but above 45.3 kbar $\frac{d\nu}{dp}$ is roughly halved, the frequency increasing by only 5cm^{-1} in 54.7 kbar, of 9cm^{-1} in 45.3 kbar for the low pressure slope.

All other bands in phase II (and probably in phase III) are due to $g - u$ combinations (since first overtones are clearly forbidden in a centro symmetric group): The assignment of these bands by Main and Hornig is used in the discussion.

The two phonon diamond cut off makes the signal/noise ratio above 1600cm^{-1} very low, and little information can be obtained for this region. The most dramatic pressure dependence of a combination is that of $\nu_5 + \nu_{16}$ which occurs at 1402cm^{-1} at 1.6 kbar (Adams and Appleby), and by 76.9 kbar is hidden by ν_{19} at 1488cm^{-1} .

A weak unassigned band at 1135cm^{-1} is observed above 76 kbar, and an absorption centred around 865cm^{-1} can be seen at 45.3 kbar. The broad, asymmetric shape of this band suggests that it has several unresolved components, possibly the result of the site group splitting of the absorption.

Summary and Conclusions

Two new designs of diamond anvil cell have been tested, as have two new types of diamond anvil.

The extension of the piston and cylinder afforded greater mechanical stability, and this should be borne in mind when design of future DAC is contemplated. However, the material from which the central insert was fabricated proved far from ideal, since it was found to corrode very easily. This corrosion appeared a surface phenomenon and could be removed by polishing but the action of polishing loosened the piston in the cylinder and lost much of the advantage gained. A material with the compressive strength of tool steel but a greater corrosion resistance should be utilised.

Use of tungsten carbide anvil supports was successful. Normally even when an intact diamond was removed the anvil support was found to have been indented, but the tungsten carbide showed no indentations even though a pressure of 266 kbar was attained. (Damage did occur around the radiation port, but this was due to failure of the diamond not to the intact diamond 'sinking' into the surface.)

The cell body, presser plate and lever arms of the dynocell were all considerably more substantial than in earlier designs. This was clearly advantageous, as even at pressures in excess of 200 kbar, no deformation of any of these was observed. Twisting of the cell body subsequent misalignment of the presser plate has been observed in older cells at much lower pressures (ca. 50 kbar).

In general, damage to diamonds could be attributed to either initial misalignment of the diamond faces or movement of one or other anvil under applied pressure and subsequent misalignment. The former even under very low pressures (eg. hand pressure) could cause the loss of facets (or parts of facets) as large stress would be generated around the indenter (i.e. the misaligned diamond). The latter was believed to be the most common cause for the destruction of anvils, notable exceptions to this being the first diamond to fail in the dynocell (see section 3.5a), and a diamond in an early cell which was seen to split vertically into two halves. This was presumably due to some extensive fault in the stone.

Of the new types of stone tested, the solid anvils, being more akin to gem cut diamonds than previous designs attained a higher pressure than had been previously achieved within the group. Whether this is due to the anvil design or the improved cell design is uncertain.

The first split anvil gave reasonable results, achieved a pressure of ca. 150 kbar before yielding. The fact that only half the stone was made useless was clearly an economically attractive point. The failure of the second was believed to be due to misalignment between the two halves of the composite anvil. If these composite anvils were to be considered for general use, a more reproducible method of mounting the parts would clearly be necessary.

More stringent alignment checks would be beneficial, if time consuming. The method of Mao and Bell (12), in which the pressure contours across the face of a stone is mapped would be appropriate

Raman and mid infrared spectra of benzene have been recorded to 100 kbar. The existence of benzene (II) was not indicated by Raman spectroscopy. However the internal mode spectra show several new features.

References

1. Wier, E., Lippincott, E.R., Van Valkenberg, A., Bunting, E.N.,
J. Res. Nat. Bur. Stand. A, 63 55 (1959).
2. Piermarini, G.J., Barrett, J.D., and Block, S., Rev. Sci. Instrum.
44, 1 (1973).
3. Bassett, W.A., Merrill, L., Rev. Sci. Instrum., 45, 290 (1974).
4. Bassett, W.A., Stock, P.W., Takahashi, T., Rev. Sci. Instrum.
38, 37 (1967).
5. Adams, D.M., Payne, S.J., Martin, K., Appl. Spectroscopy 27,
277 (1973).
6. Payne, S.J., PhD Thesis (1975).
7. Appleby, R., PhD Thesis (1977).
8. Schock, R.N., Jamieson, J.C., J. Phys. Chem. Solids 30, 1527 (1969).
9. Mao, H.K., Bell, P.M., Carnegie Inst. of Washington Yearbook (1976 -
77) 646.
10. Bassett, W.A., Takahashi, T., Adv. in High Pressure Res. 4, 165 (1974).
11. Mao, H.K., Bell, P.M., Science, 200, 1145. (1978)

12. Adams, D.M., Appleby, R., JCS (Faraday II) 1896 (1977).
13. Ellenson, W.D., Nicol, M., J. Chem. Phys. 61, 1380 (1974).
14. Taddei, G., Bonadeo, M., Marzocchi, M.P., Califano, S.,
J. Chem. Phys., 58, 966 (1971).
15. Main, R.D., Hornig, D.F., J. Chem. Phys., 17 1236 (1949).

CHAPTER 4

AN INFRARED STUDY OF FERROCENE AT HIGH PRESSURES

AND LOW TEMPERATURES

CHAPTER 4

AN INFRARED STUDY OF FERROCENE AT HIGH PRESSURES AND LOW TEMPERATURE

4.1 Introduction

Since its discovery in 1951 (1,2), ferrocene (bis cyclopentadienyl iron II) has been a compound of considerable interest to both chemists and physicists.

At ambient conditions the crystal structure of ferrocene (I) is $P 2_1/a = C_{2h}^5$, with $z = 2$ (3). The heat capacity shows a double lambda transition with maxima at 163.9 and 169K (4). Neutron diffraction measurements at ambient temperature have indicated a high degree of disorder, for which two possible interpretations have been advanced (5). However two recent investigations of ferrocene I by X ray (6) and neutron diffraction (7) have shown definitely that "the disorder of the cyclopentadienyl rings results from the presence of molecules in different orientations distributed randomly throughout the crystal". Further, there is no longer reason to believe that a major fraction of molecules in crystalline room temperature ferrocene have the "centrosymmetric staggered structure". The molecular centre of symmetry implied by the monoclinic space group is thus only statistical in nature.

At 169K there is an order-disorder phase transition followed at 163.9K by a first order structural phase change to ferrocene II which has a triclinic cell (8, 9), the structure of which is not yet completely determined (6), although recent

low temperature Raman results (10) suggest that $z \geq 8$.

The electrical conductivity of ferrocene changes with pressure, first passing through a minimum at ca. 5 kbar, then increasing at pressures above this. It was concluded, nevertheless, that no phase change occurred below 20 kbar (11). However Duecker and Lippincott (12), using an ungasketed diamond anvil cell (DAC) reported visual and infrared spectroscopic observations which they interpreted in terms of a transition to a new high pressure phase, which they labelled ferrocene III. They estimated the transformation pressure to be 11.5 ± 0.5 kbar.

Ferrocene crystals, in the absence of an applied pressure disintegrate explosively near 110K, this phenomenon being apparently unrelated to the lambda point changes (13).

It can be seen that the solid state information in the literature which pertains to ferrocene is somewhat confused. It was decided therefore to examine its response to pressure using infrared spectroscopy. Apart from Duecker and Lippincott's brief comment, there is only one other report of the infrared spectrum of ferrocene under pressure (14) in which an ungasketed DAC was used to study the ν (M-ring) and ring tilt skeletal modes. There was however no discussion of phase behaviour.

4.2 Experimental

Recrystallised commercial ferrocene was used.

Infrared spectra in the $400 - 1800\text{cm}^{-1}$ were obtained using a diamond anvil cell and simple KBr beam condenser (15) in a Perkin-Elmer 580 Infrared

spectrometer. The sample, immersed in Nujol was contained within a 0.5mm hole in a 0.05mm inconel gasket. Thus, an approximately hydrostatic pressure was exerted on the sample by the Nujol. This is in contrast to the severe shear stresses which develop when a gasket is not employed (as was the case in the work of Duecker and Lippincott (12)). Pressures were measured by the ruby R line method (16, 17). Vibrations above 1800cm^{-1} could not be observed due to the two phonon absorption of diamond. For ferrocene this only results in the loss of information for the ν (C-H) modes, and the skeletal bend ν_{22} . Far Infrared spectra were obtained using an extensively modified Beckman RIIC FS620 interferometer.

Low temperature spectra were obtained using a KBr disc. The disc was mounted in a Specac variable temperature cell, and spectra were recorded on a Perkin-Elmer 580B spectrometer.

4.3 Results and Discussion

Mid infrared spectra of ferrocene under approximately hydrostatic pressures are given in Figure 4.1. Figure 4.2 shows far infrared spectra at various pressures. These results are summarised on Table 4.1. Low temperature spectra of ferrocene are shown in Figure 4.3.

The assignment of Winter, Curnette and Whitcomb (18) is the foundation upon which these discussions are based. They studied oriented crystals of ferrocene in polarised radiation and offered a very full assignment.

Figure 4.1

I.r. transmission spectra at ambient temperature of ferrocene at various pressures (kbar). A single scan ($35 \text{ cm}^{-1} \text{ min}^{-1}$) was used for each spectrum at 3.7 cm^{-1} spectral slit width. The cut-offs are determined by absorption in diamond and KBr respectively.

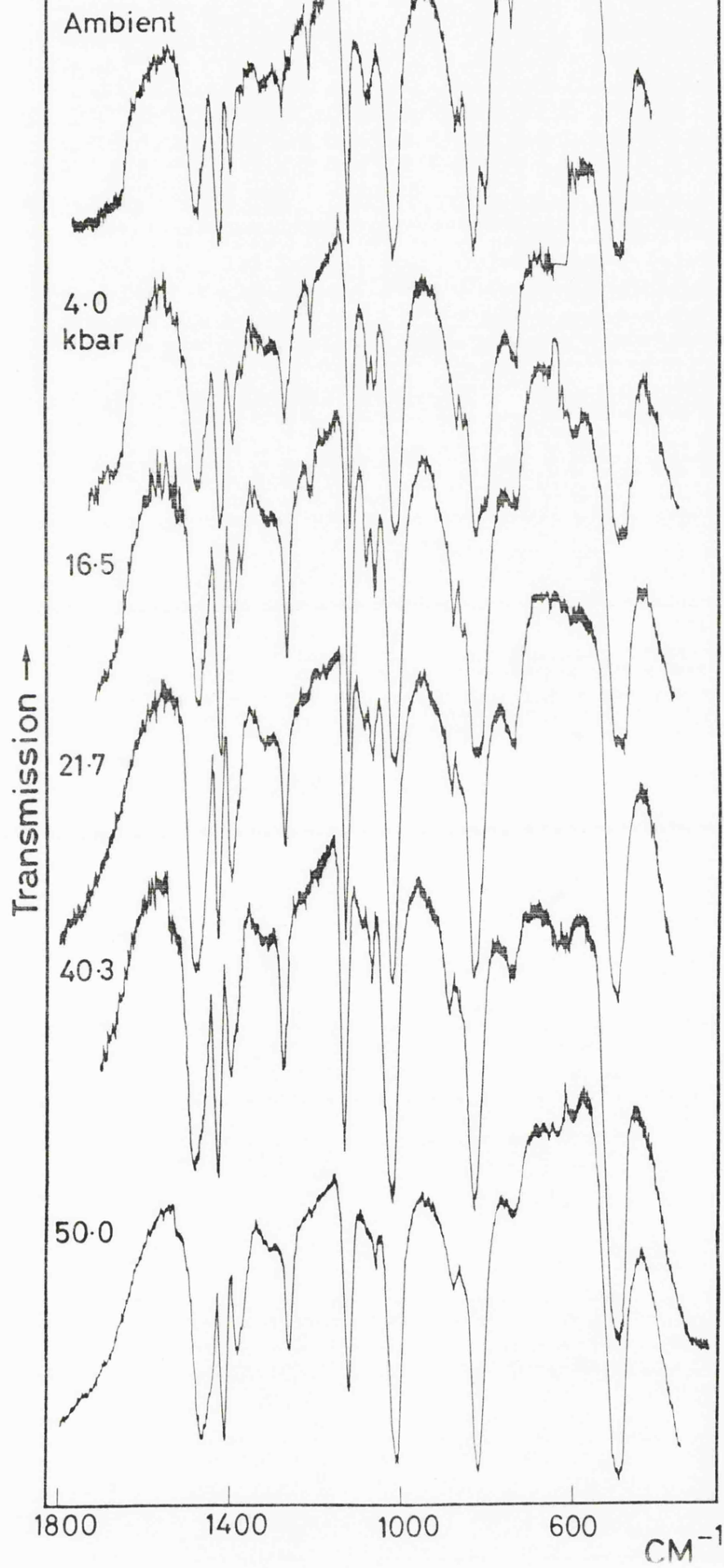
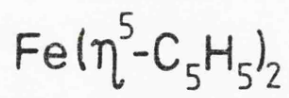
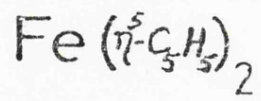


Figure 4.2

Far i.r. transmission spectra of ferrocene in the region of ν_{22} , \underline{E}_{1u} at ambient temperature and various pressures.



Transmission ↑

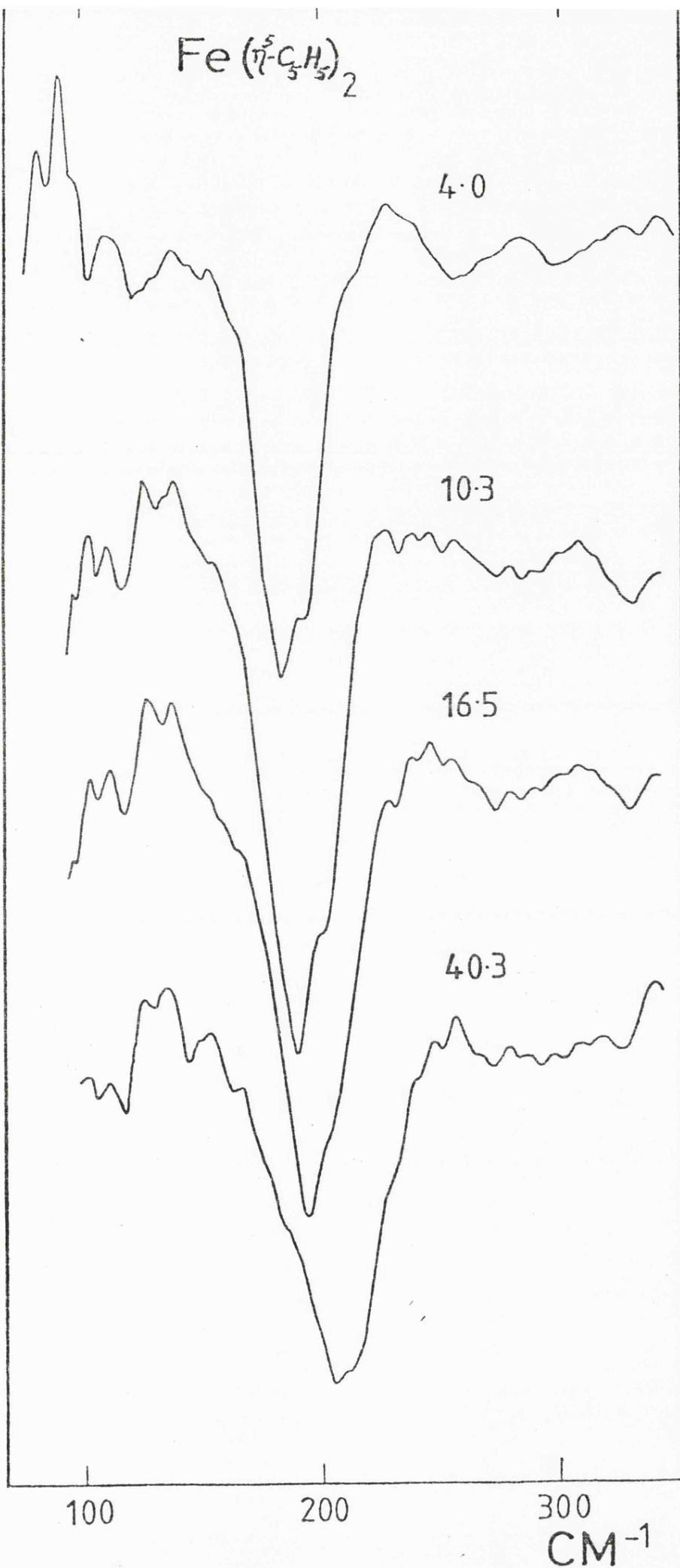


Figure 4.3

I.r. transmission spectra of ferrocene at various temperatures at ambient pressure. Note the effect of the phase transitions at 169 and 163.9 K.

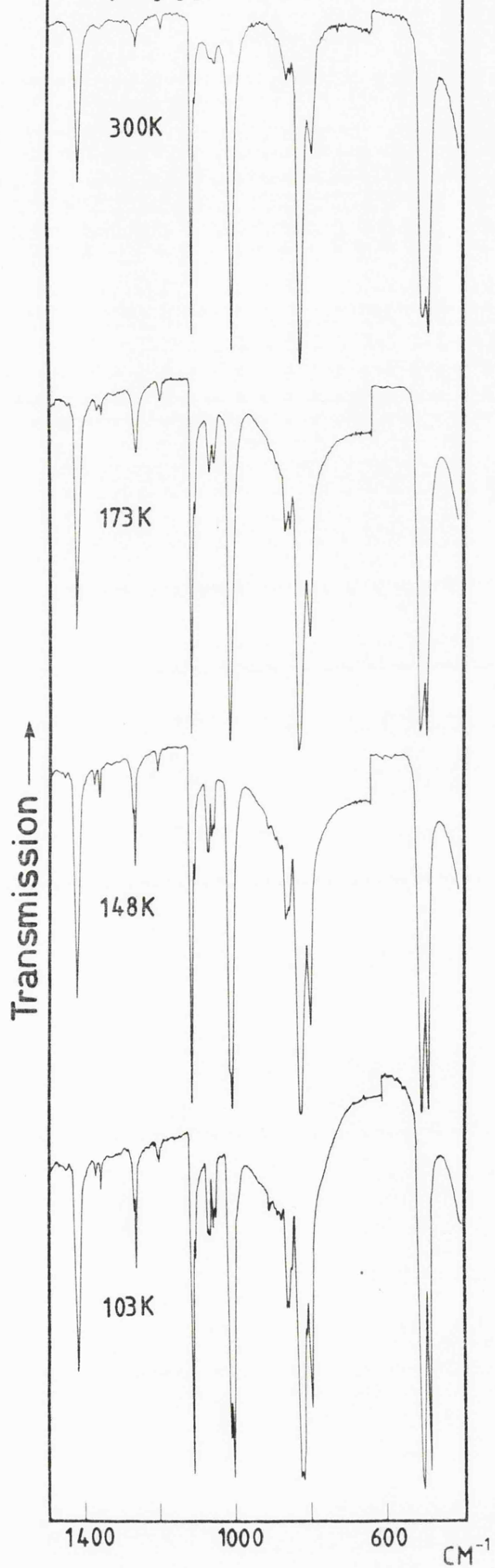
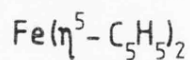


Table 4.1 I. r. band positions (cm⁻¹) and their Gruneisen constants (γ_i) for ferrocene at various pressures.

Pressure/kbar	0.001	4.0	10.3	16.5	21.7	40.3	50.0	γ_i
ν_{20} E_{1u}	1409vs	1409vs	1410vs	1410vs	1410.5vs	1411vs	1411vs	0.005
$\nu_{30} + \nu_{22}$	1350w	1354w	1357w	1360w	<u>a</u>	<u>a</u>	<u>a</u>	0.045
ν_5 A_{1u}	1255w	1255wm	1255m	1255ms	1257ms	1259ms	1260ms	0.007
ν_{30} E_{2u}	1189wm	1194wm	1198wm	1200w	1200vw			0.043
ν_{10} A_{2u}	1106vs	1109vs	1111vs	1114vs	1117vs	1119vs	1120s	0.043
ν_{31} E_{2u}	1057wm	1064m	1069m	1070m	1074w	1075vw	vw	0.074
	1048wm	1048m	1050m	1050wm	1054wm	1055wm	1057wm	0.026
ν_{18} E_{1u}	1000vs	1001vs	1003vs	1005vs	1008vs	1009vs	1010vs	0.037
ν_{19} E_{1u}	855wm	860wm	866wm	869wm	875wm	875wm	875wm	0.108
	845wm	845sh	846sh	849sh	850sh			0.027
ν_9 A_{2u}	817vs	819vs	820vs	818vs ^b	818vs	818vs	820vs	0.036
$\nu_4 + \nu_{11}$	790m	800sh	805sh					
$\nu_{21} + E_{1u}$	483vs	484vs	486vs	490vs	490vs	492vs	494vs	0.067
ν_{11} A_{2u}	180vs	185vs	192vs	195vs	185sh	185sh		
ν_{22} E_{1u}	194sh	194sh	202sh	204sh	207vs	210vs		0.366

a Shifts under Nujol band

b Represents average of the two merged bands

Table 4.2

I.r. band positions (cm^{-1}) for ferrocene at various temperatures.

	Ferrocene I		Ferrocene II		
	300 K	173 K	148 K	123 K	103 K
ν_{20}	1413	1414	1414	1415	1415
$\nu_{30} + \nu_{22}$	1360 1353	1362 1351	1363 1350	1364 1350	1365 1350
ν_5	1270 sh 1260	1260	1261 1256	1261 1256	1261 1256
ν_{30}	1193	1195	1196	1196	1196
ν_{10}	1109 1100 sh	1109 1100	1109 1100	1109 1100	1109 1100
ν_{31}	1061 sh 1051	1061 1051	1062 1053 1046	1062 1053 1046	1067 1064 1053 1045
ν_{18}	1003.5	1004	1008 1002	1009 1002	1009 1002
ν_{33}			903 883 873	904 884 872	904 885 872
ν_{19}	855.5 846	860 847	859 855 849	859 855 845 825	859 855 845 825
ν_9	818	819	819.5	819 806	819 806
$\nu_4 + \nu_{11}$	789	792.5	793	794	794
ν_{21}	493	499	500	501	502
ν_{11}	479	481	482	483	483

Phase Behaviour

The ν (C-H) modes and the skeletal bend ν_{22} occur above 1500cm^{-1} . All the other Infrared active fundamentals of ferrocene ($3A_{2u} + 4E_{1u}$) fall in the region $400 - 1500\text{cm}^{-1}$ and were observed at high pressure. All frequencies showed small increases in frequency as the pressure was increased, corresponding to relative shifts

$$\frac{1}{\nu_i} \frac{d\nu_i}{dP},$$

which trend slowly downward with increase in frequency

(see Figure 4.5). Division of the relative shifts by the isothermal compressibility, χ_T , yields values of the Gruneisen constants, γ_i , which relates the fractional increase of frequency of the i^{th} mode to the fractional decrease in volume. Thus;

$$\frac{\Delta \nu_i}{\nu_i} = \gamma_i \left(\frac{\Delta V}{V} \right) \quad \text{and} \quad \gamma_i = \frac{1}{\chi_T \nu_i} \left(\frac{d\nu_i}{dP} \right)_T$$

No value of χ_T is available for ferrocene, but organic materials usually have compressibilities close to $1 \times 10^{-2} \text{ kbar}^{-1}$. A value of $\chi_T = 1.13 \times 10^{-2} \text{ kbar}^{-1}$ was assumed (see below). On this basis the γ_i 's shown in Table I were obtained. They range from 0.08 to 0.108, and are comparable with values reported for internal modes of other molecular crystals such as S_8 (19) S_4N_4 (20) as reported by Zallen, and $C_{10}F_8$ (21) studied by Adams and Shaw.

Duecker and Lippincott (11) claimed that ν_{10} was raised to 1135cm^{-1} on entering their Phase III above 11.5 kbar, provided that a single crystal was used. They noted that with polycrystalline material the transition was not easily induced, but with several pressure cycles a band was obtained at 1135cm^{-1} . In the present work, in which the sample experienced more nearly hydrostatic conditions, there is no sign of a new band at 1135cm^{-1} and that ν_{10} was shifted to only 1120cm^{-1} by 50 kbar. However, when a sample was examined in an ungasketed DAC Lippincott's result was reproduced (Figure 4.4). To further the impression of a new phase, ν_5 becomes very prominent at 1265cm^{-1} , and ν_{30} (1200cm^{-1}) is barely detectable.

In addition to the Infrared active A_{2u} and E_{1u} fundamentals discussed above, the spectra show two combinations (790 and 1350cm^{-1}) which also increase in frequency with increase in pressure. The 790cm^{-1} band has been assigned to the combination of $\nu_4 + \nu_{11}$. The 1390cm^{-1} band, which has been assigned to ν_{30} (inactive) and ν_{22} (E_{1u}), shifts + 10cm^{-1} in 16.5 kbar. ν_{22} , however, shifts by + 24cm^{-1} in this interval. This assignment must therefore be open to question.

The most notable changes with pressure are exhibited by three modes, ν_5 (A_{1u}), ν_{30} and ν_{31} (E_{1u}), which are inactive under strict D_{5h} symmetry but which are permitted in the solid state by the low site symmetry. ν_5 (1255cm^{-1}) shows a small positive shift and steadily increases in intensity with increase in pressure. This is not unexpected; the site field exerted by neighbouring molecules will become stronger as the unit cell size is reduced. The lower component of ν_{31} (at 1048cm^{-1})

Figure 4.4

Effect of a shear stress upon the i.r. spectrum
of ferrocene.

$\text{Fe}(\eta^5\text{-C}_5\text{H}_5)_2$

Transmission \uparrow

1800

1400

1000

600

cm^{-1}

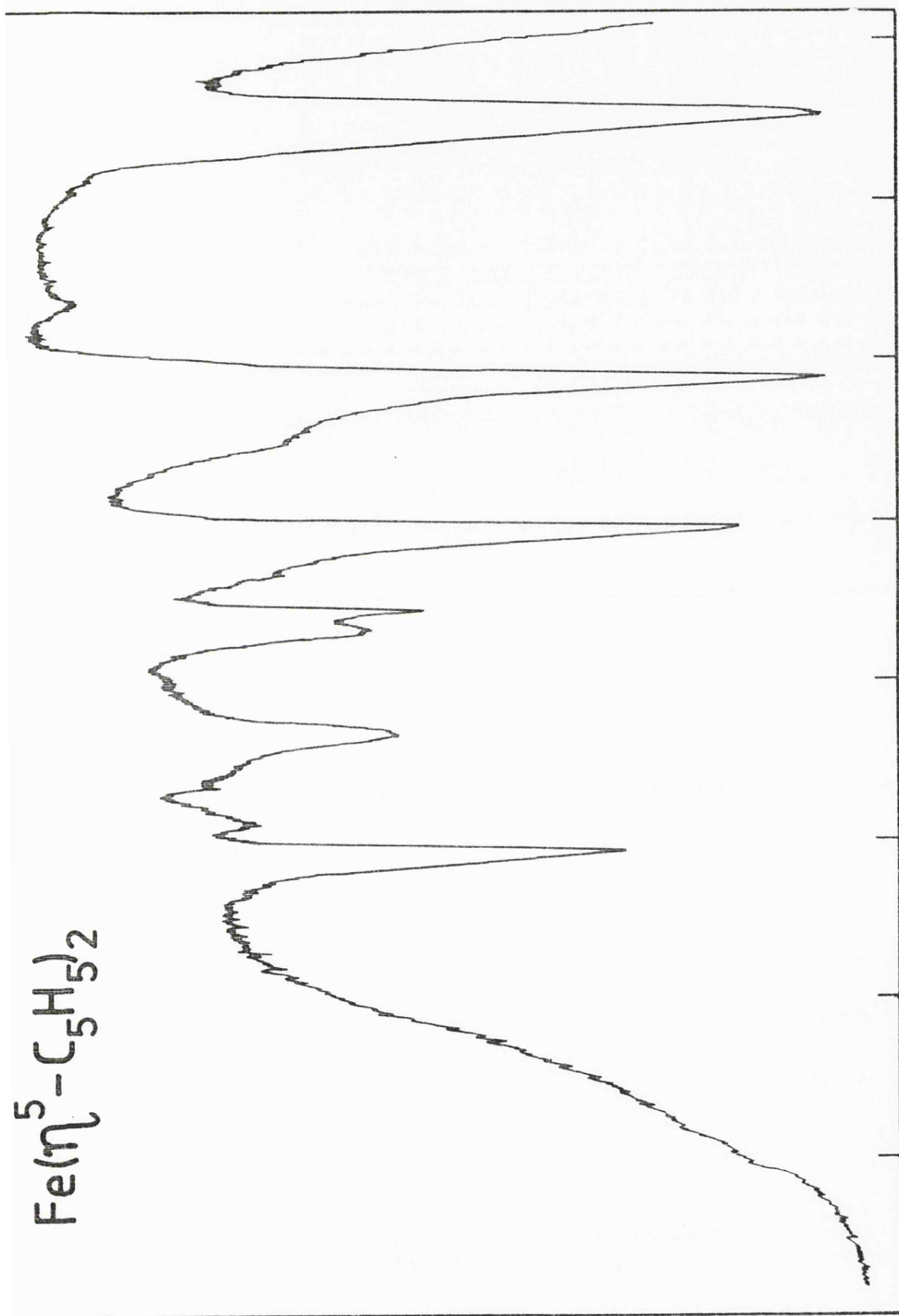
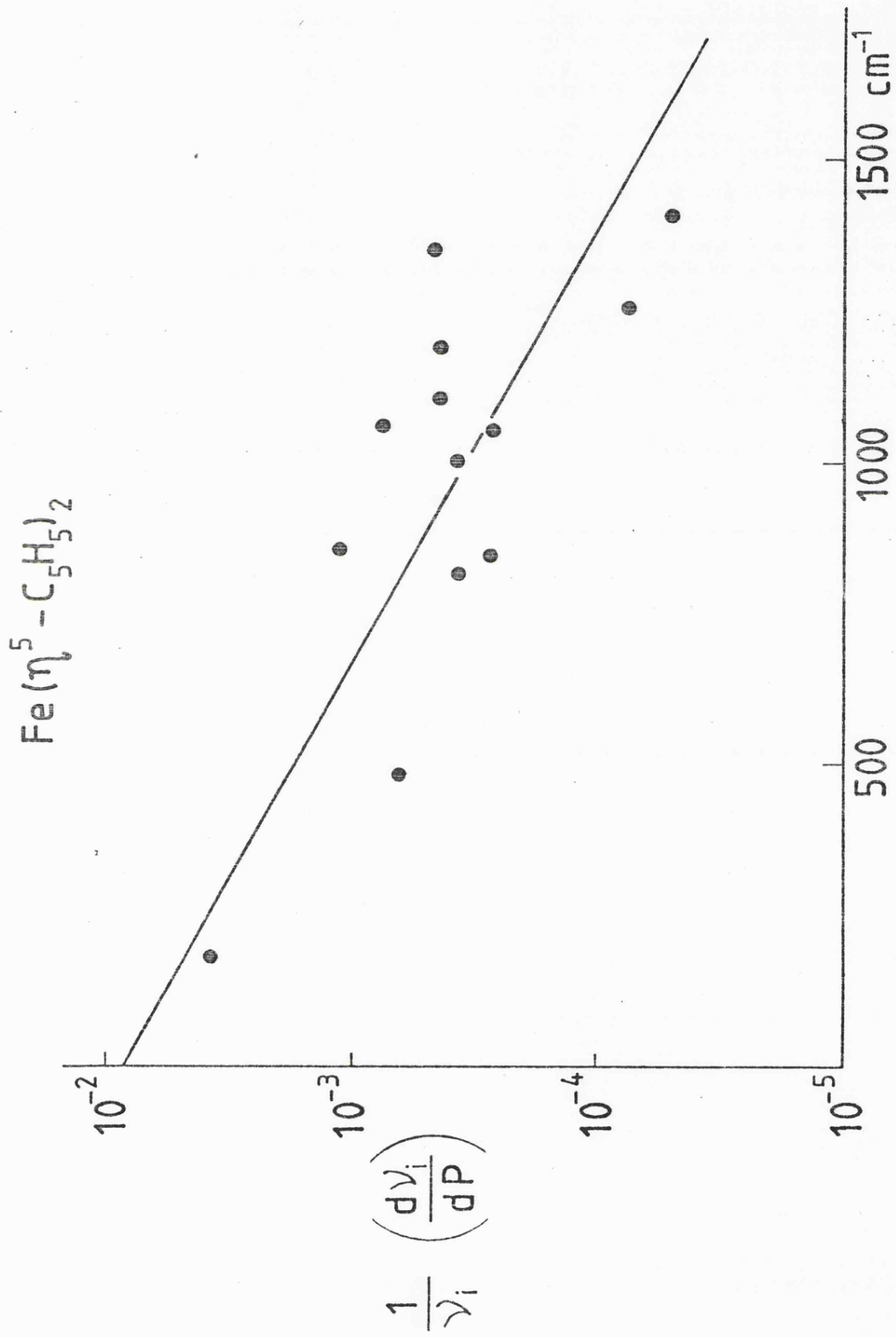


Figure 4.5

The variation with frequency of the relative shifts for the mid-i.r. bands of ferrocene.



behaves similarly. In contrast, its accompanying component (1057cm^{-1}) steadily decreases, as does ν_{30} , which is barely visible at 21.7 kbar. It is the removal of these two bands on raising the pressure that constitutes evidence in favour of a high pressure phase transition, although the intensity attained by ν_5 might also be regarded as indicative of a change of structure. The major changes in ν_5 , ν_{30} and ν_{31} takes place between 10.3 and 16.5 kbar are therefore consistent with Duecker and Lippincott's claim of a phase transition at 11.5 ± 5 kbar although, as noted above, their observation of the reaction of ν_{10} to pressure could only be reproduced under shear stress.

The spectral changes noted above under both hydrostatic and shear stress conditions, support the existence of a phase change. A plausible suggestion is that it involves a re-orientation of the molecules to accommodate more efficient packing.

Phonon Shifts

Shifts of phonon frequencies with temperature may be considered as arising from two distinct contributions, related by the equation:-

$$\left(\frac{d\nu}{dT} \right)_P = \left(\frac{d\nu}{dT} \right)_V - \frac{\alpha}{\chi_T} \left(\frac{d\nu}{dP} \right)_T$$

The first term on the right hand side of the equation is the volume independent self energy shift representing the change in anharmonic phonon-phonon interactions with temperature at constant volume. The second term is the thermal strain shift, resulting from the volume dilation on raising the temperature. (This will be discussed more fully in Chapter 5.)

From the unit cell constants of ferrocene at 298 and 173 K (7) a value of the average volume thermal expansion coefficient, α , may be deduced; $\alpha = 2.27 \times 10^{-4} \text{ K}^{-1}$. No value for the isothermal compressibility χ_T has been reported in the literature. However, organic materials commonly have $\chi_T \approx 10^{-2} \text{ kbar}^{-1}$. Since ferrocene is largely organic material, modified by inclusion of rather more compressible Fe - ring bonds it is unlikely that χ_T will be below this value and is possibly a little larger. α / χ_T is thus taken as $2 \times 10^{-2} \text{ K}^{-1} \text{ kbar}$ and used to compute the values shown in Table 3 for the thermal strain term.

The results show a considerable spread of behaviour, so much so that no general conclusions can yet be drawn, although the eventual accumulation of many such data for molecular crystals may reveal general patterns of behaviour.

Table 4.3 Anharmonic shift terms for ferrocene (all terms $10^{-2} \text{ cm}^{-1} \text{ K}^{-1}$).

ν/cm^{-1}	Total shift ^a	Self-energy ^b	Thermal strain ^c
1409	-0.79	-0.64	0.15
1350	0	1.33	1.33
1255	0	0.20	0.20
1189	-1.58	-0.46	1.12
1106	0	1.12	1.12
1057	0	1.72	1.72
1048	0	0.61	0.61
1000	-0.39	0.42	0.81
855	-3.54	-1.51	2.03
845	-0.79	-0.28	0.51
817	-0.79	-0.15	0.64
493	-4.73	-4.02	0.71 ^d
479	-1.58	-0.87	0.71 ^d

$$\underline{a} \quad \left(\frac{d\nu}{dT} \right)_P$$

$$\underline{b} \quad \left(\frac{d\nu}{dT} \right)_V$$

$$\underline{c} \quad \frac{\alpha}{\chi_T} \left(\frac{d\nu}{dP} \right)_T$$

d Same pressure shift used for both bands as they are not clearly resolved in the d.a.c. spectra.

4.4 Conclusions

Far and mid Infrared spectra of ferrocene have been examined up to 50 kbar under approximately hydrostatic conditions in a gasketed diamond anvil cell, and under shear stress without gaskets. The results provide evidence in support of Duecker and Lippincott's claim of a phase transition at about 11.5 ± 0.5 kbar, which is sluggish under shear stress.

Ambient pressure low temperature spectra have been obtained to 103K, and the temperature induced frequency shifts have been analysed in terms of thermal strain and phonon self energy contributions, although no general pattern emerged.

Further systematic study of ferrocene type compounds is desirable, with particular attention to the lattice mode region. Infrared data at pressures substantially in excess of 50 kbar are necessary ^{t_0} to establish whether stress induced changes are associated with those which appear below 50 kbar under hydrostatic conditions, although the DAC in which this work was performed were not thought sufficiently stable to be taken above 50 kbar.

References

1. Kealy, T.J., Pauson, P.L., Nature 168 1039 (1951)
2. Miller, S.A., Tebboth, J.A., Tremaire, J.F., J. Chem. Soc. 632 (1952).
3. Dunitz, J.D., Orgel, L.E., Rich, A., Acta. Cryst 9 373 (1956).
4. Edwards, J.W., Kingston, G.L., Mason, R., Trans Faraday Soc. 56 660 (1960).
5. Willis, B.T.M., AERE Report (Harwell) R3708 (1961).
6. Seiler, P., Dunitz, J.D., Act. Cryst. B35 1068 (1979).
7. Takuagawa, F., Koetzle, T.F., Act. Cryst. B35 1074 (1979).
8. Hyams, I.J., Ron, A., J. Chem. Phys. 59 3027 (1973).
9. Hyams, I.J., Chem. Phys. Lett. 18 399 (1973).
10. Char, K., Sourisseau, C., Lucazeau, G., Proc. 6th Internat. Conf. Raman Spect., Schmid, E.D., et al (Eds) Heyden, London P. 432 (1979).
11. Okamoto, Y., Chang, T.Y., Kantor, M.A., J. Chem. Phys. 41 4010 (1964).

12. Duecker, H.C., Lippincott, E.R., J. Chem. Phys. 46 3691 (1967).
13. Bodenheimer, J.S., Low, W., Phys. Lett., 36A 253 (1971).
14. Nakamoto, K., Udovitch, C., Ferraro, J.R., Quattrochi, A., Appl. Spectroscopy 24 606 (1970).
15. Adams, D.M., Sharma, S.K., J. Phys. E. 10 838 (1977).
16. Piermarini, G.J., Block, S., Barnett, J.D., J. Appl. Phys. 44 5377 (1973).
17. Adams, D.M., Appleby, R., Sharma, S.K., J. Phys. E. 9 1140 (1976).
18. Winter, W.K., Cumutte, B., Whitcomb, S.E., Spectrochimica Acta. 12 1085 (1959).
19. Zallen, R., Phys. Rev. B 9 4485 (1974).
20. Zallen, R., Slade, M.L., Phys. Rev. B 18 5775 (1978).
21. Adams, D.M., Shaw, A.C., Mackenzie, G.A., Pawley, G.S., J. Phys. Chem. Solids (1979) in the press. ~~41~~, 149 (1980)

CHAPTER 5

A STUDY OF THE INFRARED, RAMAN AND X RAY DIFFRACTION SPECTRA
OF K_2PtCl_6 AND K_2ReCl_6 AT HIGH PRESSURES AND LOW TEMPERATURES

CHAPTER 5

A STUDY OF THE INFRARED, RAMAN AND X RAY DIFFRACTION SPECTRA OF

K_2PtCl_6 AND K_2ReCl_6 AT HIGH PRESSURES AND LOW TEMPERATURES

5.1 Introduction

A major aim of this research was to elucidate some of the underlying causes of the pressure dependence of vibrational modes of solids. This involves a detailed study of various anharmonic parameters which are, in turn, related to observables. It is necessary to set this theory within the context of our whole understanding of theories of the energy, and energy distribution in solids. An outline is therefore given of the major features of this aspect of solid state physics.

The total internal energy of a crystal is simply the sum of the individual vibrations. The first realistic attempts to calculate the total internal energy U , was that of A.Einstein, who, in a paper entitled "Planck's Theory of Radiation and the Theory of Specific Heat" took the following approach.

Consider a crystal as an assembly of independent oscillators, each having the same circular frequency ω_E . The energy of each oscillator is quantized in units of $\hbar\omega_E$. Einstein showed that the average energy, \bar{U} of the system of N atoms at temperature T was

$$\bar{U} = \frac{3N \hbar \omega_E}{\exp \frac{\hbar \omega_E}{k_B T} - 1} \dots 1$$

where k_B is Boltzmann's constant. The specific heat is then given by;

$$C_v = \frac{d\bar{U}}{dT} \quad \dots 2$$

Einstein's theory does not, however, give quantitatively correct results for any material over a wide range of temperature. This is inevitable, since the model upon which it is based is much too simple.

The next stage in the refinement of this model is to consider the crystal to be periodic; that is, to consider the system as a repeating three dimensional array. In such an array U depends, not on the displacements of the atoms from their equilibrium positions but on its relative displacement to its neighbours. The motion of such a system is now most readily described in terms of travelling waves, propagating through the lattice. Each of these waves, termed lattice vibrations by Born, is characterised by a wave vector, a frequency and certain polarisation properties. These waves are the normal modes of the crystal and are quantized as for a simple harmonic oscillator of the same frequency.

Instead of one frequency associated with the crystal there is now a range of frequencies, which depend in a complicated way on the interatomic forces. Born and Von Karman took this into account in their paper "On the Theory of Specific Heat" published in 1913. A paper in 1912 by Debye with the same title set out a theory, which was less accurate in principle than that of Born and von Karman. It was, however, more successful in practice because of its simplicity.

In his theory he treated the normal modes of vibration as if they were waves in a continuous isotropic medium, instead of a system where the mass is concentrated at discrete points. Debye's "T³ law for the specific heat of a solid at low temperatures" can be formulated (1).

$$C_v = \frac{12}{5} \pi^4 N k_B \frac{T}{\Theta_D}^3 \quad \dots 3$$

This greatly simplifies the frequency distribution, compared to Born and von Karman's system, and like Einstein's theory makes C_v the same function of $\frac{T}{\Theta_D}$ for all crystals, where Θ_D is the Debye characteristic temperature of a crystal.

Since the frequency distribution introduced by Debye has some of the features of the actual frequency distribution of a crystal, the theory fits adequately all but the most accurate measurements of the specific heat of simple crystals. It was not until the 1930's that the deficiencies of Debye's theory began to be noticed in comparisons of theory and experimental results.

The sophistication which Debye's theory lacked was provided by Laval, who returned to Born and von Karman's theory. An explanation of the system proposed by Laval is given below.

If the force of an atom is precisely proportional to its displacement to neighbouring atoms, then each normal mode will propagate independently, and the principle of superposition will apply. This system will now constitute a harmonic crystal, and so the harmonic approximation can be formally stated; that when an atom is displaced, the forces acting on that atom are proportional to the first power

of displacement. Thus, for a crystal with one atom per unit cell, the force on the atom in cell 1, in the x direction, due to the atom in cell 1' is

$$F_{1x} = \left(\frac{\partial \phi(r)}{\partial x} \right)_{r=r_1'-r_1} \quad \dots 4$$

where $\phi(r)$ is the potential energy of two atoms separated by r . Now displace the atom at r_1' by u_{1y} in the y direction. The change in the x component of the resultant force on the atom at r_1 is

$$\Delta F_{1x} = u_{1y} \left(\frac{\partial^2 \phi(r)}{\partial x \partial y} \right)_{r=r_1'-r_1} \quad \dots 5$$

Such a crystal will have no coefficient of expansion. Also its elastic properties will be independent of temperature, unlike a real crystal in which the forces are only approximately linear.

The harmonic approximation can be seen to work best at low temperatures, where the displacements of atoms are very small compared to interatomic distances. Hence it serves usually as a first approximation with non linear (anharmonic) terms treated as a perturbation over the whole temperature range. In fact anharmonic elastic constants are not independent of temperature, and an increase of 10% or more in going from ambient temperature to O/K is fairly typical.

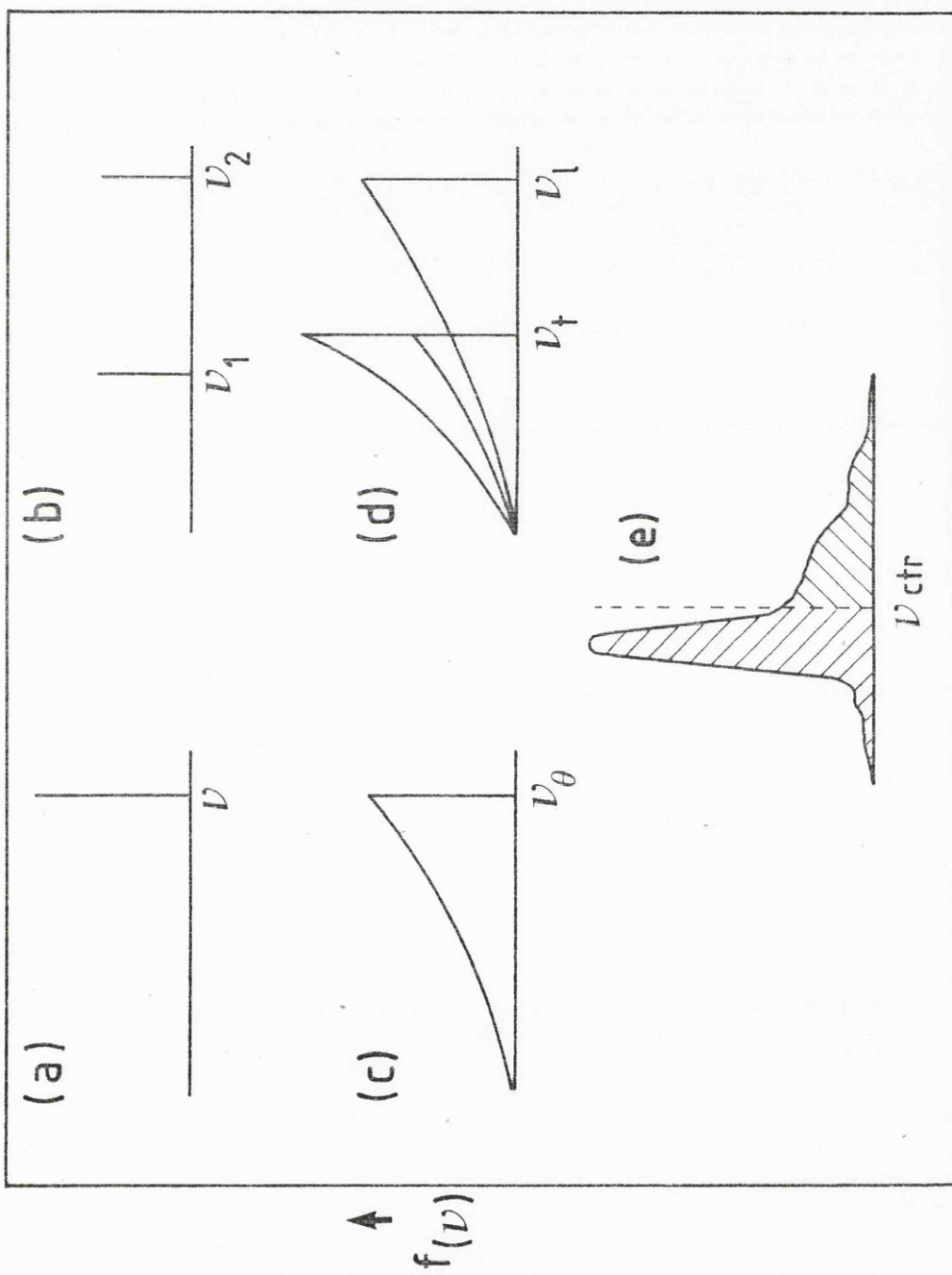
The anharmonicity involved is a consequence of the contribution of the conduction electrons to the specific heat of the solid (unless, of course, the material is an insulator). A very general result for the contribution of conduction electrons is (2);

$$C_e = \frac{2}{3} \pi^2 k_B^2 n(E)_F T \quad \dots 6$$

Figure 5.1

Graphical representation of the various
characteristic frequencies as proposed by

- (a) Einstein in 1907
- (b) Nernst and Lindemann in 1911
- (c) Debye in 1912
- (d) Born and von Karman in 1931 and 1923
- (e) Plendl (5) in 1960



where $n(E)_F$ is the density of electron states at the Fermi energy. Since the lattice contribution (see equation 3) varies approximately as T^3 , the electronic contribution becomes larger at low temperatures. This inclusion of the thermal electron contribution to the specific heat is known as the 'Exact' theory of specific heat.

However, it must be noted that the 'Exact' theory still involves the harmonic approximation. The specific heat considered this far has been written as C_V , that is at constant volume. It may equally be written as C_p , because a crystal in which the interatomic forces depend linearly on relative displacements would have no coefficient of expansion. A derivation based on standard results of thermodynamics leads to (3)

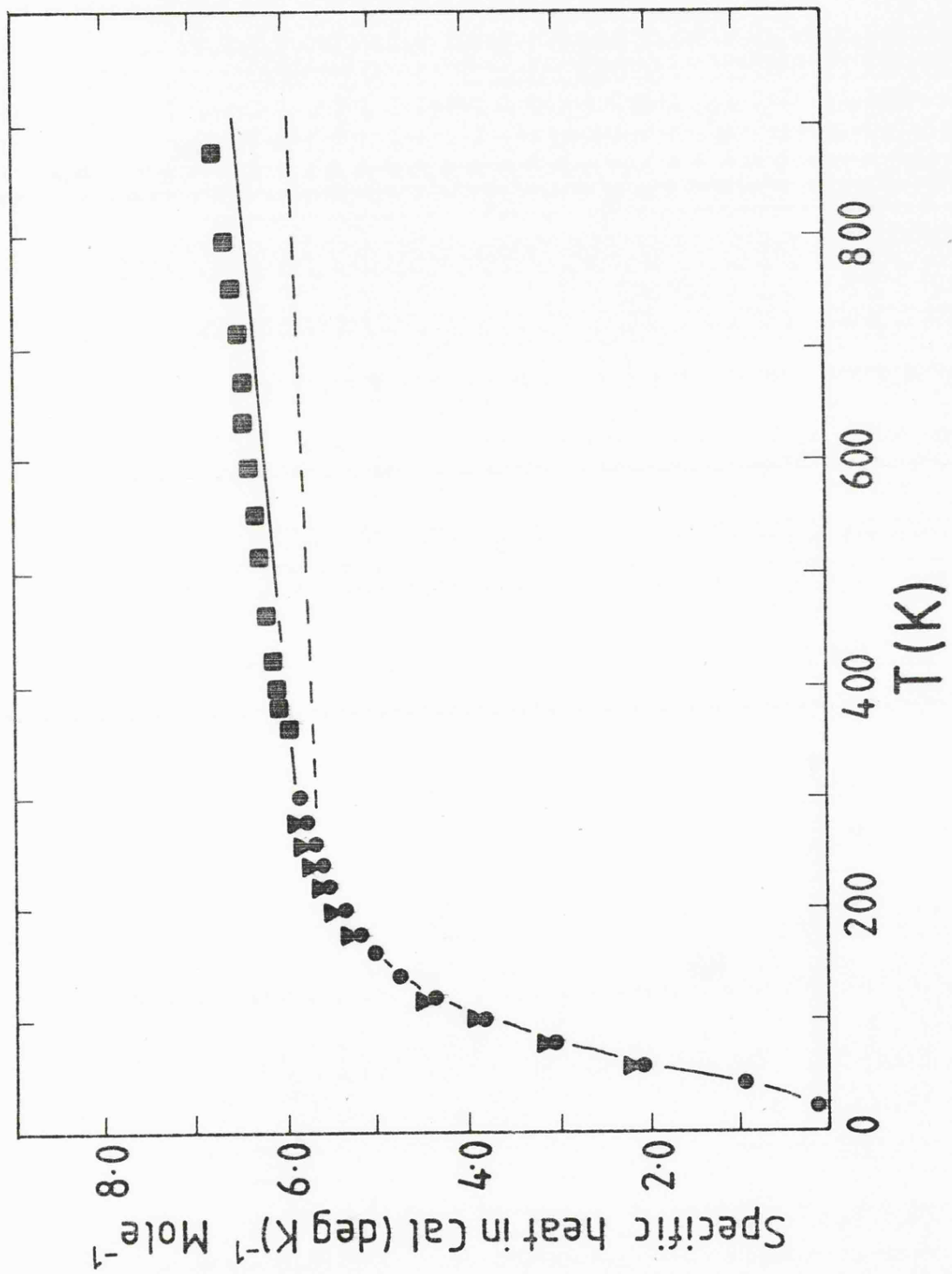
$$C_p - C_V = T V \beta^2 / K \quad \dots 7$$

where β is the volume coefficient of expansion, and K is the compressibility. The difference is negligible at low temperatures, but becomes appreciable for temperatures comparable with Θ_D . For example with lead at room temperature $C_p = 26.75$ and $C_V = 25.20 \text{ J deg}^{-1} \text{ mole}^{-1}$. This is an indication that anharmonic effects cannot be neglected in attempting to predict the specific heat over a wide temperature range.

Miller and Brockhouse (4) have made neutron scattering measurements on copper. The dotted line in Figure 5.2 gives C_p as predicted on the basis of the harmonic approximation, while the full line includes an allowance for anharmonic interactions. The experimental points lie above the line by an amount which agrees

Figure 5.2

Plot of the specific heat, C_p , of copper against temperature. The dotted line indicates C_p as predicted by the harmonic approximation, the full line makes allowance for anharmonic interactions.



well with the expected electronic contribution C_e . The processes contributing to the specific heat for Cu over a temperature range of 800K are therefore apparently well understood.

It has been stated that for most materials anharmonic effects are relatively small, and can be treated ^{as a} perturbation, becoming more important as the temperature increases. The recognition of anharmonicity in its own right, however, will allow a more accurate view of crystal dynamics to be gained. Anharmonic forces are considered as repulsive forces, whose presence, in addition to harmonic attractive forces, cause non linearity in the cohesive forces in a solid.

The first consideration is the now allowed phenomenon of thermal expansion. The change in volume of a crystal which would accompany a change in temperature will affect physical properties of the crystal, quite apart from any direct effect of the temperature change.

When a crystal expands, its elastic energy increases, but this may be compensated for by a decrease in the free energy resulting from a lowering of the phonon frequencies. The equilibrium volume is that which minimises the free energy. At relatively high temperature the free energy of the lattice vibration (5) is

$$F_{Lv} = k_B T \sum_{\vec{q}, j} \ln \left(\frac{\hbar w(\vec{q}, j)}{k_B T} \right) \quad \dots 8$$

where $w(\vec{q}, j)$ is the frequency w of the j th mode, characterised by wave vector q .

When a cubic crystal is expanded from volume V to $V + \Delta V$, the increase in elastic energy is

$$U_{el} = \frac{(\Delta V)^2}{2\kappa V} \quad \dots 9$$

where κ is the compressibility. The free energy therefore becomes

$$F_{IV} = k_B T \sum_{\bar{q}, j} \ln \left(\frac{\hbar w(\bar{q}, j)}{k_B T} \right) + \frac{(\Delta V)^2}{2\kappa V} \quad \dots 10$$

by putting $\frac{dF}{dV} = 0$ we obtain

$$\frac{\Delta V}{V} = -\kappa k_B T \sum_{\bar{q}, j} \frac{1}{w(\bar{q}, j)} \left(\frac{dw(\bar{q}, j)}{dV} \right) \quad \dots 11$$

Introducing

$$\gamma(\bar{q}, j) = \frac{-V}{w(\bar{q}, j)} \left(\frac{\partial w(\bar{q}, j)}{\partial V} \right) = - \frac{\partial \ln w(\bar{q}, j)}{\partial \ln V} \quad \dots 12$$

this gives, for the volume strain

$$\frac{\Delta V}{V} = \frac{\kappa k_B T}{V} \sum_{\bar{q}, j} \gamma(\bar{q}, j) \quad \dots 13$$

$\gamma(\bar{q}, j)$ is called the mode Gruneisen parameter. We now consider a general expression for F_{IV} at any temperature instead of the high temperature situation above. The expression for F_{IV} is (6)

$$F_{IV} = k_B T \sum_{\bar{q}, j} \ln \left(2 \sinh \left(\frac{\hbar w(\bar{q}, j)}{2k_B T} \right) \right) \quad \dots 14$$

one obtains, for the volumestrain, at the expense of more algebra

$$\frac{\Delta V}{V} = \frac{k_B}{V} \sum_{q,j} (\bar{n}(q,j) + \frac{1}{2}) \hbar \omega(q,j) \gamma(q,j) \quad \dots \quad 15$$

which merely reduces to equation 13 when the mean energy of any mode can be replaced by $k_B T$. Hence, the coefficient of volume expansion is given by

$$\beta = \frac{d}{dT} \left(\frac{\Delta V}{V} \right) = \frac{k_B}{V} \sum_{q,j} C(q,j) \gamma(q,j) \quad \dots \quad 16$$

where $C(q,j)$ is just the contribution of the mode (q,j) to the specific heat. If the dependence of frequency on volume can be taken as the same for all modes, i.e. $\gamma(q,j) = \gamma$, a constant, equation 16 becomes

$$\beta = k_B \gamma C \quad \dots \quad 17$$

where C is the specific heat of unit volume. Although, as will be shown, there is good reason to believe that $\gamma(q,j)$ will not be the same for all modes, for many materials the coefficient of expansion closely follows the specific heat.

The second major consideration which follows from the recognition of anharmonicity is that interactions between normal modes are permitted. The net effect of these interactions is to open up channels for decay of phonon energies. If these interactions were absent, then the spectral profile of the lattice vibrations would be a set of undamped, temperature independent resonances. The interactions also lead to changes in the phonon energies, together with the development of finite lifetimes for the vibrations (5), (6).

The temperature and pressure dependencies of each phonon in the Brillouin zone arises therefore in two separate ways. Firstly thermal expansion creates a temperature-dependent shift of each phonon from the harmonic normal mode value. Secondly the anharmonic coupling permitted between phonons causes a further temperature-dependent shift of the phonon energies. This second contribution can be distinguished from the effects of thermal strain, because the latter factor gives rise to temperature dependence of phonon frequencies even when the crystal is held under isochoric conditions (that is, is held under a pressure which at some temperature T, returns the crystal volume to that at absolute zero; this would mean that no thermal expansion would have occurred, and the shift evaluated would be solely due to anharmonic coupling between phonons).

The theoretical temperature dependence of the optic phonons of alkali halides (7) and silver and thallium halides (7) have been considered by Lowndes, an outline of which is shown below.

The temperature dependence of each phonon frequency in the Brillouin zone stems from anharmonicity in the two ways suggested above. This can be formulated as follows; the harmonic frequency $w^h(\vec{q}, j)$ is shifted by a term due to thermal strain in the crystal on raising the temperature from OK to TK; thus

$$w_T^E(\vec{q}, j) = w^h(\vec{q}, j) + w_T^E(\vec{q}, j) \quad \dots \quad 18$$

the suffices h and E denoting harmonic, and thermal expansion respectively.

This 'quasiharmonic' frequency $w_T^E(\bar{q}, j)$ is that which would result if the only effect of anharmonicity was to allow thermal expansion, i.e. $w_T^E(\bar{q}, j)$ is dependent on the volume of the crystal only. But, as stated previously, anharmonic terms also permit coupling of normal modes, which change phonon frequencies and give them finite lifetimes. At a temperature T and frequency Ω each of the quasiharmonic frequencies suffers a frequency dependent shift of

$$w_T^A(\bar{q}, j, \Omega) + i\Gamma(\bar{q}, j, \Omega) \quad \dots \quad 19$$

(Lowndes (6))

The real part of this shift gives a shift in the observable frequency of the mode, and the complex part gives a finite lifetime to the vibration. Thus the quasinormal frequency $w_T(\bar{q}, j)$ which is the solution for Ω , given by

$$\Omega^2 = w_T^E(\bar{q}, j)^2 = 2w^E(\bar{q}, j) \Delta w_T^A(\bar{q}, j, \Omega) = w_T(\bar{q}, j)^2 \quad \dots \quad 20$$

the suffix A denoting anharmonic coupling of the modes.

Therefore the quasinormal frequency, being the frequency measured in any resonance experiment can be shown to be

$$\dots \quad 21$$

$$[w_T(\bar{q}, j)]^2 = [w_h(\bar{q}, j)]^2 + 2w^h(\bar{q}, j) [\Delta w_T^A(\bar{q}, j, \Omega) + w_T^E(\bar{q}, j)]$$

This can be rewritten for the $\bar{q} = 0$ wavevector, i.e. considering the zone centre phonons only. At an applied pressure P, which is applied to reduce the volume and shape of the crystal to that at absolute zero we have

$$[w_{Tp}(0, j)]^2 = [w^h(0, j)]^2 + 2w^h(0, j) \Delta w_T^A(0, j, \Omega) \quad \dots \quad 22$$

The $\Delta w_T^E(o, i)$ term will be zero if the volume is that which would occur at OK, for the reasons explained above.

We can also write, at OK and no applied pressure

$$w_{oo}(o, i)^2 = w^h(o, i)^2 + 2w^h w_o^A(o, i, \Omega') \quad \dots \quad 23$$

where $\Omega \approx \Omega'$. By substituting for $w^h(o, i)$ from 23 into 22 we obtain

$$\begin{aligned} w_T^A(o, i, \Omega) - w_o^A(o, i, \Omega) &= \frac{w_{Tp}(o, i)^2 - w_{oo}(o, i)^2}{2w^h(o, i)} \\ &= \frac{w_{Tp}[(o, i)]^2 - [w_{oo}(o, i)]^2}{2w_{oo}(o, i)} = f(T) \quad \dots \quad 24 \end{aligned}$$

The above relation thus allows an experimental determination of the change in the anharmonic self energy between temperature T and OK. It can also be shown that above the Debye temperature f(T) is linear and therefore be extrapolated to OK to enable the evaluation of $w_o^A(o, i, \Omega)$ and thence $w_T^A(o, i, \Omega)$.

The effects of anharmonicity are, however, more far reaching than just the modification of energy levels, and three examples of the consequences of anharmonicity are listed below.

- (i) The harmonic oscillator selection rule $\Delta w_i = \pm 1$ is relaxed by anharmonicity. This relaxation allows observation of more than the fundamental frequency w_i in certain cases. Even so,

it must be noted that the transitions allowed under anharmonic dominance must still conform to restrictions imposed by symmetry. A characteristic feature of the spectrum of an anharmonic molecule is the appearance of overtone transitions $\Delta w_i = \pm 2, \pm 3$, etc., combination transitions, eg. with $\Delta w_i = \pm 1$ simultaneously with $\Delta w_j = \pm 1$, together with still more complicated transitions involving two or more quantum numbers.

(ii) A feature of gas phase vibrational spectra, also important in the solid state is the phenomenon of hot bands. In the simplest case of a diatomic molecule, if the system were harmonic the $w = 1 \rightarrow 2$, $w = 2 \rightarrow 3$, etc., would be coincident with the $w = 0 \rightarrow 1$ fundamental. The anharmonicity leads to a series of slightly different frequencies for the transitions $w \rightarrow w + 1$.

(iii) A more subtle phenomenon associated with anharmonicity is that of Fermi resonance. If two modes of similar energy have some symmetry component common to both, this can lead to a more intimate interaction than is the general case. This interaction can be seen as either a shift of one or the other, or both components from their expected value, and/or a marked change in relative intensity of their absorption spectra.

Various theoretical studies of the temperature and pressure dependence of phonon frequencies have been made. Maradudin and Fein (5) have studied the effects of anharmonicity on neutron scattering. These results have been further confirmed by expressions for thermal deformations and frequency shifts in terms of force constants by Maradudin (9). The results of these studies can be applied to infrared and Raman work. Cowley (5), (10), and Ipatova, et al (11) have given more general treatments. In both Maradudin (5) and Cowley (6) it was shown that w_T^A (see equation 24) is made up of cubic and quartic terms in anharmonicity, where the cubic term is always negative, and the quartic term may be positive or negative. Lowndes (8) gives a very full account of this, and the use of many-body thermodynamic Greens functions as a quantitative tool for handling anharmonicity. The theory he used (presented in equations 18 - 24) gave values which were in good agreement with experimental results for ionic crystals. The use of finite strain parameters (12) has led to more exact theoretical expressions. Loudon (13) and Mitra (14) have reviewed a number of experimental studies.

Having proved that the anharmonic selfenergy between T and OK can be determined by a study of $w(o, j)$ with T and P (equation 24) how can these variables be related?

If

$$w_i = w(o, j) = f^1(TP)$$
$$\text{i.e. } \ln w_i = f^2(TP) \quad \dots \quad 25$$

then for an infinitely divisible isotropic system

$$d(\ln w_i) = \left(\frac{\partial(\ln w_i)}{\partial T} \right)_P dT + \left(\frac{\partial(\ln w_i)}{\partial P} \right)_T dP \quad \dots 26$$

Also if $\ln V = f^3(P, T)$... 27

then

$$d \ln V = \left(\frac{\partial(\ln V)}{\partial T} \right)_P dT + \left(\frac{\partial \ln V}{\partial P} \right)_T dP \quad \dots 28$$

if 26 and 27 are both true then we can write $\ln w_i$ as a function of

$$\ln w_i = f^4(T, V) \quad \dots 29$$

$$d(\ln w_i) = \left(\frac{\partial \ln w_i}{\partial T} \right)_V dT + \left(\frac{\partial \ln w_i}{\partial V} \right)_T dV \quad \dots 30$$

so substituting for $d \ln V$ from equation 28 into equation 30 we obtain

$$d(\ln w_i) = \left(\frac{\partial \ln w_i}{\partial T} \right)_V dT + \left(\frac{\partial(\ln w_i)}{\partial(\ln V)_T} \right)_T \left[\left(\frac{\partial \ln V}{\partial P} \right)_T dP + \left(\frac{\partial(\ln V)}{\partial T} \right)_P dT \right] \quad \dots 31$$

comparing coefficients in 31 and 26

for dT

$$\left(\frac{\partial(\ln w_i)}{\partial T} \right)_P = \left(\frac{\partial(\ln w_i)}{\partial T} \right)_V + \left(\frac{\partial(\ln w_i)}{\partial(\ln V)_T} \right)_T \left(\frac{\partial(\ln V)}{\partial T} \right)_P \quad \dots 32$$

for dP

$$\left. \frac{\partial(\ln w_i)}{\partial P} \right|_T = \left. \left(\frac{\partial \ln w_i}{\partial(\ln V)} \right) \right|_T \left. \left(\frac{\partial(\ln V)}{\partial P} \right) \right|_T \quad \dots 33$$

Rearrange 33 and substitute into 32 we obtain

$$\left. \left(\frac{\partial(\ln w_i)}{\partial T} \right) \right|_P = \left. \left(\frac{\partial(\ln w_i)}{\partial T} \right) \right|_V + \left. \left(\frac{\partial(\ln w_i)}{\partial P} \right) \right|_T \left. \left(\frac{\partial \ln V}{\partial T} \right) \right|_P \left. \left(\frac{\partial P}{\partial(\ln V)} \right) \right|_T \quad \dots 34$$

(a) (b) (c)

Thus we can see that the change in mode frequency that occurs with a change in temperature, at constant pressure P is caused by two components, labelled (b) and (c) in equation 34. (b) is the rate of change of frequency with temperature of the system under isochoric conditions. (c) can be understood as the change of frequency if the volume of the crystal at TK is returned to that at OK. (Lowndes (6)).

In macroscopic terms the equation becomes

$$\Delta_T w_i | P = \Delta_T w_i | V + \Delta w_i | T \quad \dots 35$$

Both 34 and 35 have been derived and reported in the literature (6, 8, 15, 16).

So we have now divided the frequency shift with temperature into (c), a thermal expansion term, which will be a measure of $\Delta w^E(o, j)$ (See equation 19) and a term at constant volume, (b), which will be a measure of $(\Delta w_A^T(o, j) - \Delta w_O^A(o, j))$ as the quasi-harmonic frequency remains constant under constant volume (equation 21, 22).

i.e.

$$\begin{aligned} \Delta w^E(o,i) &= \Delta w_i|_T \\ \Delta T w_i|_V &= \Delta w_T^A(o,i) - \Delta w_O^A(o,i) \end{aligned} \quad \dots 36$$

Lowndes (7)

provided that the mode selfenergies are small, such that at OK

$$\frac{w^E(o,i)}{w(o,i)} \simeq 1 \quad \dots 37$$

Of the greatest importance is that all the terms in equation 35 can be measured experimentally. $\Delta T w_i|_P$ by direct spectroscopic observation of frequencies at varying temperatures and constant pressure, and $\Delta w_i|_T$, which is more easily understood in the form shown in equation 34; this is evaluated by measuring the relationship between (i) the frequency of a mode with pressure at constant temperature; (ii) the change in volume of the unit cell with temperature at constant pressure, and (iii) the variation in volume with pressure at constant temperature.

Term (c) can also be written as $-\alpha \gamma_i$, where α is the volume thermal expansion coefficient, and γ_i the mode Gruneisen parameter, which are defined as follows;

$$\alpha = \left(\frac{\partial (\ln V)}{\partial T} \right)_P, \quad \gamma_i = \frac{1}{K} \left(\frac{\partial (\ln w_i)}{\partial P} \right)_T \quad \dots 38$$

$$K = - \left(\frac{\partial \ln V}{\partial P} \right)_T = \left(\frac{1}{V} \cdot \frac{\partial V}{\partial P} \right)_T$$

K is the isothermal compressibility of the system.

So we can see that terms (a) and (c) can be measured directly. We can therefore obtain (b), which is $\Delta w_T^A(o, j) - \Delta w_O^A(o, j)$ and the anharmonic self energy calculated. To allow evaluation of the components in term (c) we must now consider the experimental procedure necessary.

The change in mode frequency with pressure at constant temperature was observed with the sample contained in a DAC, and used in conjunction with a Raman or far infrared spectrometer. For variation of frequency with temperature, a cryostat was utilised in conjunction with a far ir or Raman spectrometer.

For volume and temperature variation at constant pressure a single crystal was examined by X ray diffraction, but as will be related, the data obtained here were not considered sufficiently consistent for use in this analysis. Consequently an estimate of the volume thermal expansion coefficient was obtained by utilising data obtained by Dimitropoulos (17). Finally the variation of volume with pressure was studied by loading a DAC with the powdered sample, and used on an X ray camera.

The compounds chosen for this study were K_2PtCl_6 and K_2ReCl_6 . These were selected for two main reasons.

The first is their relatively simple spectra having three well defined infrared active modes, and in principle four Raman active modes. In practice the Raman active lattice mode in K_2PtCl_6 was not observed. However the ν_5^t 2g bending vibration was recorded, which was not reported in a previous high pressure study of K_2PtCl_6 (18).

The Eg mode of K_2ReCl_6 was also not observed.

The second reason for this choice is that these two compounds both have the antifluorite structure, i.e. they are cubic, crystallising in space group $Fm\bar{3}m = O_h^5$. The choice of isotropic compounds is significant, as the developed theory is significantly effected by anisotropy. Equation (22) can only strictly be true if the volume at O/K has the same shape as the volume produced by application of some pressure P at temperature T; that is, the volume change must constitute an isotropic contraction of the lattice.

A more general form of the frequency dependence would be obtained if instead of using:-

$$\ln w_i = f^3 (V, T) \quad (\text{equation 29})$$

we consider

$$\ln w_i = f^4 (a, b, c, T)$$

where a, b, c are the crystallographic axes of the system.

A non isotropic medium would therefore greatly increase the complexity of the situation, hence the choice of a cubic system.

The thermodynamics of anisotropic solids is considered in (19), an example of which is TeO_2 (20) being tetragonal.

The phase transitions of K_2ReCl_6 at low temperature are ignored for the purpose of this analysis.

5.2 Experimental

K_2PtCl_6 was obtained from May and Baker, and recrystallised from water. K_2ReCl_6 was obtained from material prepared by S.J. Payne, and recrystallised from water. The high pressure experiments were performed in a Mk II DAC, described in Chapter 2.

Far infrared experiments were performed with the sample contained in a 0.05mm thick inconel gasket, with a gasket hole of 0.5mm diameter and Nujol used as a hydrostatic medium for the range $40 - 400\text{cm}^{-1}$. To enhance the resolution of the lattice mode, the experiments were repeated using a similar gasket, but with silicone oil as a hydrostatic medium, and replacing the 25μ beam splitter with a 50μ film, thus converting the range of the FS 620 to $20 - 200\text{cm}^{-1}$.

Raman experiments were performed with a 0.2mm thick gasket, with a 0.4mm diameter hole using 4 : 1 methanol/ethanol as the pressure transmitting fluid. A Coderg T800 spectrophotometer and photon counting were used.

The high pressure X ray experiments were carried out using the modified X ray cell, with 0.25mm thick gaskets with 0.5mm diameter holes, and utilising a 0.2mm collimator (see Chapter 2) and $\text{Mo}/\text{K}\alpha$ radiation.

Low temperature ambient pressure infrared and Raman experiments used a closed circuit CTI liquid helium (Model 21) cryostat which covered a range from 12 - 300K, controllable to better than 0.5K. The cryostat was used in conjunction with a Beckman FS720 interferometer, and Coderg T800 spectrometer.

Low temperature X ray measurements were made on a small single crystal (ca. 0.6mm^3) mounted on a Stoe Weissenberg camera, with a Stoe liquid nitrogen cryostat, and $\text{CuK}\alpha$ radiation. The stability of the temperature control proved very low. Although exposures at several temperatures were made on the same film to avoid shrinkage errors, and high values of 2θ ($2\theta \gg 130^\circ$) were measured, the instability of the temperature proved the overriding factor. This caused the values of the lattice parameters to have such scatter that any curve fitting performed resulted in fits of negligible significance.

It would have been preferable to have used a powder sample with the CTI, this having much better temperature control, and a much wider range (the lowest temperature attainable on the Stoe crystal proved to be ca. 130K, cf. 12K for the CTI.) However a powder sample failed to give any lines at high values of 2θ .

The error in the values of lattice parameters obtained by the high pressure experiments were considered to be $\pm .2\text{\AA}$. The magnitude of this error was due to the fact that no high 2θ scatter could be observed through the DAC. The value obtained for the compressibility of K_2PtCl_6 was however half that calculated in Chapter 6. As the compressibility of K_2ReCl_6 is known (21), and accords fairly well with the calculated value, an independent anharmonicity calculation was performed using the value of compressibility obtained by the methods used in Chapter 6.

The frequency versus pressure and temperature data were fitted to straight lines by a NAG linear regression routine.

A computer programme was constructed to perform the analysis of pressure and temperature dependence of the vibrational modes by R.Appleby.

5.3 Results and Discussions

The far infrared and Raman spectra at various temperatures and pressures are given in Figures 5.3, 5.4, 5.6, 5.7. Wavenumbers versus temperature and pressure are given on Tables 1 and 2, and plots of wavenumber versus temperature and pressure are given on Figure 5.5 and 5.8. The X ray data are given on Figure 5.10 and Table 3. The figure from which the thermal expansion data were obtained is given as Figure 5.11, and an explanation of the procedure followed is given below. Plots of volume versus temperature and pressure, and the compressibility χ ^{are} given on Figure 5.12. Plots of $\Delta_T w_i | P$, $\Delta_T w_i | V$, and $\Delta w_i | T$ are given in Figures 5.14, 5.15, 5.13 for K_2PtCl_6 (χ experimental) K_2PtCl_6 (χ calculated) and K_2ReCl_6 (χ calculated).

The far infrared spectra of K_2ReCl_6 are given in Chapter 6. Raman work was performed by R.W. Berg, as were the infrared and Raman thermal data for K_2ReCl_6 .

Values of compressibility were obtained via the method of Mifca as described in Chapter 6 and are given on Table 5.7. The marked difference in the values of compressibility of K_2PtCl_6 obtained by experiment and theory are noted, but not understood at present. However, the calculated value of χ for K_2ReCl_6 corresponds fairly well with that determined by Dimitropoulos (21) of $7.2 \times 10^{-3} \text{ kbar}^{-1}$.

Figure 5.3

Raman spectra of K_2PtCl_6 at various pressures.
Obtained with a spectral slit width of 2.0cm^{-1}
with 100 mw of 6328\AA radiation at the sample.

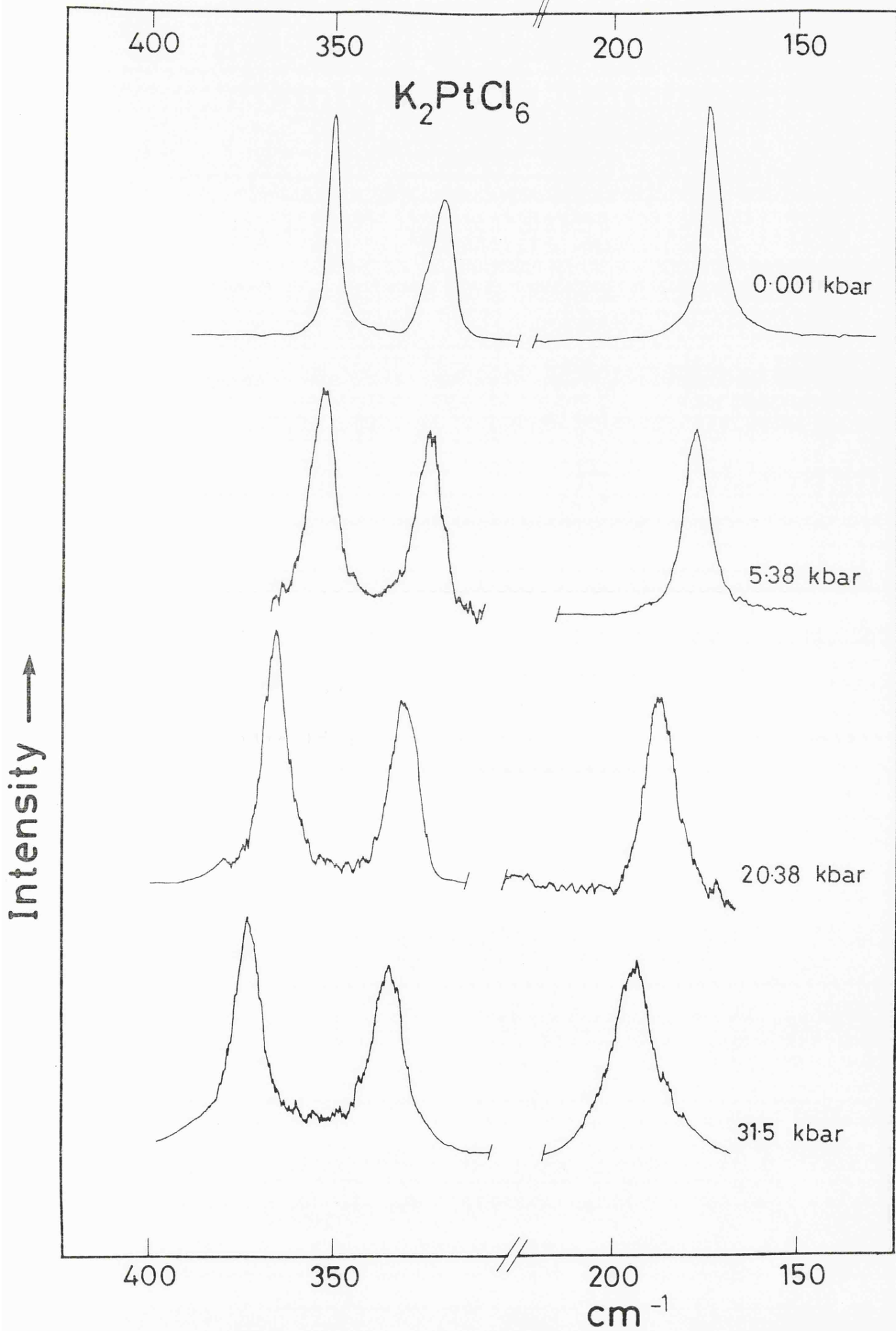


Figure 5.4

Far infrared spectra of K_2PtCl_6 at various pressures.

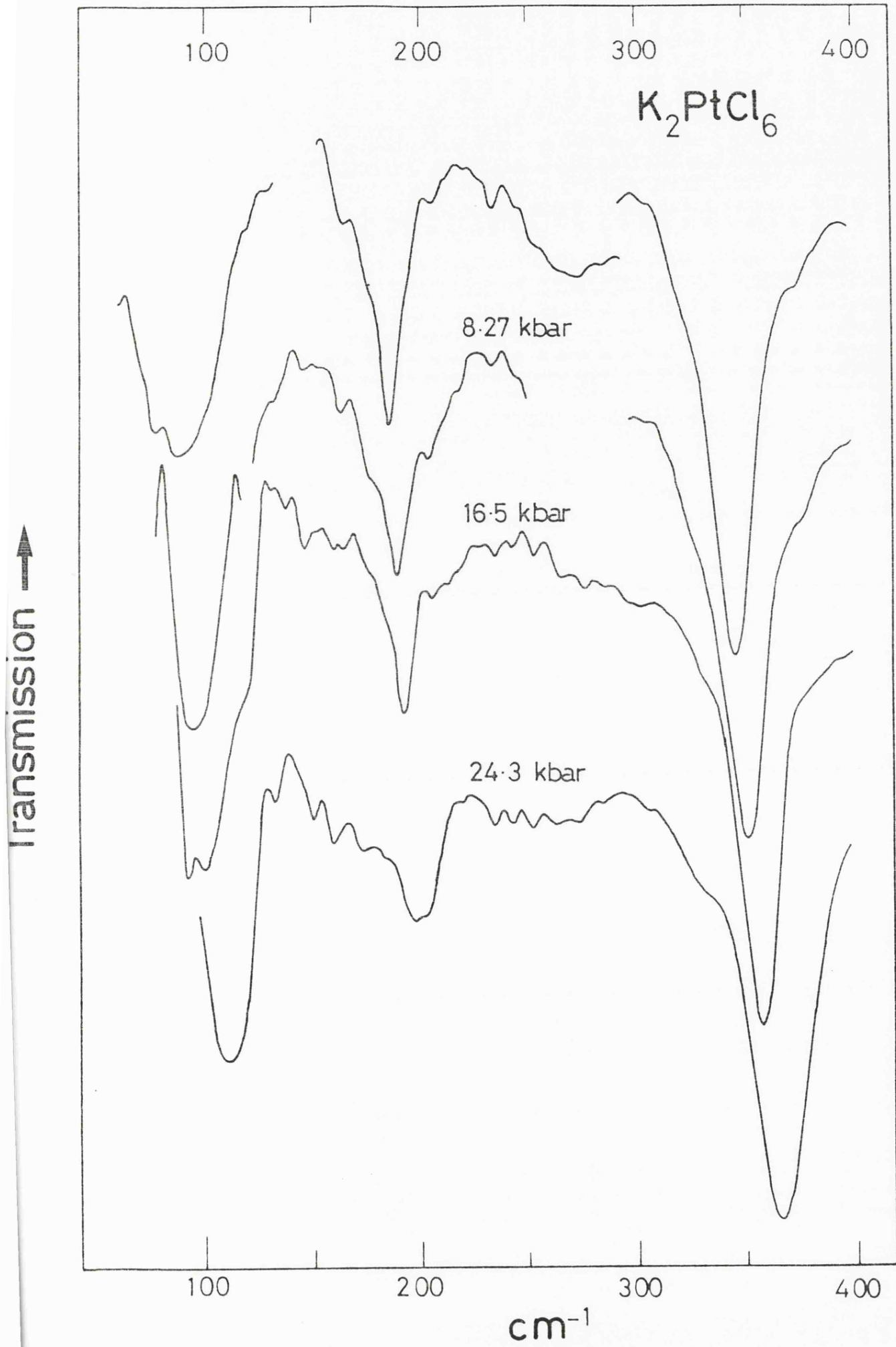


Figure 5.5

Plot of the fundamentals for K_2PtCl_6 against pressure.

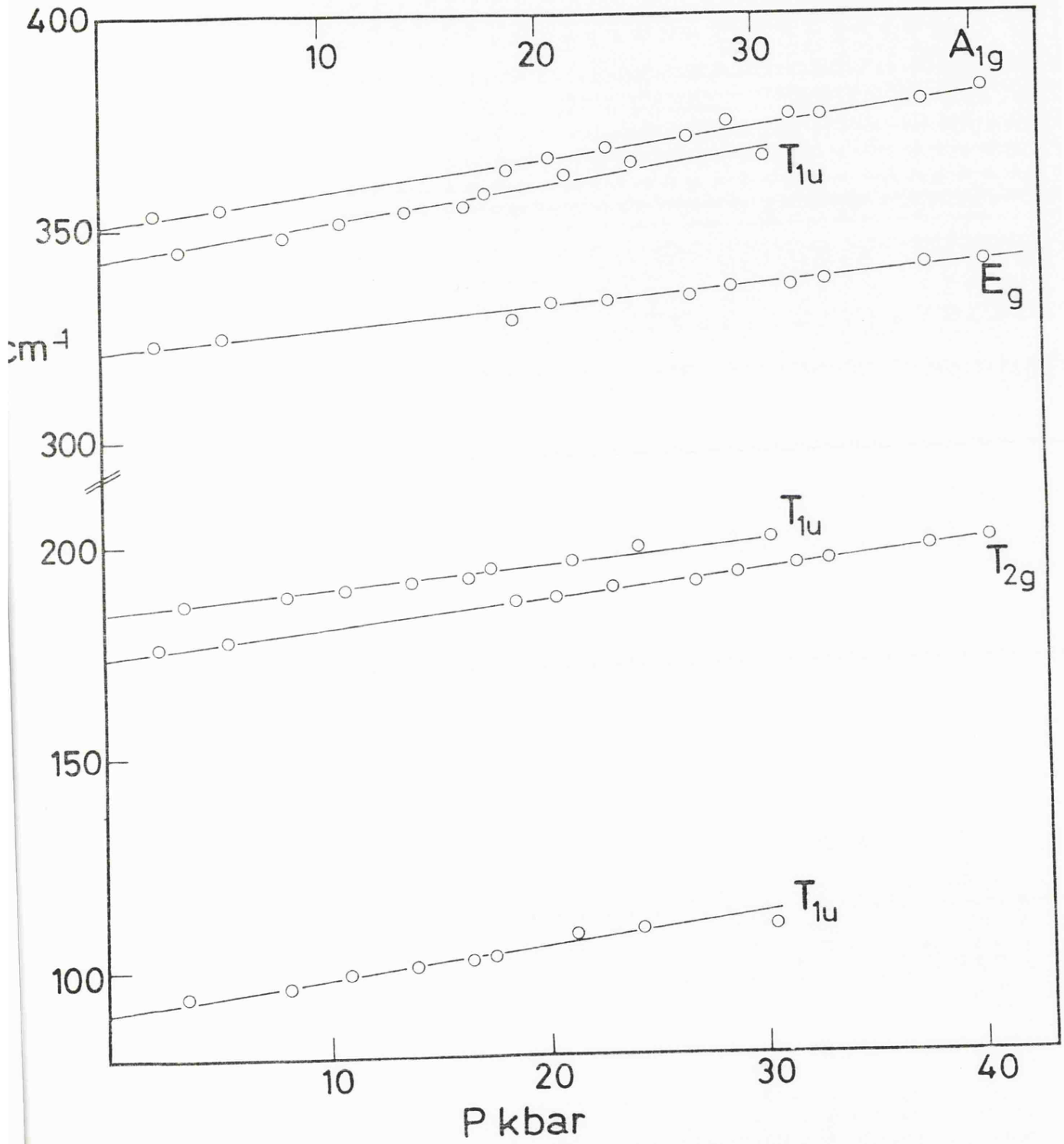


Figure 5.6

Raman spectra of K_2PtCl_6 at various temperatures.

Spectra were obtained with a spectral slit width of 1.8cm^{-1} with 50 mw of 6328\AA radiation at the sample.

(The reason for the split of ν_2 at low temperatures is not understood.)

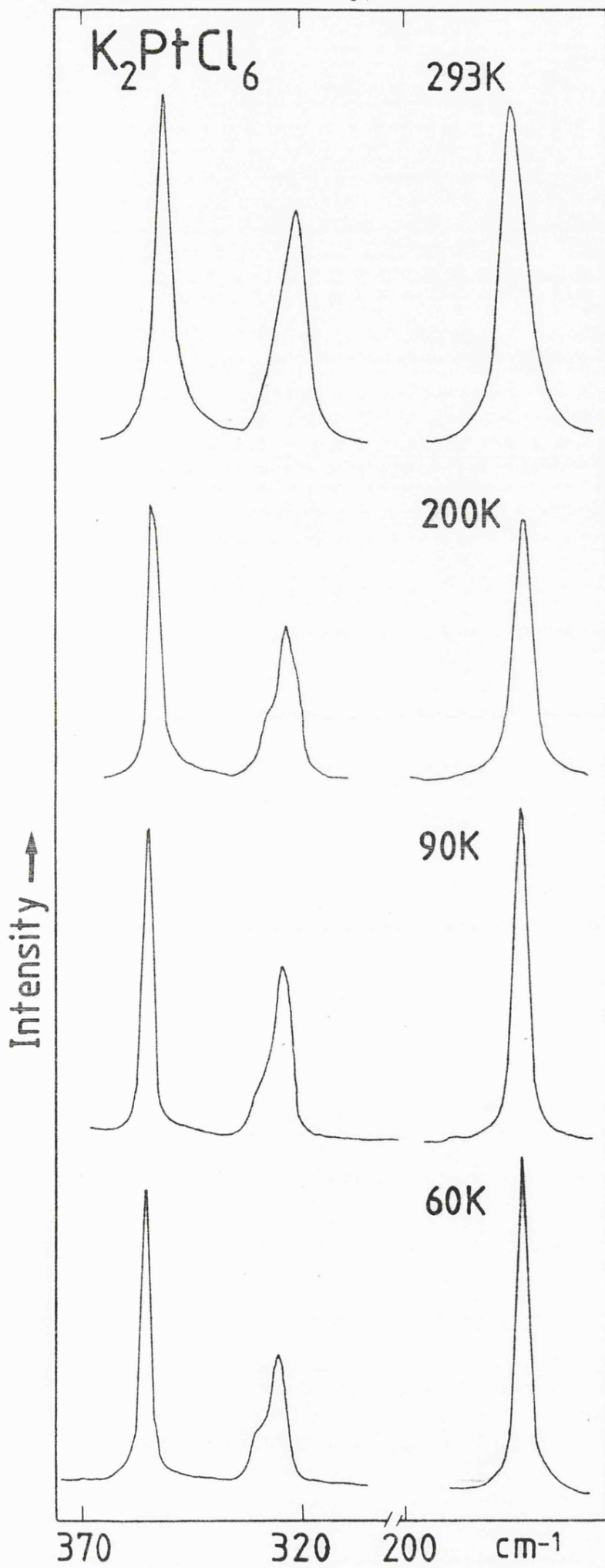


Figure 5.7

Far infrared spectra of K_2PtCl_6 at various temperatures.

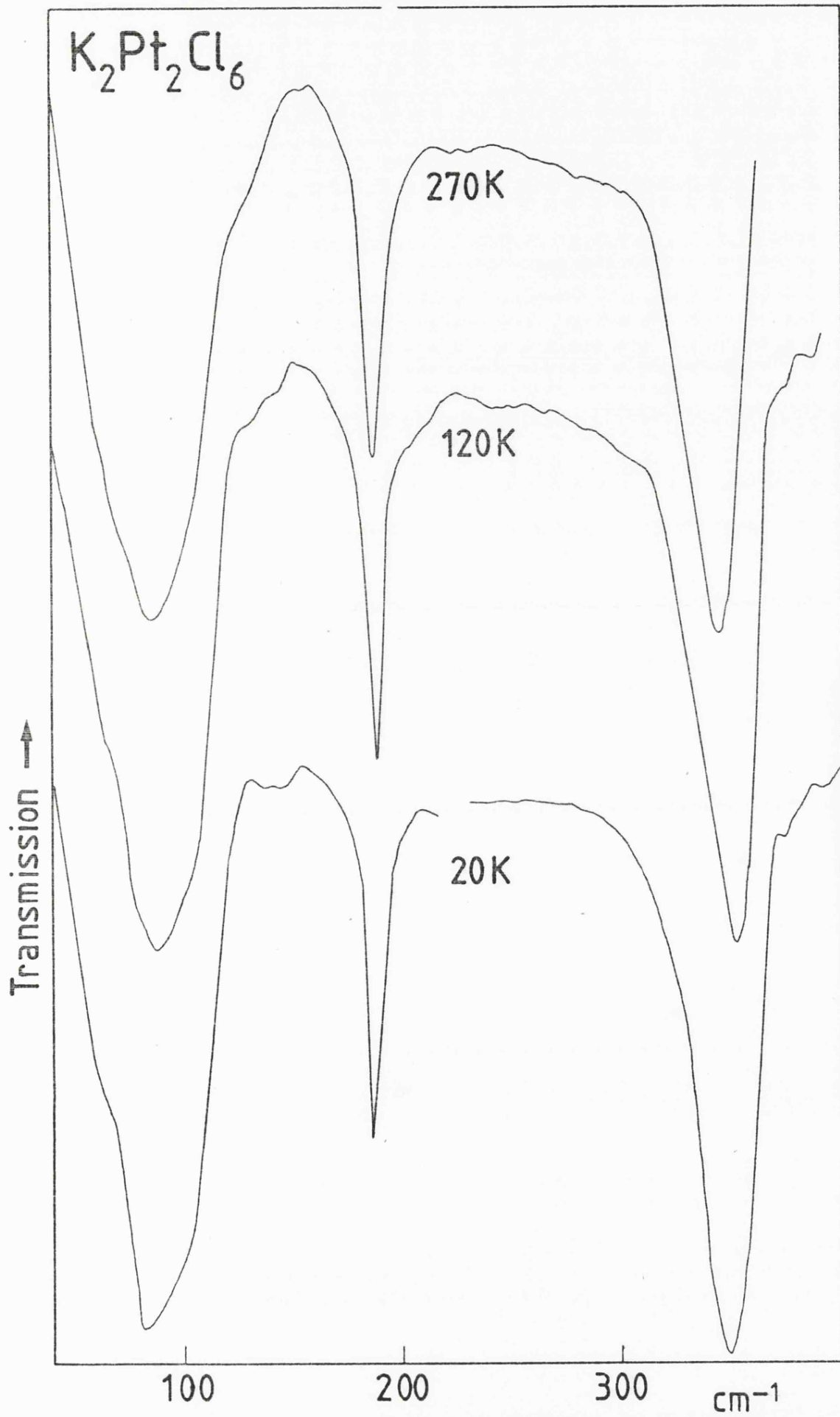


Figure 5.8

Plot of the fundamentals for K_2PtCl_6 against temperature.

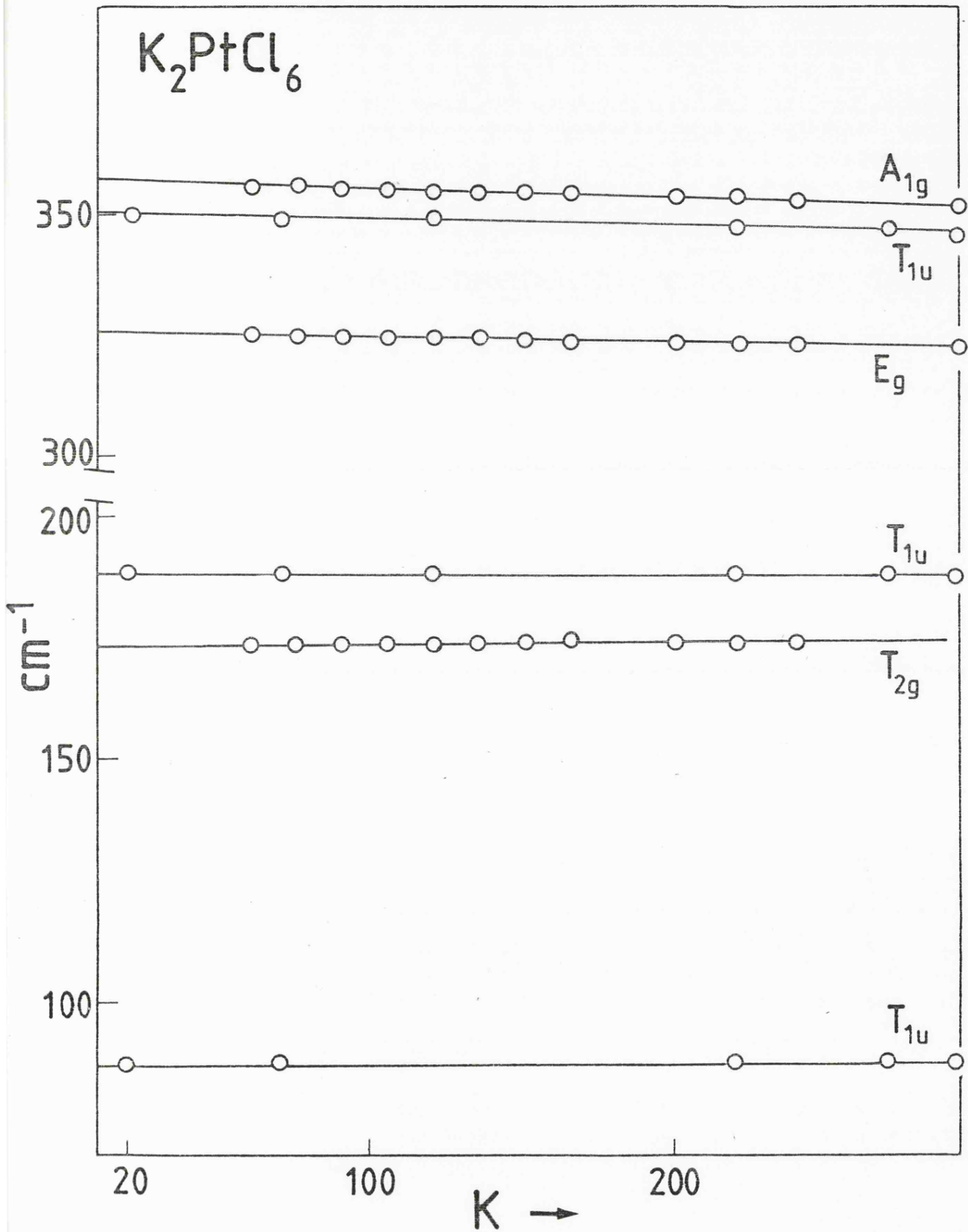


TABLE 5.1 The wavenumbers/cm⁻¹ of K₂PtCl₆ at various temperatures and ambient pressure.

Far Infrared

T(K)	T _{1u} (ν _L)	T _{1u} (ν ₄)	T _{1u} (ν ₃)
300	88	187	345
260	88	187	346
180	88	188	348
120	88	188	349
60	87	189	350
20	87	189	350

Raman

T(K)	T _{2g} (ν ₅)	E _g (ν ₂)	A _{1g} (ν ₁)
300	175	322	351
260	174	322	352
180	174	323	354
120	174	324	355
60	173	325	356
20	173	325	357

TABLE 5.2

The wavenumbers (cm^{-1}) of K_2PtCl_6 at various pressures (kbar).

Far Infrared

P(kbar)	$T_{1u}(\nu_1)$	$T_{1u}(\nu_4)$	$T_{1u}(\nu_3)$
3.5	94	186	345
8.3	96	188	348
10.9	99	189	351
13.9	101	191	353.5
16.5	102	192	355
17.5	103	194	358
21.2	108	196	362
24.3	109	199	365
30.4	110.5	201	366

Raman

P(kbar)	$T_{2g}(\nu_5)$	$E_g(\nu_2)$	$A_{1g}(\nu_1)$
2.4	175.8	323	353.5
5.4	177.5	324.5	354.5
18.7	186.5	329	363.5
20.4	187.5	332	366.5
23.1	189	332.5	368.5
26.9	191.5	334	371.0
28.9	193	335.5	374.5
31.5	194.5	336	375.5
33.1	196	337	376
37.7	199	340.5	379.5
40.4	200.5	341	382.0

Figure 5.9

X ray diffraction photograph of K_2PtCl_6 at ambient (full circles) and 41.8 (arcs at higher 2θ values) kbar. Intense spots arc due to diffraction from the diamond.

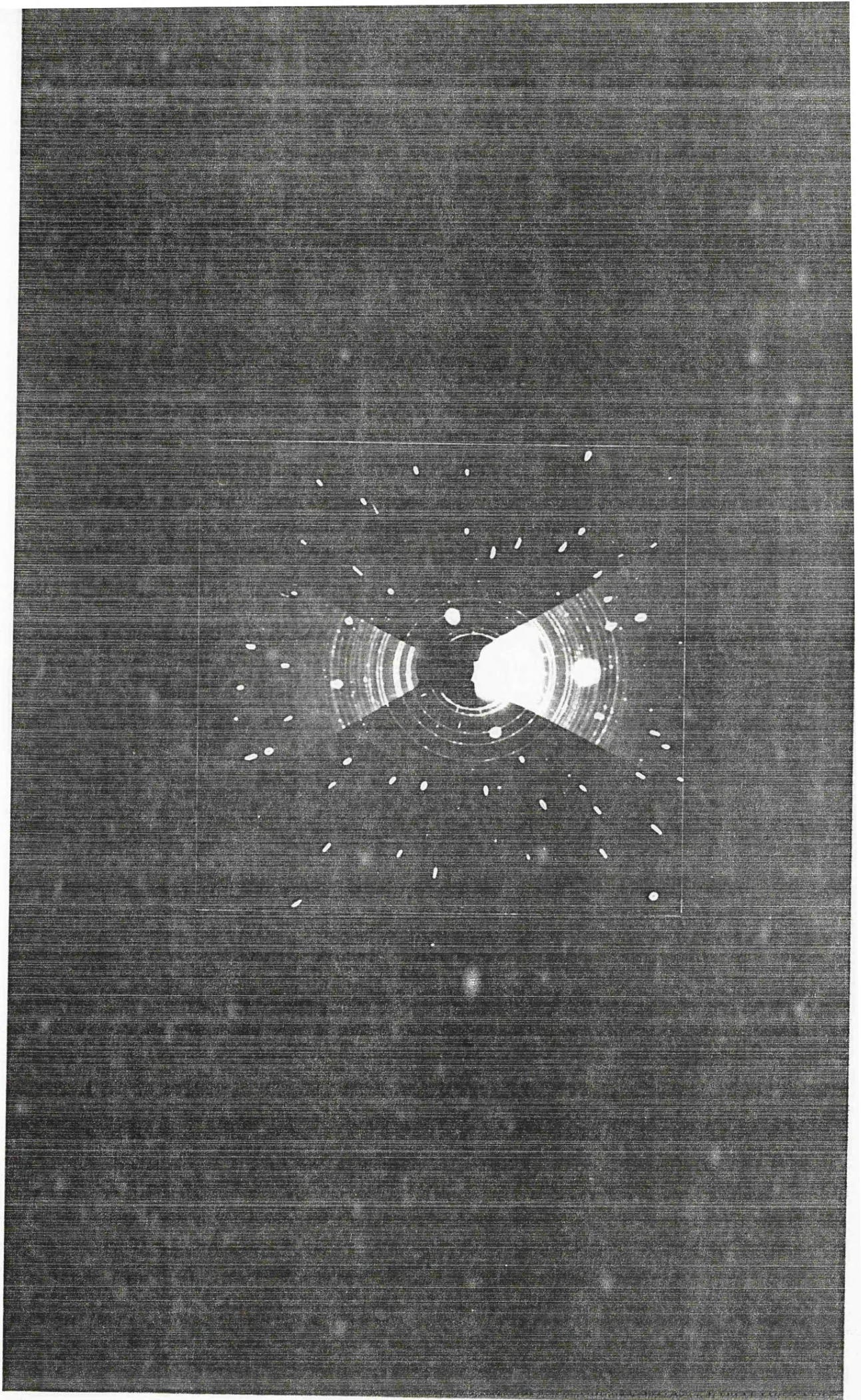


Figure 5.10 Plot of a_{300} (Å) v pressure (kbar)

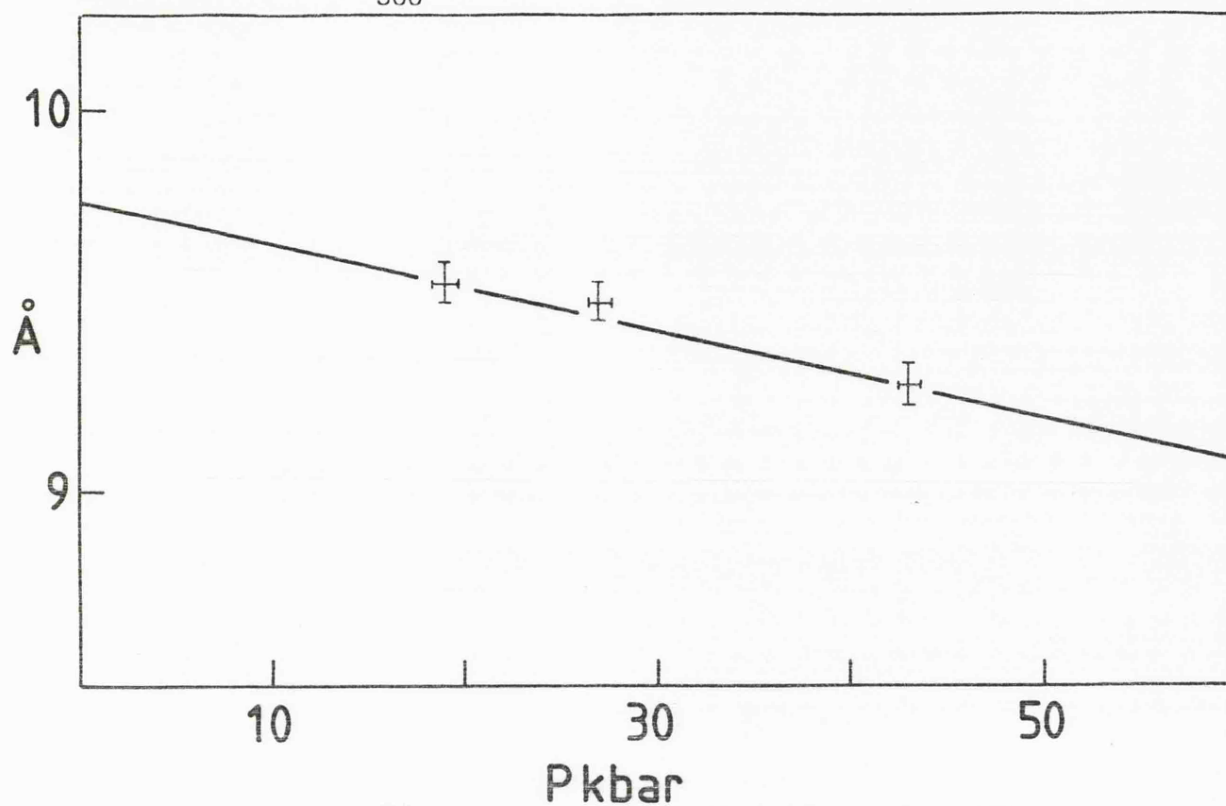


TABLE 5.3 Values of a_{300} (Å) the lattice constant of K_2PtCl_6 at 300K against pressure, as measured in high pressure X ray experiment.

P (kbar)	a (Å)
0.001	9.751
18.8	9.58
27.9	9.50
42.8	9.28

$$\text{Gradient} = 1.11 \times 10^{-2} \text{ \AA/kbar}$$

$$\begin{aligned} \text{Compressibility at ambient pressure} &= \frac{9.751^3 - (9.751 - 0.0111)^3}{9.751^3} \\ &= 3.38 \times 10^{-3} \text{ kbar}^{-1} \end{aligned}$$

The anharmonicity analyses were performed using both calculated and measured values of compressibility for K_2PtCl_6 and the measured compressibility of K_2ReCl_6 . Since the calculated and measured values for K_2PtCl_6 differ almost by a factor of two, the results obtained by using the calculated value for K_2PtCl_6 were compared with those for K_2ReCl_6 .

Thermal Expansion

As described, attempts to obtain volume/temperature data by X ray methods were unsuccessful. There are, to our knowledge, no thermal expansion data in the literature for K_2PtCl_6 . However, Armstrong (17) has studied the linear thermal expansion of K_2ReCl_6 and K_2OsCl_6 . Values of α obtained from these studies show that the linear thermal expansion coefficients for the rhenium and osmium salts are very similar. It was felt therefore that these values would be a reasonable estimate of the linear expansion coefficient of K_2PtCl_6 .

The plot of linear expansion coefficient obtained from (17) is shown in Figure 5.11. The values for K_2OsCl_6 were used simply because the scale of the original figure made more accurate measurements possible. The plot (to be found in Ref. 21) was then photographically enlarged to ca. 40cm square, and values of α measured at various temperatures.

The computer analysis requires, however, volume/temperature data. It was necessary therefore to evaluate the volume of the system at various temperatures. Using the available information, that is, the lattice parameter at 300K, and values of α with temperature, the following procedure was followed

in order to generate the volume at a given temperature T.

The change in lattice parameter, a , on raising the temperature from 0/K to T/K can be formulated as:-

$$a_T = a_0 \left(1 + \int_0^T \alpha dT \right) \quad \dots \quad 39$$

(NB: $\int \alpha dT$ is necessary, since α is temperature dependent)

Equally 39 can be considered for a temperature change from T/K to 300K ($T < 300$).

$$a_T = a_{300} \left(1 - \int_T^{300} \alpha dT \right) \quad \dots \quad 40$$

So $\int_T^{300} \alpha dT$ must be evaluated to obtain the lattice parameter at T, and hence the volume at T. This integral was evaluated using Simpson's Rule, which states that

$$\int_a^b f(x) = \frac{\Delta x}{3} (y_0 + 4y_1 + 2y_2 + 4y_3 + \dots + 4y_{n-1} + y_n)$$

where Δx is the temperature interval chosen, and y_0 is α at Temperature T_0 , y_1 is α at T_1 and so on.

Values of α , $\int_T^{300} \alpha dT$, a_T and V_T are given on Table 5.4. These were applied to both K_2PtCl_6 and K_2ReCl_6 in the succeeding analyses.

The Debye Temperature

In order to extrapolate $\Delta_T w_i |V$ to OK (so as to evaluate w_0^A) it is necessary to calculate the Debye temperature of the material. Plendl (14) gives a formula:-

$$\theta_D = \left(\frac{h}{k} \right) v_{\text{centro}} \quad \dots \quad 41$$

Figure 5.11

Interpolated linear thermal expansion coefficient in the
pseudocubic $\langle 111 \rangle$ direction for K_2OsCl_6 .

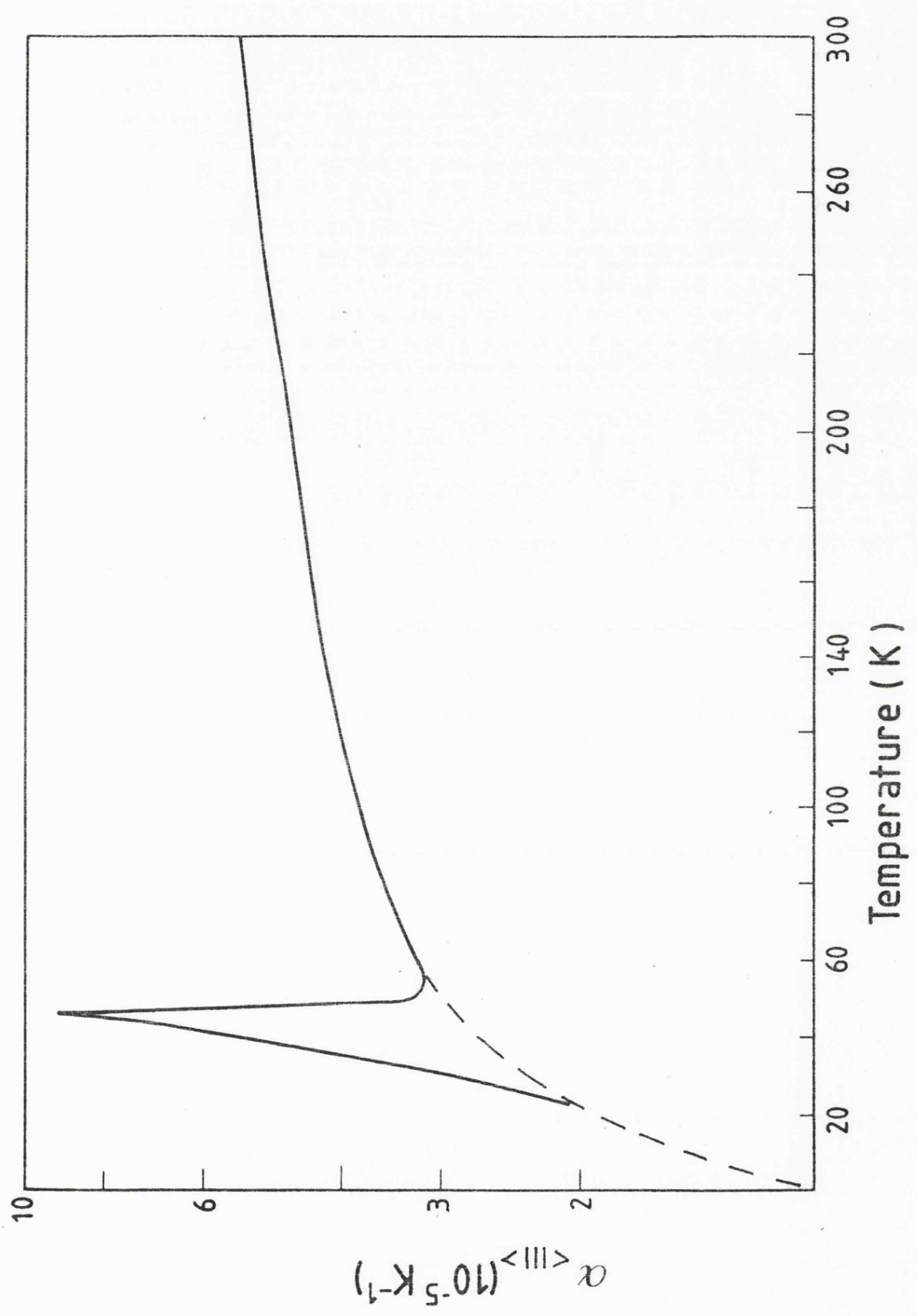


TABLE 5.4 Values for T , α_T , $\int \alpha dT$, a_T and V_T for K_2PtCl_6
using values of α obtained from (17)

$T(K)$	$\alpha_T(\times 10^{-5} K^{-1})$	$\int_T^{300} \alpha dT(\times 10^{-5} K^{-1})$	a_T	V_T
300	5.6		9.75	927.14
280	5.42	110.55	9.740	924.01
260	5.26	216.4	9.729	921.14
240	5.06	318.42	9.720	918.32
220	4.87	411.45	9.711	915.75
200	4.68	506.88	9.702	913.12
180	4.49	598.65	9.693	910.59
160	4.33	686.89	9.684	908.17
140	4.16	775.10	9.675	905.75
120	4.00	856.75	9.667	903.52
100	3.83	935.13	9.659	901.38
90	3.72	972.97	9.656	900.35
80	3.58	1009.44	9.652	899.35
70	3.40	1044.44	9.649	898.39
60	3.24	1077.76	9.646	897.48
50	3.04	1109.31	9.643	896.63
40	2.74	1138.34	9.640	895.84
30	2.36	1163.83	9.638	895.15
20	1.95	1185.11	9.635	894.57

where θ_D is the Debye temperature of the material, h is Planck's constant, k is Boltzmann's constant and ν_{centro} is the centro frequency of the infrared spectrum of the material; that is the frequency at which the centre of gravity of the spectrum is located. The usual way to evaluate this is by measurement of the reflectance spectrum of the system, but no such work has been performed for K_2PtCl_6 .

However, it is stressed that the region of the spectrum considered need only be that which contains the frequencies which contribute to the specific heat of the solid. This effectively means that one need only consider the lattice mode region of the spectrum.

As K_2PtCl_6 has only one infrared active lattice mode this can then be taken as being the centro frequency.

$$\text{Taking } h = 6.626 \times 10^{-34} \text{ Js, } k = 1.38066 \times 10^{-23} \text{ JK}^{-1}, \text{ and} \\ \nu_{\text{centro}} = 88 \text{ cm}^{-1} = 2.638 \times 10^{12} \text{ Hz.}$$

$$\theta_D = 126.6 \text{ K}$$

It must be noted that this assumption will lead to a lower limit of θ_D , as there will be in general some contribution to the specific heat from internal modes, such as ν_4 in K_2PtCl_6 which is low enough in energy, and of the correct symmetry to interact with ν_L . Since it is not known to what extent this is true, an allowance of ca. 10% has been made, and θ_D has been considered as 140K. Since ν_L for K_2ReCl_6 is only 2 cm^{-1} different (86 cm^{-1}) to that of K_2PtCl_6 , θ_D was taken as ca. 140K for K_2ReCl_6 also.

TABLE 5.5

The wavenumbers/cm⁻¹ of K₂ReCl₆ at various temperatures and ambient pressure

Far IR

T(K)	T _{1u} (ν _L)	T _{1u} (ν ₄)	T _{1u} (ν ₃)
300	84	172.5	332.5
223	84	172.5	324
193	83.5	172	325
173	84	172	326
140	84	172	326
115	84.5	172	327
103	85	172	326
80	85.5	173	327

Raman

T(K)	T _{2g} (ν ₅)	E _g (ν ₂)	A _{1g} (ν ₁)
300	176.0	ABSENT	357.5
260	175.5		357.5
180	174.0		357.0
120	173.5		357.0
100	173.0		356.5
60	172.5		565.5

TABLE 5.6

The wavenumbers/cm⁻¹ of K₂ReCl₆ at various pressures and ambient temperature.

Far IR

P (kbar)	T _{1u} (ν _L)	T _{1u} (ν ₄)	T _{1u} (ν ₃)
5.3		182	336.5
11.7		185	340
13.2		185	338
16.3	98	186	341
18.0	98	186.5	340
25.0	99	188	345
27.2	101	189	346
34.3	104	191	350

Raman

P (kbar)	T _{2g} (ν ₅)	E _g (ν ₂)	A _{1g} (ν ₁)
1.9	177.5	ABSENT	359.5
2.4	179.5		360.5
8.6	183.5		365.5
15.9	185		369
17.8	187.5		371
22.0	190.5		374.5
23.8	191.5		376.5
28.8	195.5		381.0
33.1	196.5		382.0

TABLE 5.7

Values of $\frac{dw}{dT}_p$ and $\frac{dw}{dP}_T$ for K_2PtCl_6 and K_2ReCl_6 , together with standard errors, compressibilities at ambient pressure (K_2PtCl_6 calculated, K_2ReCl_6 measured).

	$\frac{dw}{dT}_p \times 10^3$	S.E. ($\times 10^3$)	$\frac{dw}{dP}_T$	S.E.	300 ($\times 10^{-3}$ kbar $^{-1}$)
<u>K_2PtCl_6</u>					
v_1	-20.6	0.4	0.78	0.02	
v_2	-15.2	0.9	0.49	0.17	
v_3	-18.0	0.2	0.81	0.06	6.3
v_4	- 7.0	0.2	0.55	0.04	
v_5	4.85	0.6	0.65	0.0	
v_L	3.4	0.7	0.7	0.05	
<u>K_2ReCl_6</u>					
v_1	- 5.03	<u>a</u>	0.75	0.02	
v_2		ABSENT			
v_3	-24.4		0.46	0.04	7.2
v_4	2.65		0.29	0.02	
v_5	14.6		0.61	0.03	
v_L	3.72		0.33	0.09	

a values for $\frac{dw}{dT}_p$ provided by R.W. Berg - no standard error data available.

Far Infrared and Raman Spectra of K_2PtCl_6

The spectra behaved normally with increase in pressure, all modes exhibiting a blue shift of varying magnitude. However the t_{2g} bend (ν_5) and the t_{1g} lattice mode both shifted to lower frequency with decrease in temperature. A similar temperature dependence was noted with the ν_4 and ν_5 fundamentals of K_2ReCl_6 .

Results of the computer anharmonicity analysis

For each vibrational mode, $\Delta w|_T$, $\Delta_T w|_P$, $\Delta_T w|_V$ were computed as discussed in the introduction. Tables 5.8 and 5.9 summarise these for K_2ReCl_6 and K_2PtCl_6 (χ calculated). Table 5.10 gives the frequency shift with temperature, and the relative contributions of Δw_T^E and Δw_T^A . It is noted that increasing the thermal strain in the system by increasing the temperature always causes a shift to lower frequency. This can be clarified; $-\Delta w|_T$ is the change in frequency on raising the pressure, at constant temperature T , to restore the volume of the crystal to that at OK. This can be seen from the tables to always be positive. By increasing the pressure, and thus restoring the volume to OK, this effectively removes the thermal expansion contribution to the mode frequency. Therefore, if removal of thermal expansion gives a positive shift, then increasing the thermal strain in a system will decrease the mode frequency. This is not an unexpected result. Another general feature of the K_2ReCl_6 sets of data is that the magnitude of the contributions of both self energy and thermal strain parameters increase with increasing temperature. This does not rigorously hold true for the K_2PtCl_6 results.

Figure 5.12

Plots of

- (a) volume/ \AA^3 versus temperature/K
- (b) volume/ \AA^3 versus pressure/kbar
- (c) compressibility ($\times 10^4 \text{ kbar}^{-1}$) versus pressure

for K_2PtCl_6 and K_2ReCl_6 . Note that these plots are obtained using values of χ calculated by the method of Mitra et al.

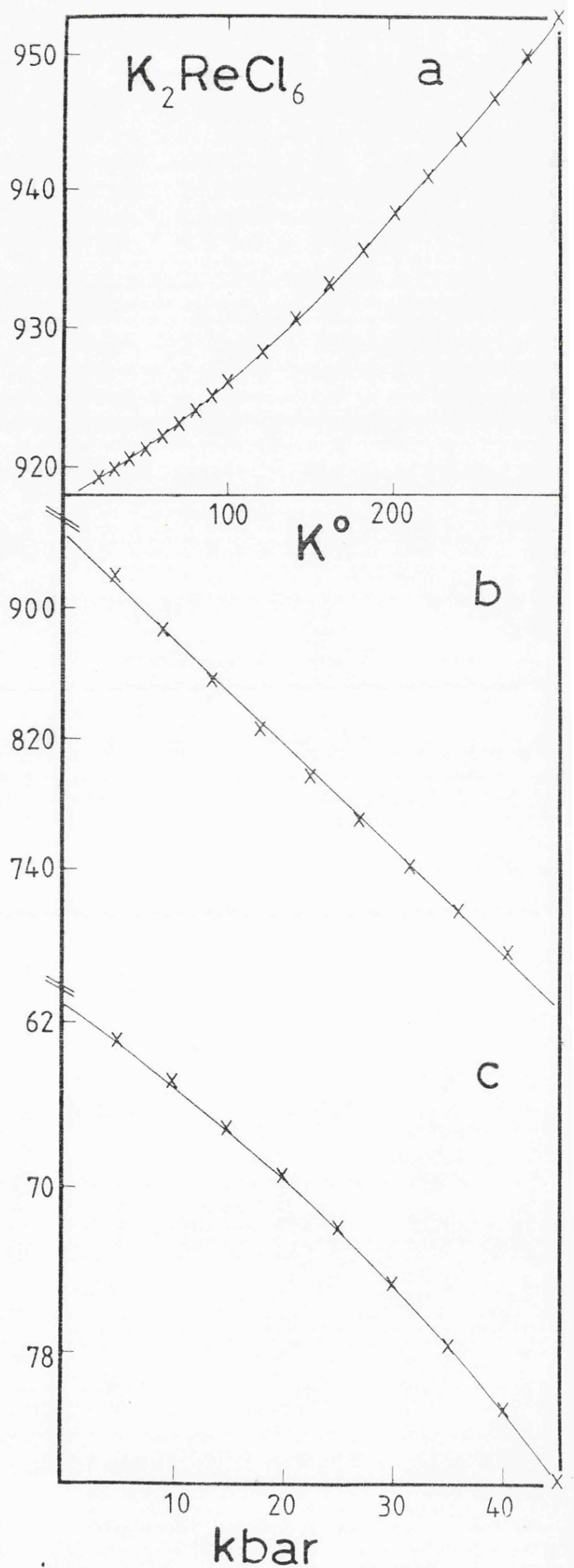
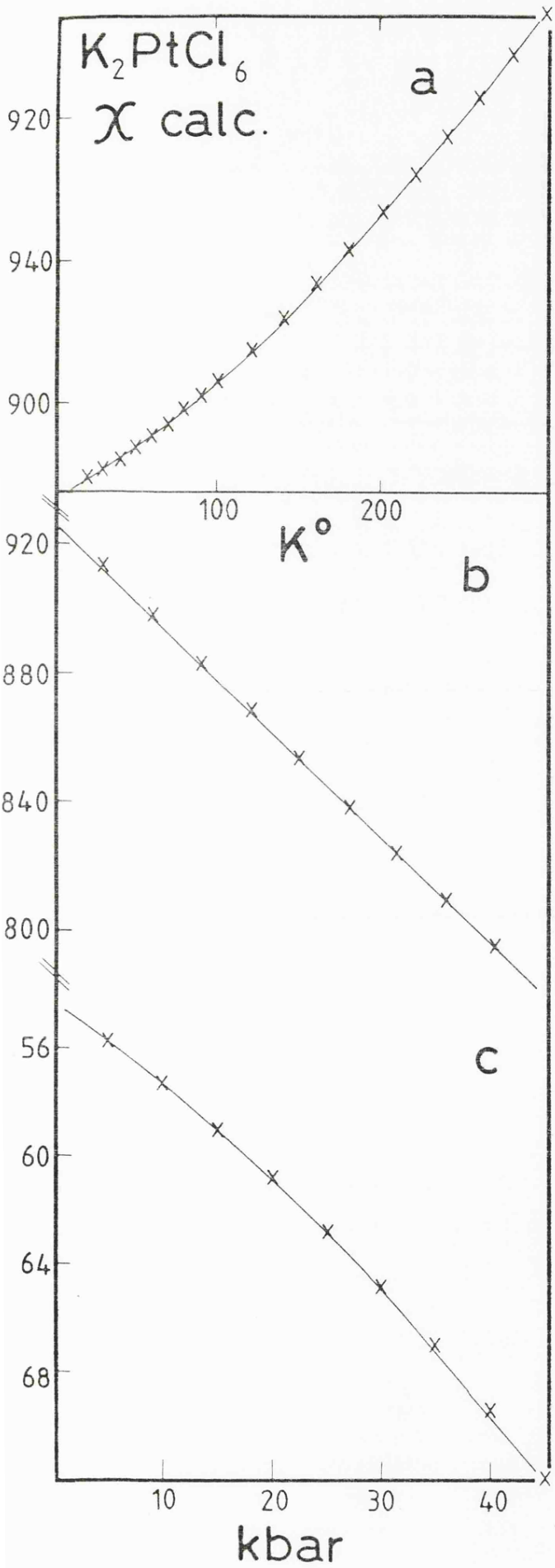


Figure 5.13

Computer analysis of the vibrational modes of
 K_2ReCl_6 .

$$(i) = \Delta W_T^A = \Delta_T W_i|_V \text{ (see equation 35)}$$

$$(ii) = - \Delta W_T^E = - \Delta W_i|_T$$

$$(iii) = \Delta W_T \text{ observed}$$

The extrapolation of i to OK (= W_O^A) is also shown.

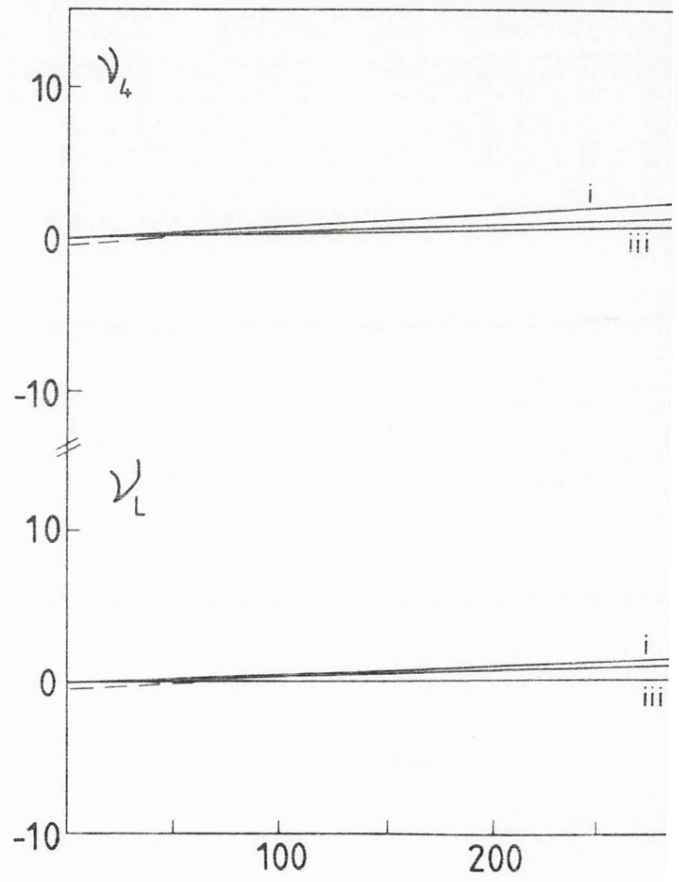
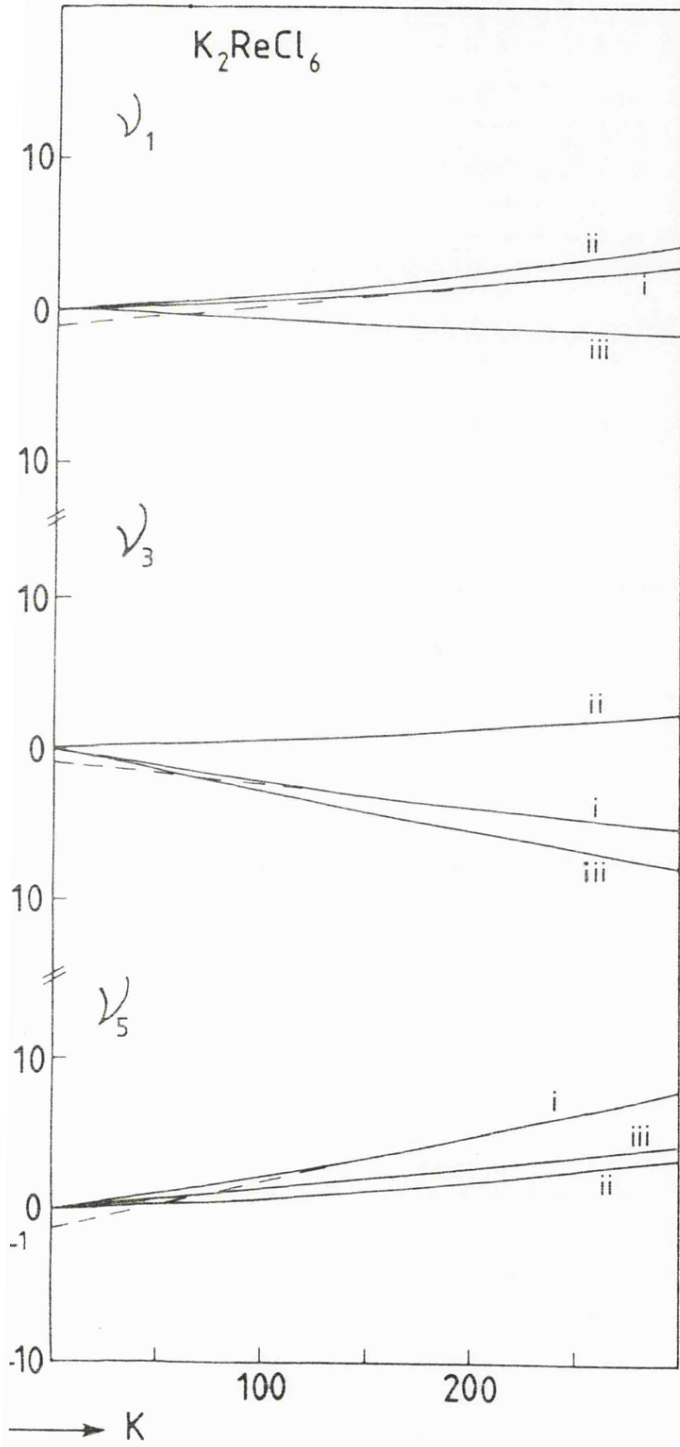


Figure 5.14

Computer analysis of the vibrational modes of

K_2PtCl_6 (χ calculated).

$$(i) = \Delta W_E^A = \Delta_T W_i|_V$$

$$(ii) = - \Delta W_T = - \Delta W_i|_T$$

$$(iii) = \Delta W_T \text{ observed}$$

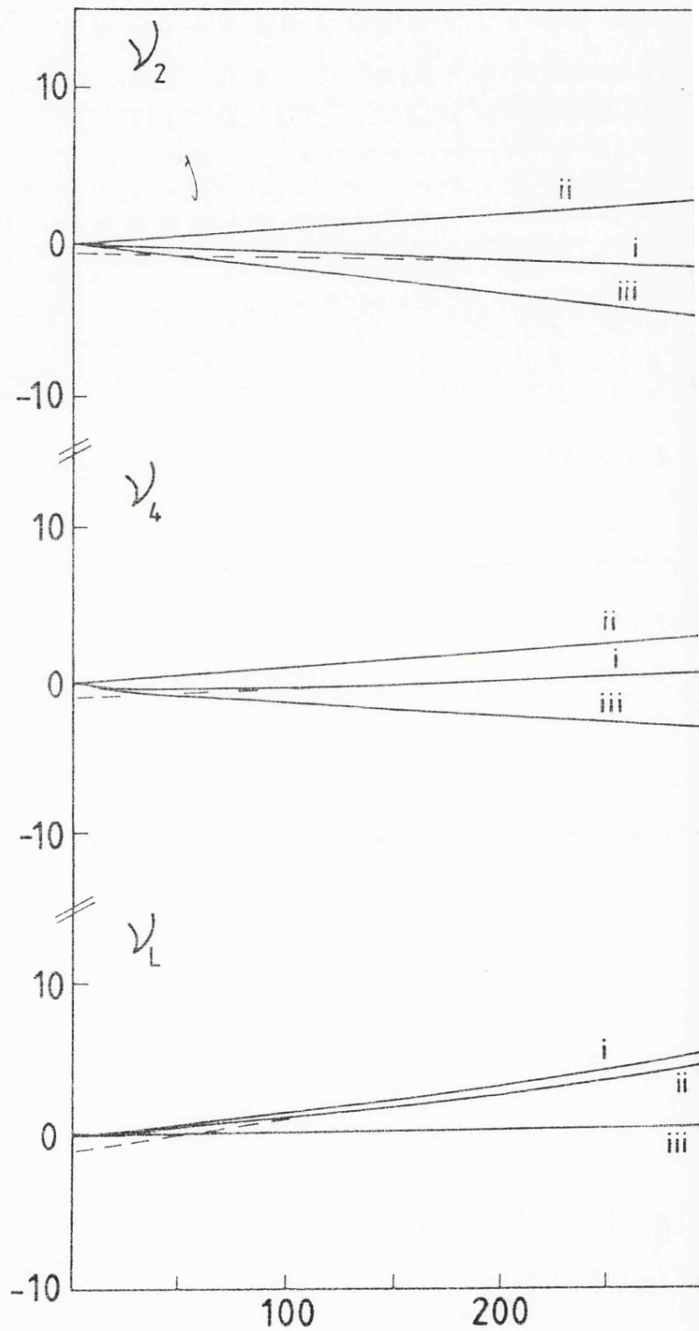
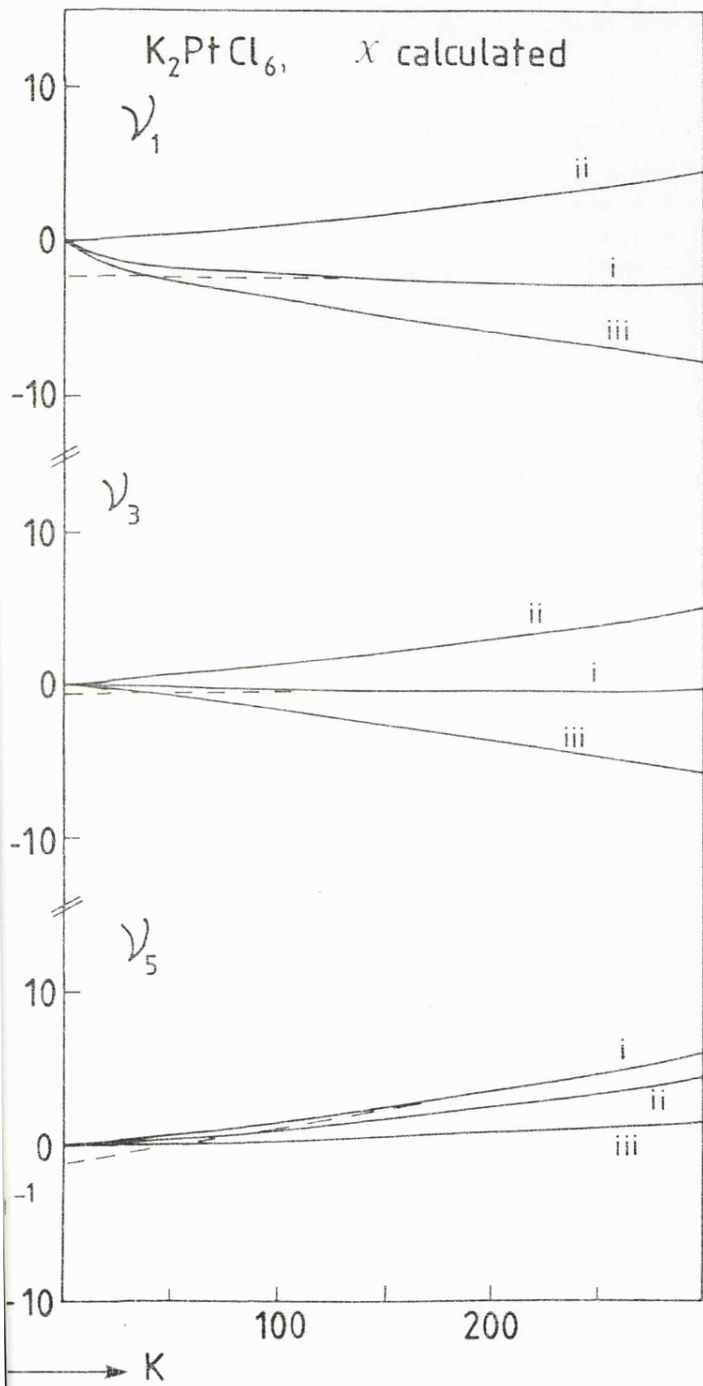


Figure 5.15

Computer analysis of the vibrational modes of

$K_2Pt_6Cl_6$ (χ measured)

$$(i) = \Delta W_T^A = \Delta_T W_i|_V$$

$$(ii) = -\Delta W_T^E = -\Delta W_i|_T$$

$$(iii) = \Delta W_T \text{ observed}$$

Note increase in thermal expansion term (ii) due to decrease in compressibility.

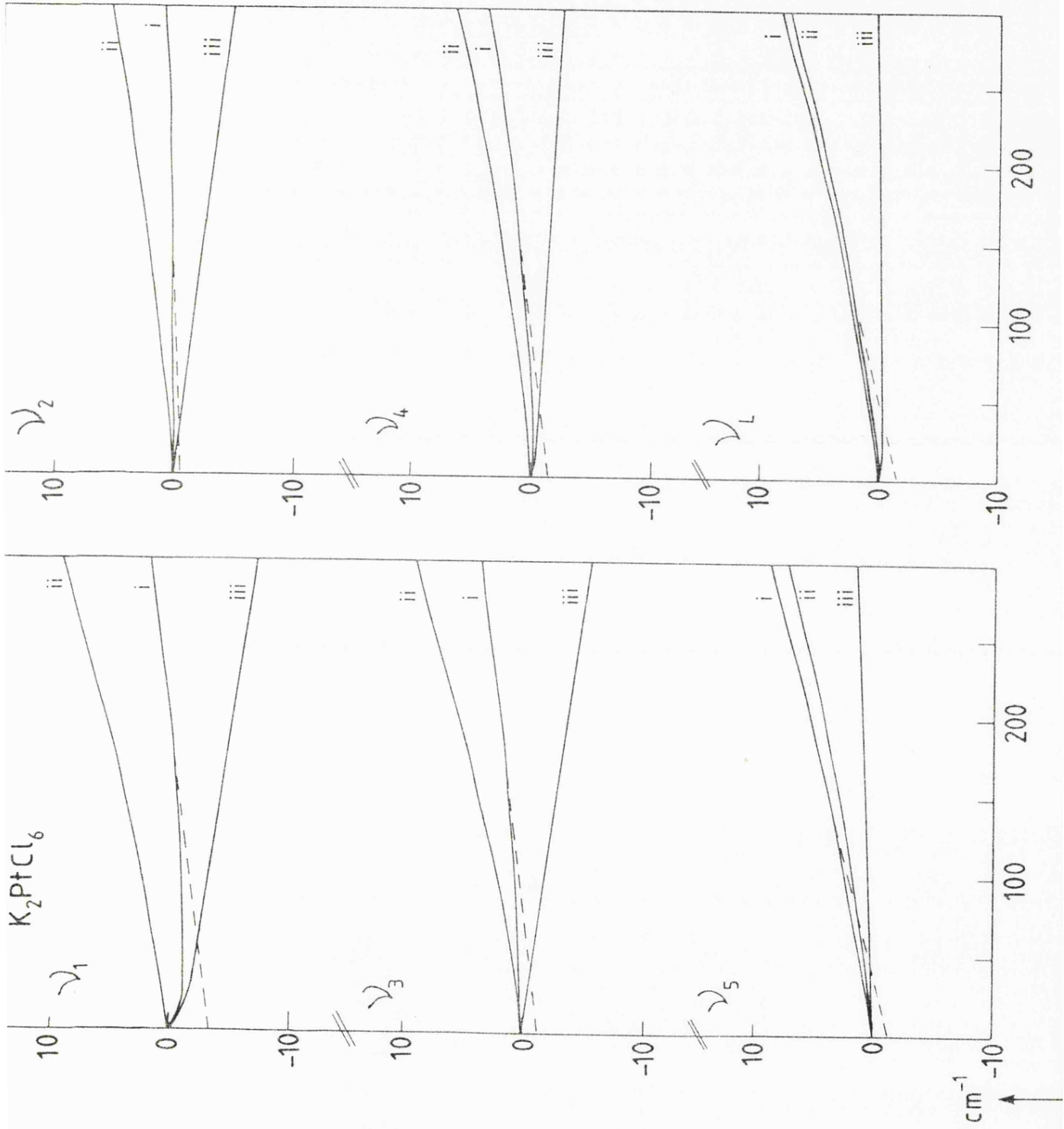


TABLE 5.8 The contributions of the self energy, $\Delta_T w|V$ and thermal strain $\Delta w|T$, to the shift in frequency with temperature $T w/p$ for K_2PtCl_6 , using the calculated compressibility in the analysis. (All in cm^{-1}).

	$\Delta_T w V$					$\Delta_T w P$					$\Delta w T$				
	60	120	180	260	300	60	120	180	260	300	60	120	180	260	300
ν_1	-1.7	-2.0	-2.2	-2.2	-1.9	-2.4	-3.6	-4.9	-6.6	-7.1	0.7	1.6	2.7	4.4	5.2
ν_2	-0.5	-0.8	-1.0	-1.1	-1.1	-0.9	-1.8	-2.7	-3.8	-4.4	0.4	1.0	1.7	2.7	3.3
ν_3	-0.1	-0.2	-0.2	0.0	0.1	-0.8	-1.9	-3.0	-4.5	-5.3	0.7	1.7	2.8	4.5	5.4
ν_4	-0.3	-0.1	0.2	0.8	1.2	-0.8	-1.2	-1.7	-2.2	-2.5	0.5	1.1	1.9	3.0	3.7
ν_5	0.9	1.9	3.2	4.9	5.9	0.3	0.6	0.9	1.3	1.5	0.6	1.3	2.3	3.6	4.4
ν_L	0.8	1.8	2.9	4.6	5.5	0.2	0.4	0.5	0.7	0.9	0.6	1.4	2.4	3.9	4.7

TABLE 5.9 The contributions of the self energy $\Delta_T^w|V$ and thermal strain $\Delta_T^w|P$ to the shift in frequency with temperature $\Delta_T^w|T$ for K_2ReCl_6 .

	$\Delta_T^w V$					$\Delta_T^w P$					$\Delta_T^w T$				
	60	120	180	260	300	60	120	180	260	300	60	120	180	260	300
ν_1	0.3	0.8	1.4	2.4	2.9	-0.3	-0.6	-0.9	-1.3	-1.5	0.6	1.4	2.3	3.7	4.4
ν_2							A B S E N T								
ν_3	-1.3	-2.3	-3.2	-4.4	-4.8	-1.7	-3.1	-4.6	-6.6	-7.5	0.4	0.8	1.4	2.2	2.7
ν_4	0.5	1.0	1.5	2.3	2.7	0.3	0.5	0.6	0.9	1.0	0.2	0.5	0.9	1.4	1.7
ν_5	1.4	2.9	4.4	6.8	8.0	0.9	1.8	2.6	3.8	4.4	0.5	1.1	1.8	3.0	3.6
ν_L	0.2	0.4	0.7	1.2	1.4	-0.1	-0.2	-0.3	-0.4	-0.5	0.3	0.6	1.0	1.6	1.9

From Table 5.10 it can be seen that, in general, the relative self energy contribution to the mode frequency increases as temperature decreases, which is as expected, as the thermal strain is necessarily zero at OK, but the self energy is subject to zero point fluctuations, and may have a finite value at OK.

Peercy, Samara and Morosin (22) observed that for SnI_4 , a molecular crystal, that the thermal dependencies of the external modes were dominated by the volume (strain) term. This is at variance with results observed for K_2PtCl_6 , but in agreement with those for K_2ReCl_6 . This discrepancy may be due to the unusual temperature dependence of the K_2PtCl_6 lattice mode, although Peercy, et al, found an order of magnitude difference, which has not been observed in K_2ReCl_6 .

Tables 5.11, 12 and 13 show the quasiharmonic and pseudoharmonic contributions, with the self energy shifts resolved into $\Delta w_T^A(o,t)$ and $\Delta w_O^A(o,t)$. This is done by extrapolation of $\Delta_T w(o,t)_V$, that is the self energy shift, to OK, giving $\Delta w_O^A(o,t)$. This is a valid procedure provided that the self energies at OK are small, (see equation 37).

$\bar{\Delta}_o$, a term first calculated by Wong (23) given by $\frac{\Delta w_O^A}{v_o}$ where v_o is the frequency at OK of mode w ;

Using this parameter he found for dichlorobis (pyridine) zinc (II) that $\bar{\Delta}_o$ scaled in the following manner for the various modes of vibration.

$$(v = \text{stretching}, \quad \delta = \text{bending})$$

TABLE 5.10 Shift in frequency with temperature of K_2ReCl_6 and K_2PtCl_6 (X calc), together with the relative contribution of thermal strain to self energy for each shift.

	K_2ReCl_6 Δw_{TIP}				
	60	120	180	260	300
$w_T - w_O$					
$A_{19} \frac{\Delta w T}{\Delta T^w V}$	-0.3	-0.6	-0.9	-1.3	-1.5
	-2.0	-1.8	-1.6	-1.5	-1.5
E_g	A B S E N T				
$w_T - w_O$					
$T_{1u} \frac{\Delta w T}{\Delta T^w V}$	-1.7	-3.1	-4.6	-6.6	-7.5
	0.3	0.3	0.4	0.5	0.6
$w_T - w_O$					
$T_{1u} \frac{\Delta w T}{\Delta T^w V}$	0.3	0.5	0.6	0.9	1.0
	0.4	0.5	0.6	0.6	0.6
$w_T - w_O$					
$T_{2g} \frac{\Delta w T}{\Delta T^w V}$	0.9	1.8	2.6	3.8	4.4
	0.4	0.4	0.4	0.4	0.5
$w_T - w_O$					
$T_{1u} \frac{\Delta w T}{\Delta T^w V}$	0.1	0.2	-0.3	-0.4	-0.5
	-1.3	-1.3	-1.3	-1.3	-1.4

	K_2PtCl_6 Δw_{TIP}				
	60	120	180	260	300
$w_T - w_O$					
$A_{19} \frac{\Delta w T}{\Delta T^w V}$	-2.4	-3.6	-4.9	-6.6	-7.1
	0.4	0.8	1.2	2	2.7
E_g					
$w_T - w_O$					
$T_{1u} \frac{\Delta w T}{\Delta T^w V}$	-0.9	-1.8	-2.7	-3.8	-4.4
	0.8	1.3	1.7	2.5	3.0
$w_T - w_O$					
$T_{1u} \frac{\Delta w T}{\Delta T^w V}$	-0.8	-1.9	-3.0	-4.5	-5.3
	7.0	8.5	12.0		-54.0
$w_T - w_O$					
$T_{1u} \frac{\Delta w T}{\Delta T^w V}$	-0.8	-1.2	-1.7	-2.2	-2.5
	1.6	11.0	-9.5	-3.8	-3.1
$w_T - w_O$					
$T_{2g} \frac{\Delta w T}{\Delta T^w V}$	0.3	0.6	0.9	1.3	1.5
	0.7	0.7	0.7	0.7	0.7
$w_T - w_O$					
$T_{1u} \frac{\Delta w T}{\Delta T^w V}$	-0.2	0.0	0.1	0.4	0.5
	-0.7	1.0	1.0	0.9	0.9

TABLE 5.11

The contribution of the self energy to the shift in mode frequency in K_2ReCl_6 split into the zero temperature contribution, and the temperature dependent part, together with ν_0 and $\bar{\Delta}_0$.

	ν_0	Δw_0^A	$\bar{\Delta}_0$ ($\times 10^2$)	Δw_T^A					Δw_T^E				
				60	120	180	260	300	60	120	180	260	300
ν_1	356.0	0.9	0.2	-0.6	-0.1	0.5	1.5	2.0	-0.9	-2.0	-3.2	-3.7	-4.4
ν_2				A B S E N T									
ν_3	322.5	-0.8	0.2	-0.5	-1.5	-2.4	-3.6	-4.0	-0.4	-0.8	-1.4	-2.2	-2.7
ν_4	176.0	-0.2	0.1	0.7	1.2	1.7	2.5	2.9	-0.2	-0.5	-0.9	-1.4	-1.7
ν_5	171.0	-0.7	0.4	1.4	2.9	4.5	6.7	7.9	-0.5	-1.1	-1.8	-3.0	-3.6
ν_L	86.5	-0.4	0.4	0.6	0.8	1.1	1.6	1.8	-0.3	-0.6	-1.0	-1.6	-1.9

TABLE 5.12 The contribution of the self energy to the shift in mode frequency of K_2PtCl_6 (\times calculated), split into the zero temperature contribution, and the temperature dependent part, together with ν_0 and $\bar{\Delta}_0$.

	ν_0	$\Delta_{w_0}^A$	$\bar{\Delta}_0 (\times 10^2)$	$\Delta_{w_T}^A$					$\Delta_{w_T}^E$					
				60	120	180	260	300	60	120	180	260	300	
ν_1	358.4	-2.5	0.7	0.8	0.5	0.3	0.3	0.6	0.6	-0.7	-1.6	-2.7	-4.4	-5.2
ν_2	326.1	-0.7	0.2	-0.2	-0.1	-0.3	-0.4	-0.5	-0.4	-0.4	-1.0	-1.7	-2.7	-3.3
ν_3	350.4	-0.5	0.1	-0.6	-0.7	-0.7	-0.5	-0.4	-0.4	-0.7	-1.7	-2.8	-4.5	-5.4
ν_4	189.3	-1.1	0.6	0.8	1.0	1.3	1.9	2.2	-0.5	-0.5	-1.1	-1.9	-3.1	-3.7
ν_5	172.9	-0.9	0.5	1.8	2.9	4.1	5.8	6.8	-0.6	-0.6	-1.3	-2.9	-3.6	-4.4
ν_L	870	-0.9	1.0	1.7	2.7	3.9	5.6	6.4	-0.6	-0.6	-1.4	-2.4	-3.9	-4.7

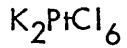
TABLE 5.13

The contribution of the self energy to the shift in mode frequency of K_2PtCl_6 (χ measured) split into the zero temperature contribution, and the temperature dependent part, together with ν_0 and $\bar{\Delta}_0$.

	ν_0	Δw_0^A	$\bar{\Delta}_0 (\times 10^2)$	Δw_T^A					Δw_T^E				
				60	120	180	260	300	60	120	180	260	300
ν_1	358.4	-3.3	0.1	2.1	2.4	3.0	4.1	5.1	-1.2	-2.8	-4.6	-7.4	-8.9
ν_2	326.1	-1.1	0.3	1.0	1.0	1.3	1.9	2.3	-0.8	-1.7	-2.9	-4.6	-5.6
ν_3	350.4	-1.3	0.4	1.8	2.3	3.1	4.5	5.3	-1.3	-2.9	-4.8	-7.7	-9.3
ν_4	189.3	-1.6	0.9	1.6	2.3	3.1	4.6	5.3	-0.8	-1.9	-3.2	-5.2	-6.2
ν_5	172.9	-1.5	0.9	2.8	3.4	5.2	9.0	10.4	-1.0	-2.3	-3.8	-6.2	-7.4
ν_L	87.5	-2.0	2.0	1.3	2.8	4.7		10.9	-1.1	-2.5	-4.1	-6.6	-8.0

$$\nu_{\text{lattice}} \approx \delta_{\text{lattice}} > \nu_{\text{Zn-N}} > \nu_{\text{Zn-Cl}} > \delta_{\text{N-Zn-N}}$$

If this parameter is calculated for K_2PtCl_6 and K_2ReCl_6 we obtain;



$$\nu_{\text{lattice}} > \nu_1 (\text{A}_{1g}) > \nu_4 (\text{T}_{1u}) > \nu_5 (\text{T}_{2g}) > \nu_2 (\text{E}_g) > \nu_3 (\text{T}_{1u})$$



$$\nu_{\text{lattice}} = \nu_5 > \nu_1 = \nu_3 > \nu_4$$

This agrees with Wong's observation that $\bar{\Delta}_0$ is largest for ν_L (or equally large for ν_L and ν_5 of K_2ReCl_6) but no other correlation appears obvious.

Lowndes (8) has studied the effect of anharmonicity in alkali halides, and has obtained both experimental values for the parameters involved, and has calculated these same parameters. This he achieves by the use of temperature dependent-time ordered Green's functions, which describe anharmonic interactions between normal modes of vibration, and have been described in detail by Maradudin and Fein (5) and by Cowley (6). These functions are capable of evaluating both the real and the complex part of the pseudoharmonic frequencies of an anharmonic crystal. The studies evaluate the following parameters; $\Delta w^E(o,t)$ $\Delta \frac{A}{T}(o,t,w_t)$, $\Gamma(o,t,w_t)$: a further parameter $\Delta \frac{A}{T}(o,t,o)$ is obtained but not explained. It is believed that this parameter enables the temperature dependent self energy contribution of the frequency shift of a mode to be resolved into two parts; a frequency dependent part, evaluable at w_t , and a zero frequency part, evaluated

by suitable studies of ϵ_0 , the dielectric constant of the material at zero frequency. The frequency dependence of the self energy is believed to occur due to the asymmetry of the potential function describing an anharmonic system. That is, in the harmonic approximation a quadratic function is used to describe the system, which is symmetrical about the zero displacement term. The "average position" is therefore independent of frequency; when cubic and quartic terms are introduced, the function is no longer symmetric, and the "average position" is dependent upon the potential energy of a mode, that is, the frequency of a mode.

As stated previously, $\Delta^A(o,t,w)$ can be resolved into two parts

$$\Delta^A(o,t,w) = \Delta^A(o,t) + \bar{\Delta}^A(o,t,w) \quad \dots 42$$

where:-

$$\Delta^A(o,t,w) = \Delta w_T^A$$

$$\Delta^A(o,t) = \Delta^{(4)}(o,t) + \Delta^{(8)}(o,t)$$

$$\bar{\Delta}^A(o,t,w) = \Delta^{(6)}(o,t,w) + \Delta^{(8)}(o,t,w)$$

where $\Delta^{(4)}$, $\Delta^{(8)}$ indicate first and second order quartic anharmonicity, and $\Delta^{(6)}$ is second order cubic anharmonicity.

A summary of Lowndes findings may be of value in the subsequent consideration of K_2PtCl_6 .

- i) $\Delta_o^A(o,t,w)$ are small, ca. a few per cent of $w_{oo}(o,t)$.
- ii) In general $\Delta_T^A(o,t,w)$ are negative at all temperatures, becoming larger in magnitude as the temperature increases. The exception to

this is the value obtained for $\Delta_5^A(o,t,w)$ for KF, which is positive, possibly an indication of the dominance of the first order quartic term, which is positive. (The second order quartic term always appears negative.)

- iii) The increasing magnitude and sign of $\Delta_T^A(o,t,w)$ are as expected from calculated values, due to the dominance of the second order quartic and cubic terms at higher temperatures.
- iv) The self energies have, in general, smaller temperature dependencies than the thermal strain terms.

The thermal expansion terms show well defined trends as the alkali metal is varied, or the halide is varied. Changing the alkali metal $K \rightarrow Na \rightarrow Rb \rightarrow Cs$ has little effect at low temperatures, but at 300K gives a marked ordering; $\Delta_{300}^E Li^+ > Na^+ > K^+ > Rb^+$; similarly at 300K, variation of the halides give; $\Delta_{300}^E F^- \gg Cl^- > Br^- > I^-$. The variation of $\Delta_T^A(o,t,w)$ shows less clear trends when alkali metals or halogens are varied.

The calculation of the various parameters appears to indicate that the approximation used is more successful at predicting thermal strain behaviour than self energy shifts, the former having reasonably good correspondence between experiment and theory, but the latter showing considerable variation with the theoretical value of $\Delta_T^A(o,t,w)$ consistently more positive than the measured value but with varying orders of magnitude difference.

The errors in such a treatment as performed in this chapter need careful consideration.

The most obvious limits to the accuracy of the analysis is the use of the linear expansion coefficient for K_2OsCl_6 since although it is very close to that of K_2ReCl_6 , it is obviously not fully correct to use the same coefficient for both $ReCl_6^{2-}$ and $PtCl_6^{2-}$.

The second source of error is in the compressibility estimate. Again, whilst the calculated compressibilities are in reasonable agreement they would appear not to be fully accurate.

An inaccuracy that many workers in this area seem to disregard is that the thermal expansion coefficient changes with temperature, as does the compressibility with pressure. The computer analysis used goes some way to remedy this, i.e. fits a line of finite gradient to input volume/pressure data thus giving a compressibility which varies somewhat with pressure.

The extrapolation of $\Delta_T w_i|_V$ to OK, by which a value of Δw_o^A is obtained obviously limits the accuracy of this determination. Whilst the approximation can be shown to be valid, (7) the fitting of a suitable straight line to $\Delta_T w_i|_V$ above the Debye temperature could cause considerable variation in the value of Δw_o^A . This was performed by least squares analysis in this case, and the generated standard errors at the intercept at OK were small, the regression coefficient always being greater than 0.95.

Considering equation 35, $\Delta_T w_i |_P$ is known to better than 0.5cm^{-1} but $\Delta w_i |_T$ term involves perhaps the biggest approximation, this is that the relationships between volume, and temperature, and frequency and pressure is considered to be approximately that at temperatures between 0 and 300K, i.e. the Gruneisen parameter γ_i is assumed to be the same at 0K and 300K. Lowndes (8) considers this to be "an adequate approximation" by determination of γ_i at low temperatures. This requires the compressibility to be determined by X ray methods at low temperatures, and this is not possible with our equipment. In the light of Lowndes data the error in this is taken as less than 5%.

As previously related, Lowndes (8) split γw_T^A into frequency dependent and frequency independent parts (see equation 42), and then theoretically evaluated the first and second order quartic and cubic terms. It is shown that cubic contributions are always negative and quartic contributions may be positive or negative (dependent upon the relative size of the first and second order components).

It is not possible to divide the self energy shifts for K_2PtCl_6 and K_2ReCl_6 in this manner, however, as this requires knowledge of the harmonic frequency, and the 'Fourier Transformed anharmonic force constants' throughout the Brillouin zone.

It can be seen however that in K_2PtCl_6 and K_2ReCl_6 at high temperatures the quartic anharmonicity appears, in general, to be dominant, since values of Δw_T^A normally appear to become more positive as temperature increases. These findings are at variance with those of Lowndes (8) who finds quartic dominance to be greatest at low temperature.

Exceptions to this are ν_2 for K_2PtCl_6 , which begins positive, indicating dominance of the first order quartic term, then becomes negative as temperature is increased. This must be due either to an increase in the second order quartic term, or increase in cubic contribution, or both. It is not possible to resolve these without the data explained above.

As shown in Table 6.10 no clearly defined dominance of either self energy or thermal strain manifests itself in the total shift observed for the vibrational modes considered. This is in contrast with the results of Peercy and Samara (22) who suggest that Δw_T^E should be an order of magnitude larger than Δw_T^A , especially for lattice modes.

Gervais and co workers (24) consider, for Be_2SiO_4 , that cubic anharmonicity is prominent in internal modes, whilst both cubic and quartic terms contribute to external modes. It must be borne in mind, however, that Be_2SiO_4 is a mainly covalent lattice and their treatment may well be incorrect, as they considered the material as Be cations in an SiO_4 lattice. In CsBr, and CsCl studied by Lowndes (8) however, Δw_T^A (for the infrared lattice mode) began negative at OK and became positive, as do many of the modes of vibration of K_2PtCl_6 and K_2ReCl_6 in this study. This would appear to indicate that both cubic and quartic terms can contribute to the thermal dependence of internal and external modes of anharmonic materials.

Summary

An introduction to theoretical treatment of anharmonicity is given, and is applied to K_2PtCl_6 and K_2ReCl_6 . The results show that the pressure and temperature dependencies of such systems are not simple. The errors in such a calculation are discussed, and improved results could be obtained if accurate values of thermal expansion coefficient and compressibility were available.

To obtain the significance of these results, it would be desirable to undertake a more extensive project with A_2MX_6 compounds. A more reproducible method for compressibility and thermal expansion coefficient need be found.

References

1. For a derivation of this see Chapter 6: "The Dynamics of Atoms in Crystals" W.Cochran, 1973 Arnold.
2. Mott, N.F., Jones, H., The theory of the properties of metals and alloys. 1963 V.O.P. Oxford.
3. Becker, R., Theory of Heat. 1967 Springer Berlin.
4. Miller, A.P., Brockhouse, B.N., Can. J. Phys. 49 704 (1971).
5. Maradudin, A.A., Fein, A.E., Phys. Rev. 128 2589 (1962).
6. Cowley, R.A., Adv. Phys. 12 421 (1971).
7. Lowndes, R.P., J. Phys. C; Solid St. Phys. 4 3083 (1971).
8. Lowndes, R.P., Rastogi, A., Phys. Rev. B. 14 3598 (1976).
9. Maradudin, A.A., Phys. Stat. Solidi 2 1483 (1962).
10. Cowley, R.A., J. Phys. (Paris) 26 659 (1965).
11. Ipatova, I.P., Maradudin, A.A., Wallis, R.F., Phys. Rev. 155 882 (1967).
12. Slaggie, E.L., Phys. Rev. 2B 2230 (1970).
13. Lowdon, R., Adv. Phys. 13 423 (1964).
14. SS. Mitra in Optical Properties of Solids Ch. 14, ed S. Nudelman
SS. Mitra Plenum Press, New York (1969).

15. Wong, P.T.T., J. Chem. Phys. 66 2347 (1977).
16. Percy, P.S., Morosin, B., Samara, G.A., Phys. Rev. (B) 8 3378 (1973).
17. Willemsen, H.W., Martin, C.A., Meincke, P.P.M., Armstrong, R.L., Phys. Rev. B 16 2283 (1977).
18. Adams, D.M., Payne, S.J. *JCS Dalton* 215 (1975)
19. Thuston, R.N., Physical Acoustics Ed. W. Nason (1964).
20. Percy, P.S., Fritz, J., Samara, G.A., J. Phys. Chem. Solids 36 1105 (1975).
21. Dimitropoulos, C., et al., J. Mag., Res. 30 415 (1978).
22. Percy, P.S., Samara, G.A., Morosin, B., J. Phys Chem. Solids 36 1123 (1975).
23. Wong, P.T.T., J. Chem. Phys 63 5108 (1975).
24. Gervais, F., Piriou, B., Cabarines, F., Phys. Stat. Solidi B 55 143 (1973).

CHAPTER 6

AN INFRARED AND RAMAN STUDY OF THE PRESSURE DEPENDENCE

OF SOME COMPLEXES OF THE FORM A_2MX_6

CHAPTER 6

AN INFRARED AND RAMAN STUDY OF THE PRESSURE DEPENDENCE OF SOME COMPLEXES OF THE FORM A_2MX_6

6.1 Introduction

In Chapter 5 the changes in frequency of vibrational phonons with variations in temperature and pressure were evaluated for K_2PtCl_6 and ascribed to anharmonicity within the system. A resumé of the problem may be of value here.

If a crystal having only harmonic forces were compressed, the equilibrium positions of the atoms or units would move closer together but the force constants would remain the same, as the component atoms must be considered to be connected by ideal springs, and thus would exhibit no pressure or temperature dependence.

Anharmonic terms (cubic and quartic) must be included to the potential function to account for these, and other, manifestations of the interactions of normal modes. Thus (1)

$$U = U_0 + \frac{1}{2} \sum_{l, l'} k_{\alpha\beta}(l, l') u_{\alpha}(l) u_{\beta}(l') + \frac{1}{6} \sum_{l, l', l''} k_{\alpha\beta\gamma}(l, l', l'') u_{\alpha}(l) u_{\beta}(l') u_{\gamma}(l'') + \dots$$

where $k_{\alpha\beta}(l, l') = \frac{d^2 U}{d u_{\alpha}(l) d u_{\beta}(l')}$

and $k_{\alpha\beta\gamma}(l, l', l'') = \frac{d^3 U}{d u_{\alpha}(l) d u_{\beta}(l') d u_{\gamma}(l'')} \quad 1$

where the α cartesian component of the displacement of the l^{th} atom from its equilibrium position is given by $u_{\alpha}(l)$.

An attempt to understand these shifts in relation to the structural and geometrical changes induced by the application of a stress may be approached essentially in two manners.

First the available data may be analysed in terms of lattice dynamical theories, and then seek to understand the physical parameters causal to these effects. Secondly we may attempt to identify the operative factors by the study of a series of structurally related materials.

Clearly if suitable treatments were adopted then these two approaches should converge, but it was felt that the second view was of greater value, in giving a qualitative understanding of the factors, before involved calculations are attempted.

With a view to the above, the hexahalogen complexes A_2MX_6 (where A is group 1 metal, and M^{4+} is some transition metal) are particularly attractive. These crystallise in the antiperovskite structure (O_5^h), the components may be easily varied, and are readily available, and hence provide a suitable group for study.

6.2 Theoretical Considerations

Mode frequency $\nu_j(\underline{k})$ increases with decrease in volume, and the constant which relates this proportional increase in frequency with pressure induced decrease in volume is the Gruneisen parameter, $\gamma_j(\underline{k})$.

$$\frac{\Delta v_i}{v_i} = \gamma_i(\underline{k}) \left(\frac{-\Delta V}{V} \right)_T \quad 2$$

The isothermal compressibility of a solid χ_T , is defined as

$$\chi_T = \frac{-1}{V_T} \frac{dV}{dP}_T = \frac{d(\ln V)}{dP}_T$$

so the Gruneisen parameter can be accessed experimentally.

$$\begin{aligned} \gamma_i(\underline{k}) &= \left(\frac{-d(\ln v_i(\underline{k}))}{d \ln V} \right)_T = \frac{1}{\chi_T} \left(\frac{d(\ln v_i(\underline{k}))}{dP} \right)_T \quad 3 \\ &= \frac{1}{\chi_T v_i(\underline{k})} \left(\frac{d v_i(\underline{k})}{dP} \right)_T \end{aligned}$$

It can be seen that $\gamma_i(\underline{k})$ differs from $\frac{d(\ln v_i(\underline{k}))}{dP}_T$, the 'relative shift' $= \frac{1}{v_i(\underline{k})} \left(\frac{d v_i(\underline{k})}{dP} \right)_T$ only by a constant $\frac{1}{\chi_T}$, the

reciprocal of the isothermal compressibility. Therefore values of the relative shift can be compared directly within a material, but if we wish to compare mode shifts between materials we need values, or at least relative values, of χ_T for the compounds studied.

These data have not been published for the series under consideration.

However in a paper by Plendl (1), an attempt was made to correlate the compressibility of a material with other physical properties, and an empirical relation was derived which connected the compressibility of a non metallic solid with its cohesive energy

and molecular volume. The formula is:-

$$\chi_T = \frac{m Z N}{n} \frac{V}{U} = \frac{m Z N}{n} \frac{a_0^3}{U} \quad 4$$

where a_0 is the lattice parameter at ambient pressure, n = number of atoms per unit cell, m = number of component atoms, N = Avagadros' number, Z = the maximum valency of an atom or ion. Plendl has justified this relation by testing it against forty five crystalline compounds (binaries and ternaries), representing nine different structures.

Zallen (2) has shown, for molecular crystals (in which intermolecular forces are \gg than intramolecular ones), that far from being frequency independent, the mode Gruneisen parameter varies strongly and systematically over the optical phonon spectrum, but that the idea of a basic vibrational scaling law could be preserved in the form of a bond stiffness-bond length relation, $k \propto r^{-6\gamma}$, with k being the force constant, r the bond length and γ the 'bond scaling parameter' of order unity which is presumed to apply to both inter- and intramolecular forces. This analysis revealed in broad agreement with experiment, that the behaviour of $\gamma_i(k) \approx v_i(k)^2$. However in a recent paper Wong (3) found that for an ionic crystal (CsZnCl_4) and previously (4) for dichlorobis (pyridine) zinc (II) that the Gruneisen parameter of the normal modes were seemingly independent of mode frequencies.

Although evaluation of the Gruneisen parameter is of value in describing the consequences of anharmonicity there is no explicit recognition of anharmonicity in equation (3).

Maradudin (5) has derived general forms for pressure and temperature induced mode shifts beginning with an anharmonic potential function which are of considerable complexity but capable of simplification for some special cases. Considering a face centred cubic crystal described by the nearest neighbour central force field, experiencing a uniform external pressure, P, we have

$$\delta_i(k) = \frac{1}{v_i(k)} \left(\frac{d v_i(k)}{dP} \right)_T \propto \frac{r_0^2}{k_{\alpha\beta}^2} k_{\alpha\beta\gamma} \quad 5$$

where r_0 is the nearest neighbour interatomic distance, $k_{\alpha\beta}$ the harmonic and $k_{\alpha\beta\gamma}$ the cubic anharmonic force constant. The inverse dependence upon the quadratic force constant accords with experience, and the direct proportionality of the stress induced relative shift to cubic anharmonicity emphasises the fact that its existence is a failure of the harmonic approximation. Since the compounds studied are of antiferroite structure type, the above assumptions are not unreasonable, and the equation is taken as a good first order description of the behaviour of their normal modes.

The complex general form of Maradudin's expression for the stress induced shift of a phonon frequency includes terms in atomic displacements, being based on (1), and this pressure dependence effects the dielectric response of the material. The low frequency (Σ_0) and high frequency (Σ_∞) dielectric constants differ from each other by the sum of the oscillator strength ΣS_i of the crystal modes. The extended Lydanne Sachs Teller relation

$$\prod_i \frac{v_i(\text{LO})}{v_i(\text{TO})}^2 = \frac{\Sigma_0}{\Sigma_\infty} \quad 6$$

where ν_i (LO) and ν_i (TO) are the longitudinal and transverse optic frequencies of the i th phonon. Substituting $\Sigma_0 = \Sigma_\infty + \Sigma S_i$ we have (by the binomial expansion)

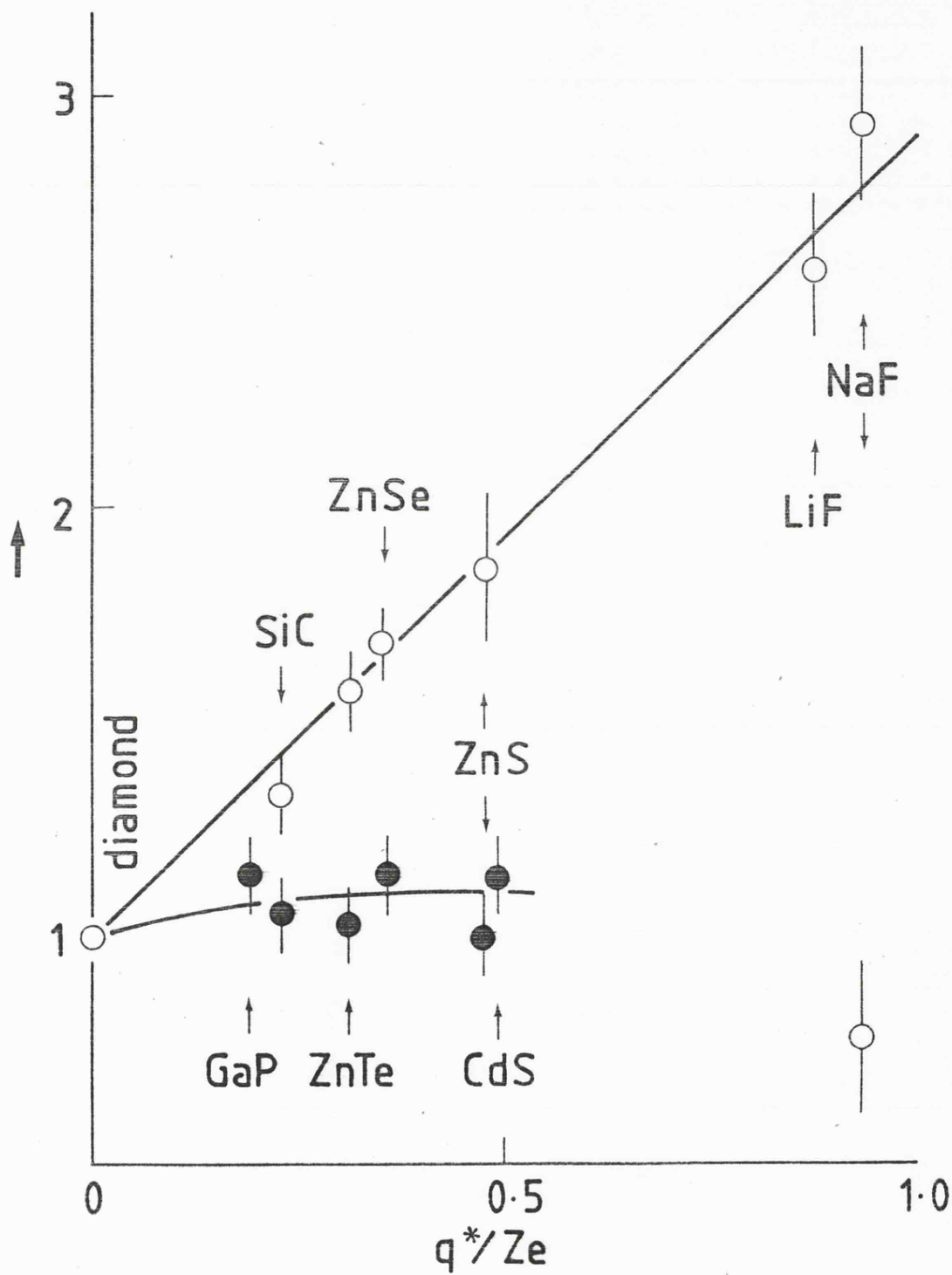
$$\prod_i \left(\frac{\nu_i(\text{LO})}{\nu_i(\text{TO})} \right)^2 = 1 + \frac{\Sigma S_i}{2 \Sigma_\infty} \quad 7$$

Since the effect of pressure is to decrease ΣS_i it follows that the right hand side of (7) will decrease. The corresponding reduction in the magnitude of the quantity on the left hand side will manifest itself in a change of the relative values of the LO and TO phonons, which will therefore be expected to shift under pressure at different rates. This has in fact been observed by Mitra (6) and co workers, who have shown that for a number of crystals with the wurtzite or zincblende structure that $\nu(\text{LO})$ is almost independent of pressure whereas $\nu(\text{TO})$ rises with increase in pressure (see Figure 6.1). There also appears to be a relationship between the ionicity of a material and the ratio of Gruneisen parameters $\gamma_{\text{TO}} / \gamma_{\text{LO}}$ which arises because the contribution of atomic displacements to Σ_0 is relatively more important in compounds of higher ionicity. With these general principles in mind we can observe and attempt to account for trends in the materials under investigation. Firstly an important point must be stressed.

All earlier work (8,9,10) on the infrared and Raman spectra of these materials was performed in a diamond anvil cell without gaskets, whereas the present data has been acquired under much more nearly hydrostatic conditions. There appear significant differences between the sets of data, in particular the shifts of the infrared active ν_3 mode of the anions were greatly underestimated in the earlier work.

Figure 6.1

Optic Mode Gruneisen parameters versus the effective charge per electron. Full circles represent LO modes, empty circles TO modes.



6.2 Experimental

Far infrared spectra were obtained from a Mark II DAC, in conjunction with an extensively modified Beckman R11C FS 620 interferometer.

The sample was contained in an Inconel gasket, 0.05mm thick, with a gasket hole of 0.4mm initial diameter, using Nujol as a pressure transmitting medium.

Pressure calibration by means of measurement of the shift in the R_1 and R_2 fluorescence bands in Ruby, were performed on a Coderg T800 Raman spectrometer, with a Spectra Physics 164 - 04 Kr^+ ion laser, using a spectral slit width of $\approx 1\text{cm}^{-1}$ ($\approx 0.003\text{nm}$), and laser power of 100mw at the source, (ca. 60mw at sample).

Nujol freezes at ca 14 kbar, thus up to this pressure the sample experiences completely hydrostatic pressure. The R_1 and R_2 lines are very sensitive to pressure gradients, both in their separation and shape, but even above the f.p. of the Nujol their separation remained constant, and their shape was relatively constant, with a slight broadening at higher pressures; therefore pressures above 13 were taken as being hydrostatic, and values of pressure are quoted as accurate to better than ± 0.5 kbar.

As each spectrum obtained as the result of six sets of data, which took ca. 3 hours to compile, it was necessary to allow the sample to equilibrate for ca. 4 hours, since it was found that the pressure in the cell slowly increased with time for the first few hours after pressure application. This was believed to be due to relaxation in the gasket thus allowing the sample to experience a slightly increased

pressure. Using a 25% beam splitter should access the spectral region of 40 - 400 cm^{-1} to the interferometer, but radiation below 100 cm^{-1} is of low intensity. In the past work on these hexahalides, gaskets were not employed, consequently this increases the aperture of the cell with respect to the present situation. Obviously this leads to increased transmission characteristics, and as a consequence of this vibrational phonons below 100 cm^{-1} were able to be observed, whereas with gasketed samples and the accompanying lower radiation port the low energy end of the spectrum was in general lost in amplifier noise, etc.

These low energy modes were, however, observable if a different beam splitter and hydrostatic medium combination were used, (i.e. 50% B/S, and Si oil instead of Nujol) and this was performed in the case of K_2PtCl_6 for the purposes of the more complete analysis presented in Chapter 5. However, the requirements for collecting a high pressure set of data for this low energy end were identical to those for the more routine region, the consequence of this being an effective doubling in the time needed to perform the experiments, and it is due to this time factor that the infrared active lattice modes were in general not observed.

High Pressure Raman experiments were carried out in a Mark III DAC, the majority of those being performed by Rolf. W. Berg, Chem. Dept. A, The Technical Univ. of Denmark, 2800 Lyngby, Denmark, with the exception of the work on K_2PtCl_6 and K_2PtBr_6 which were carried out by the author using spectral slit widths of ca. 2 cm^{-1} , and laser power (Kr^+) of 200 - 300 mW.

Figure 6.2

Far infrared spectra of K_2ReCl_6 at ambient (a) and 34.2 kbar (b),
and K_2OSCl_6 at ambient (a) and 24.1 kbar (b).

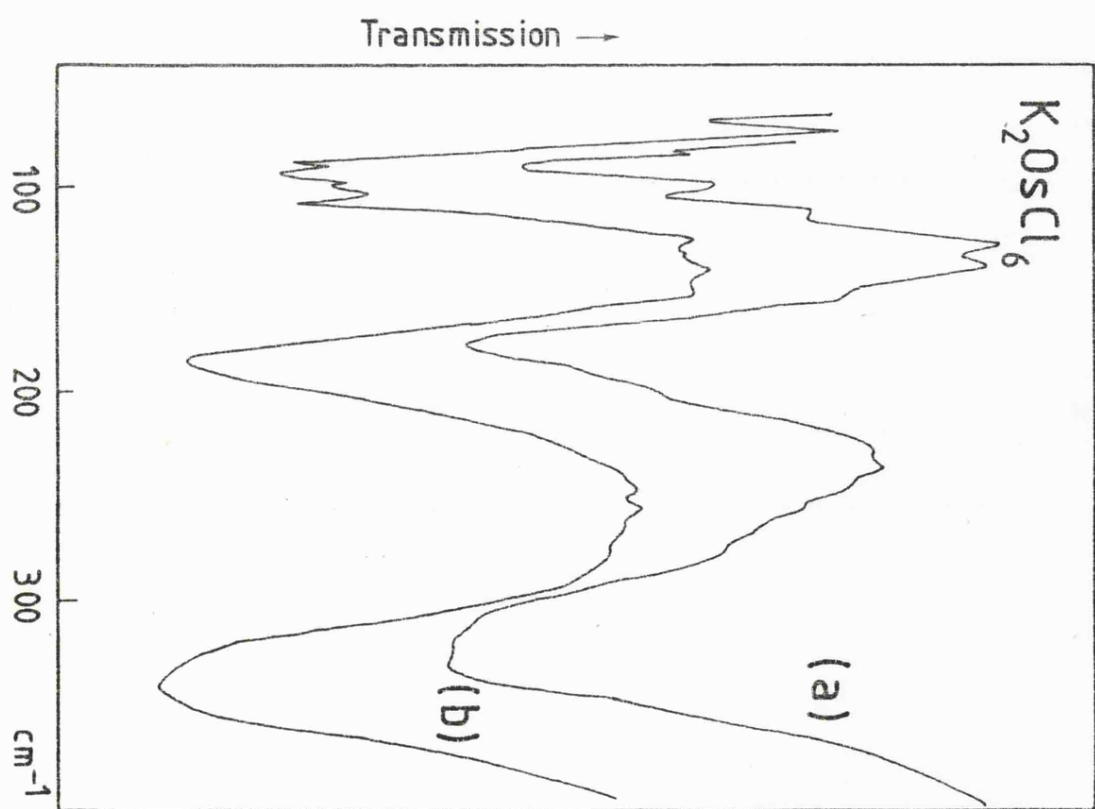
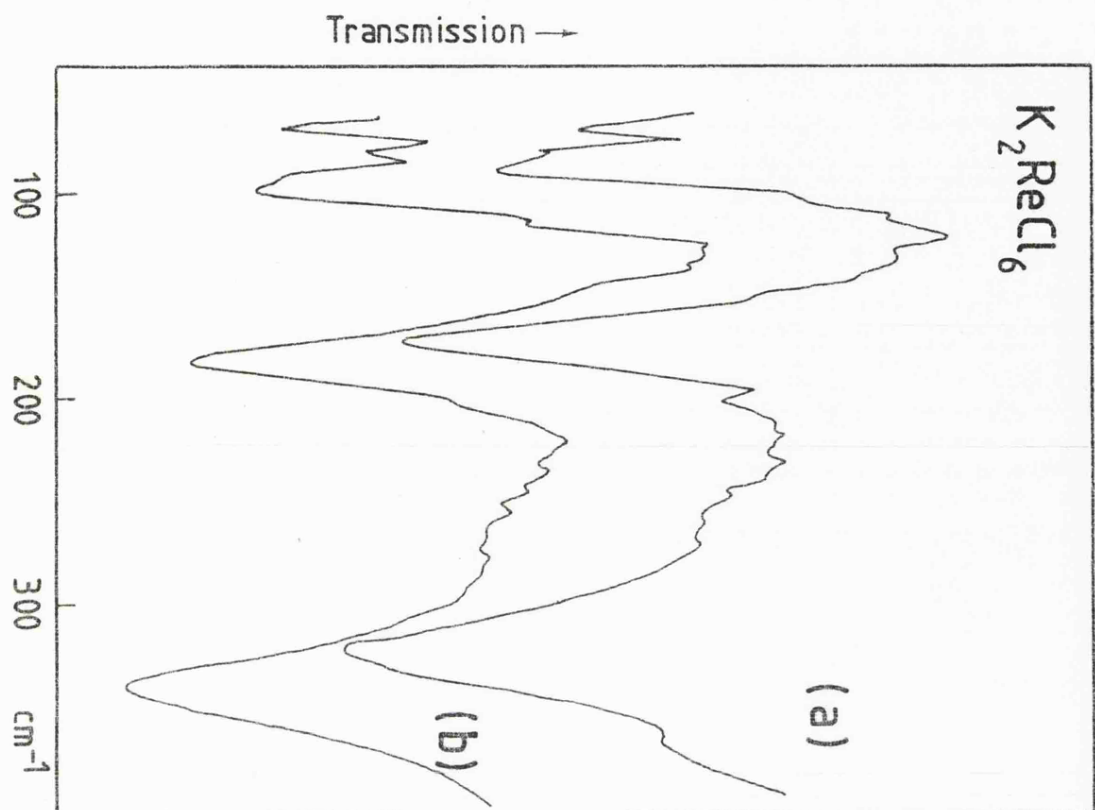


Figure 6.3

Far infrared spectra of K_2IrCl_6 at ambient (a) and 40.1 kbar (b),
and K_2PdCl_6 at ambient (a) and 34.0 kbar (b).

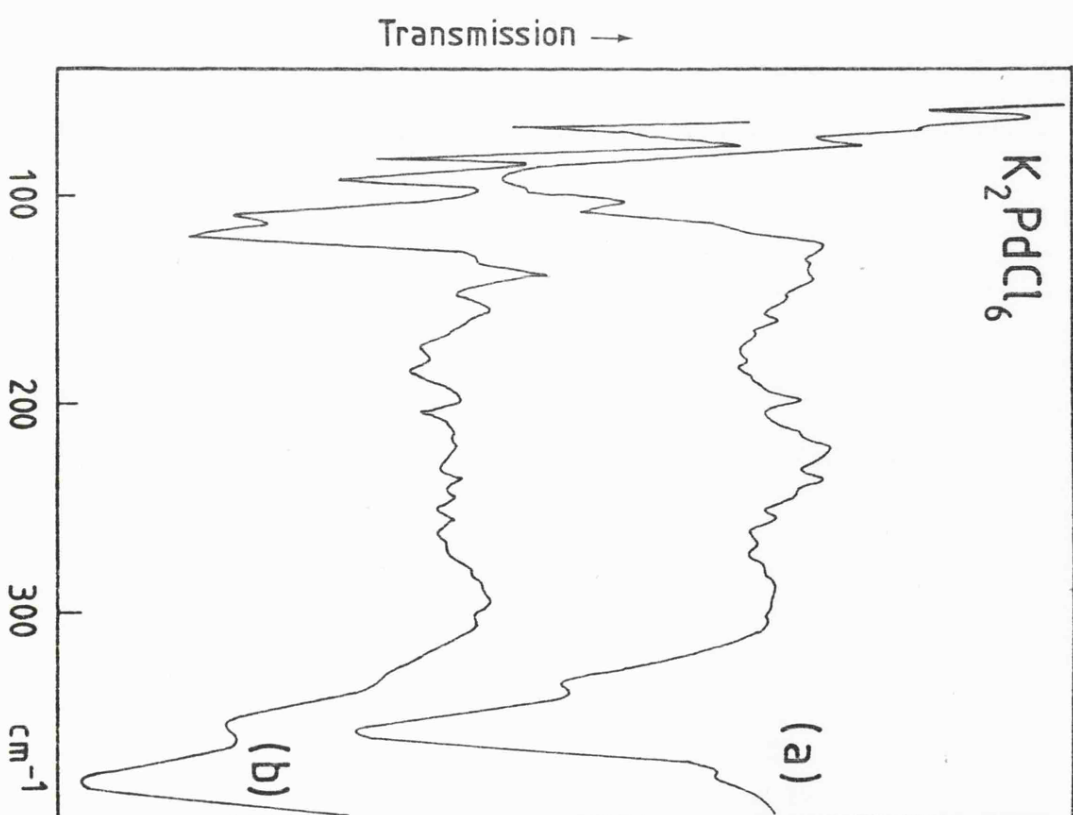
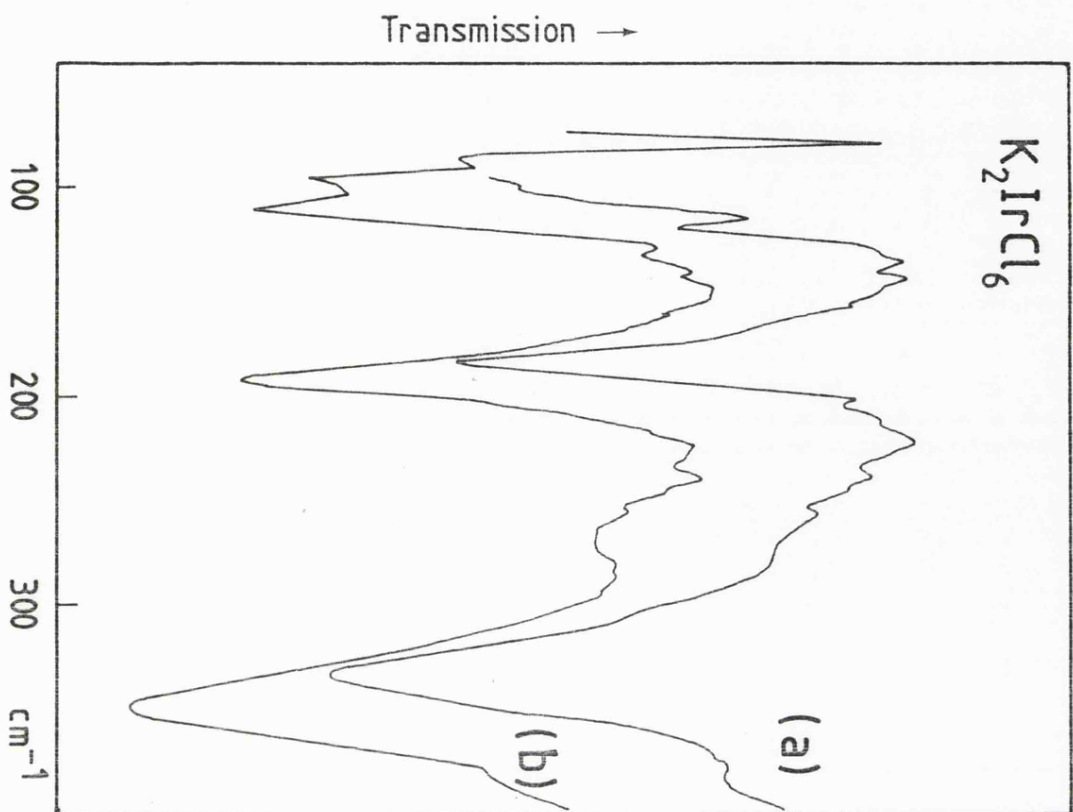


Figure 6.4

Far infrared spectra of Rb_2PtCl_6 at ambient (a) and 31.9 kbar (b),
and Cs_2PtCl_6 at ambient (a) and 30.8 kbar (b).

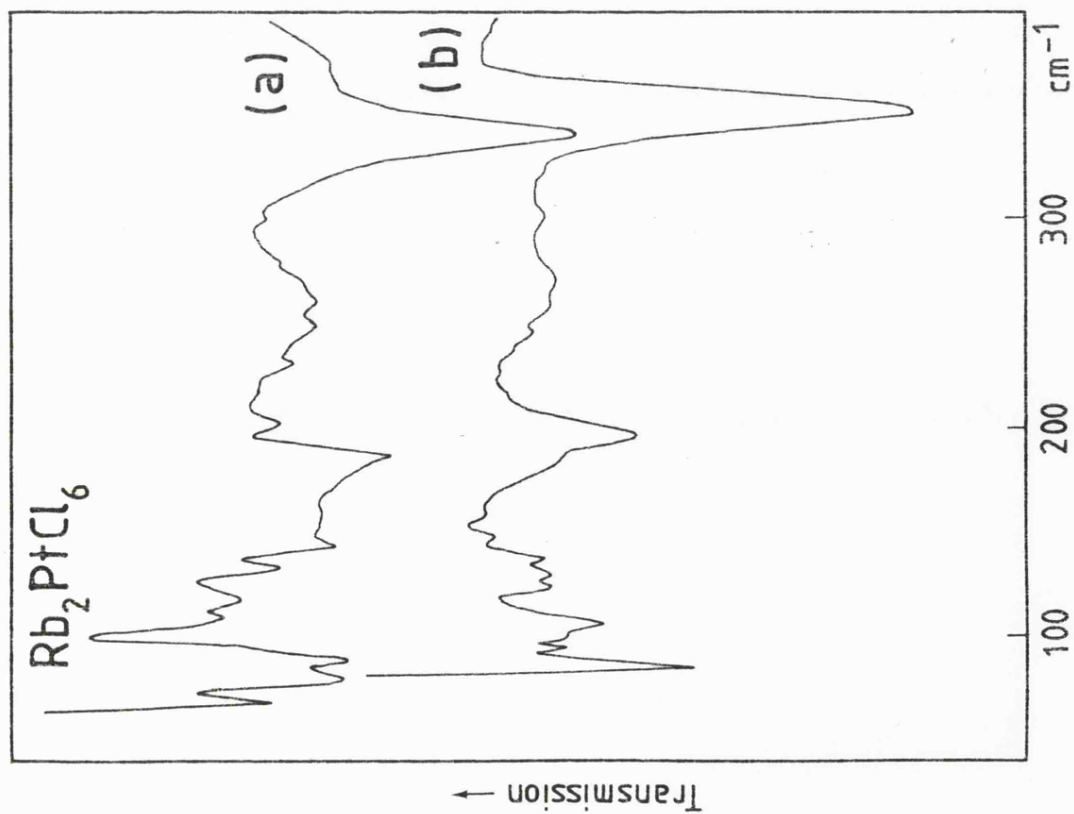
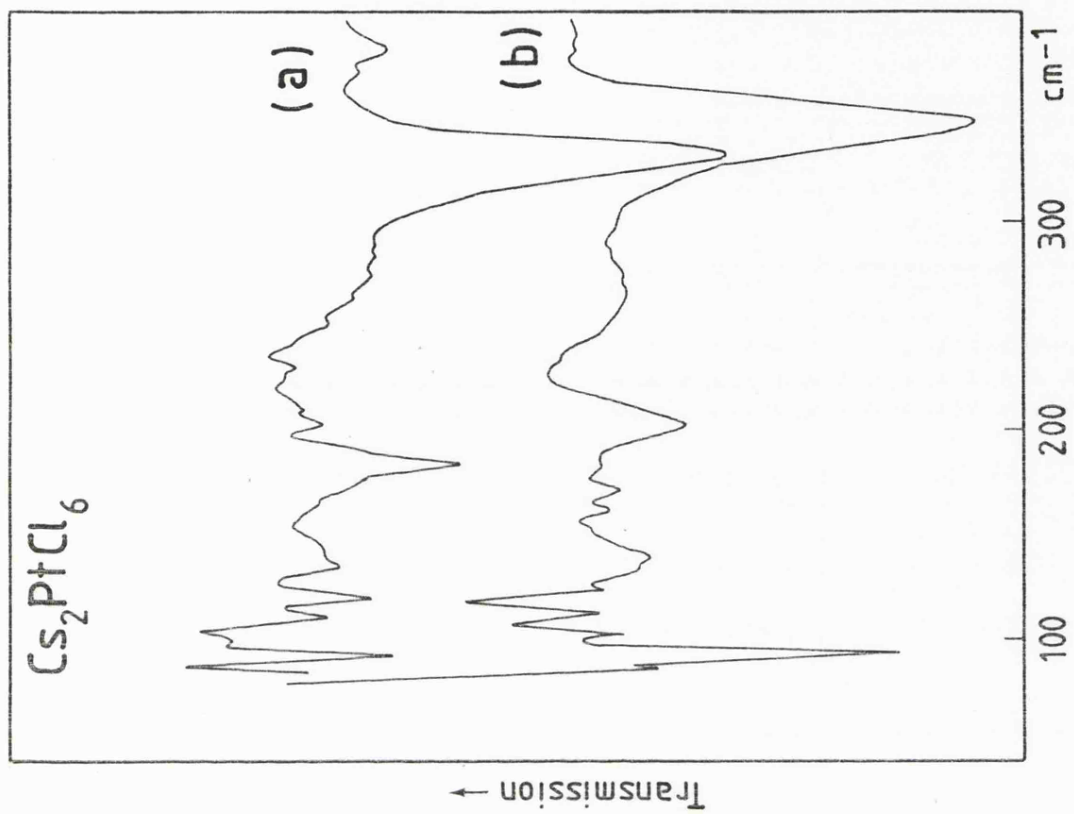


Figure 6.5

Far infrared spectra of Tl_2PtCl_6 at ambient (a) and 25.0 kbar (b),
(Tetramethylammonium) $_2$ and PtCl_6 at ambient (a) and 28.7 kbar (b).

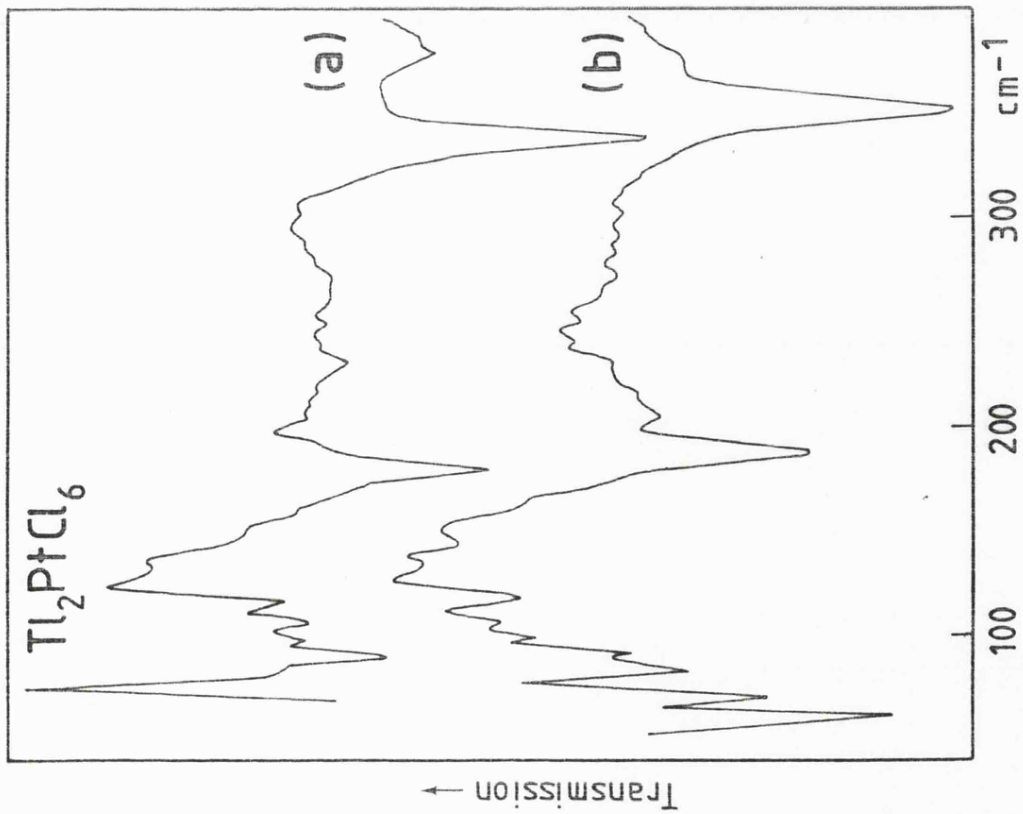
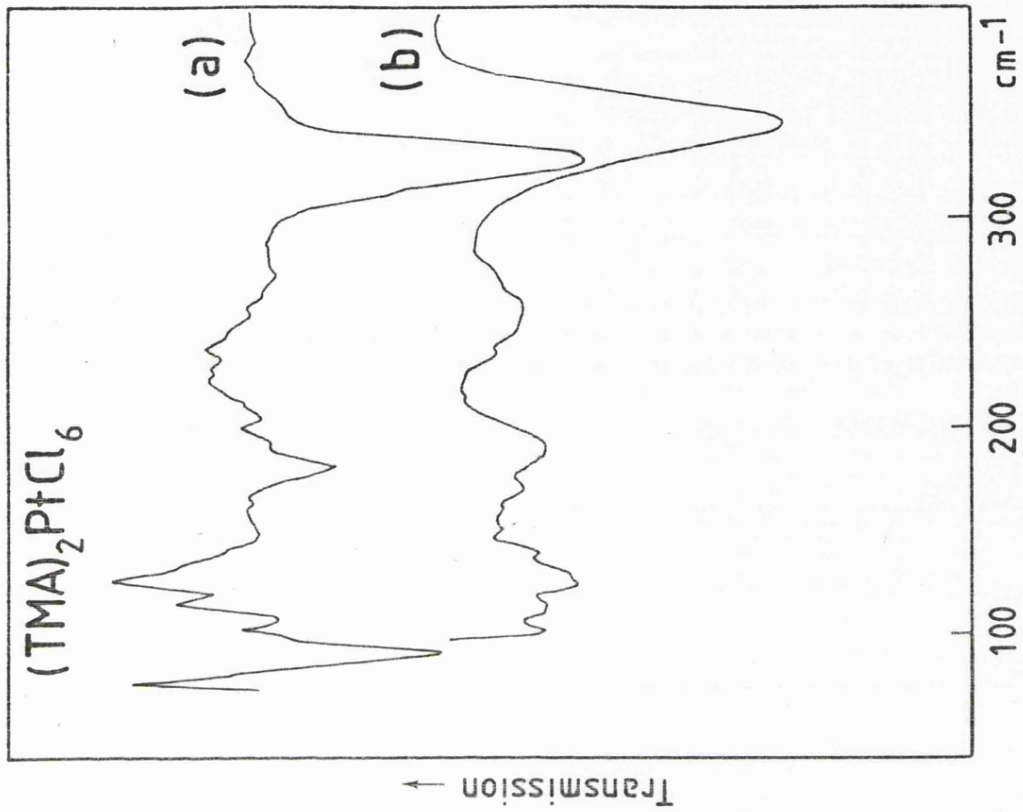


Figure 6.6

Far infrared spectra of K_2PtBr_6 at ambient (a) and 25.3 kbar (b),
and K_2SnCl_6 at ambient (a) and 23.7 kbar (b).

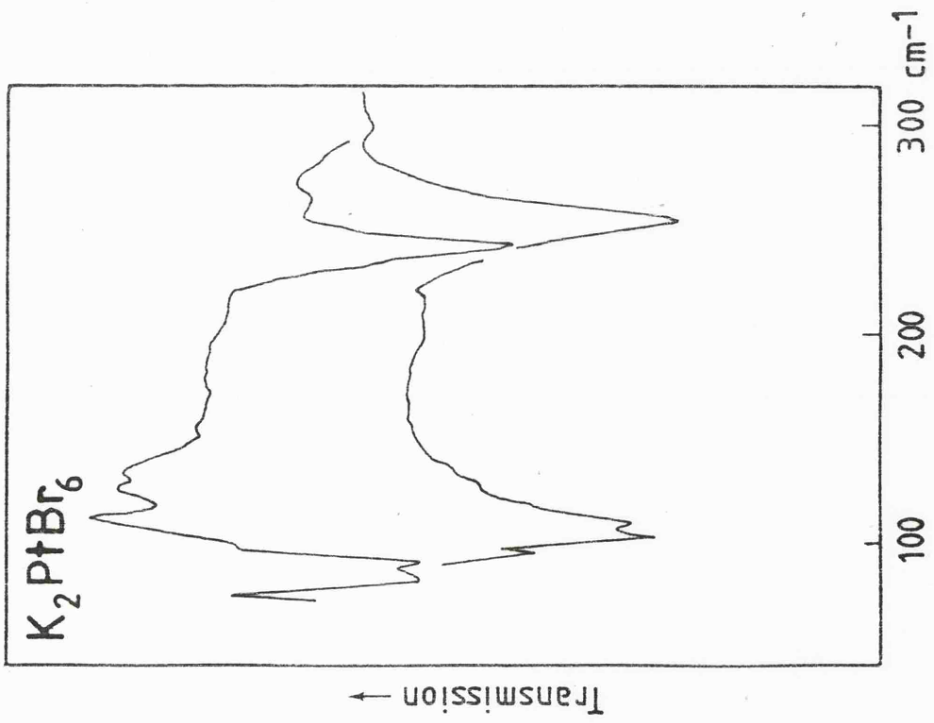
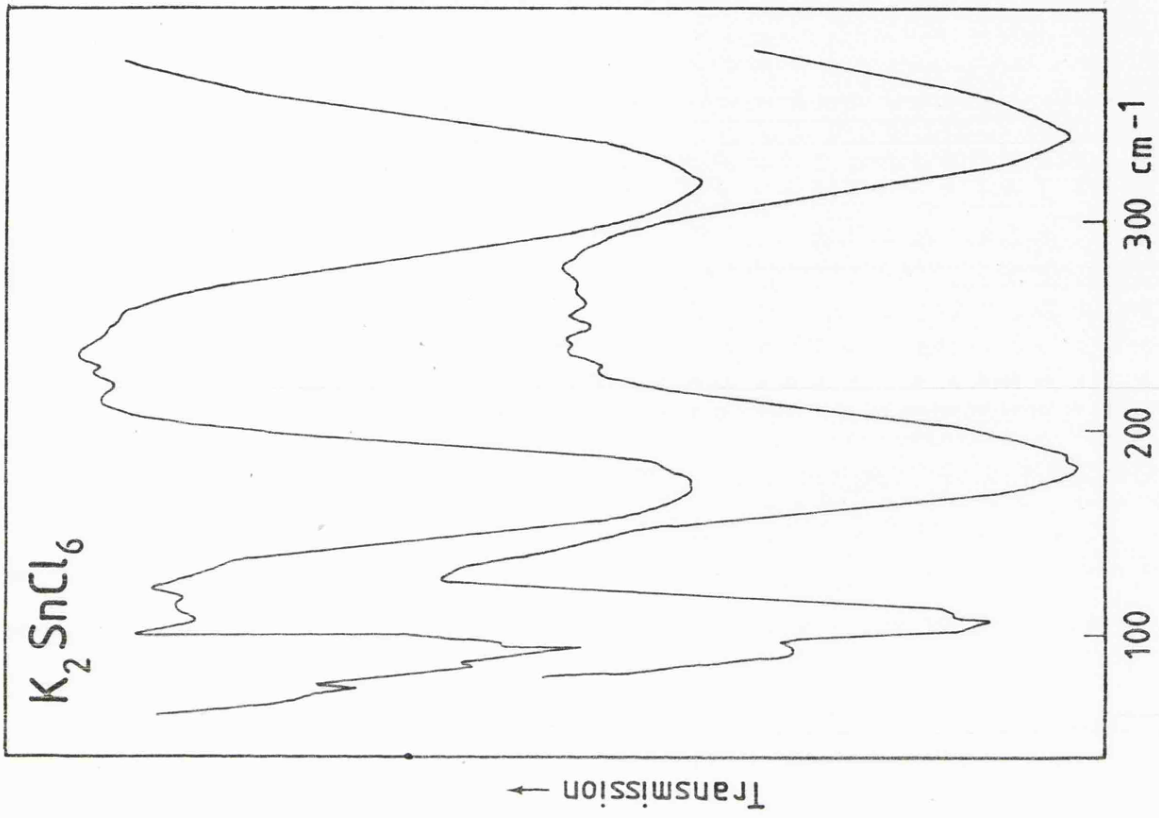


Figure 6.7

Far infrared spectra of Rb_2TeCl_6 at ambient (a) and 25.0 kbar (b)
(Tetramethylammonium) $_2$ and TeCl_6 at ambient (a) and 22.6 kbar (b).

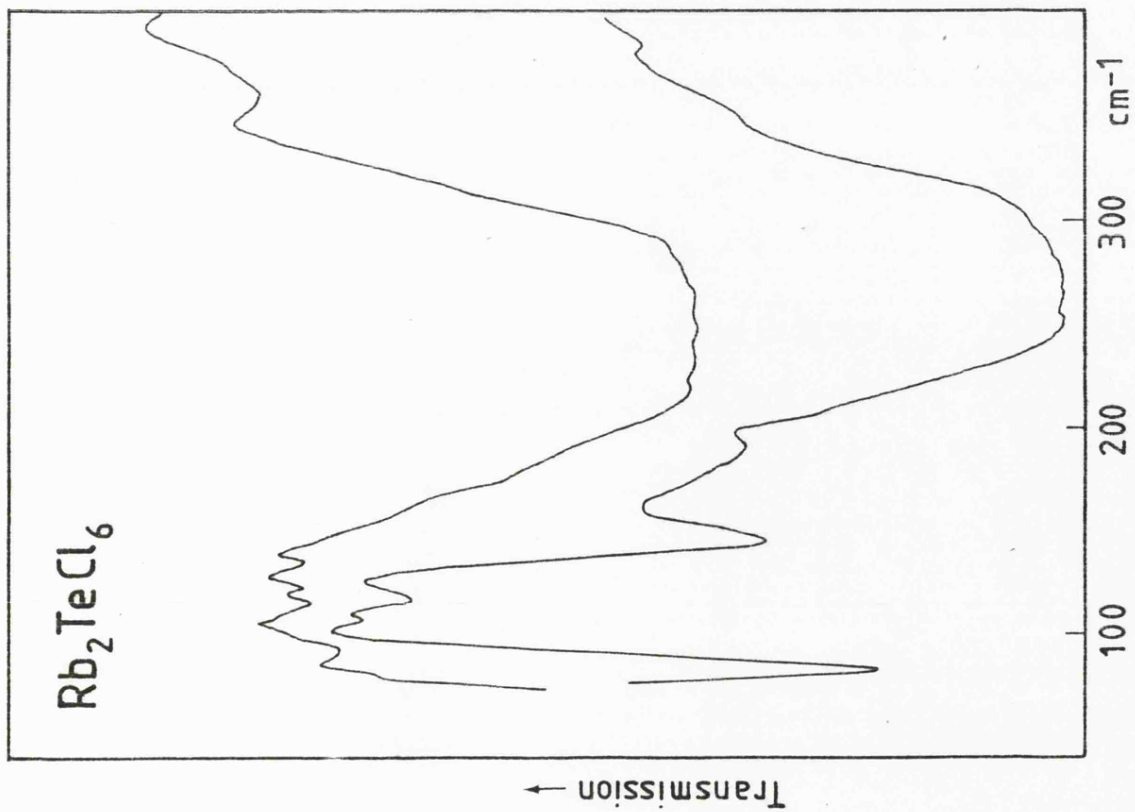
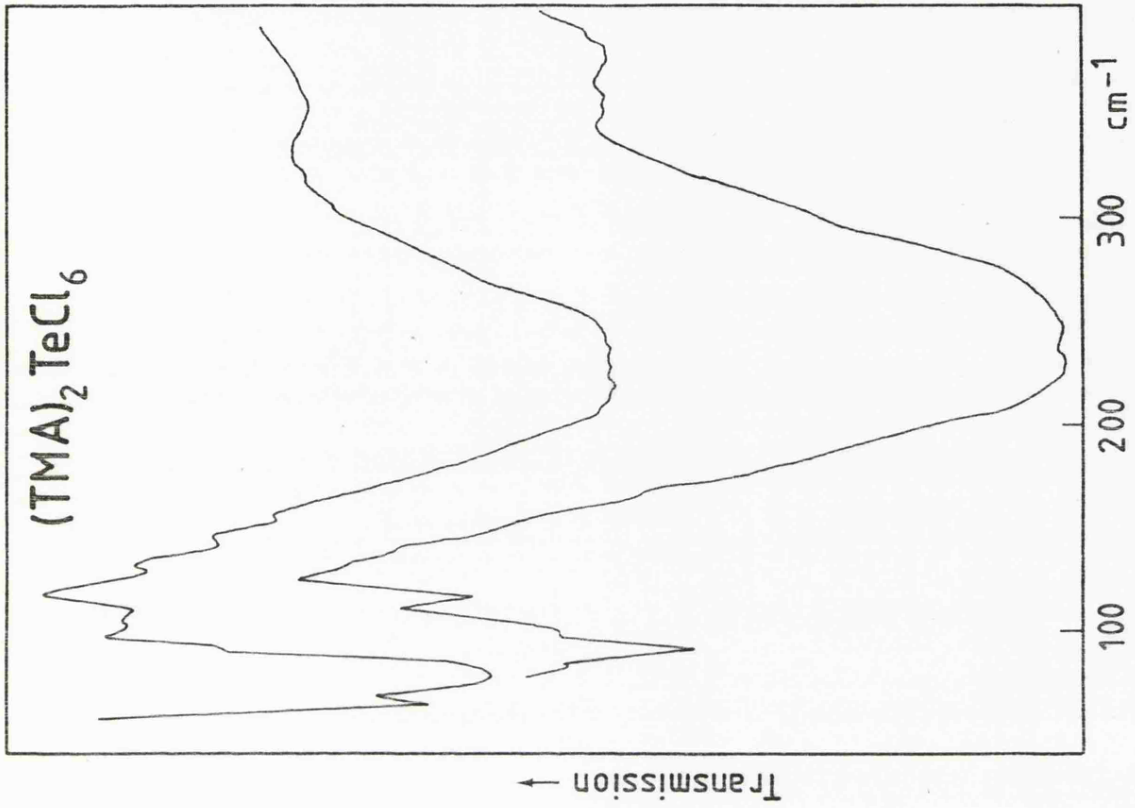
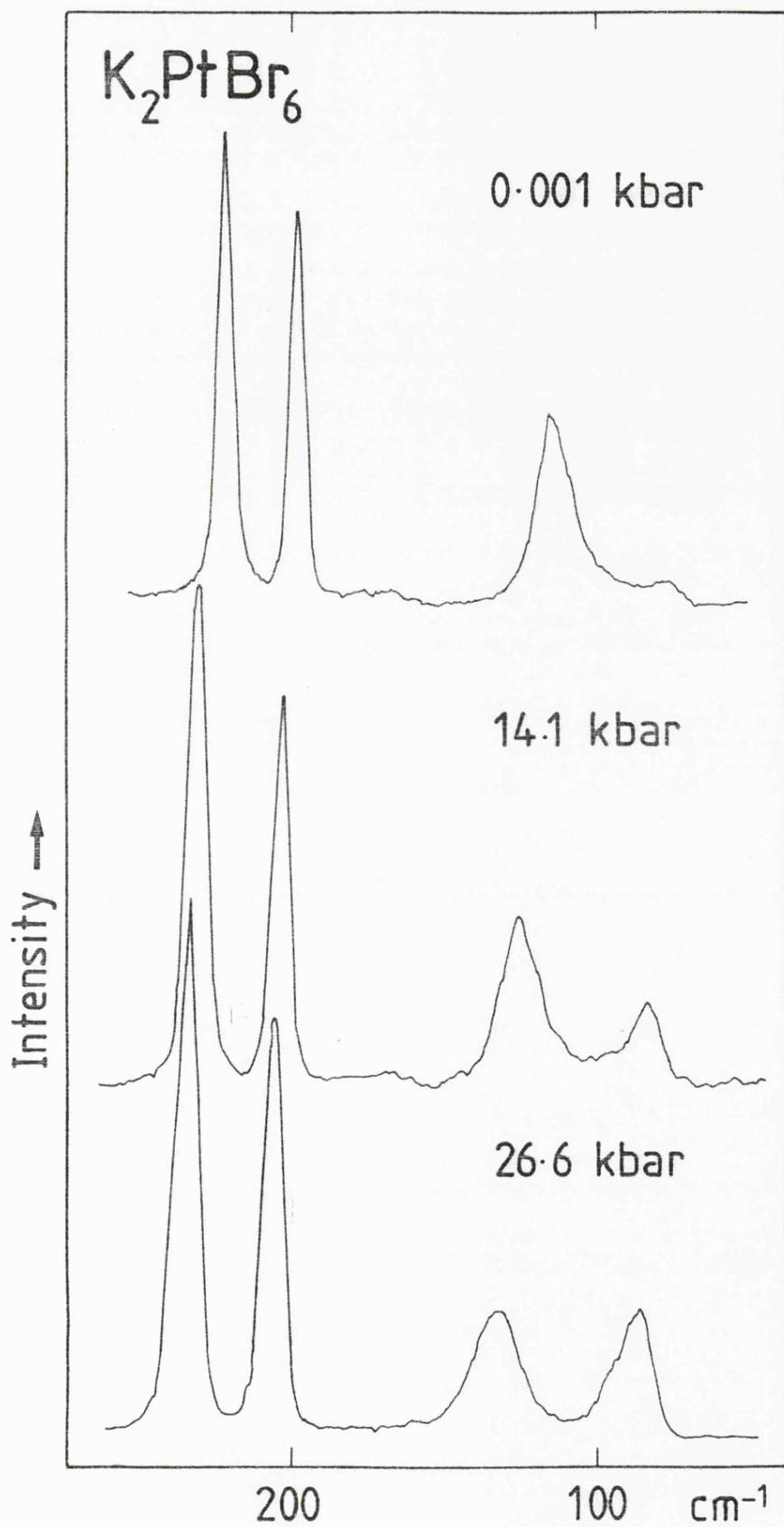


Figure 6.8

Raman spectra of K_2PtBr_6 at ambient temperature and various pressures. Spectra recorded at laserpower of 200 mw (Kr^+ , 6328\AA) and slit width of ca. 2cm^{-1} .

Note the intensity increase of the lattice mode coupled with a decrease in the intensity of ν_5 .



6.3 Results and Discussion

Results are collected on Table 6.1, which shows the gradients of straight lines in ν_i/cm^{-1} vs. P/kbar space (obtained by least squares fit to the available data), where ν_i is the observed frequency, together with standard errors.

All the materials considered have the antiferite structure, crystallising with space group O_h^5 , $Fm\bar{3}m$ at ambient temperature and pressure.

Far Infrared spectra are shown in Figures 6.2 to 6.7, being at ambient (a) and some elevated pressure (b). The high pressure spectrum for each was chosen at ca. 25 kbar, to facilitate a semi quantitative comparison of the phonon shifts experienced by the specimens.

Raman spectra are in the possession of R.W. Berg, and consequently, Raman figures are now shown, apart from those for K_2PtBr_6 , which were performed by the author, these being given on Figure 6.8.

Table 6.2 gives the relative shifts, $\frac{d\nu_i(k)}{dP} \frac{1}{\nu_i(k)}$ for the substances studied.

Infrared and Raman Spectra

The spectra obtained showed that all modes observed exhibited a blue shift on experiencing pressure, of varying magnitude.

Figure 6.9

Plots of infrared mode frequency (cm^{-1}) versus pressure (kbar)
for K_2OsCl_6 and K_2IrCl_6 .

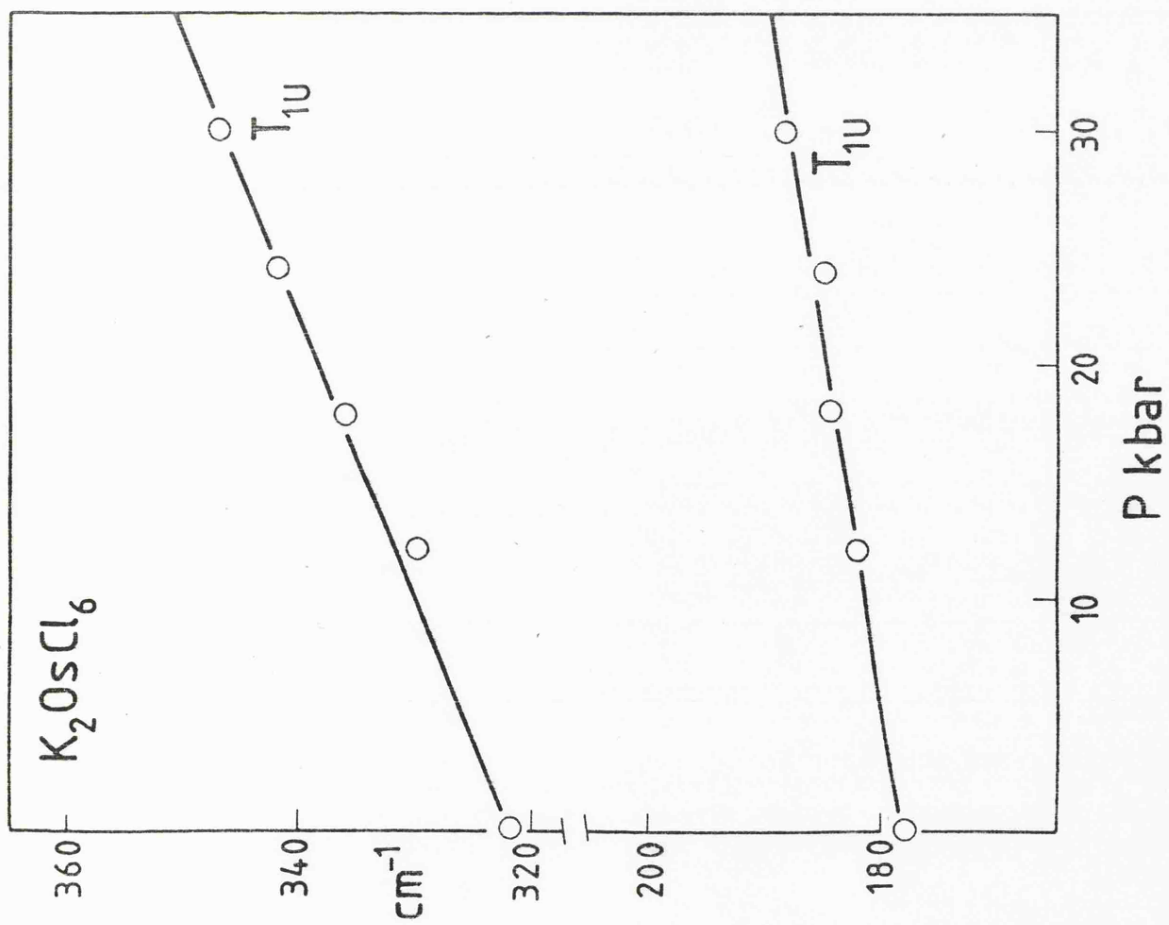
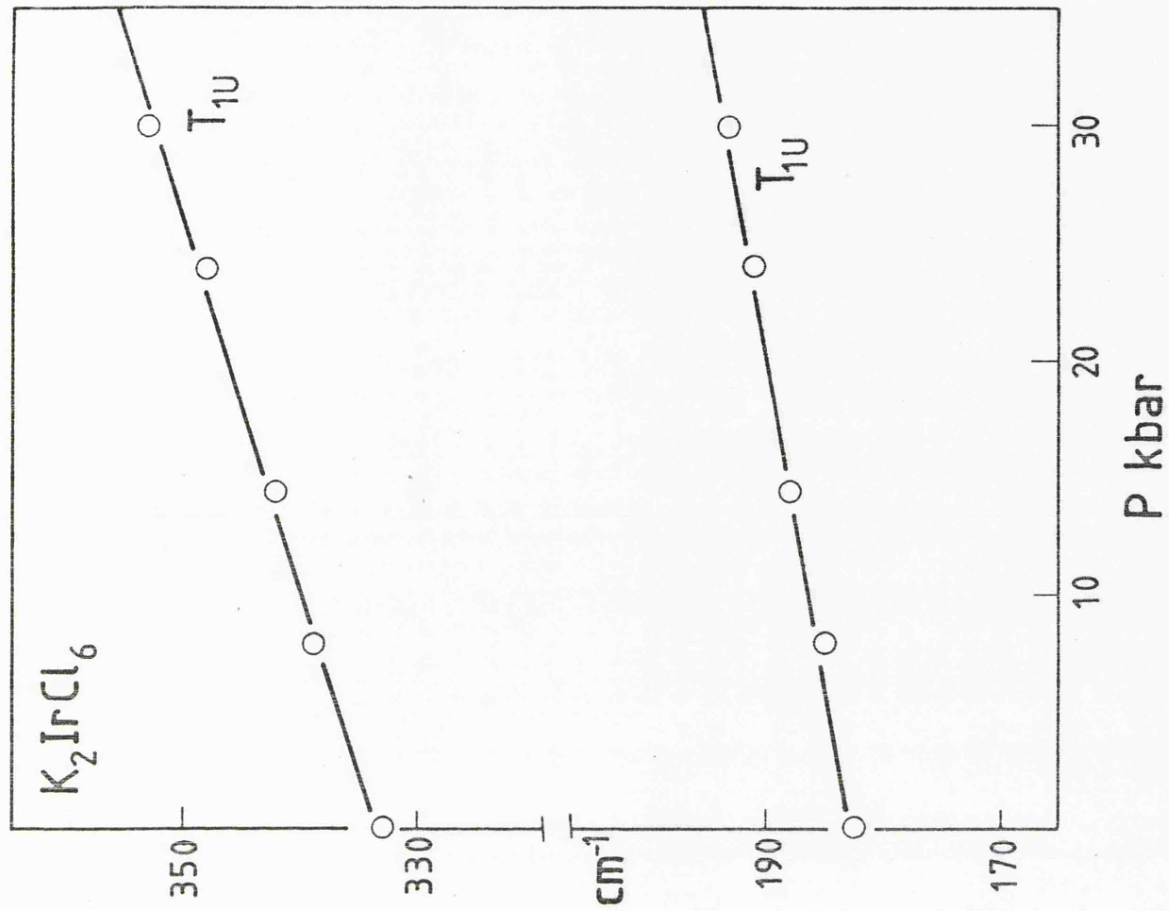


Figure 6.10

Plots of infrared mode frequency (cm^{-1}) versus pressure (kbar)
for K_2PdCl_6 and K_2ReCl_6 .

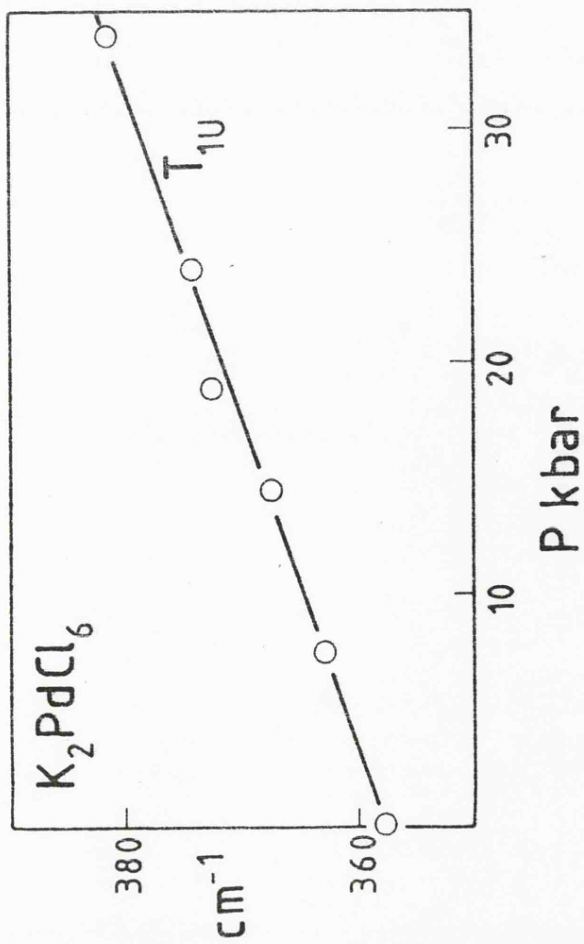
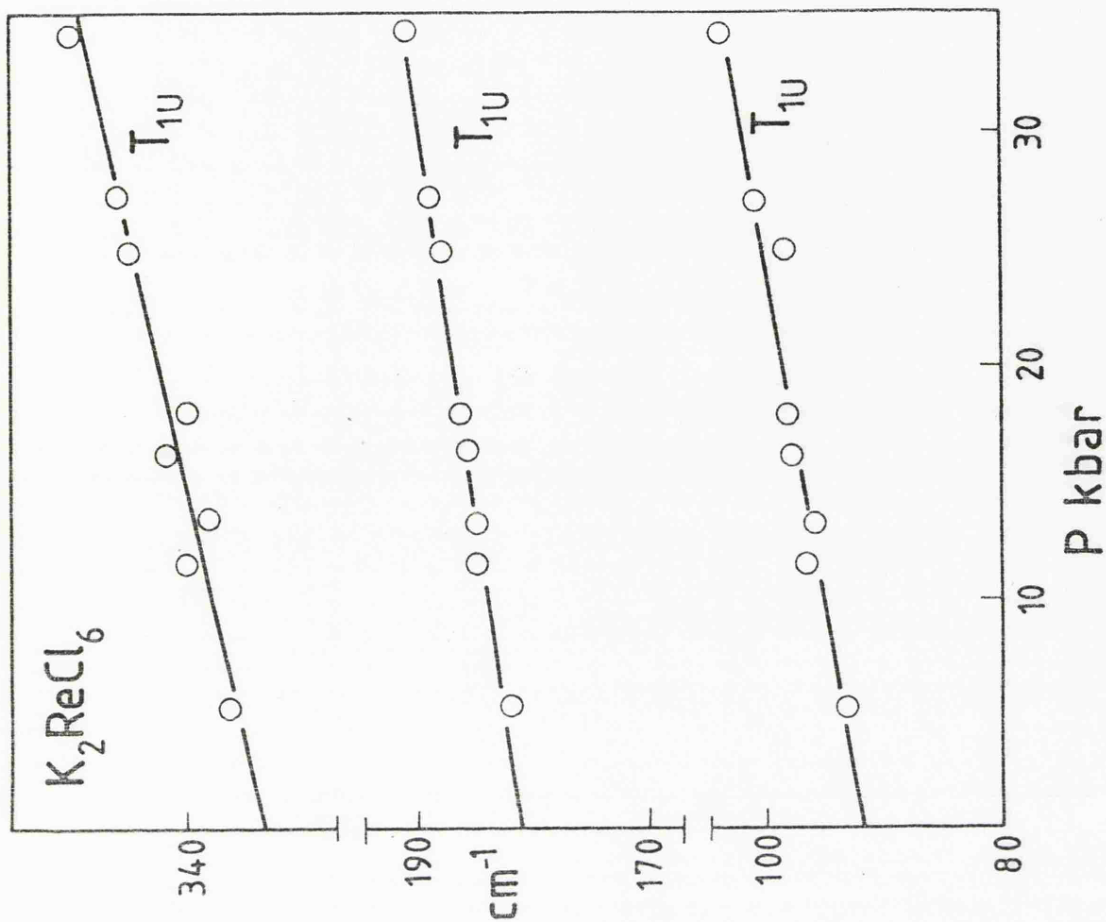


Figure 6.11

Plots of infrared mode frequency (cm^{-1}) versus pressure (kbar)
for Rb_2PtCl_6 and Cs_2PtCl_6 .

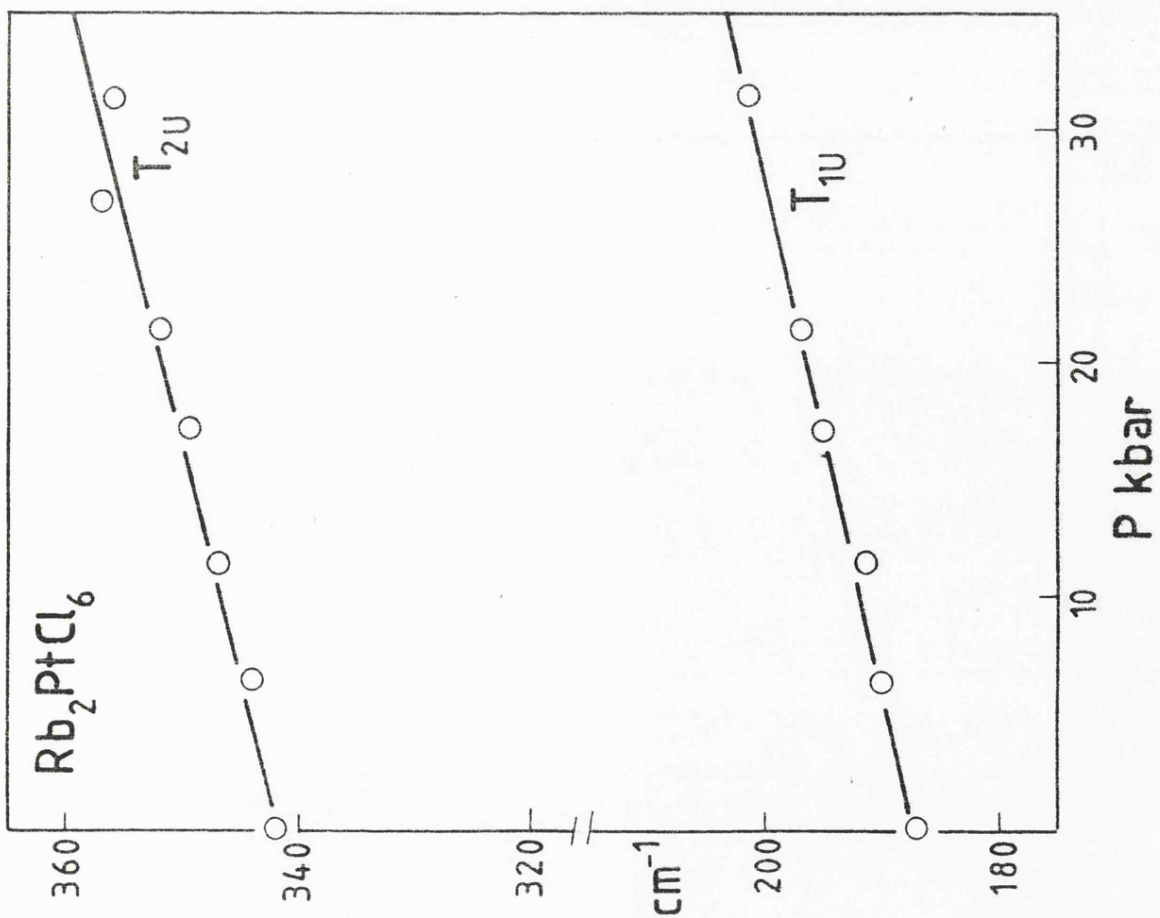
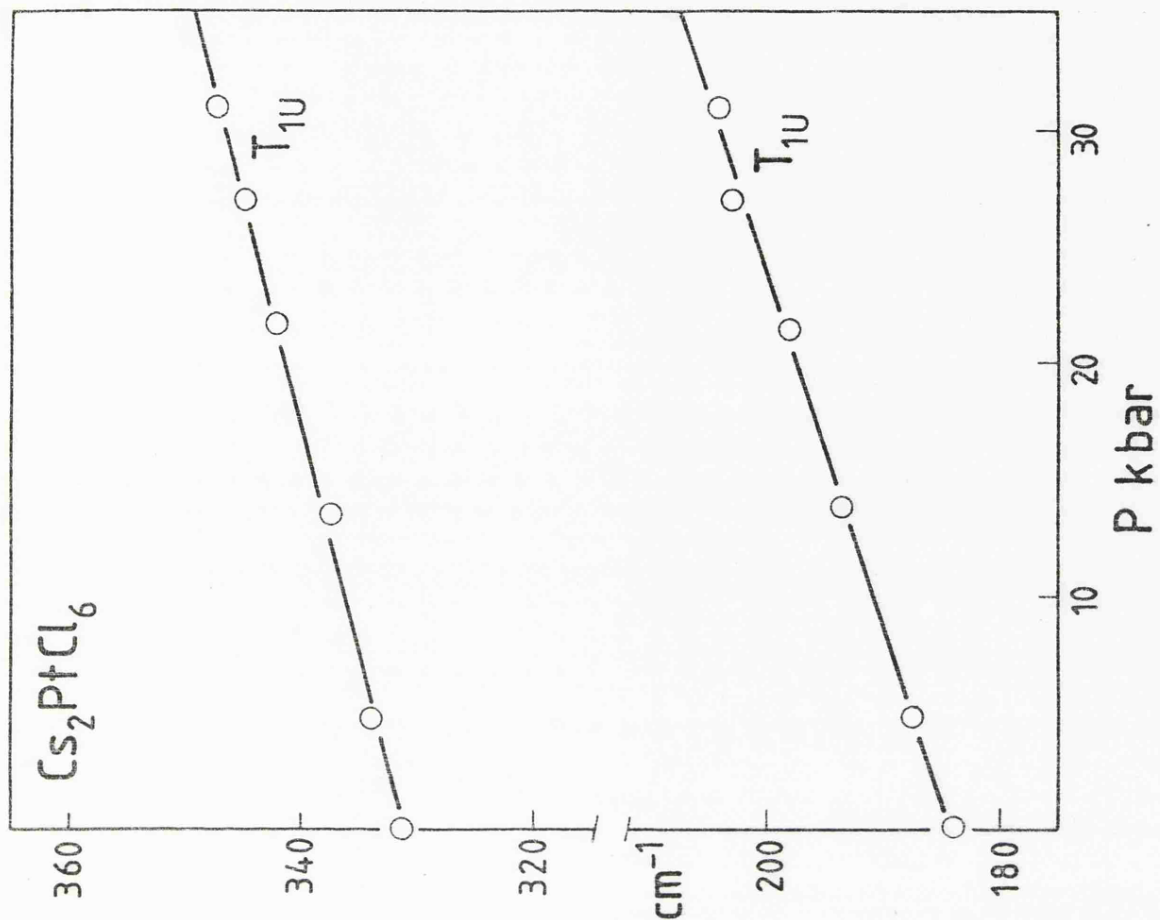


Figure 6.12

Plots of infrared mode frequency (cm^{-1}) versus pressure (kbar)
for Tl_2PtCl_6 , $\text{TMA}_2\text{PtCl}_6$ and $\text{TMA}_2\text{TeCl}_6$.

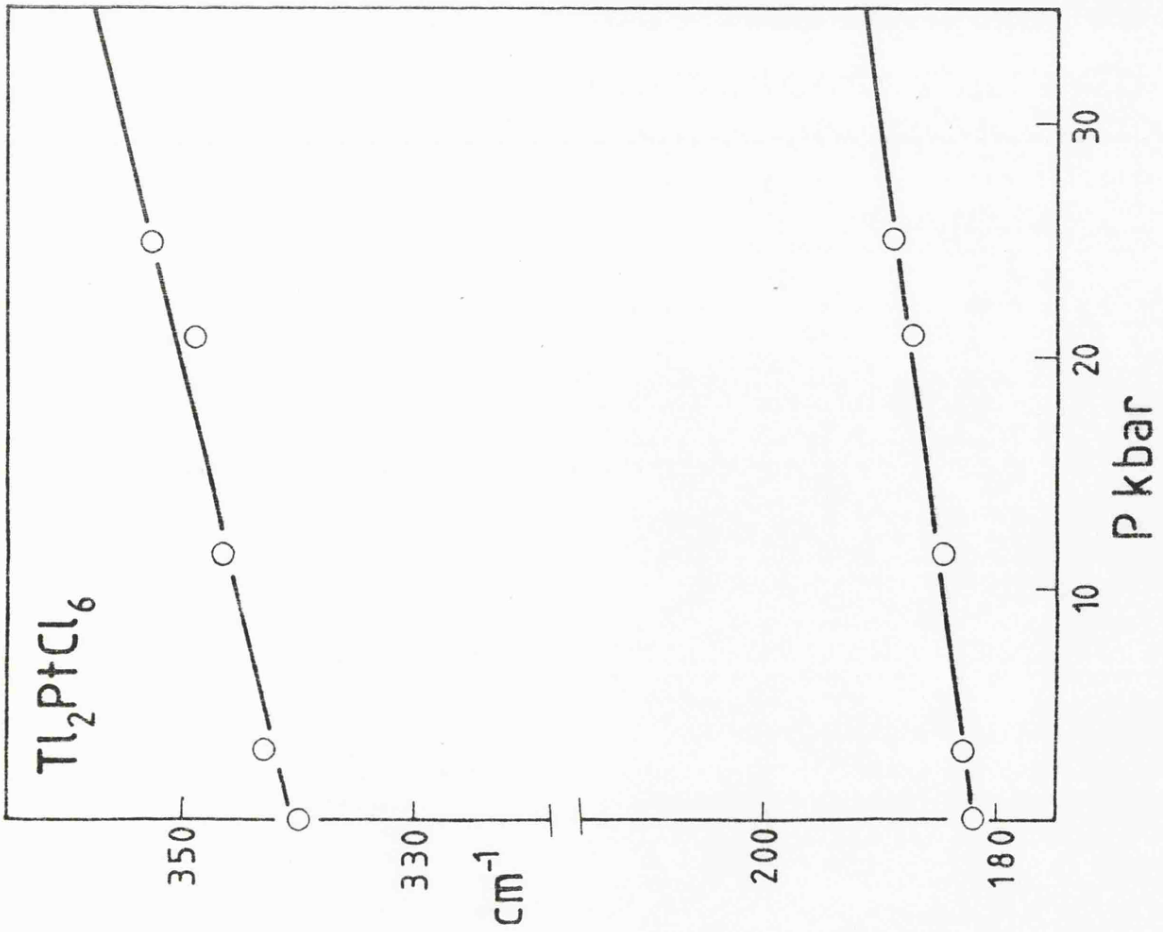
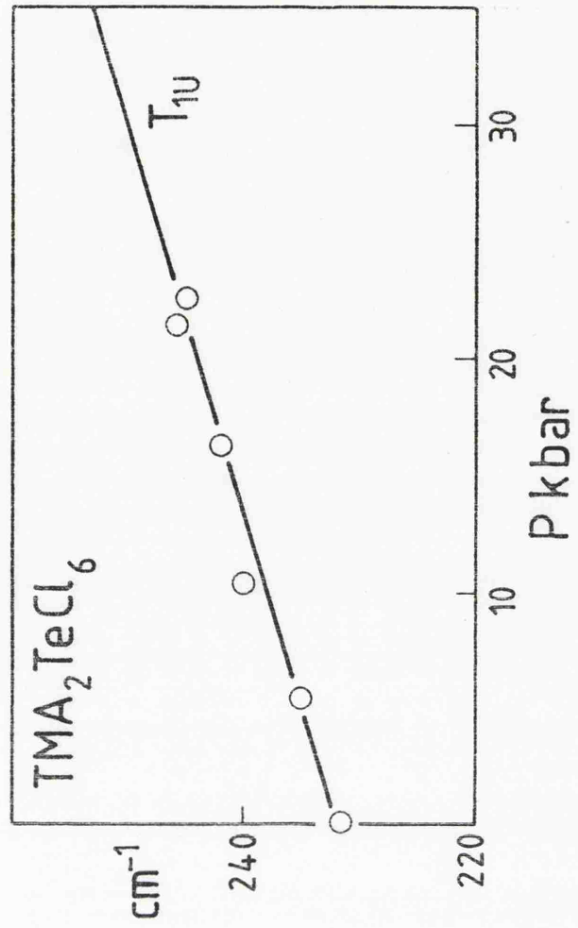
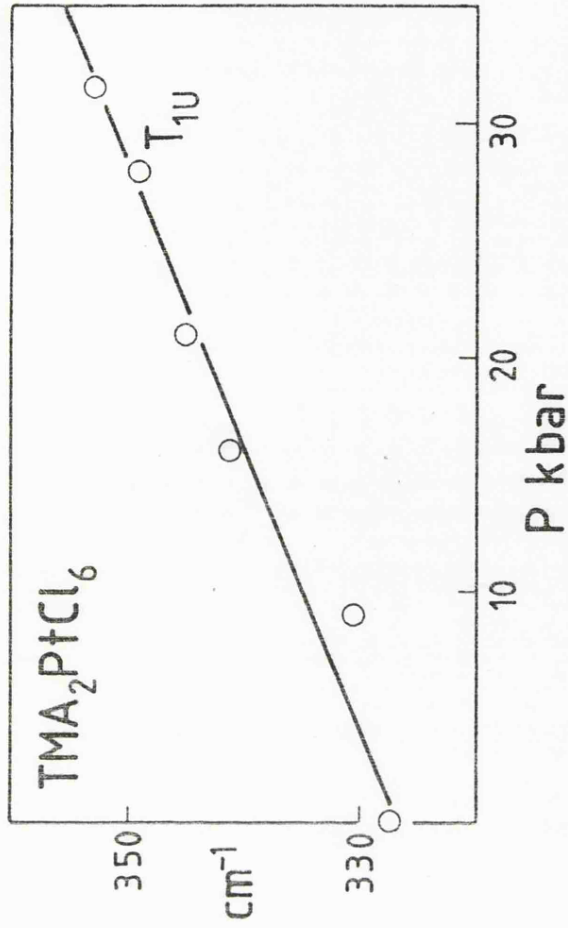


Figure 6.13

Plots of infrared mode frequency (cm^{-1}) versus pressure (kbar)
for K_2SnCl_6 and Rb_2TeCl_6 .

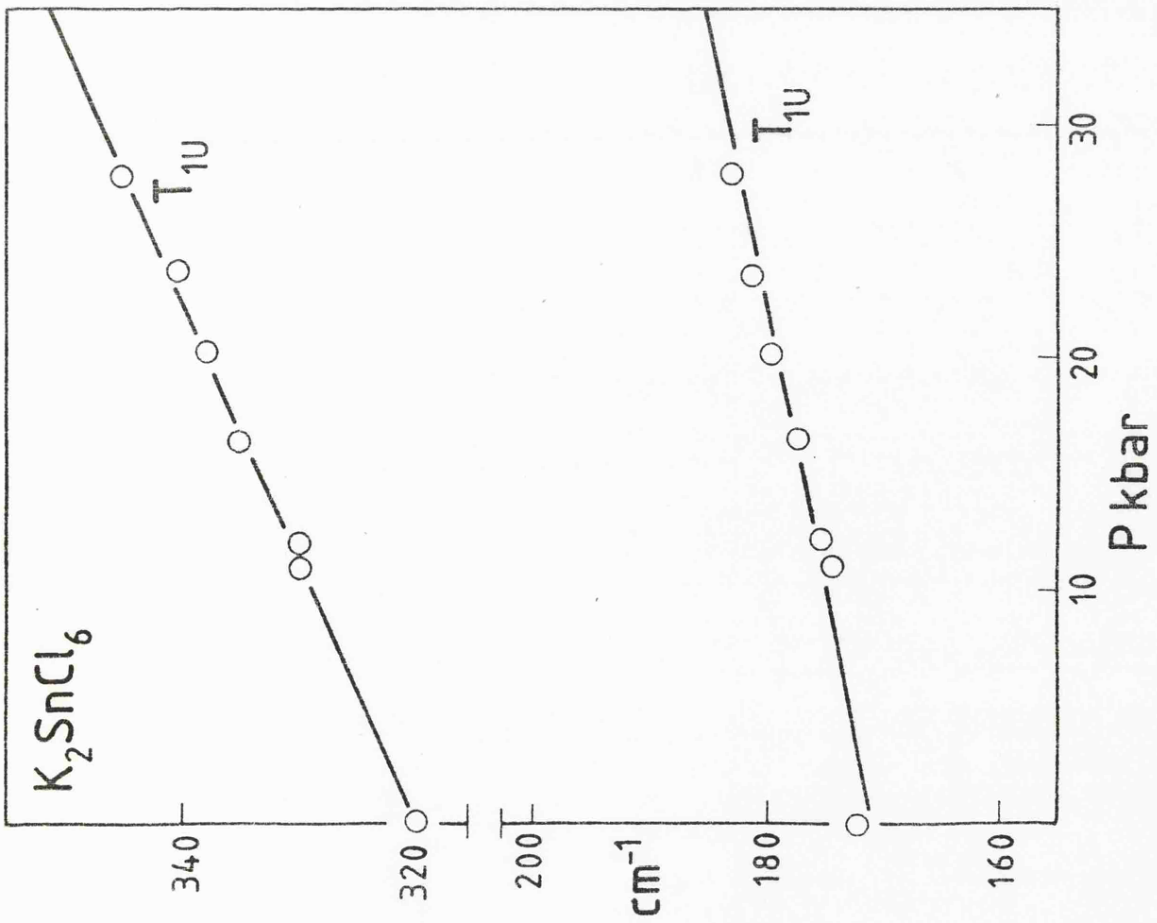
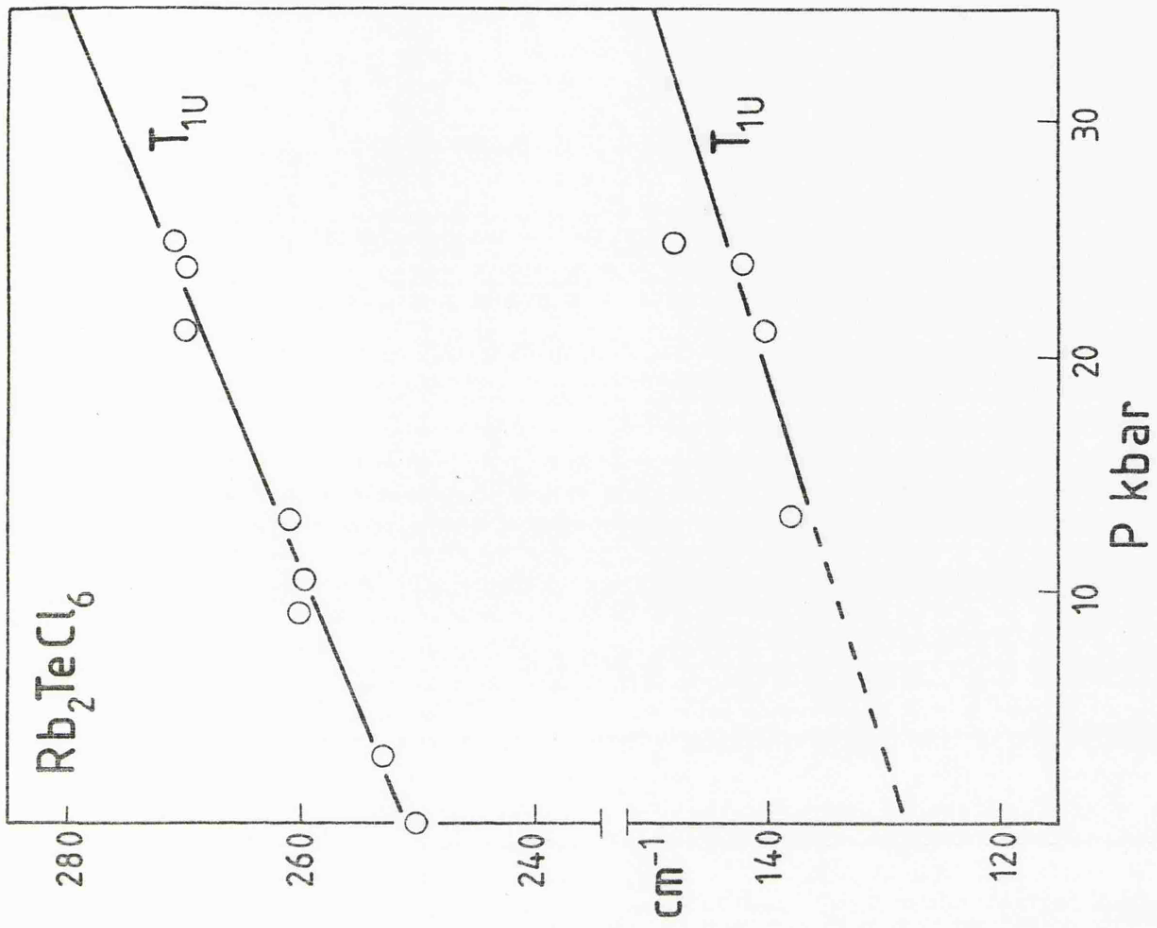
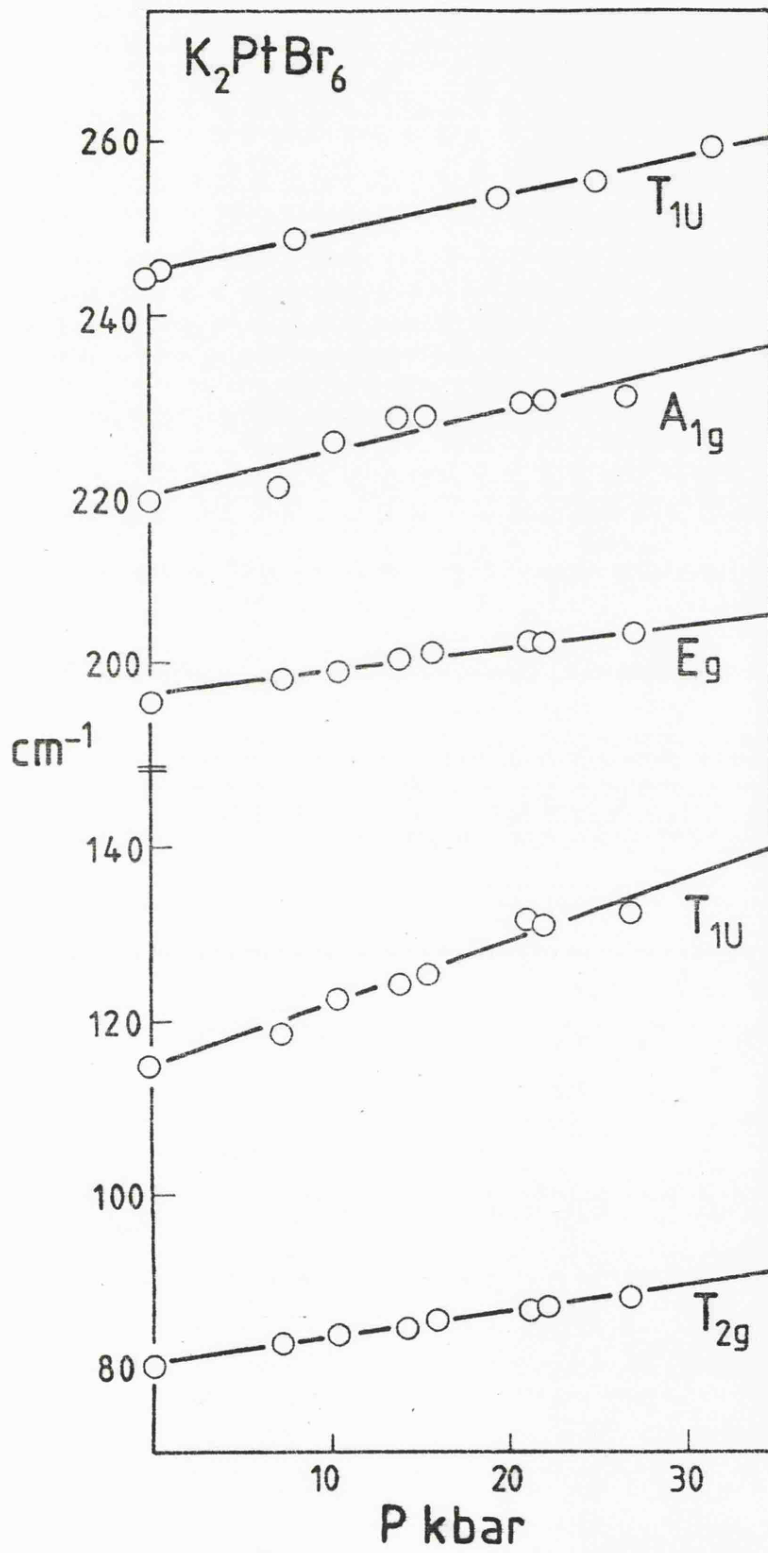


Figure 6.14

Plots of infrared and Raman mode frequency (cm^{-1}) versus pressure (kbar) for K_2PtBr_6 .



K₂MCl₆ (M = Re, Os, Ir, Pt)

The far infrared of these materials all exhibited clearly defined ν_3 and ν_4 vibrations, the only feature of note is the variable intensity of ν_4 w.r.t. ν_3 as ν_4 is much weaker in the PtCl₆²⁻ salt than the others, and IrCl₆²⁻ perceptibly weaker than Re, Os materials. The change in band intensity can be understood from ligand field theory. The formal oxidation state of the metals under consideration is (+ IV), hence the number of d electrons on the metals are Re(d³) Os(d⁴) Ir(d⁵) Pt(d⁶). The complex anions MCl₆²⁻ are all low spin, and so as the series is traversed, so the set of orbitals become increasingly populated, which places increasing charge concentration between the M - Cl bonds in the equatorial plane of the ion, and thus will hinder the motion of the atoms in the ν_4 vibration: so it is therefore reasonable that as these orbitals are filled, then the intensity of ν_4 will decrease.

The T_{1u} lattice modes were all evident but the positions of these were made uncertain by noise, however, to allow the analysis of K₂ReCl₆ as in Chapter 5 the position of the lattice mode was measured at what was taken to be the half height, and were quoted as such.

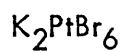
Raman spectra of K₂ReCl₆ were obtained, and the absence of the ν_2 mode was noted. The Osmate and Iridate complexes were deeply coloured, and Raman results were not possible for this reason.

K₂PdCl₆

The far infrared of this substance showed no activity in the region in which ν_4 would be expected but a pressure sensitive shoulder was clearly present on ν_3 , the reason for the existence of which is not clear. ν_3 was observed to be very sharp, in comparison with similar vibrations for the Re, Os, Ir complexes.

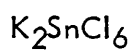


The K, Rb, Cs salts of PtCl₆²⁻ all show similar spectra, with ν_3 and ν_4 all well defined, but the lattice modes were less pronounced than in the previous compounds, ν_5 appears to be vanishingly weak for Rb₂PtCl₆. ν_4 for the tetramethylammonium salt was weak at ambient pressure, and became increasingly difficult to resolve from the background as pressure was increased. No Raman data are available for Tl₂PtCl₆ TMA₂PtCl₆.

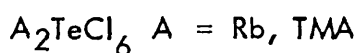


No ν_4 vibration was discernable for KtPtBr₆ above 100cm⁻¹, but ν_3 was clearly defined.

An interesting feature was noted in the Raman spectrum of this substance; namely an increase in intensity of the lattice mode (which was observed only in K₂PtBr₆) coupled with a decrease in the intensity of ν_5 with pressure. This was thought to be due to Fermi resonance between the two modes.



All infrared allowed modes were evident, with ν_4 being notably more intense than in other salts studied.



In both of these specimens a broad absorption assigned to ν_3 dominated the region between 100 and 400cm⁻¹. At elevated pressures, the appearance of a further vibration (assigned to ν_4) was noted for the rubidium complex but no such response was observed for the tetramethylammonium compound.

Table 6.1 Vibrational frequencies (wavenumbers/cm⁻¹) and their shifts with pressure for complex halides A₂MX₆.

Compound	ν ₁		ν _o	ν ₂		ν ₃		ν _o	ν ₄		ν ₅		ν _L (i.r.)	
	ν _o	Δν/ΔP ^b		s.d. ^c	Δν/ΔP	s.d.	ν _o		Δν/ΔP	s.d.	ν _o	Δν/ΔP	s.d.	ν _o
K ₂ PdCl ₆						357	0.70	0.03						
K ₂ ReCl ₆	357.5	0.75	0.02	abs.		330	0.46	0.04	177	0.29	0.02	176	0.61	0.03
K ₂ OsCl ₆						329	0.83	0.06	178	0.30	0.05			86
K ₂ IrCl ₆						336	0.62	0.05	184	0.35	0.03			86
K ₂ PtCl ₆	351	0.78	0.02	320	0.49	0.17	345	0.81	0.06	187	0.55	0.04	174	0.65
Rb ₂ PtCl ₆	375.5	0.68		318	0.43		342	0.65	0.11	187	0.39	0.09		88
CS ₂ PtCl ₆	335.3	0.59		311	0.31		332	0.52	0.02	186	0.66	0.02	172.7	1.05
Tl ₂ PtCl ₆							335	0.45	0.04	181	0.28	0.02		
(TMA) ₂ PtCl ₆							327	0.87	0.13					
K ₂ PtBr ₆	218.5	0.48		195.5	0.29		244.5	0.42	0.02				114.5	0.74
K ₂ SnCl ₆	320.7	0.96		272	0.67		320	0.88	0.03	172	0.43	0.10	169	0.80
Rb ₂ TeCl ₆	300.6	1.09		253	0.64		250	0.82	0.04	125 ^f	0.65	0.35		
(TMA) ₂ TeCl ₆							238	0.98	0.04					

^a Value at ambient pressure. ^b In cm⁻¹ kbar⁻¹. ^c Standard deviation ^d TMA = tetramethyl ammonium ^e Raman-active lattice mode

^f Absent at ambient pressure; appears at elevated pressure

Table 6.2 Relative shifts, $\frac{1}{\nu_i(k)} \frac{d\nu_i(k)}{dP}$ T, for complex halides A_2MX_6 under hydrostatic pressure (10^{-2} kbar $^{-1}$).

	ν_1	ν_2	ν_3	ν_4	ν_5	ν_L (i.r.)	ν_L (Raman)
K_2PdCl_6	<u>a</u>		0.20				
K_2ReCl_6	0.21	<u>b</u>	0.14	0.16	0.35	0.36 ^c	
K_2OsCl_6	<u>a</u>		0.26	0.17			
K_2IrCl_6	<u>a</u>		0.18	0.19			
K_2PtCl_6	0.22	0.15	0.23	0.29	0.37	0.79	
Rb_2PtCl_6	0.18	0.13	0.19	0.30	0.45		
Cs_2PtCl_6	0.17	0.10	0.16	0.35	0.60		
$(TMA)_2PtCl_6$	0.18	0.19	0.27		0.23		
K_2SnCl_6	0.30	0.24	0.27	0.25	0.47		
Rb_2TeCl_6	0.36	0.25	0.32	0.50	0.64	0.82	
$(TMA)_2TeCl_6$			0.26				
K_2PtBr_6	0.22	0.15	0.17		0.65		0.37

a Raman spectra could not be obtained for these deeply coloured materials.

b ν_2 is vanishingly weak.

c Approximate value.

d TMA = tetramethylammonium

Table 6.3

Compressibilities for complex halides A_2MX_6 calculated using equation 4. ($\underline{m} = 3$, $\underline{z} = 2$, $\underline{n} = 36$).

	$a/\text{\AA}^a$	$U/\text{kJ mol}^{-1a}$	$\gamma/10^{-6}\text{bar}^{-1}$
K_2ReCl_6	9.84	1416	6.753
K_2OsCl_6	9.729	1447	6.387
K_2PtCl_6	9.755	1468	6.347
Rb_2PtCl_6	9.901	1464	6.654
Cs_2PtCl_6	10.215	1444	7.409
Tl_2PtCl_6	9.779	1546	6.071
K_2PtBr_6	10.293	1423	7.692
K_2SnCl_6	10.002	1352	7.428
Rb_2TeCl_6	10.233	1321	8.141

a Data from reference 6

Table 6.4

Gruneisen parameters for complex halides A_2MX_6
calculated from the data of tables 2 and 3.

	ν_1	ν_2	ν_3	ν_4	ν_5	ν_L (i.r.)
K_2ReCl_6	0.77	-	0.51	0.59	1.28	1.32
K_2OsCl_6			1.01	0.66		
K_2PtCl_6	0.87	0.60	0.93	1.15	1.48	3.10
Rb_2PtCl_6	0.68	0.51	0.72	1.14	1.69	
Cs_2PtCl_6	0.59	0.33	0.53	1.19	2.04	
Tl_2PtCl_6			0.55	0.63		
K_2PtBr_6	0.71	0.48	0.56		2.10	1.2 ^a
K_2SnCl_6	1.01	0.83	0.93	0.84	1.60	
Rb_2TeCl_6	1.11	0.78	0.99	1.54	1.96	2.51

^a Raman-active lattice mode

The isothermal compressibilities of the samples were calculated as in equation (4). Literature values for α_0 and $U^{(1)}$ and are shown in Table 6.3. These were then used to obtain the mode Gruneisen parameters $\gamma_i(k)$ collected on Table 6.4. These parameters may now be compared throughout the materials studied.

6.4 Trends in the Gruneisen parameters

(i) The data obtained in this series of experiments support the general trend noted by Zallen (2) that $\gamma_i(k)$ is frequency dependent and increases on going from high to low frequencies; this appears to be at variance with work performed by PTT Wong (3) on an ionic system, who finds no correlation between frequency and mode Gruneisen. At present few reliable data on lattice modes exist, but those we do have support this trend, which would appear to be a consequence of the existence of the $k \propto \beta$ term in the denominator of equation (5). A further study is required to collect far infrared data on the shift of the lattice mode under hydrostatic conditions, and then this relation may be tested more adequately, by using known values of force constants which govern the behaviour of lattice modes of the K_2PtCl_6 structural type.

In every case studied, the Raman active t_{2g} bending mode (ν_5) has a greater Gruneisen parameter than those of any of the Pt - Cl bond stretching modes, and indeed of any of the metal halogen stretches ($\nu_1 \rightarrow \nu_3$), the greatest value of $\gamma(\nu_5)$ occurring for K_2PtBr_6 , being

2.04, and the least for K_2ReCl_6 being 1.28. The infrared active bend ν_4 (t_{1u}) also usually (but not invariably) has $\gamma_i(k)$ greater than any of the stretches. The exceptions to this are K_2OsCl_6 with $\gamma(\nu_4)$ of 0.66 of $\gamma(\nu_3)$ of 1.01, and K_2SnCl_6 , in which the Gruneisen for ν_4 is 0.84, whereas that for ν_3 is .93. These observations also support Zallen's general trend, the $k \propto \beta$ term being less for a bend than a stretch in the same system.

(ii) Within the $PtCl_6^{2-}$ series, two general patterns emerge. The prior observation concerning $\gamma(\nu_4)$ and $\gamma(\nu_5)$ always hold true, that is $\gamma(\nu_4) < \gamma(\nu_5)$. The $\gamma_i(k)$ s for ν_1 , ν_2 and ν_3 all increase from Co^+ to Rb^+ to K^+ ($\gamma(\nu_1) = 0.59, 0.68, 0.87$, $\gamma(\nu_2) = 0.33, 0.51, 0.6$, $\gamma(\nu_3) = 0.53, 0.72, 0.93$, for Cs^+ , Rb^+ , K^+ respectively) whilst those for ν_4 and ν_5 decrease. $\gamma(\nu_2)$ is consistently lower than $\gamma(\nu_1)$ and $\gamma(\nu_3)$, but the order of the latter two is variable. This also applies throughout all the compounds studied.

In the matrix secular equation $|GF - E\lambda I| = 0$, the G matrix elements of ν_1 and ν_2 are identical, but the force constants governing ν_1 are greater than those for ν_2 (eg. $K + 4F$ for ν_1 , and $K + 0.7F$ for ν_2 in the Urey Bradley force field); hence ν_1 is always greater in energy than ν_2 . If the main factor affecting the trend in $\gamma_i(k)$ with change of cation is $k \propto \beta$, then $\gamma(\nu_2)$ should always be greater than $\gamma(\nu_1)$, whereas the reverse appears to be consistently true. This leads one to consider that in fact $k \propto \beta$ is not the overriding factor, and that the anharmonicity (i.e. the departure from ideal behaviour) is greater for ν_2 than for ν_1 .

The increase in γ_i ($i = 1$ to 3) from Cs^+ to K^+ salts of PtCl_6^{2-} parallels the order of the mode frequencies themselves. Shimanouchi (15) has measured the force constants for a series K^+ , Rb^+ , Cs^+ , which were 1.86, 1.81 and 1.73 $\text{md}/\text{\AA}$ respectively. Taking these factors into consideration it would appear that the harmonic force constant ^{is not} causing the major change in $\gamma_i(k)$ in this series, rather it is the anharmonicity that increases from Cs^+ to K^+ .

The trends found for the PtCl_6^{2-} salts in this work are paralleled by those very recently reported by Breiteringer et al (12) for the corresponding PtBr_6^{2-} salts. The same explanation can be tendered for these as for the PtCl_6^{2-} series.

For the bending modes ν_4 (t_{1u}) and ν_5 (t_{2g}), $\gamma_i(k)$ decreases from Cs^+ to K^+ ; that is the reverse of the trend for the stretching modes. The implication is therefore that the harmonic force constants are the major influence for the trend in $\gamma_i(k)$ for ν_4 and ν_5 , rather than the anharmonic force constants. This theory is supported by evidence for triatomic systems, for which full potential constants have been evaluated, the stretch-stretch constants k_{rr} and k_{rrrr} are at least an order of magnitude greater than all other cubic and quartic constants (13).

(iii) For K_2PtBr_6 ν_4 and ν_1 (t_{1u}) are both below 100cm^{-1} and hence were not observed. However (ν_3) is .56 compared with .925 for the equivalent mode in K_2PtCl_6 . Breiteringer (12) et al have recently reported

mode shifts for ν_1 , ν_2 and ν_5 of K_2PtBr_6 which are also consistently less than those for K_2PtCl_6 . The Gruneisen parameters $\gamma_i(k)$ would be expected to be even lower due to the greater compressibility of K_2PtBr_6 compared with K_2PtCl_6 . $\gamma_i(k)$ values might be expected to be greater than those for K_2PtCl_6 since the $\nu(Pt - Br)$ modes are ca. 230cm^{-1} and are determined by lower force constants (see equations 3 and 5 and Zallen's relationship). That the reverse is true implies that lower values of the anharmonic force constants are also involved, which is consistent with the comments under (ii) above.

(iv) Considering the data collected for the other salts studied it is notable that almost all $\gamma_i(k)$ values for K_2SnCl_6 and Rb_2TeCl_6 are greater than those for the transition metal salts. In the case of tellurium this is unsurprising as there is known to be a non-bonding electron pair in an a_{1g} orbital around the metals atom, greatly reducing the $Te-Cl$ bond stretching force constants below what would otherwise be expected.

For the Pd, Os and Ir salts no Raman data were obtained due to their deep colours. $\gamma(\nu_3)$ for K_2PdCl_6 is 0.79 compared with .925 for K_2PtCl_6 , whereas $\nu_3(Pd) > \nu_3(Pt)$. This again implies that the anharmonic force constants principally determine the magnitudes of these Gruneisen parameters.

6.5 Conclusions

Far Infrared and Raman mode frequency shifts have been observed for a series of A_2MX_6 complexes under hydrostatic conditions. Using compressibilities calculated from unit cell constants and lattice energies, Gruneisen parameters $\gamma_i(\underline{k})$ have been obtained for all the observed modes.

The new data reveal a little about the complex factors affecting phonon shifts in these salts. The general trend, recognised by Zallen that $\gamma_i(\underline{k})$ decreases with increase of mode frequency, ν_i is supported by these results. Increases in $\gamma_i(\underline{k})$ for PtCl stretching modes of A_2PtCl_6 for $A = Cs^+$ to K^+ are considered as being primarily due to an increase in the anharmonic force constants in the series, whereas the reverse dependence found for the bending modes is attributed to changes in harmonic force constants. Lower values of $\gamma_i(\underline{k})$ found for K_2PtBr_6 compared to K_2PtCl_6 are believed to be due to lower values of anharmonic force constants.

TABLE 6.5 Infrared mode frequencies (cm^{-1}) at ambient and elevated pressures (kbar) for some A_2MX_6 complexes.

A_2MX_6	P(kbar)	$\nu_3(\text{cm}^{-1})$	$\nu_4(\text{cm}^{-1})$	$\nu_L(\text{cm}^{-1})$	A_2MX_6	P(kbar)	$\nu_3(\text{cm}^{-1})$	$\nu_4(\text{cm}^{-1})$	
PtCl_6	5.3	336.5	182.0	95.0	Ti_2PtCl_6	0.001	340.0	182.0	
	11.7	340.0	185.0	97.5		3.8	343.0	183.0	
	12.3	338.0	185.0	96.5		11.4	346.5	184.5	
	16.3	341.8	186.0	98.0		20.8	349.0	187.5	
	18.0	340.0	186.5	98.5		25.0	352.5	189.6	
	25.0	345.0	188.0	98.0					
	27.2	346.0	189.0	101.0		$(\text{TMA})_2\text{PtCl}_6$	0.001	327.5	
	34.2	350.0	191.0	104.0			8.8	331.5	
				15.8	341.0				
OsCl_6	0.001	322.0	178.0			21.0	345.0		
	12.1	330.0	182.5			28.7	348.0		
	17.8	336.5	184.5			32.3	351.5		
	24.1	342.0	185.0						
	29.2	346.0	189.0		K_2SnCl_6	0.001	320.0	172.0	
				11.3		330.0	174.0		
IrCl_6	0.001	336.0	184.0			12.0	330.0	175.0	
	7.9	339.0	186.0			17.2	335.5	177.5	
	14.7	341.5	188.5			20.3	338.5	179.5	
	24.0	248.5	191.0			23.7	340.5	182.0	
	29.0	350.5	193.5			28.0	343.0	184.0	
	40.1	356.5	197.0						
RbCl_6	0.001	357.5			Rb_2TeCl_6	0.001	250.0		
	7.5	363.0				3.0	253.0		
	14.5	367.5	v. weak			9.3	260.0		
	18.8	372.5				10.5	261.0		
	24.0	374.0				13.3	261.0	138.0	
	34.0	381.5				21.2	270.0	140.0	
						24.0	270.6	142.0	
				25.0	271.0	148.0			
PtCl_6	0.001	342.0	187.0		$\text{TMA}_2\text{TeCl}_6$	0.001	231.0		
	6.5	344.0	190.0			5.6	235.0		
	11.5	347.0	191.5			11.3	240.0		
	17.1	349.5	195.5			16.3	242.0		
	21.5	352.0	197.0			21.4	246.0		
	31.7	350.5	201.5			22.6	245.5		
PtCl_6	0.001	331.0	184.0						
	4.9	334.0	187.5						
	13.5	337.5	193.5						
	21.6	342.0	198.0						
	27.0	345.0	203.0						
	30.8	347.5	204.0						

TABLE 6.6 Raman mode frequencies (cm^{-1}) at ambient and elevated pressure (kbar) for K_2PtBr_6 .

K_2PtBr_6	ν_1	ν_2	ν_5	ν_L
0.001	217.5	194.5	114.5	80.0
7.4	222.0	198.0	118.5	82.5
10.5	225.5	199.0	122.5	83.5
14.1	228.0	200.5	124.5	84.5
15.8	228.0	201.0	126.5	85.5
21.3	229.5	202.5	131.5	86.5
22.1	229.5	202.0	131.0	87.0
26.6	230.0	203.0	132.5	88.0

References

1. Plendl, J.N., Mitra, S.S., Gielesse, P.J., Phys Stat Solidi 12 367 (1965).
2. Zallen, R., Phys Rev. B. 9 4485 (1974).
3. Wong, P.T.T., J. Chem. Phys. 66 2347 (1977).
4. Wong, P.T.T., J. Chem. Phys. 63 5108 (1975).
5. Maradudin, A.A., Phys. Stat. Solidi 2 1493 (1962).
6. Mitra, S.S., Brafman, O., Daniels, W.B., Crawford, R.K., Phys. Rev. B 186 942 (1969).
7. Feraro, J.R., J. Chem. Phys. 53 117 (1970).
8. Adams, D.M., Payne, S.J., JCS Dalton 407 (1974).
9. Adams, D.M., Payne, S.J., JCS Dalton 215 (1975).
10. Adams, D.M., Findlay, J.D., Coles, M.C., Payne, S.J., JCS Dalton 371 (1976).
11. Jenkins, H.B.D., Private Communication.

12. Breitinger, D., Bauer, G., Haegler, W., Emmert, L., Krass, W.,
Proc. Raman Conf. Bangalore 318 (1978).
13. Califano, S., Vibrational States Wiley, Chichester, (1976) p 285.

CHAPTER 7

AN INFRARED STUDY OF THE METASTABLE PHASES OF CaCO_3

CHAPTER 7

AN INFRARED STUDY OF THE METASTABLE PHASES OF CaCO₃

7.1 Introduction

The relatively abundant mineral Calcium Carbonate (CaCO₃) occurs in three structurally distinct forms: Calcite, the rhombohedral form, CaCO₃(I), $R\ 3c = D_{3d}^6$; the orthorhombic aragonite, $Pnma = D_{2h}^{16}$, and vaterite, which is hexagonal, $P6_3/mmc = D_{6h}^4$.

At ambient conditions the thermodynamically stable phase of CaCO₃ is calcite whilst aragonite is the stable phase at high pressures. At temperatures below 200°C, however, the calcite/aragonite phase transition is so sluggish (in the absence of mineralisers) that it can be ignored. The stability field of vaterite is not well established. The structures of the phases of calcium carbonate are given by Wyckoff (11).

Two other phases of CaCO₃ were discovered in 1939 by Bridgmann (1) using isothermal compression of normal calcite at room temperature. These phases labelled CaCO₃ (II) and (III) were detected by discontinuities in the isothermal compressibility: one at 14 kbar due to the CaCO₃(I:II) transition, the other at 18 kbar, representing the CaCO₃(II:III) transition. These new phases are within the stability field of aragonite (which is denser, 2.95 g/cm³ cf 2.71 g/cm³ for calcite), and are believed to be metastable with respect to it. Jamieson (2) from high pressure X ray powder study deduced that the transition calcite: CaCO₃(II)

creates an anion disordered form of normal calcite, with possibly the c axis halved. Davis (3) however disagreed with the suggested mechanism of anion disorder for the production of the metastable calcite polymorphs, and cites experimental evidence to show that such disorder would increase, not decrease the length of the c axis.

Using X ray powder data many speculations on the structure of CaCO_3 (II) and (III) have been based on analogues with phase diagrams of other alkaline earth carbonates and the alkali metal nitrites. Prominent amongst these suggestions are that CaCO_3 (II) is isostructural with the high temperature anion disordered phase of NaNO_3 (5) or with ferroelectric KNO_3 (II) (6,7) and that CaCO_3 (III) is isostructural with the high pressure KNO_3 (IV) phase of potassium.

A definitive single crystal X ray diffraction study by Merrill & Bassett (4) showed CaCO_3 (II) to be monoclinic, $P2_1/C$, with a doubling of the unit cell along the c axis relative to calcite (that is, CaCO_3 (II) is tetramolecular, whereas calcite has $Z = 2$). This single crystal work on CaCO_3 (II) shows how unreliable conclusions drawn from powder data alone can be, and therefore the structure of CaCO_3 (III) must be considered sub judice. It is also notable that the high pressure Raman spectra of Fong and Nicol (6) suggest that CaCO_3 (II) does not have the structure of ferroelectric KNO_3 (II) phase, and that spectral data for CaCO_3 (III) are also inconsistent with those of KNO_3 (IV). Structural data for the various solid phases of CaCO_3 are shown in Table 7.1.

Figure 7.1

The phase diagram of CaCO_3 (Merril & Bassett, Acta Cryst.
B31 343 (1975)).

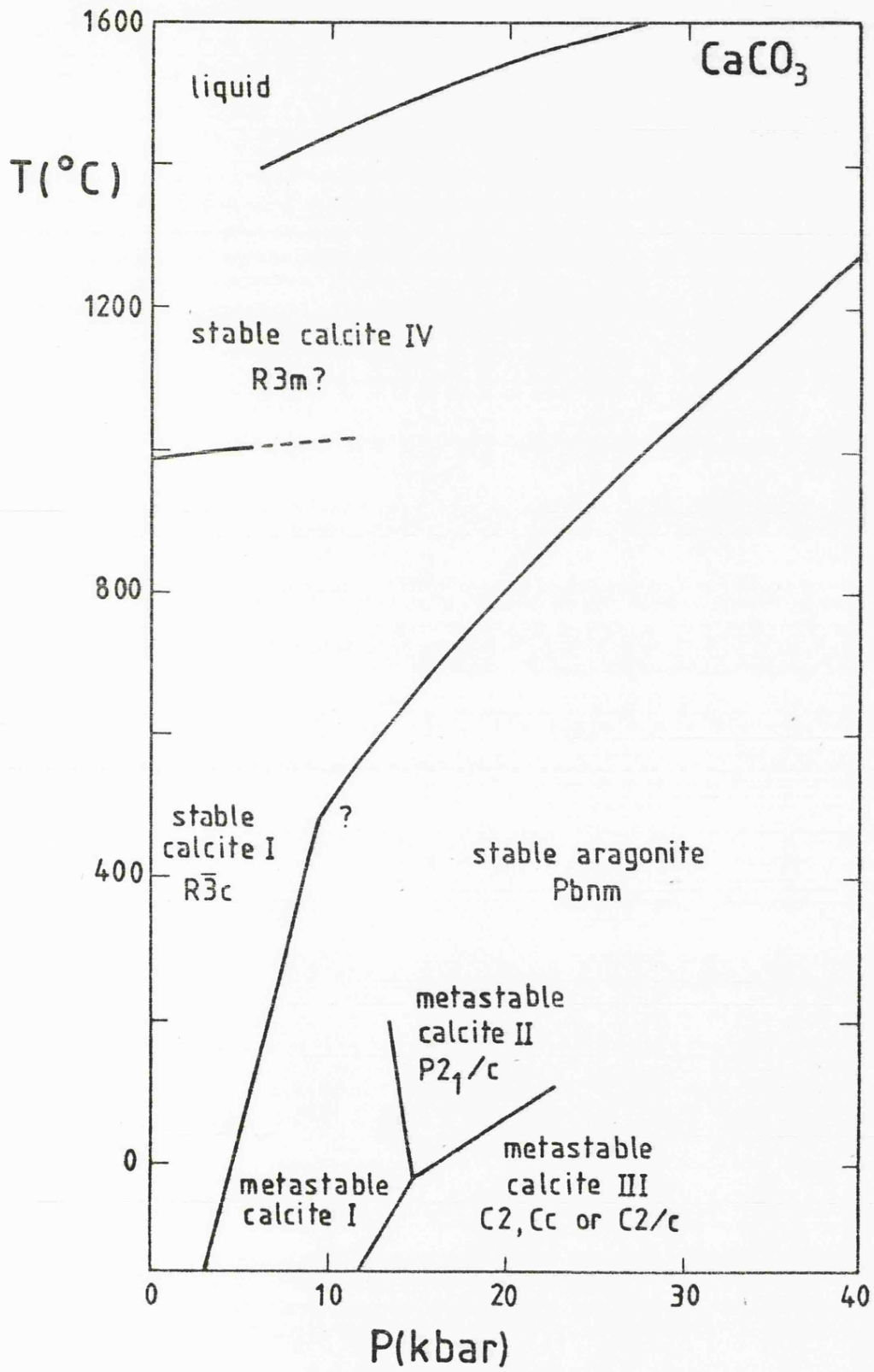


TABLE 7.1

Structural data for the solid phases of CaCO_3

Phase	Calcite CaCO_3 (I)	CaCO_3 (II)	CaCO_3 (III)	Aragonite	Vaterite
Crystal System	Rhombohedral	Monoclinic	Not known	Orthorhombic	Hexagonal
Space group	$R3c = D_{3d}^6$	$P2_1/c = C_{2h}^5$		$Pnma = D_{2h}^{16}$	$P6_3/mma = D_{6h}^4$
Z	2	4		4	2
Atom sites	Ca 2b C 2a O 6e	All on 4e (general)		Ca 4c C 4c O 4c, 8d	
CO_3^{2-} site symmetry	D_3	C_1		C_3	
Reference	12	4		12	13, 14

X ray powder work (2) showed that up to 24 kbar there are no phase transitions in either aragonite or vaterite. Fong and Nicol (6) also demonstrated that the spectra of $\text{CaCO}_3(\text{II})$ and $\text{CaCO}_3(\text{III})$ suggest that neither have the aragonite nor vaterite structures.

The metastable phases of calcium carbonates have been investigated previously using DAC in the infrared region of the spectrum. However, the data obtained suffered from two restrictions; (i) In no case was the sample under hydrostatic pressure, hence due to the large shear stresses present, pure phases were not observed. This is particularly notable in the work of Cifrutak (9) where even at 61 kbar residual bands of $\text{CaCO}_3(\text{II})$ were observed; (ii) No external mode (i.e. far infrared) work has been performed. The only pseudo hydrostatic Raman work on CaCO_3 was that of Fong and Nicol. This was performed in a Drickamer cell, where the sample is surrounded by a solid medium (eg. NaCl) as opposed to the liquid used in our experiments.

7.2 Experimental

Calcite powder was obtained from the Geology Department, University of Leicester. Samples were loaded into the DAC without grinding, as the process of grinding would almost certainly have caused the transformation calcite - aragonite, and thus invalidated the experiments.

The sample was contained within a 0.5mm gasket hole in a 0.05mm inconel gasket, with Nujol as the hydrostatic medium.

Figure 7.2

Mid Infrared spectra of CaCO_3 at various pressures.

Calcite

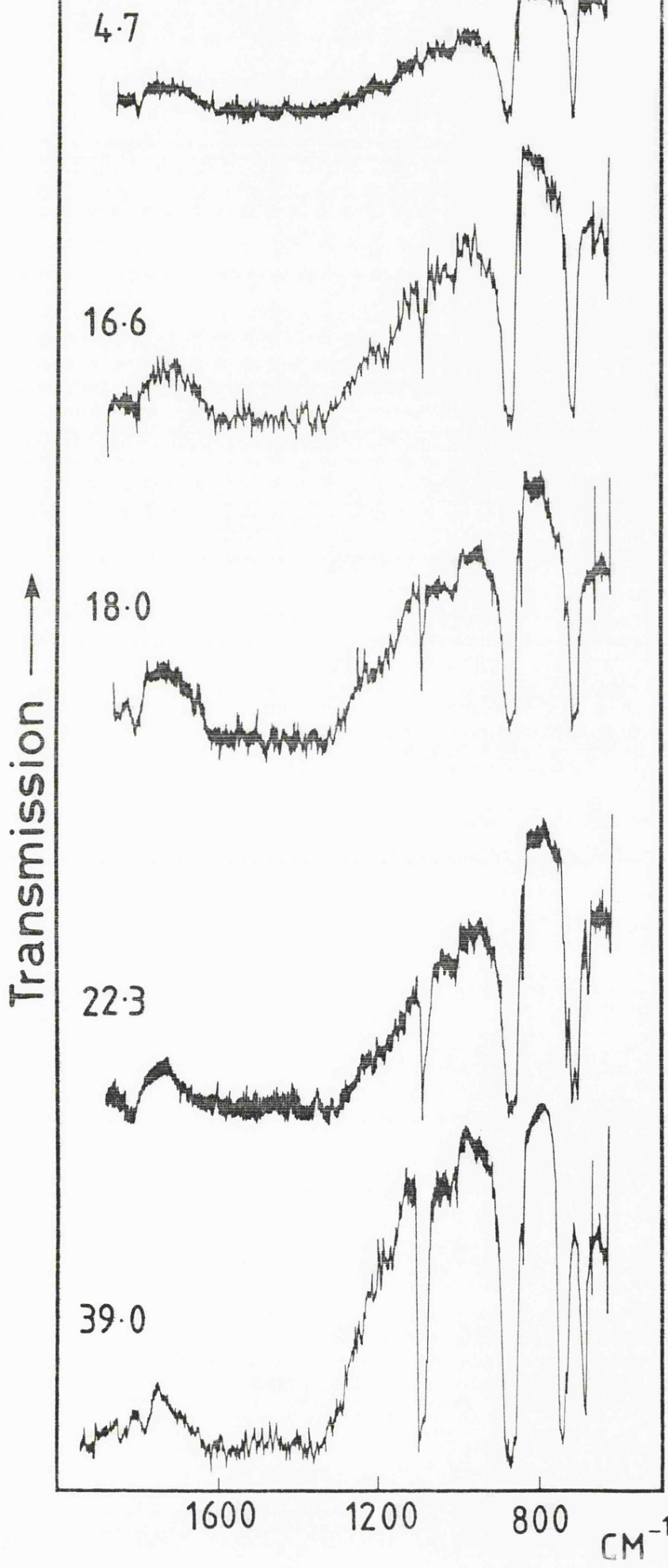


Figure 7.3

Far Infrared spectra of CaCO_3 at various pressures, obtained with a gasketed sample.

CaCO₃ (Calcite)

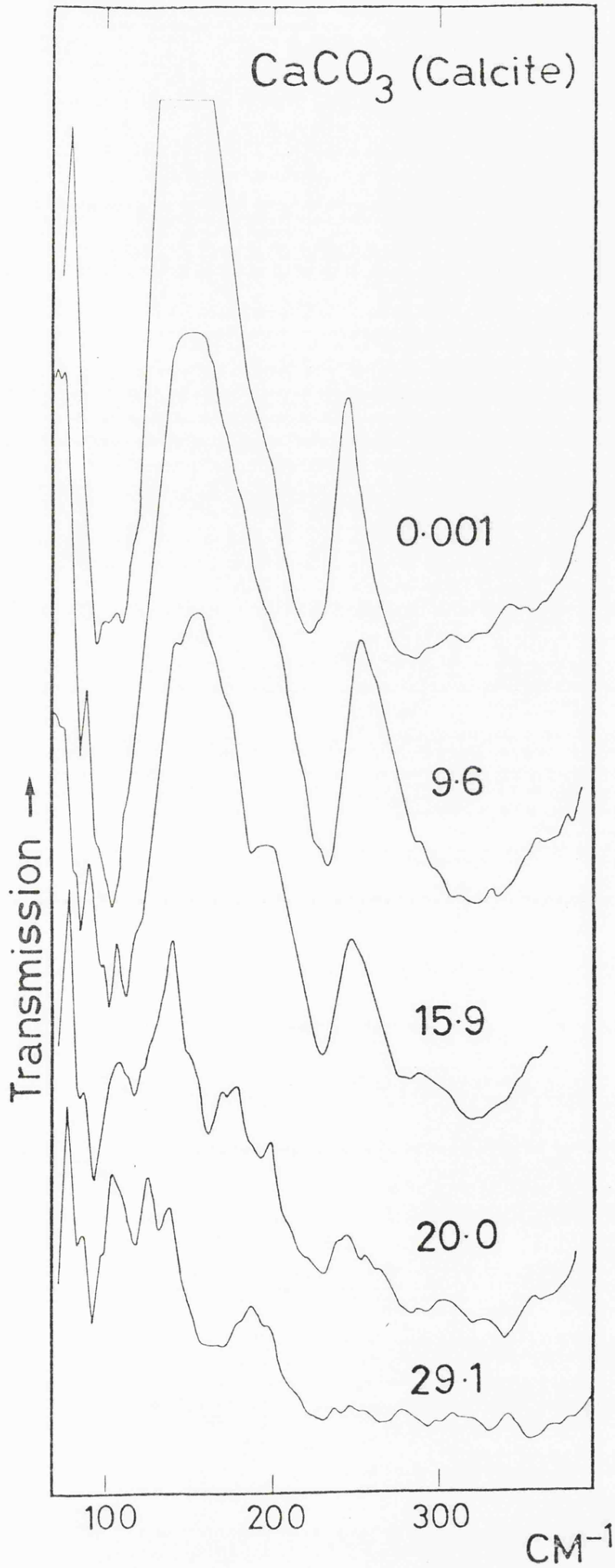


Figure 7.4

Far Infrared spectra of CaCO_3 at various pressures, obtained with an ungasketed sample.

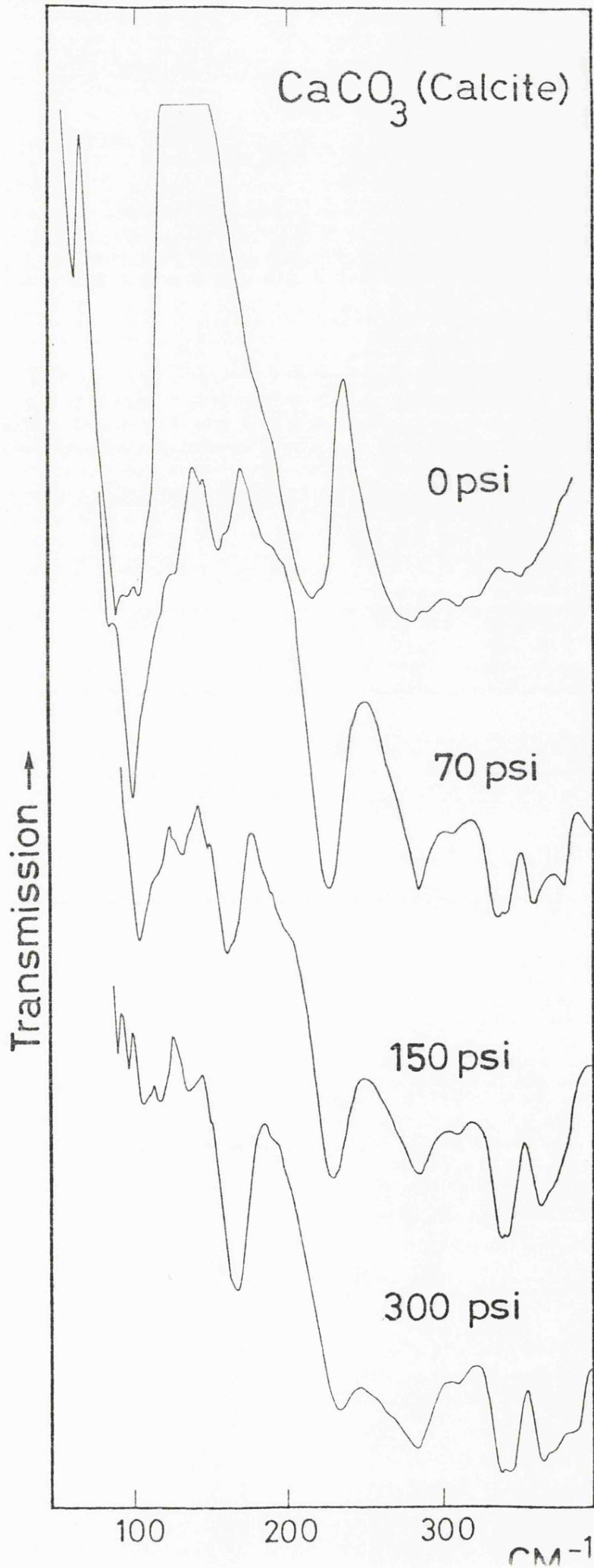


TABLE 7.2

Mid-i.r. wavenumbers/cm⁻¹ for CaCO₃ at
ambient temperatures and various pressures

	$\nu_1 + \nu_4$	ν_1	ν_2	ν_4	Phase
P/kbar					
0.001					
4.7	1795vw	-	877s,br	715s	Calcite/I
10.0	1802vw	1090vw	880s,br	717s	
16.6	1802vw	1088m	785s,br	712s	II
18.0	1805w	1092m	874s,br	735sh, 713s	
22.3	1815w,br	1090m-s	875s,br	738s, 722s, 712s, 685m	II/III
		1080sh			intergrowths
23.3	1815w,br	1090s	875s,br	737s, 722s, 710s, 685m	
		1080sh			
32.7	1835vw	1092s	876s,br	740s, 727sh, 685m-s	III
	1780vw	u.sh.			
39.0	1835vw	1094s	876s,br	740s, 730sh, 685s	III
	1780vw	u.sh.			

TABLE 7.3

Far-i.r. wavenumbers/cm⁻¹ for CaCO₃ at
ambient temperatures and various pressures

P/kbar	0.001	9.6	15.9	20.0	29.1
v/cm ⁻¹	103 ^b	105 ^b	102		
			113	117	117
					133
					160
				163	172
			188	192	
	222	231	232		
	250 ^c	270	280	200	200
			300		
	Phase	I	I	II	II

b Known to be the average of two bands.

c Indicates several unresolved bands above this value.

The far infrared spectra were obtained using a Beckman RIIC FS620 interferometer, and the mid infrared region studied by the use of a Perkin-Elmer 580 spectrophotometer. All mid infrared were recorded using integrated scan mode 1, with a 16 x multiplier employed to increase the signal/noise ratio.

7.3 Results and Discussion

Data for the infrared and far infrared regions are given in Tables 7.2 and 7.3 respectively, and Figures 2,3,4. Selection rules for CO_3^{2-} internal modes in CaCO_3 (I and II) are given in Table 7.4 and factor group analyses in Table 7.5 (obtained by the method of Adams and Newton (10)).

The internal mode region of calcite exhibits three infrared active vibrations, ν_2 , ν_3 and ν_4 (see Table 7.4) and three Raman allowed transitions ν_1 , ν_3 and ν_4 . A study of the Raman spectra of CaCO_3 has recently been performed by Fong and Nicol (6) and will be considered in conjunction with this work. Cifrutak(9) and Schock & Katz (10) have performed mid infrared work which predate this study, but it must be borne in mind that the samples studied by Cifrutak were ungasketed, and thus experiencing non hydrostatic pressure.

7.3 (i) The ν_1 region

The transition from CaCO_3 (I) = calcite, to CaCO_3 (II) is indicated by the appearance of a strong band in the ν_1 region at 1088cm^{-1} in the 16.6 kbar spectrum. This is particularly dramatic as ν_1 is infrared forbidden in CaCO_3 (I), although we do observe a very weak absorption at ca. 1090cm^{-1} evident by 10.7 kbar indicating

TABLE 7.4

Selection rules for the internal modes of CaCO_3 (I) and (II).

		CaCO_3 (I) = Calcite			CaCO_3 (II)	
		x2		x4		
D_{3h}		D_3	$D_{3d}^{a,b}$		C_1	C_{2h}^b
Ion		Site	Crystal		Site	Crystal
ν_1	a_1' (Ra)	$\nu(\text{CO}_3)_s$	A_1 (Ra)	$A_{1g} +$ (Ra) 1088	A_{1u} (inact.)	A
ν_2	a_2''	$\pi(\text{CO}_3)$	A_2 (ir)	$A_{2g} +$ (inact.)	A_{2u} (ir) 872	A
ν_3	e'	$\nu(\text{CO}_3)_a$	E (Ra, ir)	$E_g +$ (Ra) 1432	E_u (ir) 1407	2A
ν_4	e' (Ra, ir)	$\delta(\text{CO}_3)$	E (Ra, ir)	$E_g +$ (Ra) 714	E_u (ir) 712	2A

$6(A_g + B_g + A_u + B_u)$

a Frequencies from reference 11.

b These columns sum to give the rows vib of Tables 7.5 A and B.

deviation from the D_3 symmetry. This behaviour was also observed by Cifruk (9) and Schock and Katz (8), although Schock and Katz found that the band remained after pressure release. Cifruk attributes this to formation of the aragonite polymorph, the thermodynamically stable form at high pressures, although evidence for this is lacking. Appearance of a weak, formally forbidden ν_1 infrared absorption has been found from many materials which adopt the calcite structure but the reason for this is thought to be due to a small amount of anion disorder. Below 22.3 kbar ν_1 appears as a single sharp band within the limits of our resolution (3.7cm^{-1}). In the 22.3 kbar spectra a second component is clearly present (but not fully resolved); as this is just within what we believe to be the CaCO_3 (III) region, and as this structure persists to higher pressures, we consider it reasonable to attribute this ν_1 doublet to CaCO_3 (III).

In their Raman study of CaCO_3 at high pressures Fong and Nicol (5) found ν_1 to be a single band to 18 kbar and then two components with $\Delta\nu_1 = 16\text{cm}^{-1}$ above 18 kbar. However, comparison of their results with our own on a semi quantitative basis will be subject to two uncertainties which should be indicated. Firstly, the Drickamer cell design (used by Fong and Nicol) is known to subject the sample to some small shear stresses in addition to the desired compression. This may well affect the frequencies of vibrational modes. Secondly, they were not using the now almost universal Ruby line calibration technique (which they pre dated). Useful comparisons between the two sets of data may still be made.

TABLE 7.5

Factor group analyses for CaCO_3 (I) and (II)

A. CaCO_3 (I) $D_{3d}^6 = R3c$, $Z = 2$

	D_{3d}	A_{1g}	A_{2g}	E_g	A_{1u}	A_{2u}	E_u
Ca	2b	0	0	0	1	1	2
C	2a	0	1	1	0	1	1
O	6e	1	2	3	1	2	3
N_{Total}		1	3	4	2	4	6
T_A					0	1	1
T		0	1	1	1	1	2
R		0	1	1	0	1	1
Γ_{vib}		1	1	2	1	1	2
Activity		Ra	-	Ra	-	ir	ir

B. CaCO_3 (II) $P2_1/c = C_{2h}^5$, $Z = 4$
All atoms on 4e

	C_{2h}	A_g	B_g	A_u	B_u
N_{Total}		15	15	15	15
T_A				1	2
T		6	6	5	4
R		3	3	3	3
Γ_{vib}		6	6	6	6
Activity		Ra	Ra	ir	ir

 T_A = acoustic and T = optic branch translatory modes.R = librational modes. Γ_{vib} = internal modes.

For CaCO_3 (II) both Raman and infrared spectra should exhibit a doublet in the ν_1 region if full factor group splitting occurs. As neither Fong and Nicol, Cifrutak nor ourselves find this to be the case, we must enquire whether site symmetry group rules correspond to the observables more closely. Carbonate is on general sites; the single ν_1 mode is therefore active and coincident in both infrared and Raman spectra. Fong and Nicol found ν_1 at 1096cm^{-1} at 14 kbar, whereas at 16.6 kbar we find it at 1088cm^{-1} . It is altogether possible that Fong and Nicol's pressures are slight underestimates. Thus CaCO_3 (III), which they indicate as having examined at 18 kbar is now believed not to be formed until 22 kbar. Since ν_1 increases slightly with pressure, see Table 7.2, then it is probable that the Raman and infrared frequencies are coincident within experimental error. It would be desirable, however, to directly examine these frequencies on the same sample.

Both Fong and Nicol and ourselves found that on entering CaCO_3 (III) ν_1 becomes a doublet. If we take their 18 kbar spectrum as comparable to ours at 23.3 kbar (i.e. both samples were just within the CaCO_3 (III) phase, then the Raman bands are about 8cm^{-1} higher than the infrared ones. If this difference is significant, the implication is that CaCO_3 (III) has a centrosymmetric cell. Non coincident infrared/Raman doublets also imply that the cell has $2\bar{2}2$.

7.3 (ii) The ν_2 Region

The ν_2 vibration is originally a single band in all three phases, and shows a remarkable insensitivity to pressure increase. Both Fong and Nicol and the present work found no significant increase in frequency in ν_2 in CaCO_3 (III) over a 20 kbar range. ν_2 is rather broad in all three phases. In Phase I this is undoubtedly due to the lo-to splitting (10) of 19cm^{-1} which is large relative to that of ν_4 . This large splitting means that the presence of the reflectance component of this band will become evident, and will give the band a broad appearance. This is not an unreasonable explanation of the ν_2 region spectra for phases II and III also. It is altogether possible that unresolved components be within the ν_2 band profiles, but it is noted that Fong and Nicol's Raman spectra likewise show no splitting here.

The difference between the 16.6 kbar value for ν_2 in CaCO_3 (II) = 875cm^{-1} , and that of Fong and Nicol at a nominal 14 kbar, = 866cm^{-1} are too large to be accounted for (bearing in mind the marked pressure in sensitivity of ν_2) by the errors considered in the ν_1 discussion. Whatever experimental conditions cause the difference in the observed value for a given frequency for our two data sets, the difference $\nu_1 - \nu_2$ is 230cm^{-1} for Fong and Nicol, and 213cm^{-1} for the present work. It would therefore appear that the Infrared and Raman components of ν_2 are genuinely non coincident, but that the remaining factor group component expected in each spectrum, corresponding to the observed component in the other, is vanishingly weak.

7.3 (iii) The ν_4 Region

This region is possibly the most structurally informative region. Theory predicts a single, doubly degenerate infrared active band, (E_u) and an analogous Raman active vibration (E_g). This is observed in practice, the Infrared and Raman band (δ) both showing a modest pressure dependence. ν_4 appeared to be a multicomponent envelope at 16.6 and 18.0 kbar, but no components clearly resolve until Phase III was entered.

In Phase III the most characteristic new feature was a prominent infrared absorption at 685cm^{-1} , accompanied by a Raman active analogue (δ) at 695cm^{-1} . The obvious separation from the now characteristically complex part of the ν_4 spectrum at frequencies $> 710\text{cm}^{-1}$, together with the evidence (from ν_1 and ν_2) of small factor group splittings, strongly argue for the presence of two crystallographically distinct anions in the unit cell. This, together with the other internal and external mode evidence, leads to the suggestion that CaCO_3 (III) is formed from CaCO_3 (II) by the unit cell of (II) doubling in some direction to give $Z = 8$.

Our apparent but unresolved splitting for CaCO_3 (II), together with an accompanying resolved splitting in the Raman spectra of Fong and Nicol, appears to support the idea of the dominance of site group other than factor group rules. Thus, the site rules would

predict ν_4 to be a doublet (2A) in Phase II, which is Infrared/Raman coincident, and this is, to within the limits of experimental error, as observed.

The mid infrared spectra obtained at 22.3 and 23.3 kbar appear to be of (II/III) intergrowths as judged by other ν_4 region behaviour. This is unsurprising, as we are still very close to the transition pressure. However, above 30 kbar we are clearly observing the spectrum of CaCO_3 (III), a much simpler spectrum consisting of bands centred near 685 and 740cm^{-1} , with a clearly resolved shoulder on the 740cm^{-1} band. The band at 712cm^{-1} is no longer evident, this we believe being due to residual CaCO_3 (II). It is worth observing that this band was present even at 61 kbar in Cifrulak's Infrared spectra (8) and clearly demonstrates the advantage of using gasketed samples. The Raman data for Phase III correspond well to our infrared data, Fong and Nicol's work being performed in a more hydrostatic environment than that of Cifrulak.

Finally, it is notable that the changes in the ν_4 region which characterise CaCO_3 (II) are reflected in the $\nu_1 + \nu_4$ combination, which splits into a doublet. In calcite this combination must originate from $A_{1g} (1088) + E_u (712.5) = E_u (1800.5)$. Retention of the centre of symmetry in passing to Phase II requires an analogous selection rule, and an equivalent but more complex result arises for CaCO_3 (III) if the centre of symmetry is again retained.

7.3 (iv) The external mode region

The assignments of the lattice modes of calcite are well established. Selection rules are in Table 5A. We may consider how the modes of individual ions on their sites couple. It must be emphasised that, in general, the coupling which leads to factor group selection rules is relatively weak, and therefore that lattice modes of a given basic origin (eg. vibratory) will be found in similar positions in both Infrared and Raman spectra.

Thus;

	Site		X2	D_3^6d crystal
CO_3^{2-}	D_3	$R(z) A_2$		$A_{2g} + A_{2u}$
		$R(x,y) E$		$E_g + E_u$
		$T(z) A_2$		$A_{2g} + A_{2u}$
		$T(x,y) E$		$E_g + E_u$
Ca^{2+}	S_6	$T(z) A_u$		$A_{1u} + A_{2u}$
		$T(x,y) E_u$		$2E_u$

The established assignment is; E_g 156, 283; A_{2u} 92, 303, E_u 102, 223 297. The modes at 283, 297 and 303 are considered to be mainly libratory.

In Phase (II) each libratory degree of freedom generates a representation ($A_g + A_u + B_g + B_u$). Thus, in this phase the lattice mode spectrum would be expected to consist of groups of groups of two infrared and two Raman active bands in close proximity. These pairs will themselves be located

near the positions for CaCO_3 (I).

Far infrared spectra of CaCO_3 (I) Figure 7.3 obtained in a gasketed DAC, show three main absorption features. Two almost coincident bands, at 297 and 303 respectively, from a broad region of intense absorption from about 250 to 400cm^{-1} . Below 100cm^{-1} very little energy passes through the gasketed DAC, and the spectra are to be considered as unreliable in this region. They were supplemented by several 'ungasketed' runs, given as Figure 3. The Eu mode at 223cm^{-1} moves under pressure with $d w/ d p \approx .6\text{cm}^{-1}\text{kbar}^{-1}$. Increases of frequency with pressure are also evident for the higher frequency bands, but gross overlap makes measurement of these impossible.

Phase II is most clearly characterised by the appearance of two new bands at 163 and 192cm^{-1} at 20.0 kbar. Further absorption around 260cm^{-1} fills the region between the Eu mode (at 223cm^{-1} at ambient pressure) and the higher energy bands. These new features are close to the Raman bands reported by Fong and Nicol for CaCO_3 (II) at 14 kbar (155, 204, 240), in agreement with the selection rules. Nevertheless, the total numbers of infrared and Raman active lattice mode bands found are substantially less than would be predicted by factor group analysis. As in CaCO_3 (I), it is almost certain that bands of both Ag and Bg symmetry are overlaid in the Raman spectra, and similarly for Au and Bu modes in the infrared.

On entering Phase III the far infrared spectra become yet more complex, as is to be expected from the evidence of the internal modes and the results of Fong and Nicol. They found 13 lattice mode bands between 100 and 360cm^{-1} . In our far Infrared spectrum of Phase III at 29.1 kbar, Figure 2, it is evident that many absorption bands are present, but few can be measured with any accuracy as they virtually form a continuum.

Summary

Infrared and far Infrared spectra of CaCO_3 have been recorded under hydrostatic or near hydrostatic conditions in a DAC to 40 kbars. The new data has been analysed in conjunction with the Raman results of Fong and Nicol. The spectra of CaCO_3 (II) are consistent with recent X ray single crystal studies, with the site group rather than factor group predominating and accounting for most of the features. For CaCO_3 (III) a structure is postulated where there are two crystallographically distinct sets of anions with z being at least 4 and probably 8.

References

1. Bridgman, P.W., *Amer. J. Sci.*, 237 7 (1939).
2. Jamieson, J.C., *J. Geology*, 65 333 (1957).
3. Davis, B.L., *Science* 145 489 (1964).
4. Merrill, L., Bassett, W.A., *Acta Cryst.*, B31 343 (1975).
5. MacDonald, G.J.F., *Amer. Min.*, 41 744 (1956).
6. Fong, M.Y., Nicol, M., *J. Chem. Phys.*, 54 579 (1971).
7. Weir, C.E., Lippincott, E.R., Valkenberg Van, A., Bunting, E.N.,
J. Res. Nat. Bureau Stds., 63A 55 (1959).
8. Schock, R.N., Katz, S., *Amer. Min.*, 53 1910 (1968).
9. Cifrutak, D., *Amer. Min.*, 55 815 (1970).
10. Adams, D.M., Newton, D.C., *J. Chem. Soc. (a)* 2283 (1971).
11. Decius, J.C., Hexter, R.M., "Molecular Vibrations in Crystals",
McGraw Hill, New York, p241 (1977).
12. Wyckoff, R.W.G., "Crystal Structures". Vol. 2, 2nd ed.,
Interscience, New York, 1967.

13. Sato, M., Matsuda, S., Zeit. Krist, 129 405 (1969).
14. Meyer, H.J., Zeit. Krist, 128 183 (1969).

CHAPTER 8

A STUDY OF THE EFFECT OF PRESSURE ON THE FAR INFRARED SPECTRA

OF SOME COMPLEXES $\text{Fe}(\text{O-PHENANTHROLINE})_2\text{X}_2$

CHAPTER 8

A STUDY OF THE EFFECT OF PRESSURE ON THE FAR INFRARED SPECTRA OF SOME COMPLEXES OF Fe (O-PHENANTHROLINE)₂ X₂

8.1 Introduction

Transition metal complexes which exhibit magnetic crossovers have been the subject of considerable interest.

For a free atom or ion, or ionic compound the normal spin state is that of maximum multiplicity in accordance with Hunds rule. However, with a sufficiently large ligand field, octahedral transition metal complexes with configurations d^4 , d^5 , d^6 and d^7 may adopt a low spin ground state. According to ligand field theory the transition between these states should occur discontinuously at a certain field strength Δ , often referred to as the mean spin pairing energy, This situation is best illustrated by the crossing over of ground state terms in the Tanabe-Sugano diagrams.

A large proportion of Fe (II) (d^6) compounds which are low spin involve organic ligands or ligands such as CN^- . These have vacant π antibonding (π^*) orbitals which are not too high in energy above the ground state, and have the correct symmetry to bond with the occupied metal π^* (t_{2g}) orbitals. This "back donation" of metal electrons into the ligand orbitals gives a stronger M - L band, a large ligand field splitting Δ , and a decrease in interelectronic repulsion (due to the delocalisation of the t_{2g} electrons). The high value of Δ thus experienced by

the metal ion, $>T$, causes the electrons to spin pair with the existing t_{2g} quartet.

The effect of increasing pressure and/or decreasing temperature is to decrease $d(M-L)$ and to increase the ligand field (2, 3). Thus, at a field strength Δ close to T , the separation of the two states of different multiplicity attains values within the thermally accessible range, equilibria between these states may be expected.

Although considerable effort has been spent in seeking new compounds displaying this sort of behaviour, few examples have been established definitely (4). These include compounds of d^6 and d^7 in octahedral symmetry and compounds of the configurations d^5 and d^8 in lower symmetry.

The compounds of ferrous iron with 1, 10 phenanthroline have wide interest as prototypes for biologically active compounds, and their properties have been extensively studied (5, 6, 7). 1, 10 phenanthroline is an aromatic system with nitrogens at the 1, 10 positions, each of which can coordinate to a metal ligand.

The compounds in $[\text{Fe}(\text{phen})_2\text{X}_2]^{2+}$ would seem a particularly suitable series to look for spin state equilibria within systems of configuration d^6 . The series includes both high and low spin compounds, the multiplicity of the ground state being dependent on the position of the ligand in the spectrochemical series. If $X = \text{Cl}^-$, Br^- , I^- , N_3^- , NCS^- , NCSe^- , OCN^- , HCOO^- , high spin compounds are formed, (8, 9, 10). If $X = \text{CN}^-$, CNO^- , NO_2^- diamagnetic low spin compounds are obtained (11).

Konig and Madeja (13) have measured the magnetic susceptibilities of $\text{Fe}(\text{phen})_2\text{NCS}_2$ and $\text{Fe}(\text{phen})_2\text{NCSe}_2$ and find a critical temperature of 174K for the NCS^- complex, and 232K for the NCSe^- , below which the magnetic moments decrease rapidly.

Fischer and Drickamer (14) have studied the effect of pressure on spin state by Mössbauer spectroscopy. They conclude that, with the application of moderate pressures, $[\text{Fe}(\text{phen})_2\text{X}_2]$, $\text{X} = \text{NCS}^-$, NCSe^- , N_3^- tend to convert to low spin, but with pressures above 30 - 40 kbar there would appear to be a reversal of this trend, and in fact experience a net low to high conversion. If $\text{X} = \text{CN}^-$ the complex is low spin at ambient pressure, and at high pressures shows significant conversion to high spin.

Far and mid infrared studies of $[\text{Fe}(\text{phen})_2\text{X}_2]$ have been performed under pressure (15, 16, 17) but none under hydrostatic pressure. The compounds therefore experience shear stress and the spectra reflect this.

Few assignments of the vibrations which constitute the low frequency ($< 400\text{cm}^{-1}$) infrared spectra of these materials exist. It would therefore be instructive to attempt to indicate the nature of the vibrations involved.

82. Experimental

$[\text{Fe}(\text{o-phen})_2\text{X}_2]$ where $\text{X} = \text{NCSe}^-$, N_3^- , I^- were provided by G.J. Long, University of Missouri. $[\text{Fe}(\text{o-phen})_2\text{NCS}_2]$ was prepared by the

author by first preparing $\text{Fe}(\text{o-phen})_3\text{NCS}_2$ by mixing aqueous solutions of KNCS, o-phenanthroline and ferrous chloride. This was refluxed in dichloromethane, resulting in the bis NCS complex.

Far infrared spectra were recorded on a Beckman RIIC FS620 interferometer.

Experiments were performed in a Mk II DAC, using an inconel gasket 0.05mm thick, with a 0.5mm gasket hole. Nujol was used as the hydrostatic medium and pressure calibration was by the R_1R_2 ruby line method.

No Raman data could be obtained for these deeply coloured compounds.

8.3 Theoretical Analysis of the Vibrational spectra of cis $[\text{Fe}(\text{o-phen})_2\text{X}_2]$

The vibrational spectra of these materials are extremely complex. Valuable insight has resulted from the use of metal isotopes, revealing bands in both tris phenanthroline (18, 22) and $[\text{Fe}(\text{o-phen})_2\text{X}_2]$ (16) complexes which may be attributed to M-N bond stretching, but more detailed assignments do not exist.

In order to analyse the spectrum of $[\text{Fe}(\text{o-phen})_2\text{X}_2]$ it is helpful to consider the evidence available for $\text{Fe}(\text{o-phen})_3\text{X}_2$ (18). o-Phenanthroline is of C_{2v} symmetry, and its sixty internal modes span the representation

$$\Gamma = 21 A_1 + 10 A_2 + 20 B_1 + 9 B_2$$

All the modes are Raman active, and only the A_2 modes are not infrared active.

A thorough analysis of the phenanthroline spectrum has very recently been published (19, 20). This shows that the only ligand bands $\leq 400\text{cm}^{-1}$ are;

$$\nu_{20} (A_1) - 408$$

$$\nu_{21} (A_1) - 249$$

$$\nu_{41} (B_1) - 395$$

$$\nu_{49} (A_2) - 416$$

$$\nu_{60} (B_2) - 122$$

Before analysing the spectra of $\text{FeX}_2(\text{o-phen})_2$, the somewhat simpler case of the tris complexes will be considered.

Since o-phen is a very rigid ligand this analysis is based on a model in which the spectra of its complexes are taken to arise from combinations of the translations and rotations permitted to each free molecule.

The ion $[\text{Fe}(\text{o-phen})_3]^{2+}$ has D_3 symmetry. In it each ligand is on a C_2 site. Cis $\text{Fe}(\text{o-phen})_2\text{X}_2$ has C_2 symmetry with each o-phen ligand on C_1 sites.

Therefore the following correlations may be constructed;

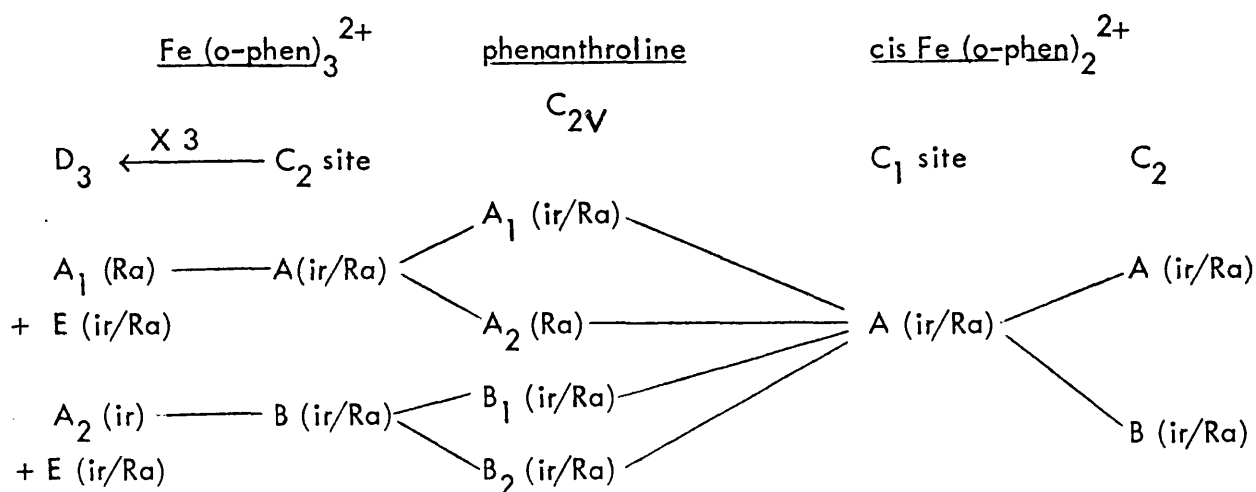


Table 8.1 Assignments of infrared bands (cm^{-1}) for $\text{Fe}(\text{o-phen})_3^{2+}$ in the $150 - 400\text{cm}^{-1}$ interval.

o-phen (a)	$[\text{Fe}(\text{o-phen})_3]^{2+}$ (a, b)	Ref 11	Present work
	375		
	359	$\nu(\text{Fe} - \text{N})$	$\nu(\text{Fe} - \text{N})$
259	296	Ligand B	$\nu_{21}, A_1; \nu_{59}, B_2$
242	288		of o-phen
	245	Ligand C	o-phen wag
	235		
	214		
	211	$\delta(\text{N Fe N})$	$\delta(\text{N Fe N})/\text{o-phen wag}$
	191		
	176	Ligand D	o-phen torsions

a Ref. 18

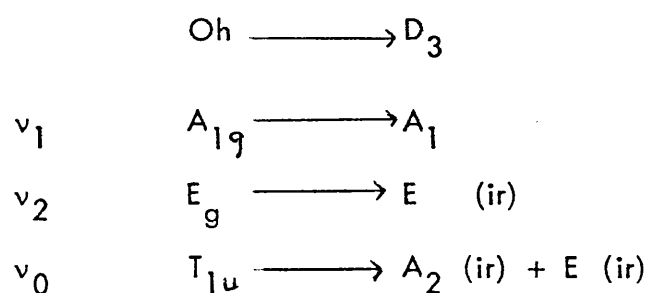
b For BF_4^- salt

The tris complexes can be considered as being formed by the combination of metal atom and three ligand. Before combination with the metal each ligand has three translational and three rotational degrees of freedom. When the complex is formed these become various types of skeletal mode. Thus

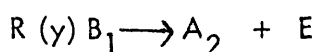
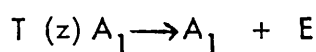
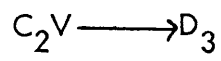
D_3	A_1	A_2	E
Fe on D_3 site	0	1	1
3 ligands translations	1	2	3
on C_2 sites, librations	1	2	3
N total	2	5	7
T_{xyz}, R_{xyz}	0	2	2
Γ vibrations	2	3	5

From this we would expect 8 skeletal vibrations ($3A_2 + 5E$) in the far infrared spectra of each tris complex. In addition to these, internal modes of the phenanthroline (19, 20) are anticipated. Three of the eight skeletal modes are attributable to $\nu(\text{Fe} - \text{N})$ vibrations. This can be shown in two ways.

First, for a regular octahedral (O_h) FeN_6 , the $\nu(\text{Fe} - \text{N})$ modes span the representation $A_{1g} + E_g + T_{1u}$. Correlating to D_3



Secondly, the $\nu(\text{Fe} - \text{N})$ can be considered as arising from (i) the T (z) translation of a phenanthroline ligand and (ii) the R (y), i.e. in plane rotation.



It is notable that for $\text{Ni}_2(\text{o-phen})_3$ these three ir active $\nu(\text{Ni} - \text{N})$ modes (located by metal isotope substitution (17)) are at 243, 260 and 300cm^{-1} (for the perchlorate). For the Fe^{II} complex only two such bands were located, at 359 and 374cm^{-1} (also for the perchlorate).

In the region above 150cm^{-1} three different salts of $\text{Fe}(\text{o-phen})_3^{2+}$ exhibit the same number of far infrared bands (18). All must therefore arise from the cation. Below 400cm^{-1} each complex shows ten absorption bands (see table 8.1), in these accord with the above theory. Thus, the strong bands near 296cm^{-1} with the ligand modes originally at 242, 259cm^{-1} . As will be described later, this strong feature remains prominent in all the $[\text{Fe}(\text{o-phen})_2 X_2]$ compounds in both high and low spin forms, and throughout all published spectra of the tris (o-phen) complexes, showing little frequency variation. A further six low frequency bands were observed, whereas only five are expected. Two possible explanations may be advanced. The additional band may be due either to crystal site splitting of one of the E modes or it may be ν_{59} of o-phen, in which case it is one of the pair of bands in the $230 - 250\text{cm}^{-1}$ region.

It is noted that more bands are found, and in the wrong positions (19, 20) than can be accounted for on the basis of inactive (in C_{2V}) free ligand modes. supposedly mode active in the complex. Hence the published descriptions of several of the low frequency modes as ligand B, C, etc.(18) is erroneous.

The theory outlined above is clearly for a single complex ion. In the crystalline state, the above prediction will be modified in two ways. Firstly the site field will (in the general case) relax the restrictions imposed by the molecular symmetry, and may lift degeneracies. This will have no noticeable effect for the cis $[\text{Fe}(\text{o-phen})_2\text{X}_2]$ compounds as the molecular symmetry (C_2) is so low that no additional bands will arise from site effects. Secondly, if there is more than one molecule in the unit cell, correlation coupling may lead to an increase in the number of bands observed. This however would normally only be observed under high resolution (and low temperature). Neither of these conditions apply in the present work. It would therefore seem reasonable to use molecular selection rules in order to attempt to attach some significance to the vibrations observed.

In addition to the internal modes and skeletal modes predicted, low frequency lattice modes may well be anticipated. From the data of Hutchinson, et al (22) the spectra of $[\text{Fe}(\text{o-phen})_2\text{X}_2]$ with $\text{X} = \text{ClO}_4^-$, BF_4^- , it can be seen that the spectra above 150cm^{-1} are essentially the same, therefore it can be asserted that they are due to the cation.

Cis $[\text{Fe}(\text{o-phen})_2 \text{X}_2]$ is of C_2 symmetry. If the X ligands are removed it can be shown that the skeletal (i.e. omitting internal modes of phenanthroline) modes span the representation

Γ skeletal = $5A + 4B$, all of which are ir/Raman active. Of these ν (Fe - N) account for $2A + 2B$.

If X is monatomic six further low frequency modes must be added (three degrees of freedom per ligand). They are

ν (Fe - X)	A + B	pr (Fe X ₂)	B	pr (Fe X ₂)	A
δ (Fe - X ₂)	A	pw (Fe X ₂)	B		

Thus the low frequency spectra may be expected to exhibit $8A + 7B$ modes plus the known internal modes of the phenanthroline ligands.

Finally it may be noted that for $X = \text{NCS}^-$, NCSe^- or N_3^- , in addition to the above $5A + 4B$ skeletal, there will be 18 further vibrations, which, for the case of Fe - NCS bonding are;

ν (C = S)	A + B	ν (C = N)	A + B	ν (M - N)	A + B
δ (NCS)	A + B	δ (CNM)	A + B	δ (MN ₂), pr (MN ₂)	A + B
(NCS)	A + B	(CNM)	A + B	pr (MN ₂), pw (MN ₂)	A + B

Of the above ν (C = S) and ν (C = N) are definitely $> 400\text{cm}^{-1}$.

The remainder however may be expected to be $< 400\text{cm}^{-1}$, and in addition with the skeletal and the known modes of phenanthroline will be expected to yield complex low frequency infrared spectra.

Figure 8.1

Infrared spectra of $\text{Fe}(\text{o-phen})_2 \text{I}_2$ at various pressures (kbar).

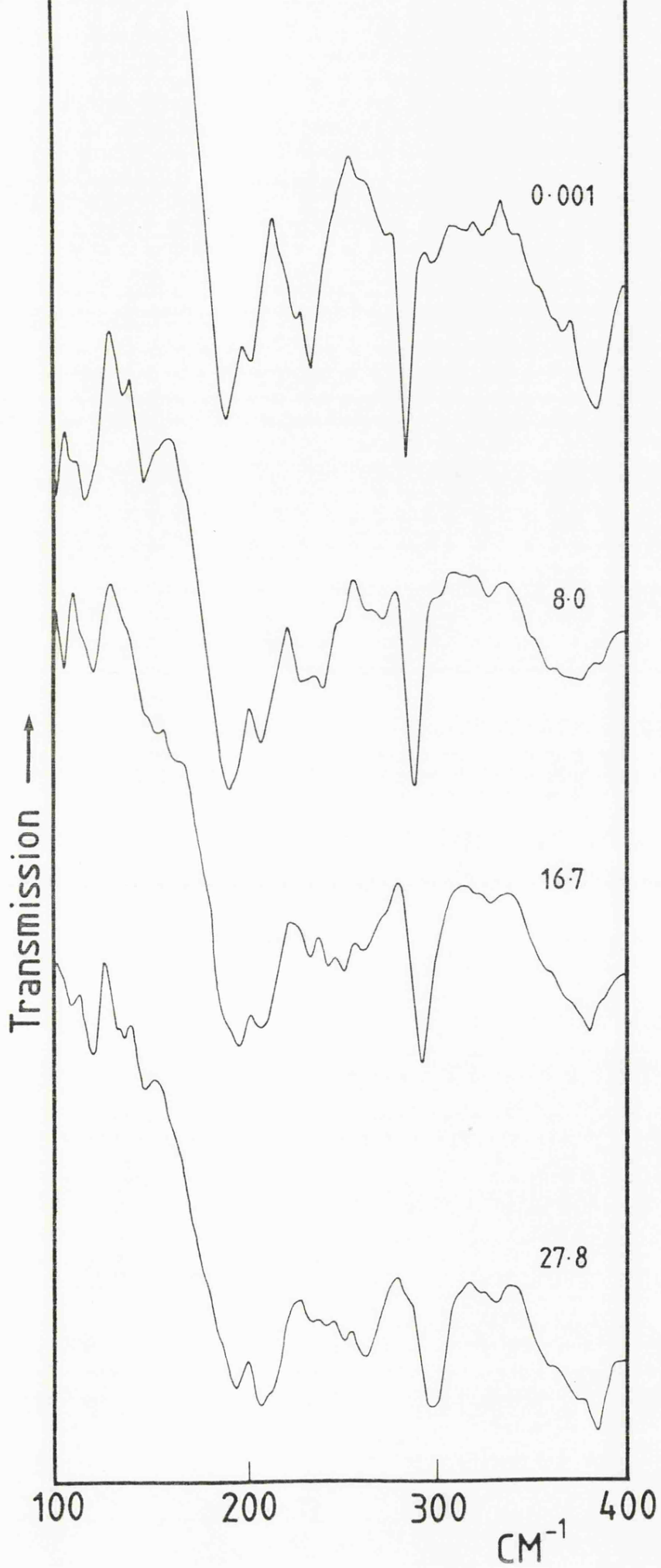
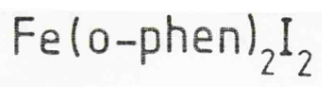


TABLE 8.2 Infrared mode frequencies/cm⁻¹ for [Fe (o-phen)₂]₂
at various pressures.

0.001 kbar	8.0 kbar	16.7 kbar	27.8 kbar
285 (s)	288.5 (s)	293 (s)	298 (s)
274 (w)	274.5 (w)	274 (sh)	
	262.5 (w)	262 (m)	264 (s)
	250.5 (sh)	251 (w)	252 (m)
236 (m)	240 (m)	243 (m)	242 (m)
227 (w)	230.5 (w)	233 (w)	234 (w)
204 (m)	207.5 (m)	207 (s)	209 (s)
190 (s)	190.5	195	195
		187.5 (sh)	186 (sh)

Figure 8.2

Infrared spectra of $\text{Fe (o-phen)}_2 (\text{N}_3)_2$ at various pressures (kbar).

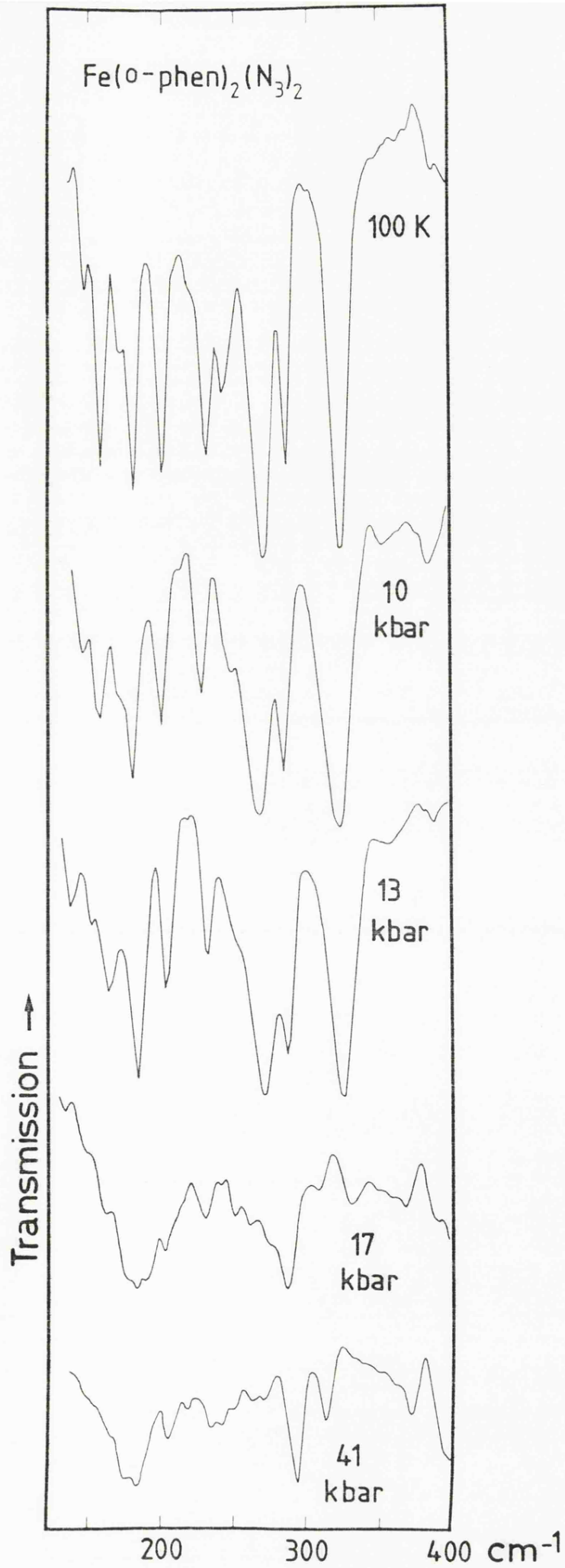
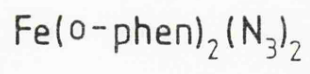


TABLE 8.3 Infrared mode frequencies/cm⁻¹ for Fe (o-phen)₂ (N₃)₂
at various pressures.

0.001 kbar (100K)	10 kbar	13 kbar	17 kbar	41 kbar
			136	146 (sh)
135	135	141		
151.5 (s)	150 (s)	153 (m)	150 (sh)	164(sh)
161 (m)	160 (sh)	166 (sh)	172 (sh)	174 (sh)
174 (sh)	173 (sh)		177 (sh)	
184 (s)	183 (s)	185 (s)	184 (m) 193	184 (m)
203 (s)	202 (s)	206 (s)	204 (m)	206 (w)
235.5 (sh)	230 (w)	233 (w)	232 (w)	235 (sh) 243 (m)
245	250(sh)	250(sh)	252 262	264 272
272 (s)	269 (s)	272 (m)	275 (sh)	
288 (s)	286 (s)	286.5 (s)	288 (s) 309	293 (s)
324.5 (s)	324 (s)	326 (s)	332 (m)	313 (m)
			368	372

Figure 8.3

Infrared spectra of $\text{Fe (o-phen)}_2 (\text{NCS})_2$ at various pressures (kbar).

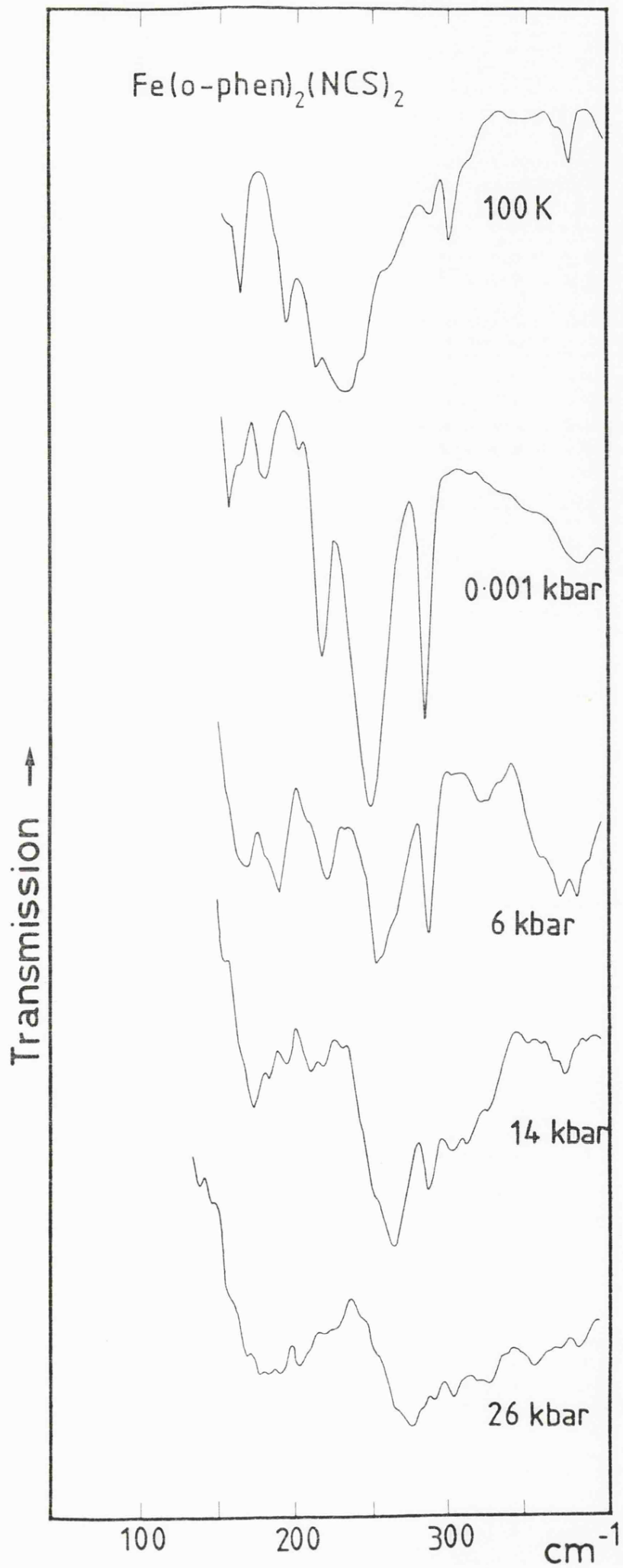


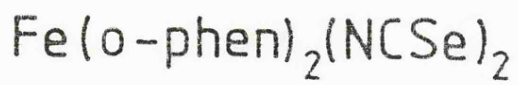
TABLE 8.4 Infrared mode frequencies/cm⁻¹ for Fe (o-phen)₂NCS₂
at various pressures.

0.001 kbar (100 K)	0.001 kbar	2.8 kbar	5.7 kbar	13.9 kbar	26.0 kbar
	298 (s)			302 (w)	<u>a</u>
285 (s)	286 (m)	286 (s)	287 (s)	288 (s)	
248 (s)	242 (s)	254 (s)	255 (s)	255 (sh)	
	230 (s)				
217 (m)	213 (m)	218 (m)	222 (m)	220 (w)	
202 (vw)	194 (m)	205 (sh)	209 (sh)	210 (w)	
179 (w)	184 (sh)	185 (sh)	189 (m)	192 (w)	
164 (w)	164 (m)	177 (m)	182 (sh)		
157 (w)					

a difficult to distinguish individual bands at this pressure.

Figure 8.4

Infrared spectra of $\text{Fe (o-phen)}_2 (\text{NCSe})_2$ at various pressures (kbar).



Transmission \rightarrow

0.001 kbar

9 kbar

22 kbar

100 200 300 400 cm^{-1}

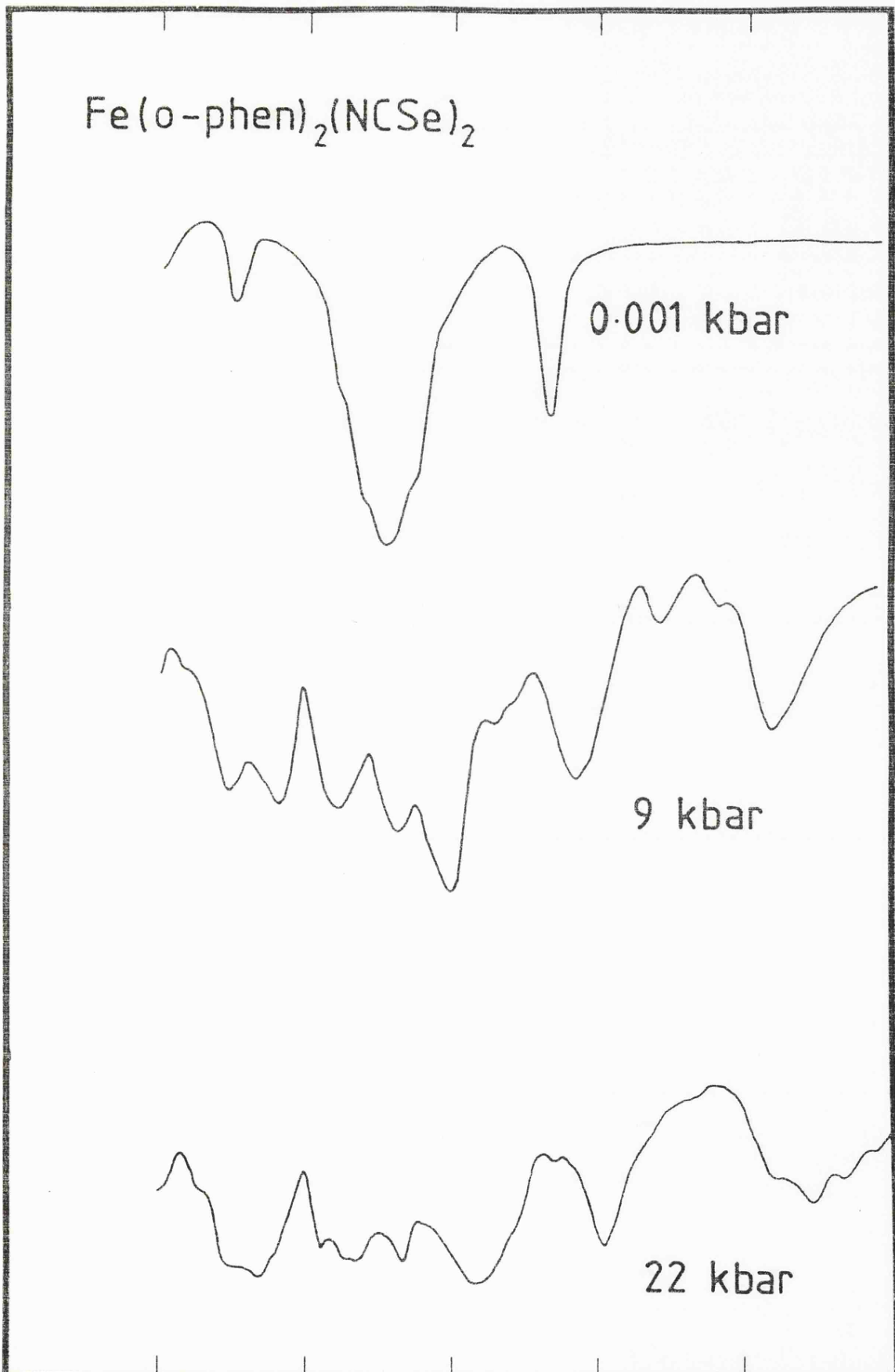


TABLE 8.5 Infrared mode frequencies/cm⁻¹ for Fe (o-phen)₂ NCS₂
at various pressures.

0.001 kbar	4.9 kbar	7.9 kbar	9.0 kbar	21.7 kbar	33.2 kbar
	356 (w)	361 (m)	360 (m)	360 (w)	360 (w)
		320 (w)	320 (m)		
284 (s)	286 (s)	287 (s)	293 (s)	302 (s)	304 (s)
			264 (w)	263 (s)	264 (s)
239 (sh)	240 (sh)	242 (s)	248 (s)	251 (s)	252 (s)
220 (sh)	225 (sh)				
	206 (sh)	208 (m)	210 (m)	216 (m)	218 (sh)
					212 (m)
	191 (m)	191 (m)	191 (m)		207 (sh)
179 (m)	182 (m)	184 (m)		184 (s)	
			174 (m)		

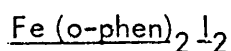
8.4 Results and discussion

Valuable work (15, 16) has been performed on cis (Fe (o-phen)₂ X₂) X = NCS, NCS_e. By the use of metal isotope technique, and low temperatures to generate the low spin forms the following metal-ligand assignments could be made.

	NCS		NCS _e	
	Low Spin	High Spin	Low Spin	High Spin
ν (Fe - N) X	532.6 528.5	252.0	530.5 527.0	228.0
ν (Fe - N) phen	379.0 371.0	220	366 360	218

The above large changes in frequency are associated with the large changes in the Fe - N bond distances and bond strengths which parallel the change in spin state. On cooling from room temperature to 100K, the Fe - N (NCS) bond length decreases by 0.08Å, and Fe - N (phen) by 0.12 and 0.16Å.

The comparison of the spectra of Fe (o-phen)₃²⁺ and cis Fe (o-phen)₂ X₂ should be helpful in the assignment of bands due to the X ligands since skeletal modes due to the o-phen ligands will be in similar positions (although different in number).



For cis [Fe (o-phen)₂ I₂] the highest of the 3A + 3B modes due to X = I will be ν (Fe - I). In cis [Fe (CO₄)₄ I₂], ν (Fe - I) modes are at 185 and 195cm⁻¹ (24). Values not dissimilar to these would be expected for the above.

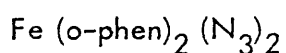
Hence, at ambient pressure, all the bands $> 200\text{cm}^{-1}$ may be attributed to skeletal modes plus the internal modes of o-phen. Conversion to the low spin complex would be expected to raise $\nu(\text{Fe} - \text{I})$ but it is probable that this will simply raise them to values comparable with $\text{cis} [\text{Fe}(\text{CO})_4\text{I}_2]$

There are no spin equilibrium data available for this material. Since $\text{I}^- < \text{Cl}^- < \text{NCS}^-$ in the spectrochemical series there is little doubt that this complex would be high spin, and that the change to low spin would be expected at somewhat higher pressure than for $\text{X} = \text{NCS}^-$. At 40 kbar Fischer and Druckamer (14) find that for $\text{X} = \text{NCS}$, the complex was about 80% converted to low spin. Comparable figures for $\text{X} = \text{Cl}$ and $\text{X} = \text{Br}$ are 17% and 30% respectively. The ambient pressure spectrum of $[\text{Fe}(\text{o-phen})_2\text{I}_2]$ (above 200cm^{-1} is fairly simple, consisting of $\nu(\text{Fe} - \text{I})$, $\nu(\text{Fe} - \text{N})$ phen, $\nu(\text{phen})$ and little else.

As noted above $\nu(\text{Fe} - \text{N}(\text{phen}))$ for $\text{X} = \text{NCS}$ and NCSe is close to 220cm^{-1} in the high spin forms and around 360 to 380cm^{-1} in the low spin forms. Therefore we would anticipate, for $\text{X} = \text{I}$, a loss of intensity in the region 220cm^{-1} with increase in pressure. From figure 8.1 the most obvious change in the spectra is a decrease in the group of bands near 240cm^{-1} , which do not entirely disappear by 27.8 kbar. Concurrently the strong bands between 150 and 200cm^{-1} , probably attributable to $\nu(\text{Fe} - \text{I})$ show new contributions consistent with increase in low spin character. In addition, progressive changes are exhibited by weaker bands in the $250 - 280\text{cm}^{-1}$ region, chiefly the growth in intensity of the band initially at 264cm^{-1} . This vibration is probably a skeletal mode with a large contribution from flapping motions of coordinated o-phen relative to the rest of the molecule having

been shifted from below 200cm^{-1} in the high spin complex. The increase in intensity is attributed to the changes in geometry consequent upon an increasing percentage of low spin isomer. Strengthening of the Fe - N (phen) bond on transition to the low spin configuration implies increased electron delocalisation onto the (o-phen) ligand. Subsequent movement of this ligand will represent the movement of an increased charge, and therefore increased dipole, hence the increased ir intensity.

The presence of further new bands in the $250 - 280\text{cm}^{-1}$ region would support the idea of the (3A + 2B) skeletal bands being shifted from below 200cm^{-1} upon transition to low spin.



The spectra of $\text{Fe (o-phen)}_2 (\text{N}_3)_2$ is complex. In addition to Fe-phen bands ($5A + 4B = 2A + 2B$ (ν (Fe - phen)) + (3A + 2B) skeletal deformations), a variety of Fe - N_3 deformations are present. It is known (25) that coordinated N_3 has ν_2 (δ NNN) $\geq 580\text{cm}^{-1}$ but that $\nu(\text{M} - \text{N}_3)$ is between 310 and 450cm^{-1} , depending upon M. Also $\delta(\text{Fe} - \text{N} - \text{N})$ modes will occur, which have never been assigned.

Comparison of the 12.8 and 17.0 kbar spectra reveal major changes consistent with a transformation to low spin. This is further developed in the 40.5 kbar spectrum. The low spin phase is characterised by new bands near 370cm^{-1} , which are consistent with assignment to $\nu(\text{Fe} - \text{phen})$ low spin.

Concurrently $\nu(\text{Fe-phen})$ high spin at 234 and 245cm^{-1} lose intensity progressively with increase of pressure. The intense bands at 324 and 271cm^{-1} also vanish upon change to low spin, and are assigned to $\nu(\text{Fe} - \text{N}_3)$ and $\delta(\text{Fe} - \text{N} - \text{N})$ respectively.

The major frequency changes in $\nu(\text{Fe} - \text{N}_3)$ and $\nu(\text{Fe} - \text{phen})$ are associated with rises in their associated deformation modes. Hence, the region below the above modes must consist entirely of (o-phen) modes plus skeletal deformations. In particular the 120 to 220cm^{-1} region experiences a general increase in frequency of many bands.

The complete loss of the intense $\nu(\text{Fe} - \text{N}_3)$ band (324cm^{-1} at ambient pressure) by 40 kbar (its presence can be detected by a residual band at 17.0 kbar) implies that conversion to low spin is essentially complete by 40 kbar. This is in conflict with the Mossbauer evidence of Fischer and Drickamer (14) which indicates that there is only about 70% conversion to the low spin isomer, at 40 kbar, and moreover that, the percentage of low spin actually decreases at pressures above 40 kbar. In view of the intensity of the $\nu(\text{Fe} - \text{N}_3)$ low spin band, it would seem unlikely that such a band could be overlooked.

The most basic difference between Fischer and Drickamers high pressure techniques and that used in this work is that pressure in a Drickamer cell (in which solid NaCl is used as the pressure transmitting medium) is far from hydrostatic. It may be that a shear stress is less effective in producing the high spin/low spin transformation. In the DAC, the high-low conversion occurs fairly sharply above 13 kbar. By 17 kbar, the intensity of the 324cm^{-1} (ambient) band suggests that some 75% of the sample may be expected to be low spin.



It is helpful to compare these spectra with those of $M(NCS)_6^{n+}$ ions (26, 27). Typically these show $\nu(M - N)$ at ca. 240, $\delta(NCS)$ near 470cm^{-1} and no further absorptions down to 150cm^{-1} . Similarly cis (Fe (Py)₄ NCSe) (28) shows;

ν CN	2070	$\nu(\text{Fe} - \text{NCS})$	266, 250
ν C = S	805	$\nu(\text{Fe} - \text{py})$	203
δ NCS	478, 482		

Hence for cis Fe (o-phen)₂ (NC X)₂ (X = S, Se), the NCX part of the spectrum from 200 to 400 should consist of $\nu(\text{Fe} - \text{NCX})$ (X = S, Se), the position of which is known from isotope work (16) and nothing else. Indeed $\nu(\text{Fe} - \text{NCS})$ is observed at 248cm^{-1} , and $\nu(\text{Fe} - \text{NCSe})$ at 229cm^{-1} .

Combining this with the general understanding of the Fe (o-phen)₂ I₂ and (N₃)₂⁻ spectra, we expect that the high - low spin transition will increase the number of bands in the 250cm^{-1} region due to the Fe-phen part of the molecule. Also, the drastic rise in ν Fe - NCX from 248 (X = S) and 229 (X = Se) will similarly raise $\delta(\text{Fe} - \text{NC})$ and other modes listed above. This would account for the new bands noted in this region. The presence of bands around 26 in both sets of spectra (at 21.7 kbar for X = Se, and 13.9 for X = S) supports the observations made for the I⁻ complex.

In the low spin form of $\text{cis-Fe}(\text{o-phen})_2\text{X}_2$ ($\text{X} = \text{NCS}, \text{NCSe}$ or N_3), $\nu(\text{Fe}-\text{Phen})$ and $\nu(\text{Fe}-\text{NX})$ are $> 350\text{cm}^{-1}$. Therefore the region below 350cm^{-1} should be similar in all three compounds, consisting, as it does, of similar deformations. Some differences should be observed due to the δ of Se mass differences.

Comparison of the 26.3 kbar $\text{X} = \text{NCS}$ spectrum with the 21.8 kbar $\text{X} = \text{NCSe}$ confirm this. Both have new bands at 304cm^{-1} and 264cm^{-1} , attributable to the Fe-phen system; and a similarly complex region from 240 to 300cm^{-1} for $\text{X} = \text{NCS}$ and from 200 to 300 for $\text{X} = \text{NCSe}$. Throughout this series, one strong band remains obstinately present in the 285 - 295 region. Its behaviour suggests that it is associated with o-phen itself, as the band is certainly not metal isotope sensitive. Free o-phen has no band in this region, but has a strong absorption at 259cm^{-1} . It is proposed that this band is raised by about 30cm^{-1} upon coordination, to become the resistant feature noted around 290cm^{-1} . If this is the case, the band originates in an in plane deformation of o-phen (ν_{21}).

Comparison of the results for $\text{Fe}(\text{phen})_2\text{NCS}$ obtained by Ferraro et al (17) under shear stress reveal a close correspondence between their work and the present.

8.5 Summary

High pressure far infrared spectra have been obtained for complexes of the form $\text{Fe}(\text{o-phen})_2\text{X}_2$ where $\text{X} = \text{I}, \text{N}_3^-, \text{NCS}^-, \text{NCSe}^-$. The vibrational spectra of these species have been theoretically analysed. For $\text{X} = \text{I}$ the high-low spin transformation does not appear complete by 28 kbar, whereas complete conversion by 40 kbar is apparent for $\text{X} = \text{N}_3^-$. The $\text{X} = \text{NCS}, \text{NCSe}$ spectra conform to the deductions drawn on the high pressure spectra of the simpler $\text{X} = \text{I}, \text{N}_3^-$ systems.

References

1. Tanabe, Y., Sugano, J., *J. Phys. Soc. Jpn*, 9 753, 756 (1954).
2. Drickamer, H.G., *Solid State Phys.* 17 1 (1965).
3. Drickamer, H.G., Zahner, M., *Adv. Chem. Phys.* 4 161 (1962).
4. References collected in Stoufer, R.C., Busch, D.H., Hadley, W.B., *J.A.C.S.* 83 3732 (1961).
5. Konig, E., *Coord. Chem. Rev.* 3 471 (1968).
6. Mason, S., *Inorg. Chim. Acta* 2 89 (1968).
7. Day, P., Sanders, N., *J. Chem. Soc.* (1967) A1530 A1536.
8. Madefa, K., Konig, E., *J. Inorg. Nucl. Chem.* 25 377 (1963).
9. Basolo, F., Dioyer, F.D., *J.A.C.S.* 76 1454 (1954).
10. Baker, W.A., Bobonich, H.M., *Inorg. Chem.* 2 1071 (1963).
11. Schilt, A.A., *J.A.C.S.* 82 3000 (1960).
12. Beck, W., Schurer, E., *Chem. Ber.* 95 3048 (1962).
13. Konig, E., Madeja, K., *Inorg. Chem.* 6 48 (1967).
14. Drickamer, H.G., Fischer, D.C., *J. Chem. Phys.* 54 4825 (1971).
15. Takemoto, J.H., Hutchinson, B., *Inorg. Chem.* 12 705 (1973).

16. Takemoto, J.H., Hutchinson, B., Inorg. Nucl. Chem. Lett. 8 769 (1972).
17. Ferraro, J.R., Takemoto, J.H., Applied Spectroscopy 28 66 (1974).
18. Takemoto, J.H., Hutchinson, B., Nakamoto, K., JACS 92 3335 (1970).
19. Altmann, W., Perkampus, H.H., Spectrochim. Acta. 35A 25 (1979).
20. Altmann, W., Klundienst, H., Perkampus, H.H., Spectrochim. Acta. 35A 259 (1979).
21. Cotton, F.A., Wilkinson, G., Advanced Inorganic Chemistry 2nd Edition p 852.
22. Saito, Y., Takemoto, J., Hutchinson, B., Nakamoto, T.K., Inorg. Chem. 11 2003 (1972).
23. Konig, E., Watson, K.J., Chem. Phys. Lett. 6 457 (1970).
24. Clarke, R.J.H., Crosse, B.C., Chem. Ind. 1593 (1969).
25. Nakamoto, K., Tevault, F., Tani, S. J Mol Struct 43, 75 (1978)
26. Sabatini, A., Bertini, I., Inorg. Chem. 4 959 (1965).
27. Hellner, E., Naturis 61 502 (1974).
28. Clarke, R.J.H., Williams, C.S., Spectrochim. Acta 22 1081 (1966).

VIBRATIONAL SPECTROSCOPY AT HIGH PRESSURES

ALAN DAVID WILLIAMS

ABSTRACT

A review of high pressure work is presented with over 100 references spanning the period from October 1976 to March 1979. A full discussion is given of the history of Diamond Anvil Cell (DAC) design.

Two new designs of DAC are tested, as are two different types of diamond anvil. Pressures in excess of 0.25 Megabars have been generated, and a study of benzene has been undertaken to test one of the new cells.

Mid and far infrared spectra of ferrocene were recorded and compared with existing data on the solid state properties of this material.

Raman and far infrared spectra of K_2PtCl_6 and K_2ReCl_6 at various temperatures and pressures have been obtained, and with thermal expansion and compressibility data, an attempt to relate the frequency shifts to anharmonic parameters has been performed. This study was extended to cover the pressure dependence of a further ten compounds of the form A_2MX_6 .

The phase behaviour of calcite ($CaCO_3$) has been examined using mid and far infrared spectroscopy to 40 kbar, and the data analysed in conjunction with the results of Fong and Nicol.

The effect of pressure and hence spin state on the far infrared spectra of some complexes of the form $Fe(phen)_2X_2$ has been studied.